Imperial College London

Model-based Aeroservoelastic Design and Load Alleviation of Large Wind Turbines

Bing Feng, Ng

Supervised by Dr. Rafael Palacios,
Prof. J. Michael R. Graham and Dr. Eric C. Kerrigan

Imperial College London
Department of Aeronautics

This thesis is submitted for the degree of
Doctor of Philosophy and the Diploma of Imperial College London.

2014

Declaration

The work in this report is based on research in Imperial College London. No part of this report had been submitted elsewhere and are all of the author's own work unless otherwise stated or referenced in the text.

The copyright of this thesis rests with the author and is made available under a Creative Commons Attribution Non-Commercial No Derivatives licence. Researchers are free to copy, distribute or transmit the thesis on the condition that they attribute it, that they do not use it for commercial purposes and that they do not alter, transform or build upon it. For any reuse or redistribution, researchers must make clear to others the licence terms of this work.

Bing Feng

Acknowledgement

My utmost gratitude goes to my primary academic supervisor, Dr. Rafael Palacios for being the beacon of light, patiently and constantly guiding me through the years of my research pursuit. Rafa has been an excellent mentor, always willing to listen and constantly offering brilliant ideas to push the research boundaries. I am truly grateful to have him as my supervisor for which he had been, and will always be, the inspiration/role model of my life. I am also extremely thankful to have Professor J. Michael R. Graham and Dr. Eric C. Kerrigan as my co-supervisors. Mike has been the source of wisdom with enormous wealth of knowledge and experience to share. Eric has been the source of ideas, navigating me through different perspectives that not only adds momentum to the project, but also proved that research is without limits.

I am grateful to have Professor William Edward Leithead from University of Strathclyde and Dr Joaquim Peiró from Imperial College London as my examiners. I would like to thank them for their time, dedication, and the insightful comments/suggestions to improve the quality of this dissertation.

I would also like to thank Dr. Henrik Hesse whom I had collaborated with to adapt the structural description in SHARP for wind turbine applications. We had spent numerous hours working together to overcome the challenges in making sure the structural dynamics of wind turbine were correctly implemented. He had been a truly wonderful colleague and a worthy mate I can trust. Through the course of the project, I also had the opportunity to work with Bart Van Parys from ETH Zurich to apply a control strategy he developed on my aeroelastic model. I would like to thank him for not only widening the scope of the current project, but also giving me the opportunity to learn a lot beyond my focus area. Further to that, I am thankful to past and present members of the Aeroelastics and Controls groups, separately, for making my time in Imperial College a terrific and memorable experience.

The sponsor for my PhD is the Singapore Innovation Programme Office (EIPO), managed by the Economic Development Board (EDB) administering the National Research Foundation Clean Energy Scholarship. I am particularly grateful to EDB which gave me this opportunity, for which I would like to express my sincere gratitude to Mr Sia Kheng Yok and Mr Goh Chee Kiong. I am also thankful to Cecilia, Li Shan and Shirley from EIPO for all the administrative

assistance and student welfare they have provided through the course of my PhD.

Beyond academic pursuits, I had been involved in student-led activities such as the Imperial College Energy Society and the Rector's Ambassadors programme. They offered me moments of respite from the piles of workload and the chance to work with brilliant people in organising activities and developing skills that are beyond the classrooms. My appreciation goes to Dr. Abraham Edo and to everyone whom I had worked with for creating the lasting and wonderful memory.

My journey to the achievements today had not been smooth and I am fortunate that there are many people along the way who had offered me their lending hands. In particular, I would like to thank Mr Eddie Koh and all the teachers from my Junior College, who are the pivots in my teenage years, changing my perspective of studies, giving me the confidence, encouragement and opportunity to shine. Looking back, it was the life-changing point in my life that made me appreciate the importance of academic pursuits. I would also like to thank Dr. Daniel P. Thunnissen, Dr. Jörg Uwe Schlüter, Dr. Sutthiphong Srigrarom, Dr. Kuan Tek Seang and all the past and present faculty members of Nanyang Technological University Aerospace Department who had coached and inspired me to pursue a PhD. In addition, my heartfelt gratitude to LTC Yeo King Wat from SAFTI SSC for being my mentor and guidance during the two and a half years of military service, instilling the independence and resilience that came in useful for me to tide through the PhD.

Despite the many roadblocks through the journey here, my parents had always been there for support and encouragement. I humbly dedicate this work to them and is greatly indebted to all they have given me for what I am today. No matter how far the journey had been and the many years I am away from them, they are always listening, caring and concerning for my well-being. There is just endless amount of thanks I would like to say to them.

Abstract

With the increase in size of wind turbine for larger energy capture, aeroelastic effects previously not seen in smaller rotors are beginning to surface as a result of increased blade flexibility. This has brought about new needs in terms of modelling requirements and methods of load control to improve the fatigue life of turbine blades. This dissertation presents an aeroservoelastic modelling approach for dynamic load alleviation in large wind turbines with trailing-edge aerodynamic surfaces. Time-domain aerodynamics are given by a linearised three-dimensional unsteady vortex-lattice method that allows better characterisation of aeroelastic responses under attached flow conditions and the direct modelling of lifting surfaces. The resulting unsteady aerodynamics is written in a state-space formulation suitable for model reductions and controller design. This approach does not rely on empirical corrections commonly found in Blade Element Momentum methods. Structural modules of the tower, potentially on a moving base, and the rotating blades are modelled using geometrically non-linear composite beams, which are linearised around reference conditions that have undergone arbitrarily-large structural displacements.

The land-based NREL 5MW reference wind turbine is chosen to demonstrate the unified aeroelastic framework, in which the coupled rotor and tower description is modelled to examine both the aeroelastic effects and potential of load alleviation. In the presence of realistic wind fields, turbine blade root-bending moments and tower deflections can be reduced by 13% using active control methods. When combined with passive mechanisms through bend-twist coupling, performance can be improved to more than 40%. The baseline configuration is further extended to cover offshore floating wind turbine concepts. The focus of this dissertation is to provide higher-fidelity efficient numerical models for linear robust controller design (LQG and $\mathcal{H}_\infty$), to achieve load alleviation in larger and more flexible wind turbines.

Contents

1 Introduction **25**

1.1 Motivation 25

1.2 Aeroelastic Modelling 29

1.3 Passive Mechanisms 32

1.4 Controllers 33

1.4.1 PID Controls 33

1.4.2 General Control Configuration 34

1.4.3 Linear-quadratic Gaussian 34

1.4.4 $\mathcal{H}_\infty$ 35

1.5 Sensors 36

1.6 Actuators 37

1.7 Active Control Devices 37

1.7.1 Trailing-Edge Flaps 38

1.7.2 Variable Aerofoil Geometry 39

1.7.3 Other Active Control Devices 40

1.7.4 Comparison of Active Control Devices and Summary 41

1.8 Research Objective 43

1.9 Present Approach 43

1.10 Outline of Thesis 45

1.11 Publications 46

2 Theoretical Formulation of Aeroelastic Model **51**

2.1 The Composite Beam Model 51

2.1.1 Beam Equations of Motion 52

2.1.2 Flexible Multi-body Dynamics 53

2.1.3 Linearised Description 55

2.2 The Unsteady Vortex-Lattice Method 56

2.2.1 Potential Flow Theory . . . 56
2.2.2 General Solution based on Boundary-Element Method . . . 57
2.2.3 Physical Considerations of Wake Dynamics . . . 57
2.2.4 Linearised Description of Time-domain UVLM . . . 58
2.2.5 State-Space UVLM Description . . . 61
2.2.6 Computation of Aerodynamic Forces . . . 61
2.3 Fluid-Structure Coupling . . . 62
2.4 Model Reduction of the Coupled Aeroelastic Description . . . 64
2.5 Final Aeroelastic Equations . . . 66

3 Numerical Verification and Implementation 69
3.1 Numerical Verification of Blade Definition . . . 70
3.2 Baseline Wind Turbine . . . 72
3.2.1 NREL 5MW Reference Wind Turbine . . . 73
3.2.2 Numerical Implementation and Verification . . . 73
3.2.3 Controller Description . . . 78

4 Numerical Simulations on Land-based NREL 5MW turbine 81
4.1 Sectional Model . . . 82
4.1.1 Load Reduction using Controllers from Converged Models . . . 82
4.1.2 Controller design with Spatially Coarse Vortex Aeroelastic Model . . . 84
4.2 Single Rotating Blade . . . 85
4.2.1 Aerodynamic Loading . . . 85
4.2.2 Rotating Aerodynamics . . . 87
4.2.3 Parameter Sizing . . . 88
4.2.4 Load Reductions in Single Rotating Blade . . . 89
4.2.5 Non-Linear Comparison . . . 91
4.2.6 Torsional Effects . . . 92
4.3 Land-Based NREL 5MW Turbine . . . 93
4.3.1 Wind Field . . . 94
4.3.2 Tower Shadow . . . 96
4.3.3 Model Reduction . . . 98
4.3.4 Passive Load Alleviation . . . 101
4.3.5 Active Load Alleviation . . . 105
4.3.6 Combined Passive and Active Load Alleviation . . . 112
4.3.7 Frequency Targeted Load Reduction . . . 115

4.4 Pitch Controls . . . 117
4.4.1 Individual Pitch Control . . . 119
4.4.2 Cyclic Pitch Control . . . 119
4.5 Summary . . . 122

5 Floating NREL 5MW Turbine with Spar Buoy 123
5.1 Floating Platform and Ballast . . . 124
5.2 Wave Kinematics . . . 128
5.3 Aeroelastic Offshore Turbine Formulation . . . 129
5.4 Numerical Verification . . . 131
5.5 Closed-Loop Performance . . . 132

6 Conclusions 139
6.1 Summary . . . 139
6.2 Key Contributions . . . 140
6.2.1 Methodology . . . 141
6.2.2 Results . . . 143
6.3 Recommendations for Future Work . . . 144
6.3.1 Improvements/Additions to Existing Simulation Framework . . . 145
6.3.2 Improvements to Control Methodology . . . 147

APPENDICES 149

A Two-dimensional Vortex Particle State-Space Aeroelastic Implementation 151
A.1 Two Degrees-of-Freedom Aerofoil . . . 151
A.2 Unsteady Aerofoil Aerodynamics . . . 152
A.3 Fluid-Structure Coupling . . . 155
A.4 Sectional Model Numerical Verification . . . 156

B Three-dimensional Vortex-Panel State-Space Aeroelastic Implementation 157
B.1 System Matrices . . . 157
B.2 Downwash Computation . . . 158
B.3 Pressure Distribution . . . 162
B.3.1 Drag . . . 163
B.3.2 Forces and Moments . . . 164
B.4 Multiple Lifting Surfaces in Full Rotor Configuration . . . 164
B.5 State-Space Coupling . . . 166

B.5.1 Discretisation of Structural Dynamics 166
B.5.2 Aerodynamic Force Mapping 167
B.5.3 Fluid Structure Coupling 168

C Analytical Solution to Rotating Beam **169**
C.1 Out-of-plane Bending 169
C.2 In-plane Bending 171
C.3 Torsion 171

D Damage Equivalent Loads **173**

E Model Reduction on Combined Rotor Description **177**

Bibliography **179**

List of Figures

1.1 Summary of load sources on a wind turbine [145]. 26

1.2 Block diagram for *smart rotor* concept. 29

1.3 General control configuration [215]. 34

1.4 Blade section with conventional (rigid) flap and variable trailing-edge geometry (deformable) [18]. 39

2.1 Multi-beam configuration with the definition of reference frames for the rotor model. 52

2.2 Multi-body configuration with the definition of reference frames for the combined rotor and tower model. The abbreviation FoR stands for Frame of Reference. 54

2.3 Typical thin lifting surface represented by the unsteady vortex-lattice method. 59

2.4 Coupling between fluid and structure. 62

2.5 Simplified block diagram of fluid-structure coupling in the aeroelastic model and closed-loop configuration with external controllers. 64

3.1 Campbell plots comparing fundamental modes of a simple rotating cantilever beam computed using the current model and analytical solutions. 70

3.2 Impact of increasing rotational effects on the Goland wing (by varying the distance between the axis of rotation and the root of the wing) on flutter tip speeds. Results are normalised against the forward flight flutter speed. 71

3.3 Root locus for the first two modes (out-of-plane bending and torsion) of the Goland wing. Case 1 - Rotational effects in both UVLM and structural model (rotational tip speeds from 80 m/s to 200 m/s). Case 2 - Rotational effects accounted for in UVLM only (rotational tip speeds from 80 m/s to 200 m/s). Case 3 - No rotational effects (rotational tip speeds from 80 m/s to 170 m/s). 72

3.4 Graphical interpretation of the NREL 5MW offshore wind turbine. The gearbox and generator are merged with the nacelle as a single point mass in the modelling, but are shown here for completeness. 74

3.5 Aerodynamic and structural models used to represent the NREL 5MW reference wind turbine. (For the purpose of clarity in visualisation of the aerodynamic wake profile, four chordwise panels (instead of 20) are used to generate the figure.) 75

3.6 Normalised flapwise aerodynamic loads for a single rotating blade and for the full rotor, subjected to an impulsively started gust. (Vertical dotted lines indicate each time a blade has rotated 120°) 76

3.7 Normalised tower top out-of-plane deflection for a stationary (parked) turbine when subject to an out-of-plane force at the blade tip. Comparing a multi-beam configuration with the constrained multi-body description. 76

3.8 Stationary mode shapes of the NREL 5MW reference wind turbine in parked configuration. The abbreviations are: Bl (Blade), Tw (Tower), SS (Side-Side), FA (Fore-Aft), DT (Drivetrain), Tor (Torsion), Asym (Asymmetric), FY (Flapwise-Yaw), FP (Flapwise-Pitch), Coll (Collective), EP (Edgewise-Pitch), EY (Edgewise-Yaw). 77

3.9 Bode plot of full aeroelastic system from gust input to blade flapwise tip deflection on one of the rotor blades (parked). Flexible tower has stiffness in the NREL 5-MW tower reduced by factor of three. 79

3.10 Time-series showing the flapwise tip deflection of the three rotor blade in response to homogeneous gust of 10% turbulence intensity (original NREL tower). 79

3.11 Simplified block diagram of control model. 80

4.1 Closed-loop block diagram for sectional model, containing turbulence filter and double integrator. 83

4.2 Section of time-series for C_L in open and closed-loop using LQG and $\mathcal{H}_\infty$ controllers. Two-dimensional case. 84

4.3 Performance of low order panel model for controller design (Figures are plotted with reducing number of panels per chord on horizontal axis). 85

4.4 Normalised spanwise aerodynamic lift on the rotating NREL 5MW blade resulting from 10° pitch. UVLM has 50 spanwise panels, 10 chordwise panels and 10 wake chords. 86

4.5 Normalised spanwise aerodynamic lift on the rotating NREL 5MW blade resulting from 10° flap actuation. UVLM has 50 spanwise panels, 10 chordwise panels and 10 wake chords. Flap occupies 10% local chord and 20% span. . . 86

4.6 Normalised aerodynamic lift with a harmonic 10° flap actuation of 1.0Hz and 2.0Hz. 87

4.7 Bode plot from a homogeneous gust input to blade flapwise RBM for the NREL blade. Four cases are considered. They include (1) blade in forward motion without rotational effect, (2) rotational effect in structures only, (3) rotational effect in aerodynamics only, (4) rotational effect in both aerodynamics and structures. 88

4.8 Effect of LQG controller on the rms reduction in blade flapwise RBM with varying flap locations along the span of the blade (Flap measures 10% span and 10% chord). 89

4.9 Reduction in rms of blade flapwise RBM and tip deflection with varying flap sizes (Mean position of flap is at 80% span). 90

4.10 Illustration of flap occupying 20% span, 10% of local chord and located at a mean position of 80% span, and the complete turbine model with flaps attached to each blade. 90

4.11 Section of the time-series for blade flapwise RBM, flapwise tip deflection, flap deflection angle, inflow and torsion. 91

4.12 Open and closed-loop tip deflection of the linear (thin-lines) and non-linear (thick-lines) models. 92

4.13 Trade-off between blade flapwise RBM and torsion in using active flap controls. 93

4.14 Flow-chart to illustrate the major steps adopted in the simulation of the full turbine model. 94

4.15 Sample wind field from Turbsim with overlaying turbine rotor and tower. . . 96

4.16 Tower shadow. 97

4.17 Tower deficit close to hub and at bottom of rotor plane for the NREL 5-MW turbine. For deficit at bottom of rotor plane (vertical), the rotor plane is vertical and at 5m ahead from the tower centreline ($x = 5$). For deficit at bottom of rotor plane (with pitch), rotor plane is pitched at 5° as per the NREL 5-MW configuration. 97

4.18 PSD of flapwise RBM for one of the rotor blades on the full turbine when subject to full wind field, including wind shear effects, and (1) no tower shadow, (2) tower shadow with a 5° rotor pitch and (3) tower shadow without rotor pitch. 98

4.19 Bode plot from homogeneous gust input to flapwise RBM and root torsion on one of the rotor blades at an instantaneous azimuth angle $\theta = 0°$. Comparing the effects of truncating structural modes on rotor by keeping the lowest (i) 60 rotor modes, (ii) 140 rotor modes and (iii) all rotor modes. In the above cases, all tower structural modes and aerodynamic states are kept. 100

4.20 Normalised Hankel Singular Values of the balanced UVLM model with respect to the largest HSV. 101

4.21 Bode plot from homogeneous gust input to blade flapwise RBM and root torsion on one of the rotor blades at an instantaneous azimuth angle $\theta = 0°$. Comparing the effect of keeping 350 aerodynamic states (with 10 tower and 140 rotor structural modes). Full model has all structural modes and aerodynamic states. 102

4.22 Illustration of twist-towards-feather and twist-towards-stall using a simple rectangular surface that is clamped on its right end and bending upwards. 103

4.23 Root locus of the NREL blade for varying degrees of elastic coupling. 104

4.24 Open-loop flapwise RBM, torsion and tower fore-aft deflection with varying degrees of elastic coupling α for the NREL wind turbine. Results are averaged across six turbulence seeds and normalised against their respective rms values at $\alpha = 0$. 105

4.25 Open and closed-loop Bode plots from homogeneous gust input to flapwise RBM on one of the rotor blades at an instantaneous azimuth angle $\theta = 0°$. Using $\mathcal{H}_\infty$ controlled trailing-edge flaps. 106

4.26 Section of time-series for the full wind turbine configuration without elastic coupling. 108

4.27 PSD of flapwise RBM on one of the rotor blades in open/closed-loop without elastic coupling. Comparing controllers tuned to 10° and 30°. 109

4.28 Closed-loop flap deflection angle using different controllers with tuning on maximum $|\beta|$ to the limits of 10° and 30°. 109

4.29 Root locus on a single NREL blade as torsional stiffness is reduced from its original value (blue circle) to 14% stiffness (red star) in intervals of 2%. . . . 110

4.30 Bode plot from flap input to blade flapwise RBM on the NREL blade as torsional stiffness is reduced. 111

4.31 Percentage reduction in flapwise RBM and open-loop rms values as torsional stiffness is reduced on a single rotating blade. 111

4.32 PSD of flapwise RBM on one of the rotor blades in open/closed-loop with and without elastic coupling. 113

4.33 Frequency responses of the second-order low, high and band-pass filters ($\omega_c = 0.5$Hz, $Q = \frac{1}{\sqrt{2}}$, $k = 1$). 116

4.34 PSD of RBM for comparing different closed-loop models with controller targeting specific frequency regions. 118

4.35 Open and closed-loop Bode plots from homogeneous gust input to flapwise RBM on one of the rotor blades at an instantaneous azimuth angle $\theta = 0°$. Using $\mathcal{H}_\infty$ controlled IPC and flap. 120

4.36 Open and closed-loop PSD of flap and individual pitch controls. 121

4.37 Open and closed-loop PSD of cyclic pitch control alone and with flaps. 121

5.1 Floating turbine with spar buoy and mooring system. 124
5.2 Configuration of floating platform (including ballast). 126
5.3 Comparing the Pierson-Moskowitz and JONSWAP spectrums. 130
5.4 Resulting platform motion of the stationary floating turbine with a regular Airy wave of height 6m and period 10s. To avoid exciting high frequency dynamics, a ramp function is prescribed for the first 100s of wave input. . . 132
5.5 Resulting tower-top fore-aft elastic deformation of the stationary floating turbine with a regular Airy wave of height 6m and period 10s. 132
5.6 Resulting platform motion of the stationary floating turbine subjected to Pierson-Moskowitz wave. To avoid exciting high frequency dynamics, a ramp function is prescribed for the first 50s of wave input. 133
5.7 Resulting tower-top fore-aft elastic deformation of the stationary floating turbine subjected to Pierson-Moskowitz wave. 133
5.8 Resulting blade tip out-of-plane deflections of the stationary floating turbine subjected to Pierson-Moskowitz wave. 133
5.9 PSD of flapwise RBM on one of the rotor blades in open-loop, comparing the land-based and floating turbine with regular and irregular waves (all in the presence of full wind field). 134
5.10 PSD of flapwise RBM on one of the floating wind turbine rotor blades in open and closed-loop with active load alleviation alone. In the presence of irregular wave, wind shear and turbulence inflow. 135
5.11 PSD of flapwise RBM on one of the floating wind turbine rotor blades in open and closed-loop with passive and active load alleviation. In the presence of irregular wave, wind shear and turbulence inflow. 135
5.12 PSD at low frequencies of tower top fore-aft deflection in open and closed-loop with passive and active load alleviation. In the presence of an irregular wave and a full wind field. 138

A.1 2-dof Structural Model. 152
A.2 Normalised pressure distribution across aerofoil in pitch and flap actuation, both delivering the same amount of aerodynamic lift force (Using 50 equally distributed vortex particles on the aerofoil and keeping a wake of 5 chord lengths). 155
A.3 Flutter boundaries of 2-dof aerofoil. Verifying current Wagner and vortex aeroelastic descriptions with Murua et al. [169]. ($a = -0.3$, $\kappa = \frac{\pi\rho b^2}{M} = 0.05$, $r_\alpha^2 = 0.25$, $b = 1.0$) 156

B.1 Simplified model definition of panel distribution. 158

D.1 M-N curve (Note that if plotted on log-log scale, this will be a straight line). 174

D.2 Goodman relationship. 175

List of Tables

1.1 Overview of wind turbine commercial and research aeroelastic codes that are used for active load alleviation [3, 68, 128, 190]. The abbreviations are, EB (Euler-Bernoulli), MBS (Multi-body dynamics), FE (Finite-element), GNCB (Geometrically non-linear composite beam), 2D (two-dimensional), elem (elements). 28

1.2 Table summarising the modelling, control and performance of variable trailing-edge (TE) geometries and rigid flaps in active load alleviation. All land-based configurations. Unless otherwise stated, all loads are referred to as the blade flapwise/out-of-plane root-bending moments. 48

3.1 Cantilever beam properties with uniform mass and stiffness distribution. (Verification case) 70

3.2 Full system natural frequencies (Hz) of the NREL 5MW wind turbine (stationary) for structural discretisation of (a) 10 tower elements and 48 elements on each blade (same as documentation [129]) and (b) 10 tower elements and 12 elements on each blade (interpolated blade properties). 78

4.1 Closed-loop performance of the NREL 5MW turbine using active flap controls across six different turbulence seeds. Negative sign implies an increase. The abbreviation %rd stands for percentage reduction. 106

4.2 Closed-loop performance using different controllers with tuning on maximum $|\beta|$ varied from 10° to 35°. For percentages, they are averaged across six turbulence seeds and for $\dot{\beta}$, the maximum values among the seeds are shown. The abbreviations are: Cont (Controller), %rd (percentage reduction), bl (blade), tw (tower), FA (Fore-Aft), def (deflection). 109

4.3 Closed-loop performance of the NREL 5MW turbine with different degrees of bend-twist coupling α from Eq. (4.8). Note that the percentage reductions without parenthesis are the additional reductions due to flaps on top of the reductions delivered by the individually bend-twist coupled blades. The percentage reductions in parenthesis (*total*) represent the performance of combined active flap control and bend-twist coupling. The abbreviation %rd represents percentage reduction. 114

4.4 Performances with high, low and band-pass filters in measurement output. The abbreviations are: %rd (percentage reduction) and tor (torsion). 117
4.5 Performances of individual pitch control against flaps (IPC/flaps). The abbreviations are: %rd (percentage reduction) and tor (torsion). 120
4.6 Performances of cyclic pitch controls alone and with flaps. The abbreviations are: %rd (percentage reduction) and tor (torsion). 121

5.1 Full system natural frequencies (Hz) of the NREL 5MW wind turbine in stationary configuration, comparing land-based and floating tower configurations (fixed-bottom without floating platform). 125
5.2 Horizontal and vertical particle velocity and acceleration for deep seas [166]. . 128
5.3 Closed-loop alleviation of blade loads on the floating NREL 5MW wind turbine under the action of a full wind field in combination with regular and irregular waves. Comparing (1) active flaps alone (2) active flaps with filtered measurements (3) combined passive ($\alpha = -0.4$) and active mechanisms. The percentage reductions in parenthesis (*total*) represent the performance of the combined active flap control and bend-twist coupling. The abbreviations are: Config (Configuration), %rd (percentage reduction), tor (torsion), Fl (Floating), reg (regular wave), irr (irregular wave), lp (low-pass). 137
5.4 Closed-loop passive ($\alpha = -0.4$) and active load alleviation of the tower top fore-aft deflection on the floating NREL 5MW wind turbine. In the presence of full wind field in combination with regular or irregular waves. The abbreviations are: Config (Configuration), %rd (percentage reduction), Fl (Floating), reg (regular wave), irr (irregular wave), lp (low-pass), FA (fore-aft motion). . 138

Nomenclature

Symbols

a	Wave amplitude (given by half the wave height)
b	Half chord length
Δb	Spanwise bound panel size in UVLM
c	Chord length
Δc	Chordwise bound panel size in UVLM
g	Gravitational acceleration (9.81ms^{-2})
h	Plunge
k	Reduced frequency
k_α	Pitch stiffness
k_h	Plunge stiffness
m_c	Total number of bound chordwise panels in UVLM
m_k	Total number of bound panels in UVLM
m_n	Number of structural beam nodes excluding clamped end
m_s	Total number of bound spanwise panels in UVLM
m_w	Total number of wake panels in UVLM
n	Time step
n_z	Normal vector to panel surface
r_α	Aerofoil's radius of gyration (normalised by b)
t	Time
u	Controller input
v	Measurement noise
$\boldsymbol{w}$	Aerodynamic downwash
$\boldsymbol{x}$	System states
x_α	Chordwise distance from centre of gravity to elastic axis (normalised by b)
x_c^{ea}	Chordwise distance from collocation point to elastic axis
x_c^h	Chordwise distance from collocation point to flap hinge
x_{ea}	Chordwise location of elastic axis
x_v	Chordwise location of vortex point
y	System output
y_c	Spanwise location of collocation point
A	Rotor swept area

$\boldsymbol{A}$	Aerodynamic influence coefficient matrix
C_L	Coefficient of lift
C_M	Coefficient of moment of aerofoil about elastic axis
C_D	Coefficient of drag
D	Drag
$\boldsymbol{F}_{ms}$	Hydrodynamic force
$\boldsymbol{F}_{buo}$	Buoyancy force
$\boldsymbol{F}_{ml}$	Mooring line force
H_s	Significant wave height
I_α	Aerofoil moment of inertia about elastic axis
I_β	Flap moment of inertia about flap hinge
L	Lift
M	Mass of system
$\boldsymbol{\mathcal{M}}$	Discrete mass matrix
M_α	Moment of aerofoil about elastic axis
$\boldsymbol{Q}_{gyr}$	Generalised gyroscopic forces
$\boldsymbol{Q}_{stif}$	Generalised stiffness forces
$\boldsymbol{Q}_{ext}$	Generalised external forces
S_α	Static moment of aerofoil about elastic axis
$\boldsymbol{T}$	Transformation matrix
T_p	Peak wave spectral period
U_∞	Velocity of flow

Greek Symbols

α	Pitch angle
α_{rp}	Rotor plane pitch with respect to vertical
β	Flap deflection angle
δ	Additional angle of attack due to gust
$\boldsymbol{\eta}$	Nodal displacements and rotation
Γ	Vortex circulation strength
κ	Inverse mass ratio
λ	Lagrange multiplier
$\boldsymbol{\nu}$	Rigid-body velocities
ω_α	Natural frequency of pitch mode
ω_h	Natural frequency of plunge mode
ω_w	Wave frequency
Ω	Angular velocity of rotor
ϕ	Mode shape
$\boldsymbol{\Phi}$	Constraint function
ρ	Density of air at sea level (1.225kgm^{-3})
ρ_w	Density of water (1,000kgm^{-3})

τ_i	Tangential vector in chordwise direction
τ_j	Tangential vector in spanwise direction
θ	Azimuth angle of rotation
Θ	Azimuth angle between blades and vertical
φ	Velocity potential

Sub-, Superscripts

$(\bullet)_0$	Equilibrium conditions
$(\bullet)_\infty$	Free-stream values
$(\bullet)_b$	Blade representation
$(\bullet)_{ext}$	External representation
$(\bullet)_{gyr}$	Gyroscopic representation
$(\bullet)_k$	Collocation point representation
$(\bullet)_r$	Rotor representation
$(\bullet)_s$	Hub representation
$(\bullet)_{stif}$	Stiffness representation
$(\bullet)_t$	Tower representation
$(\bullet)_w$	Wake representation
$(\bullet)_S$	Structural degrees of freedom
$(\bullet)_R$	Rigid-body degrees of freedom
$(\bullet)_\beta$	Flap representation
$(\bullet)_\delta$	Gust representation
$(\bullet)_\eta$	Structural representation
$(\bullet)_\nu$	Rigid-body representation
$\dot{(\bullet)}$	Derivative with respect to time t
$(\bullet)'$	Derivative with respect to space

Abbreviations

AoA	Angle-of-attack
BEM	Blade element momentum
C.G.	Centre of Gravity
DEL	Damage equivalent load
dof	Degree of freedom
EoM	Equation of motion
FoR	Frame of reference
GNCB	Geometrically non-linear composite beam
HAWT	Horizontal-axis wind turbine
nP	Number-per-revolution (1P, 2P, etc.)
PSD	Power Spectrum Density
rms	Root-mean-square
RBM	Blade root-bending moment (flapwise/out-of-plane)

TSR	Tip speed ratio
UVLM	Unsteady vortex-lattice method

Chapter 1

Introduction

1.1 Motivation

Wind turbines have been increasing in size over the past decade, both in terms of tower height and rotor diameter. At the time of writing, the largest wind turbines in operation have rotors measuring above 120m in diameter, while rotors of up to 160m are already being developed [240, 209, 85, 81, 76]. Aeroelastic effects previously not seen in smaller rotors are beginning to surface as a result of increased flexibility from the longer blades [102]. This has brought about new needs in terms of modelling requirements, as blade flexibility may have a significant effect on the performance characteristics of turbines. It also poses new technological challenges, in particular, with respect to an increased need for methods of load control to improve the fatigue life of turbine blades [30]. The situation is compounded as they are moved offshore with land becoming scarce; further offshore, they have to be placed on floating structures, resulting in a coupling of loads from both wind and wave kinematics. In fact, in the report published by the International Energy Agency on 'Global research and development needs up to year 2030', the development of advanced rotor concepts for load alleviation is one of the key sources to reducing the cost of wind energy [2].

The rationale for the up-sizing of the rotor is for larger energy capture, which can be observed through the power-output relationship of a wind turbine [200] expressed as

$$P = \frac{1}{2}\rho C_p A U_\infty^3 \,, \tag{1.1}$$

where a doubling in wind speed increases power by eight times [161, 100]. In Eq. (1.1), P is the power output, ρ is density of air at hub height, C_p is the coefficient of power, A is rotor swept area and U_∞ is the free-stream velocity. A fundamental challenge in this up-scaling of turbines is the overcoming of increased bending loads resulting from the larger mass and flexibility of the blades. Furthermore, this increase in flexibility leads to reductions in natural frequencies, potentially increasing oscillations and bringing down stability margins.

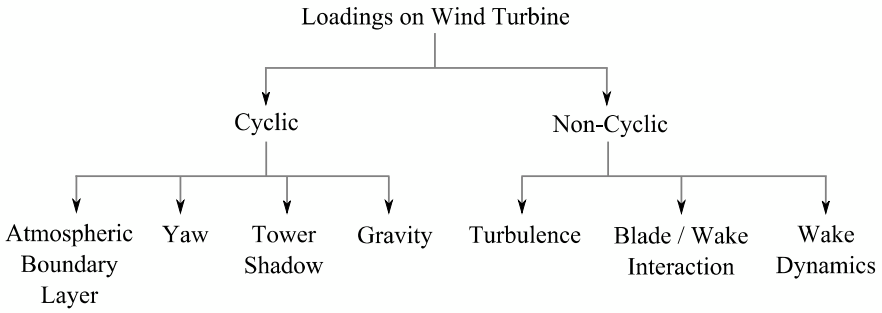


Figure 1.1: Summary of load sources on a wind turbine [145].

There are in general two types of loadings acting on wind turbines - steady and unsteady. Steady loadings depend on average wind speeds and directions and are often known through forecast or measurements. It is the unsteady loadings that are of concern, and can be further broken down into cyclic and non-cyclic loadings [55, 48]:

1. Cyclic loadings are periodic over each rotation of the turbine and can be corrected using blade pitch.

2. Non-cyclic loadings cause vibrations and extremes in loadings, thereby reducing the fatigue life of turbine blades [229].

A summary of the sources of cyclic and non-cyclic loadings is shown in Figure 1.1, highlighting the complicated environment that wind turbines operate in [145]. In this dissertation, atmospheric boundary layer, tower shadow, turbulence and blade/wake interaction will be considered.

Most turbines today are equipped with pitch control mechanisms for speed regulation and with simple re-design, can also be considered for load alleviation [42]. However, their responses may be slow and limited by the inertia of the blades [229]. Furthermore, given the long span of turbine blades, coupled with aerodynamic loadings along different sections, the resulting pitch angle may differ spanwise due to torsional flexibility. The propagation of pitching moments from blade root to tip is also not instantaneous, making full and spontaneous compensation of rapidly fluctuating loads unlikely. Hence, we require innovative blade designs with sophisticated localised active control techniques to maintain steady loadings and reduce vibrations. These active control surfaces can work in conjunction with existing pitch controls and they act to alleviate higher frequency loadings while blade pitch tackles lower frequency disturbances.

In recent years, there has been a growing interest in adopting actively controlled surfaces for load alleviation on turbine blades. Much of the technology is borrowed from aircraft applications for gust load alleviation [66, 67] and helicopter blades for vibration control and noise reductions [144, 36, 199]. Some of these concepts include the use of trailing-edge flaps,

microtabs, camber control and active twist [18]. They are commonly known as *smart rotor* concepts that combine sensors, actuators and controls for active load alleviation. Apart from control for load alleviation, *smart rotor* concepts can potentially also be used to augment power capture in below rated wind speeds [216].

While *smart rotor* concepts are mature in air vehicles, they are not readily transferable to wind turbine applications. They operate in different conditions where loadings could vary in type and in scale. For instance, wind turbines are much larger in size and their blades are subject to greater stresses. Also, inspection and maintenance on wind turbines happen less frequently than on air vehicles due to difficulty in ground access. To date, most of the investigations into *smart rotor* concepts on wind turbines had been numerical with only a couple of experiments for proof-of-concept. It is still a relatively young subject in wind energy with numerous challenges to overcome, mainly the modelling, control, implementation and finally gaining confidence and acceptance from industry.

The study of *smart rotor* concepts requires a multi-disciplinary approach, encompassing structures, aerodynamics and controls, forming the aeroservoelastic framework. A number of commercial and research aeroelastic design codes have been developed with such capabilities, including NREL's open-source FAST, DTU's FLEX5, DTU Wind's HAWC2, TU Delft's DU_SWAMP, and GL Garrad Hassan's Bladed, among others [127, 185, 141, 20, 43, 128, 190]. These well-established design codes had gone through extensive numerical and experimental validations and have been widely adopted by wind engineers. A review of these codes used for active load alleviation is documented in Table 1.1. It is evident that BEM dominates the list for the aerodynamics modelling, and accompanying it are various, mostly empirical, corrections to account for dynamic inflow, stall and tip loss effects [102, 99]. In the BEM method, the aerodynamics of control surfaces can only be modelled using two-dimensional analytical solutions or through look-up tables.

The three-dimensional vortex method that couples a panel description of the blades with a vortex blob approximation of the wakes is also considered [198]. In this model, viscous effects are introduced through surface velocity transpiration to represent mass flow difference over the boundary layer between real viscous and the equivalent inviscid flow, and flow separation is introduced through double wake shedding [35]. For the structural model, the majority are using Euler-Bernoulli or Timoshenko formulations, with full finite-element representation or assumed modes approach.

In active load alleviation, controller design plays an important role in the overall performance of the system. Almost all the codes in Table 1.1 are designed for simulation and control surfaces added in at a later stage. To obtain a control model, numerical linearisation is often used but the resulting dynamics are different from the true system. Sometimes, certain dynamics have to be explicitly neglected to obtain linear models [60, 59]. An alternative was to use system identification to build approximate mathematical models using input/output data. While this is an effective way to obtain linear models for control, its accuracy is dependent on the input signals [33] used in the excitation of system dynamics; in

Table 1.1: Overview of wind turbine commercial and research aeroelastic codes that are used for active load alleviation [3, 68, 128, 190]. The abbreviations are, EB (Euler-Bernoulli), MBS (Multi-body dynamics), FE (Finite-element), GNCB (Geometrically non-linear composite beam), 2D (two-dimensional), elem (elements).

Code	**Developer**	**Aero**	**Structures**	**Flaps**
FAST [182]	NREL	BEM	FE/Modes/MBS (EB)	Look-up table
HAWC2 [141]	DTU Wind	BEM	FE/MBS (Timoshenko)	2D analytical
FLEX5 [185]	DTU	BEM	FE/Modes	2D analytical
Bladed [43]	GL Garrad Hassan	BEM	FE/Modes/MBS (Timoshenko)	Look-up table
DU_SWAMP [20]	TU Delft	BEM	FE/Modes/MBS (Super-elem)	2D analytical
GENUVP, GAST [198]	NTUA Greece	Vortex	FE/MBS	Vortex method
SHARP [170, 180]	Imperial College	UVLM	FE/Modes/MBS (GNCB)	UVLM

wind turbine applications the identification is further complicated by the periodic behaviour of the system [233].

A review of *smart rotor* concepts [20], focusing on active flaps, documented flapwise root-bending load reductions obtained through the use of different control methods. A wide spectrum of performances was reported with results ranging from 10% up to 30% reduction in blade flapwise root-bending moments (RBM), depending on the type of controller used and also on the size and distribution of flaps. In addition, most of works in active aeroelastic control of wind turbines had relied on proportional-integral-derivative (PID) controllers [183], with only a few of the more recent works considering advanced techniques, such as linear-quadratic regulator (LQR) or predictive control [250, 20]. This was probably because the intention had normally been to show the potential of feedback control in enhancing the aeroelastic performance of turbine blades and more advanced control methods were left to be explored.

As turbines get larger, there will be bigger aeroelastic couplings and larger structural deformations than on existing rotors. An alternative solution based on the time-domain unsteady vortex-lattice method (UVLM) [242], coupled with the composite beam descriptions of the rotor blades [110], could provide a better characterisation of the unsteady rotor dynamics, assuming attached flow conditions. With a constantly changing operating environment, aerodynamic loads on the wind turbine are directly determined by unsteady effects and the UVLM is capable of capturing the underlying physics that is essential for turbine load predictions. As a result of the improved unsteady aerodynamics definition, better structural requirements can be explored to enable lighter weight designs [145]. Moreover, as opposed to the codes described above that have been designed mainly for simulation, such an approach can be directly formulated in a suitable manner for model reduction and controller design.

As mentioned, the aeroservoelastic modelling of large flexible wind turbines requires a multi-disciplinary approach that encompasses aerodynamics, structural dynamics and controls. We will provide an overview of the different methods used in wind turbine aeroelastic modelling and highlight the approaches taken to incorporate *smart rotor* concepts. In fact,

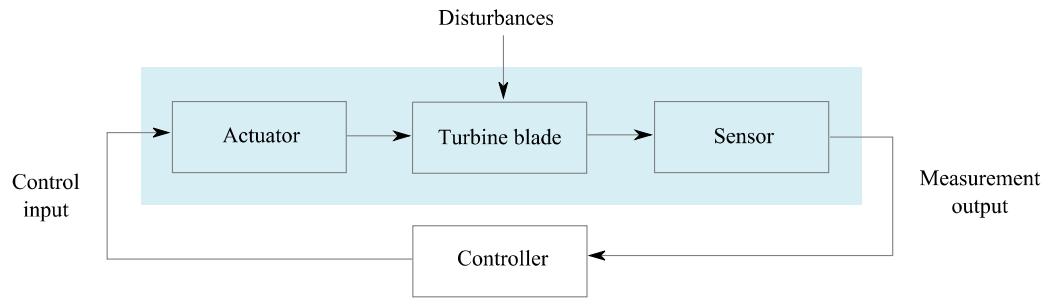


Figure 1.2: Block diagram for *smart rotor* concept.

the application of *smart rotor* concept is itself also multi-disciplinary and encompasses the combination of sensors, actuators and controls to form an interconnected system capable of actively reacting to alleviate loading on the turbine blades. As an illustration, a typical block diagram for active flap control on a wind turbine is shown in Figure 1.2. In closed-loop, sensors picks up the desired measurements which feeds into the controllers to determine the control inputs. Actuators react to the control inputs and operates the active control surfaces on the turbine blades.

In the following sections of the literature review, we will first highlight the different methods in the modelling of horizontal-axis wind turbines (HAWT) (Section 1.2), focusing on the aerodynamics and structure dynamics. Next, control methods that are commonly used in literature (PID, LQG and $\mathcal{H}_\infty$ [215]) for active load alleviation will be briefly reviewed (Section 1.4). Following which, sensors and actuators will be outlined in Sections 1.5 and 1.6, respectively, accompanied by a discussion on passive load alleviation mechanisms in Section 1.3. The load reduction potentials of different active control devices such as flaps, variable aerofoil geometries, microtabs and individual pitch controls, will be detailed from Sections 1.7.1 to 1.7.3. We will then conclude with an analysis of the works presented and establish the choice of active mechanism in Section 1.7.4.

1.2 Aeroelastic Modelling

The aeroelastic modelling of HAWT requires the definitions of unsteady aerodynamics to determine wind loadings, and structural dynamics to predict dynamical responses. The common approach to model the aerodynamics on wind turbines is through the Blade Element Momentum (BEM) method [101], which allows fast computation using tabulated aerofoil properties. With advances in computing power, Computational Fluid Dynamics (CFD) solving the Euler or Navier-Stokes equations are also increasingly being used [210, 69]. Spanning the two approaches are intermediate fidelity solutions such as the unsteady vortex lattice method that provide detailed three-dimensional flow description under the assumption of at-

tached flow conditions [131]. In all these models, there are fundamental limitations and also some degree of ambiguity on their applications to wind turbines which we will be pointing out.

BEM is essentially a combination of blade element theory to resolve the forces on a blade section, and momentum theory for control volume analysis of the forces at the rotor disc (conservation of linear and angular momentum) [161]. The reliability of the method is dependent on the availability of good aerofoil data for the aerodynamic lift and drag coefficients as functions of angle of attack [100, 102]. The method suffers from various shortcomings, for instance, the assumptions of infinite number of blades, quasi-steady aerodynamics, axisymmetric inflow and no fluid interaction between elements (no radial flow) [161]. To overcome some of these limitations, empirical corrections are often included in the BEM solution. These include:

- Tip loss effects. Due to the difference in pressure between the suction and pressure sides of the blade, air tends to flow round the tip and this reduces aerodynamic lift [207, 161, 90].
- Dynamic inflow models to account for the aerodynamic lag in unsteady flow conditions [219, 108].
- Dynamic stall models to account for delay in the onset of flow separation at a higher angle of attack than would normally occur in static conditions, using the Beddoes-Leishman model [147, 99, 7], ONERA model [164] and the Snel model [218], among others. A comparison of these models is documented in Ref. [115]. Often in literature, dynamic stall models also encompass unsteady aerodynamics [145].
- Spanwise corrections to take into account rotational effects on aerofoil characteristics [14, 220, 62]. The rotational effects on aerodynamic loads in three-dimensional models have shown to delay the onset of flow separation and stall [145].

As turbines get larger with potentially higher tip-speed-ratios and significant three-dimensional effects, BEM is also shown to over-predict aerodynamic loads [103, 203]. In addition, it is not applicable to all operating cases, in particular, yawed flow and its transient behaviour [97, 165].

BEM is essentially a two-dimensional theory [145], and in order to have the full three-dimensional description of the aerodynamics, potential-flow solutions and CFD have to be considered. CFD solves for the Euler or Navier-Stokes equations and are capable of detailed flow field predictions. With advances in computational power, simulations are possible on full HAWT [102, 69, 253]. It provides an accurate account of all relevant flow physics, geometry and viscosity. In a study of code comparison with experiments conducted by NREL [210], CFD consistently reproduced measured distribution of the aerodynamic forces, even under

highly three-dimensional flows and extreme stall conditions [102]. However, large computation overheads still remain a hurdle.

The governing equation for low-speed potential flow theory is Laplace's equation, which can be solved by representing the potential flow field in terms of singularity distributions (Green's theorem) [131, 170]. Although it is computationally more expensive than BEM, it incorporates three-dimensional effects, blade-wake interference and wake modelling. For *smart rotor* analysis, control surfaces can also be modelled directly. The main drawback of potential flow solutions in wind turbine applications had been the assumption of attached flow conditions, limiting its use in operating regimes where blades are at high angles of attack or in the inboard regions of the blade. Attempts have been made by several researchers to include viscosity and flow separation [242, 221], but there are still unresolved issues related to convergence [102].

Different wake models have been considered, ranging from free [212], prescribed [71] and rigid. In free-wake models, wake vortices convect and deform under the action of local velocity flow field. On the other hand, in prescribed and rigid-wake models, the positions of wake vortices are specified based on flow visualisations. In most cases, free-wake models are known to give better predictions of aerodynamic loads over prescribed and rigid-wake models [145]. However, free-wake models are computationally more demanding as they require to solve the Biot-Savart law at every time step [131].

Almost all the developed aeroelastic codes that are used to model *smart rotors* are fundamentally based on BEM for the aerodynamics with different treatments of the empirical corrections [127, 185, 141, 20, 43, 128, 190]. To incorporate *smart rotor* concepts in the aerodynamics, a starting point is to consider two-dimensional aerofoil sections. The analytical solution provided by Theodorsen [227] and the indicial step response by Wagner [243] are commonly used to capture the unsteady aerodynamics resulting from flap actuation. In these methods, a two-dimensional flat plate in an inviscid and incompressible flow with a planar wake is considered. For aerofoils with variable geometry, analytical solutions to the unsteady aerodynamics are provided by various authors [82, 34, 169]. To include the effects of aerofoil thickness with camber and allow wake shapes to be prescribed, two-dimensional vortex methods are used [23, 77].

These two-dimensional methods, in particular the analytical solution of Wagner [243] and Gaunaa [82], are often incorporated into the sectional aerodynamics description of BEM models. Unlike most sections of the turbine blade in which the aerodynamics are based on tabulated aerofoil data, the blade sections that contains the actuators have their unsteady aerodynamics computed using these analytical solutions, assuming attached flow and neglecting three-dimensional aerodynamic effects from the control surfaces [33, 16]. Simpler methods of directly using lift and drag coefficients from tabulated aerofoil data with flaps are also considered, resulting in quasi-steady solutions [225]. To overcome these limitations, three-dimensional vortex methods have been explored [198], accounting for both the unsteady aerodynamic and spanwise effects of the control surfaces.

The main challenge in aerodynamics modelling is in validating numerical solutions against experimental measurements to gain confidence in predictions and to better understand the limits of modelling techniques [145]. Also, as turbines get larger, simpler two-dimensional solutions such as BEM may become less valid and the computationally more expensive three-dimensional vortex method or CFD may be required.

The common approach to capture the structural dynamics of wind turbines is based on classical beam theory [114]. This is partly due to the fact that turbine components are relatively rigid. This may not be the case in modern turbines that are larger, and the higher degree of flexibility in the blades necessitates methods capable of capturing geometric non-linearities [189].

The main components of the wind turbine are the blades, tower and drive-train, and it is common to adopt a multi-body approach to fit the different components into a complete configuration. In this approach, the components are modelled as beams into which the three-dimensional properties are reduced into one-dimensional representations concentrated along the elastic axis using appropriate cross-sectional analysis methodologies [188, 72, 196]. Each component is defined in a local frame of reference (FoR), which is then combined into a global system.

Often, modal decomposition is used to truncate away higher frequency modes in the various components. This is under the assumption that eigenmodes associated with higher frequencies are not excited in the combined system, and by truncating away these high frequency modes, the size of the model can be reduced to speed up numerical computations.

In terms of modelling for controller design, the usual approach is to derive full non-linear models and then perform system identification or linearisation to obtain linear state-space models [33]. In aircraft modelling, the approach is slightly different. It is common in aircraft modelling to develop linear state-space models by combining linearised structural and aerodynamic models. Non-linearities of interest are then added to the linear model as required. This approach could be considered in wind turbine modelling and would allow better understanding of neglected non-linearities in the linear models [18]. Also, in order to provide a realistic representation of a full rotor, different control objectives such as collective pitch, spanwise distributed active devices, generator torque should be combined and included in wind turbine models.

1.3 Passive Mechanisms

Passive load alleviation in turbine blades through aeroelastic tailoring is attractive in its simplicity, design and has been well researched [238]. The main focus is predominantly on bend-twist coupling (twist-towards-feather) to reduce the angle of attack as the blade bends upwards. This modifies aerodynamic loads and can bring about positive effects on load alleviation.

Studies into the use of bend-twist coupling showed that fatigue load alleviation of 20% (up to 80%) in flapwise root-bending moments and significant reduction of maximum flapwise root-bending loads can be achieved [154]. However, when stability limits were considered, flutter and divergence speeds were reduced. A more recent study [47] detailed the design of bend-twist coupled blades and suggested its combination with individual pitch controls to bring about the full advantages of the two mechanisms. In addition, the benefits of reducing cost of energy through passive methods have also been considered [239].

1.4 Controllers

Majority of works in active load alleviation adopts the use of PID controllers, with multiple-input-multiple-output (MIMO) control strategies increasingly being considered, such as linear-quadratic Gaussian (LQG), $\mathcal{H}_\infty$ and model predictive control (MPC). We will discuss briefly some of these control approaches for which the details can be found in Refs. [183, 215, 156, 157].

1.4.1 PID Controls

PID controls have been widely studied and are common practice in industry. It relies on the use of proportional (P), integral (I) and derivative (D) actions, with each of them achieving different objectives. The proportional term changes the output proportionally to the error signal. However, using it alone leads to steady-state error, and having a large gain causes instability. Integrators are often used with proportional controllers to eliminate the steady state error by accumulating error over time to give the offset required. Yet, too large an integrator gain leads to oscillations, increased settling time and risks running into poor robustness and instability. The derivative term provides predictive action and damps out oscillations [11, 183]. However, derivative actions have high gain for high-frequency signals, which results in noise amplification. This effect can, however, be reduced if the signal is first passed through a low-pass filter.

PID controllers are shown to be effective in active load alleviation in most of the existing works. Even without optimisation, the controllers were able to achieve at least 80% reduction in lift for two-dimensional cases, and on average 5% to 35% reductions in flapwise RBM for three-dimensional cases, both through the use of flaps [78, 198] and variable trailing-edge geometries [6, 53, 83]. However, PI controllers was found in some studies to render closed-loop systems unstable resulting in torsional instability and trailing-edge flapping [83]. Also, poor stability margins in PID were reported [155]. This provided the motivation to explore further into using LQG or $\mathcal{H}_\infty$ controllers for active load alleviation.

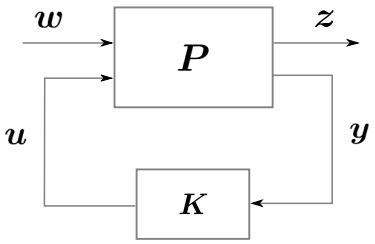


Figure 1.3: General control configuration [215].

1.4.2 General Control Configuration

The general control configuration [215] used for LQG and $\mathcal{H}_\infty$ is shown in Figure 1.3, and the system is described by

$$\begin{bmatrix} \boldsymbol{z} \\ \boldsymbol{y} \end{bmatrix} = \begin{bmatrix} \boldsymbol{P}_{11} & \boldsymbol{P}_{12} \\ \boldsymbol{P}_{21} & \boldsymbol{P}_{22} \end{bmatrix} \begin{bmatrix} \boldsymbol{w} \\ \boldsymbol{u} \end{bmatrix}, \tag{1.2}$$

$$\boldsymbol{u} = \boldsymbol{K}\boldsymbol{y}, \tag{1.3}$$

where $\boldsymbol{z}$ contains the objective variable, $\boldsymbol{u}$ is the control input, $\boldsymbol{y}$ is the plant output and $\boldsymbol{w}$ is the disturbance input. $\boldsymbol{K}$ is the compensator and $\boldsymbol{P}$ is the generalised transfer matrix (plant, weights).

The closed-loop transfer function from $\boldsymbol{w}$ to $\boldsymbol{z}$ is given by

$$\boldsymbol{z} = F(\boldsymbol{P}, \boldsymbol{K})\boldsymbol{w}, \tag{1.4}$$

where

$$F(\boldsymbol{P}, \boldsymbol{K}) = \boldsymbol{P}_{11} + \boldsymbol{P}_{12}\boldsymbol{K}(\boldsymbol{I} - \boldsymbol{P}_{22}\boldsymbol{K})^{-1}\boldsymbol{P}_{21}, \tag{1.5}$$

is the linear fractional map of $\boldsymbol{P}$ and $\boldsymbol{K}$.

1.4.3 Linear-quadratic Gaussian

An LQG controller minimises a quadratic cost function and assumes Gaussian disturbance and known statistical properties of the noise input. The controller relies on the principle of separation where the LQG is made up of a linear-quadratic regulator (LQR) and a Kalman filter.

The LQR seeks to find a linear controller such that the following deterministic quadratic cost function is minimised [156, 215]

$$J = \int_0^\infty \| \boldsymbol{z}(t) \|_2^2 \, dt = \int_0^\infty \boldsymbol{z}^\top \boldsymbol{z} \, dt = \int_0^\infty \boldsymbol{x}^\top \boldsymbol{Q}\boldsymbol{x} + \boldsymbol{u}^\top \boldsymbol{R}\boldsymbol{u} \, dt, \tag{1.6}$$

where $\| \cdot \|_2$ denotes the 2-norm or Euclidean norm. $\boldsymbol{Q}$ and $\boldsymbol{R}$ are appropriately chosen weighting matrices such that a large $\boldsymbol{Q}$ penalises the states $\boldsymbol{x}$ while a large $\boldsymbol{R}$ penalises control input $\boldsymbol{u}$. In practice, $\boldsymbol{Q} \geq 0$ and $\boldsymbol{R} > 0$.

LQR assumes all the states of the system are known. However, in practice, states are not easily measured and there will be measurement noise. Hence, the states are estimated using a Kalman filter, which has the following structure [215]

$$\dot{\hat{\boldsymbol{x}}} = \boldsymbol{A}\hat{\boldsymbol{x}} + \boldsymbol{B}\boldsymbol{u} + \boldsymbol{L}(\boldsymbol{y} - \boldsymbol{C}\hat{\boldsymbol{x}}) \,, \tag{1.7}$$

such that the choice of $\boldsymbol{L}$ minimises $E((\boldsymbol{x} - \hat{\boldsymbol{x}})(\boldsymbol{x} - \hat{\boldsymbol{x}})^\top)$ where $\hat{\boldsymbol{x}}$ are the estimated states and $E(\bullet)$ is the expected value.

The performance of LQG or LQR controllers in active load alleviation had been demonstrated by several researchers [77, 250] for two and three-dimensional models, both using flaps as the actuating surface. While the performance of LQG controller was comparable to PID, it was reported that LQG expended 50 times less energy in flap actuations [77].

1.4.4 $\mathcal{H}_\infty$

In $\mathcal{H}_\infty$ control, the objective is to minimise the peak of the maximum singular value of $F(\boldsymbol{P}, \boldsymbol{K})$ [215] in Eq. (1.5) such that

$$\| F(\boldsymbol{P}, \boldsymbol{K}) \|_\infty = \max_\omega \overline{\sigma}(F(\boldsymbol{P}, \boldsymbol{K})(j\omega)) \,. \tag{1.8}$$

The above equation can also be represented as the induced (worst-case) 2-norm where

$$\| F(\boldsymbol{P}, \boldsymbol{K}) \|_\infty = \max_{\boldsymbol{w} \neq 0} \frac{\| \boldsymbol{z} \|_2}{\| \boldsymbol{w} \|_2} \,. \tag{1.9}$$

This signifies that the worst case response of the system to an input disturbance (maximum singular value) is minimised. Hence, in the presence of bounded uncertainties, closed-loop performance and stability are guaranteed [255].

In practice, it is usual to design $\mathcal{H}_\infty$ controllers by selecting a $\gamma > \gamma_{min}$, where γ_{min} is the minimum value of $\| F(\boldsymbol{P}, \boldsymbol{K}) \|_\infty$ over all stabilising controllers. The next step is then to find all stabilising controllers $\boldsymbol{K}$ such that

$$\| F(\boldsymbol{P}, \boldsymbol{K}) \|_\infty < \gamma \,, \tag{1.10}$$

The robustness of $\mathcal{H}_\infty$ controllers in active load alleviation was clearly demonstrated in Ref. [77]. While the proportional controller used to mitigate loadings on an aerofoil was only effective for a subset of free-stream velocities, the $\mathcal{H}_\infty$ controller was able to remain effective over the entire range. The $\mathcal{H}_\infty$ controller also achieved slightly higher load reductions than

PID controllers with the same actuator limits.

In the PID, LQG and $\mathcal{H}_\infty$ control methods, tuning is often required to ensure that the control action is kept within certain bounds, often determined by actuator limits and its rates. Alternatively, MPC is an optimal control strategy based on numerical optimisation that allows such constraints to be explicitly defined [157]. The basic concept is to make use of a dynamical model to forecast system behaviour, and subsequently optimise the forecast to produce an optimal control strategy [193]. In terms of its application in active gust load alleviation in wind turbines, it has only been considered in very recent works [20, 59], both in numerical and experimental studies. MPC was shown to perform well and brought about 15% to 28% reduction in blade root loads with constraints on pre-defined actuator deflections.

1.5 Sensors

Sensors provide measurements to be fed as inputs to the controllers. The choice of measurements rely heavily on the design objectives; their positions are also crucial to ensure that the desired excitations are captured. These sensors will need to meet multiple objectives to be lightweight, robust and reliable in harsh environments. The type of sensors include strain sensors (electrical and optical), accelerometers and also inflow measurement sensors.

Strain sensors are mainly placed at the root of turbine blades for load measurements and can be classified into electrical and optical types. Electrical strain sensors include capacitance, resistance, photoelectric as well as semiconductor strain gauges. However, electrical strain sensors are not suitable to be mounted on wind turbines as they are sensitive to temperature fluctuations and require recalibration during their lifetime. Yet, they remain useful for laboratory experiments [19]. For instance, electrical strain gauges were used in an experiment to measure the flapwise RBM of a cantilevered wing under turbulent flow conditions in a water tunnel [78].

Another group of strain sensors is the optical type covering the interferometry, photoelastic and fibre optic type strain gauges. Among them, the fibre optic strain gauge is best suited for wind turbine blade monitoring given its advantages in size, weight, insensitivity to electrical interference and reliability. However, it does have the drawback of being sensitive to temperature fluctuations [18].

Accelerometers measure the acceleration of a body using two transducers. The primary transducer responds to acceleration with a displacement that is sensed by the second transducer to give an electric signal response. The primary transducer could consist of spring retained seismic mass system or double cantilever beam, while the secondary transducer can be piezoelectric, potentiometric, servo strain gauge, reluctive, capacitance or vibrating element. However, accelerometers are mainly used in bearings, generators, gearbox monitoring and seldom in blade sensing [18].

Inflow measurement is another option for sensing and it measures wind speeds ahead of the turbine for estimation and control. It is achieved through the use of pitot tubes or laser anemometry (lidar). In recent years, lidar has received significant interest among different researchers [201, 202, 45, 133], mainly for sensing the incoming wind for feed-forward speed and load alleviation control on turbines. Lidars can be mounted on the nacelle and by means of light beams, interpret the reflections on water and dust particles ahead of the rotor to provide a spatial description of the wind velocity field. This preview is typically at distances in the order of tens of meters ahead of the turbine, which are several seconds into the future [50]. However, lidars are affected by environmental conditions such as precipitation and some form of estimation is needed to account for changes in the velocity field between where it is being detected and when it finally encounters the rotor. Often, in actual implementations [60, 25, 26], a combination of all the above sensors have to be considered with their measurement objectives and locations carefully considered.

1.6 Actuators

Actuators are used to operate control surfaces and their types vary between conventional, smart materials and shape memory alloys. Among the types of conventional actuators, the most commonly used are that of the hydraulic, pneumatic and electrical types.

Hydraulic and pneumatic type actuators are subject to weight and space constraints, leakage and also regular maintenance requirements. In contrast, electro-mechanical actuators have low maintenance requirements and they are simple, fast in response and are already widely used in wind turbine applications for pitch controls [18]. They can also be used for active load alleviation, where an electro-mechanical stepper motor had been used to operate a flap in the water tunnel [78].

More advanced actuators look at the use of smart materials (piezoelectric, electrostrictive, magnetostrictive), which have the capability of sensing and respond in a controlled way to external stimuli. They are also lightweight and have the flexibility to act both as an actuator and a sensor [18]. In recent years, there has been extensive research in active controls using smart materials. In Refs. [19, 235], a combination of piezoelectric sensors and actuators were used to measure blade root-bending strains and to deform the variable trailing-edge geometries, respectively.

1.7 Active Control Devices

Active control devices will be discussed in terms of their existing modelling techniques, controller design and load reduction potential. These include the use of flaps in Section 1.7.1, variable aerofoil geometry in Section 1.7.2, other control methods (microtabs and individual pitch controls) in Section 1.7.3 and their comparison in Section 1.7.4.

1.7.1 Trailing-Edge Flaps

In modelling trailing-edge flaps for active load alleviation, one of the earliest studies was carried out at the US National Renewable Energy Laboratory (NREL) [175, 225, 226], where the investigations included response times and root-bending moments using simple PI controlled flaps in the presence of a step gust. Motivated by these studies, other researchers [17, 250, 136] also started to look into the use of flaps, and considered more sophisticated control methods with realistic turbulence inflows. In all these works, the wind turbine simulation codes were either developed in-house or commercially sourced. Their aerodynamic models all relied on BEM in which the effects of flap actuations were accounted for through look-up tables of aerodynamic data for different flap deflection angles. However, this resulted in a quasi-steady aerodynamic analysis as the dynamic effects of flap actuations were not considered. To account for the unsteady aerodynamics, some of the works considered isolating spanwise sections containing the flap and used analytical solutions to obtain the corresponding unsteady aerodynamics from flap actuation. Other methods were also explored, in particular, using vortex methods [23, 198] to develop two and three-dimensional aeroelastic models.

With modern turbine blades spanning more than 50m in length, different sections of the blade will experience different localised loadings. There is hence a need to find the optimum control strategy and distribution of flaps along the span of the blade. Through numerical studies, it had been suggested [8] to locate flaps close to the tip of the blade in order to achieve the largest moment arm if flapwise RBM is to be reduced. Also, different concepts of centralised and decentralised single or distributed flap controls had been explored [17]. It was found that using PID controllers, the largest reduction in blade flapwise RBM was achieved from decentralised and distributed flap controls (flaps were split into three sections) [20]. In terms of controller selection for active flap controls, PID controllers are most commonly used in literature and had proved to be considerably effective in load alleviation.

Experiments were also conducted to demonstrate the performance of flaps in a laboratory environment [236]. One such experiment [78] looked into the use of a small trailing-edge flap (4% chord) for active load alleviation. Small flaps have the advantage of low inertia and can be deployed at faster rates. The experiment was conducted in a water flume using a NACA 0012 aerofoil with an independently attached flap that was mounted vertically in the tank.

To date, there is no commercial application of the active flap concept on existing wind turbines, but a recent full-scale experiment was conducted [60] on a Vestas V27 turbine using frequency-weighted model predictive control. It was demonstrated that trailing-edge flaps were capable of reducing average flapwise blade root load by up to 14%. Sandia National Laboratories also designed and built turbine blades equipped with aerodynamic flaps for testing [25, 26, 27, 28]. Further to that, small-scale wind tunnel experiments were conducted by researchers from TU Delft [21]. The application of flaps on actual large wind turbines is still a challenge and further proof-of-concept is required to gain acceptance from the industry.

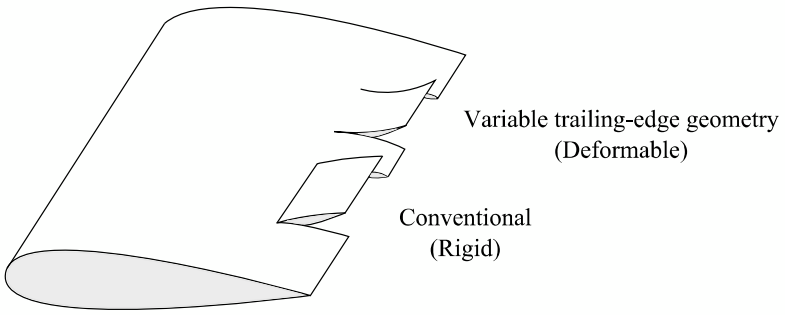


Figure 1.4: Blade section with conventional (rigid) flap and variable trailing-edge geometry (deformable) [18].

1.7.2 Variable Aerofoil Geometry

Extensive research into variable trailing-edge geometries is being conducted by Risø [31]. The difference between a conventional flap (rigid) and a variable trailing-edge geometry (deformable), both shown in Figure 1.4, is that the latter do not possess a hinge, thus reducing the incidence of flow separation and noise.

To capture the unsteady aerodynamics of the variable trailing-edge geometry, a commonly used method is that of Gaunaa's [82] from Risø. He provided an analytical solution to a two-dimensional aerofoil with variable shape, derived from thin aerofoil potential flow assumptions and employing the use of indicial response functions. Similar concepts for varying camber have also been conceptualised by other authors [169].

Due to its simplicity and computational efficiency, the method by Gaunaa [82] was adopted by several researchers [53, 6]. In Ref. [53], the analytical solution was coupled to a simple linear spring/damper structural model to demonstrate the potential of variable trailing-edge geometry for load reductions on an aerofoil section. Full turbine analysis was also considered [6] using the analytical solution to generate an aerodynamic look-up table as input to BEM for different deflections of the trailing-edge geometry. This resulted in a quasi-steady analysis as the dynamics of actuation was not included. In another study by NREL [249], a CFD code, ARC2D, was used to obtain the required aerodynamic data in the look-up table for BEM.

The ability to implement variable trailing-edge geometries on actual turbine blades is a substantial challenge in itself and a variety of concepts using piezoelectric bender and rubber trailing-edges were explored experimentally [235]. One such experiment performed wind tunnel tests on a dynamically scaled wind turbine blade with the trailing-edge actuated by piezoelectric benders [19]. To obtain a control model, system identification was performed based on measured data, and the resulting linear model was used to develop a PD controller with blade root strains as measurement feedback. The closed-loop system was able to reject

both periodic and stochastic disturbances. An extension to this work demonstrated the potential of using rubber trailing-edges as the actuator for active controls [158]. The controllers for active load alleviation using variable trailing-edge geometries are again confined to PID controllers.

Any blade-mounted control devices will have to operate in conjunction with existing collective pitch controls that are used for speed regulation. It had been demonstrated [136, 216] that trailing-edge flaps were capable of reducing fluctuations in power output and complemented pitch controls by reducing pitch angle and rate usage. Likewise, if individual pitch controls are adopted, flaps can complement by alleviating high frequency loads that are beyond the reach of pitch mechanisms and requires low energy consumption [249].

1.7.3 Other Active Control Devices

Another active control mechanism, although less often considered, is the use of microtabs [120, 149, 12]. Microtabs are small devices placed near the trailing-edge (approximately 95% of chord) of the blade section to alter camber and thus modify its aerodynamic characteristics. The benefits of microtabs lie in their mechanical simplicity and low energy consumption. The height of the tab is typically 1% to 2% of chord length, equivalent to that of the boundary layer thickness. Microtabs had been investigated extensively by Sandia National Laboratories. In one of their studies [232], the transient behaviour of microtabs deployment against that of microflaps was explored using a CFD solver, with largely similar results between the two mechanisms. However, microflaps, given its larger moment arm, appeared to have an edge over microtabs in terms of response time and lift effectiveness. In another microtabs study [247, 248] using FAST to model the turbine blade, maximum blade flapwise RBM can be reduced by 30% to 50% using PD controllers. Simulations on tower loads also showed reductions of 20-60% in peak bending moments.

A more widely studied form of active load alleviation involves the adaptation of existing collective pitch mechanisms on turbines for individual pitch controls (IPC) [223, 224, 234, 88]. Unlike flaps and microtabs, which are localised lift enhancers, IPC involves actuating the entire blade to modify the aerodynamic lift throughout. The challenge is in separating the pitch commands used for speed regulations from that of load reductions. A common method was to employ the d-q transformation [42, 44] (Coleman transformation [64, 49]) such that the control signals for collective pitch is isolated from the differential action. This is to avoid pitch commands for load alleviation interfering with speed regulation. It transforms measured load signals into a mean value and variations about two orthogonal axes (the yaw and tilt axes) that can be treated as almost independent. Controllers can then be designed to act on these out-of-plane yaw and tilt motions, for which the resulting control input are inverse transformed before feeding back to the system. This method has been shown to be effective in alleviating 1P loads [206] with promising results in field testing [46]. However, in a recent paper [155], it was demonstrated that the tilt and yaw axis cannot be treated independently

through Coleman transformation, and when analysed in the frequency domain, they exhibits strong coupling that should be taken into account in the control design.

Other non-Coleman transformation based IPC approaches have been investigated, for instance, the use repetitive control method [116] or periodic LQR design [174] on the time-varying turbine model. Instead of control design on the full turbine, single blade control based on local measurements have also been studied with benefits in terms of simplicity, implementation and not requiring the Coleman transformations [148, 142]. Nonetheless, single blade control had been found to be slightly less effective in targeting rotating components (such as blade loads) but have a huge impact on reducing loadings on stationary components (such as tower and bearings) [191]. Also, a comparison of modes and stability between systems with Coleman transformation and just averaging across all periodic states was performed [38].

The use of pitch controls is largely aimed at mitigating low frequency loadings due to their relatively slow actuation resulting from the inertia of the blades. With larger turbines, the actuated pitch angle will also vary spanwise due to the distributed aerodynamic loads and torsional effects on the flexible blades. To tackle localised loadings and higher frequency disturbances, distributed active control devices such as flaps are seen as the preferred option [249].

1.7.4 Comparison of Active Control Devices and Summary

The separate use of flaps, variable trailing-edge geometries, microtabs and individual pitch controls have shown to be effective in mitigating loadings on turbine blades. Comparisons between these active control concepts were explored by researchers from TU Delft and Sandia National Laboratories [136, 248]. In comparing the effectiveness of flaps and individual pitch control, it was shown that both methods were able to deliver similar reductions in blade flapwise RBM in low frequency disturbances. However, it was only the flaps that remained effective in high frequency loadings. Also, variable trailing-edge geometries and rigid flaps gave comparable performances [24].

Considering the different *smart rotor* concepts, this project will focus on the use of rigid flaps, which have the advantage of simplicity in actuation. As demonstrated in Refs. [248, 24], the performance of conventional flaps is comparable to that of variable trailing-edge geometries, yet it avoids complex actuating mechanisms. Compared to microtabs which are on/off devices, flaps possess linear lift characteristics with larger flapwise load reduction potentials [163, 232]. They further complement individual pitch controls by tackling the higher frequency flapwise loads and reduces fluctuations in power output. They also reduce pitch angle and rate usage [136]. Moreover, the use of flaps avoids skin fatigue issues due to complex actuation as experienced in active twist or variable trailing-edge geometries, and are superior in performances [163]. However, flaps do have the setback of having a discontinuity at the hinge that could potentially be a source of aerodynamic flow separation and noise.

A list of the works in active flap control (rigid and deformable) that are discussed in previous sections, together with their modelling descriptions and control methods, can be found in Table 1.2. It is clear that the modelling techniques, controller selections and performances reported varied greatly. The summary of performances and observations are:

- **Performances reported**
  - For 10% variable trailing-edge geometries, reductions in flapwise RBM ranged between 80% to 95% in two-dimensional aerofoil simulations, and between 15% to 25% for three-dimensional rotor blade analysis.
  - For rigid flaps of 10% chord, reductions in flapwise RBM was from 5% to 35% for three-dimensional rotor blade analysis.
  - For experiments, the spread in reductions of flapwise RBM was larger, with performances between 14% and 60% being reported.
- **Observations**
  - In general, two-dimensional aerofoil analysis predicted extremely good performances, which were not observed in three-dimensional rotor cases.
  - Variable trailing-edge geometries delivered roughly similar reductions in flapwise RBM as rigid flaps, and both their modelling had relied on look-up tables or two-dimensional analytical solutions.
  - The variety of performances reported in three-dimensional simulations were mainly due to differences in the treatment of external excitation (gust) and varying spanwise locations of the flaps. Further to that, fundamental differences in the underlying aeroelastic modelling also contributed to the mixture of performances. As mentioned, the modelling of the aerodynamics were predominantly by BEM and the aeroelastic codes were designed for simulations, for which the shortfalls had been discussed in previous sections.
  - PID controllers reported lower reductions in flapwise RBM than more advanced control methods such as LQG, $\mathcal{H}_\infty$ and MPC. Also, with feed-forward control such as periodic load anticipation, performance was higher.
  - Given the restrictions in experimental set-up, fabrication and also actuator housing, operating conditions vary greatly between the works considered. In fact, most of the experiments so far had been conducted either in the laboratory (reporting larger reductions in flapwise/out-of-plane RBM) or in the field on relatively small turbines with rigid blades [60, 28]. There is still much more to be done in terms of demonstrating experimentally the effectiveness of *smart rotor* concepts on large and flexible blades.

1.8 Research Objective

It is evident from the literature review that *smart rotor* concepts are topical. However, there are missing gaps in terms of the approach to modelling and controls, in particular, the overly simplified description of the aerodynamics and unified aeroelastic models for control design. Within this context, the research statement is established:

> *To develop a* ***higher-fidelity aeroelastic framework*** *for load analysis on large wind turbines, equipped with proposed* ***smart rotor concepts*** *for blade fatigue load alleviation using* ***robust control methods****.*

In line with the research statement, the following broad objectives and outcomes will be sought:

- Introduce a higher-fidelity efficient numerical model, coupling a state-space unsteady vortex-lattice method with a geometrically-exact composite beam model. The outcome is to provide an unified aeroelastic framework for wind turbine modelling and simulation study.
- Derive a state-space representation of the aeroelastic formulation integrating *Smart Rotor* concepts that is suitable for control design and model reductions. The desired outcome is to obtain reduced-order linear models suitable for controller design and subsequent closed-loop simulation with higher-order non-linear models.
- Present numerical test cases of the aeroelastic framework using conceptual wind turbine models (both land-based and floating) to reduce flapwise RBM using active and passive mechanisms.

1.9 Present Approach

This thesis will present an aeroservoelastic modelling approach to capture the structural response and the unsteady aerodynamics of turbine rotors for dynamic load alleviation in large wind turbines. The structural model is described using geometrically non-linear composite beams, linearised around equilibrium rotating conditions with potentially arbitrarily-large structural displacements. The time-domain aerodynamics is given by the three-dimensional unsteady vortex-lattice method, which seeks to complement and provide a direct medium fidelity solution for the unsteady rotor dynamics in attached flow conditions. It allows control surfaces to be modelled directly, accounting for three-dimensional and transient loads resulting from flap actuation.

However, there is a compromise between speed and accuracy as the UVLM description is computationally more intensive than the commonly adopted BEM methods. Nonetheless,

UVLM is still numerically more efficient than CFD, yet capable of predicting comparable loadings [203]. The aeroelastic description provided in this thesis is formulated with the intention for controller design. The resulting aeroelastic model is written in a state-space formulation, providing a physics-based (UVLM) control model that better captures the dynamics of large wind turbines. In particular, the use of the vortex-lattice method to capture the unsteady aerodynamics do not require empirical corrections or look-up tables that are commonly used in conjunction with blade-element methods.

The methodology presented here was explored for flexible aircraft applications under the integrated framework for the simulation of high aspect ratio planes (SHARP) [168, 109]. The aeroelastic description had demonstrated capabilities for static aeroelastic analysis, linear stability analysis, controller design and non-linear open-loop time-marching simulations. The challenge is in adapting the framework to the context of wind turbines, which experiences completely different flow fields and structural descriptions. With these complexities in mind, a separate framework was developed that integrates a new aerodynamic description with the multi-body dynamics of the rotor blades and tower, but relying on the same proven fundamental concepts. Only the beam properties of the blades and tower are extracted from SHARP. The new model is also equipped with active control capabilities and extension to offshore floating wind turbine concepts. Numerical verification are performed against various computational test cases to provide confidence in the simulation model. This use of vortex-lattice methods for wind turbine applications with load alleviation capabilities can also be found in the code developed by NTUA Greece as shown in Table 1.1. However, it does not employ a state-space description to the aerodynamic modelling as will be demonstrated in this study to facilitate controller design.

After the aeroelastic description is defined with the accompanying optimal control capabilities, the entire module can be used to analyse the potential of gust load alleviation in wind turbines. The NREL 5MW [129] wind turbine is used as the baseline model for this study. The starting point is a sectional analysis to lay the foundation of active concepts and examine the importance of spatial discretisation in vortex methods to strike a balance between accuracy and computation time. Moving on to a single blade, parametric studies on three-dimensional effects, flap sizing and controller design establish the baseline controllers necessary for the next stage of full turbine simulation.

The model complexity is subsequently increased to the complete land-based turbine on which the effects of multiple blades, tower dynamics and tower shadow are analysed. Passive load alleviation through aeroelastic tailoring will be integrated with active controls to derive synergies between the two mechanisms. The use of passive and active mechanisms are separately well-studied, but their integrated effects are lacking in literature. The possibility of control reversal will also be examined. Floating concepts will finally be considered to appreciate the combined effects of wind and wave motions on turbine fatigue loads, with further investigation on the potential benefits of control methods in these challenging operating environments. This study of active load alleviation using flaps on floating turbines is also not

yet established in literature.

1.10 Outline of Thesis

The study of active aeroelastic design will first build on the foundation of a simple two-dimensional model to appreciate the application of *smart rotor* concepts, in particular flaps, for reduction in flapwise RBM. This will then be developed to model the single rotating blade and the complex full wind turbine, with details of numerical implementation, verification and results presented.

Chapter 2 will present the structural and aerodynamic description of the full turbine, focusing on the UVLM state-space description with prescribed wake to define the unsteady aerodynamics. The multi-body structural dynamics are represented using geometrically non-linear composite beams (GNCB) and connected through Lagrange multipliers. Finally, the unified aeroelastic framework is obtained through fluid-structure coupling and model reductions are performed to expedite the computation process.

Chapter 3 verifies the numerical implementation against common literature for both the two and three-dimensional models, with test cases to provide confidence in the simulations. It will then introduce the baseline NREL 5MW wind turbine considered in this dissertation, describing in detail its numerical implementation and verification using the current aeroservoelastic description.

Chapter 4 presents numerical simulations on the current aeroelastic formulation and will be broken down into three major sections:

- **Section 4.1** considers the sectional model to establish a fundamental understanding of active load alleviation and control methods.
- **Section 4.2** considers the single rotating NREL blade and will first examine the spanwise aerodynamic out-of-plane loadings and parametric sizing of flaps. Preliminary load investigations using homogeneous gust models will be performed to set the foundation for control design in the full turbine model. The validity of the assumptions made in the linear model description will be tested by comparing closed-loop performances with its non-linear counterpart. Finally, the additional torsional loads that surface through active controls will be examined and methods are proposed to overcome these adverse effects.
- **Section 4.3** considers the complete land-based NREL 5MW turbine. The external wind field containing both the turbulence and shear effects are first defined. Given the large size of the model, as a result of the spatial discretisation in the UVLM, model reductions are performed prior to numerical simulations. Subsequently, both passive and active load alleviation mechanisms are considered separately and in an integrated system.

Chapter 5 considers the complete floating NREL 5MW turbine. This is an extension of the land-based turbine by including a floating platform with additional degrees-of-freedom (dof) in the structural model and aerodynamic downwash on the rotors. The disturbance input to the system is now a combination of both wind and wave motion that has the potential of increasing fatigue loads on different turbine components. The model of the floating platform will first be presented, followed by the wave kinematics, numerical verifications as well as closed-loop performances.

Chapter 6 will summarise the theoretical developments, numerical implementations and further highlight key contributions in this work. The chapter will conclude with recommendations for further work that can be considered to extend the numerical model and analysis of load alleviation on wind turbines.

1.11 Publications

The work presented in this dissertation has resulted in the following conference and journal publications:

Journal Publications

- B. F. Ng, R. Palacios, E. C. Kerrigan and J. M. R. Graham, H. Hesse. Aerodynamic load control in HAWT with combined aeroelastic tailoring and trailing-edge flaps. *Wind Energy.* [Accepted]
- B. F. Ng, H. Hesse, R. Palacios, J. M. R. Graham, and E. C. Kerrigan. Aeroservoelastic state-space vortex-lattice modeling and load alleviation of wind turbine blades. *Wind Energy*, 2014.

Conference Papers

- B. F. Ng, H. Hesse, R. Palacios, J. M. R. Graham, and E. C. Kerrigan. Efficient aeroservoelastic modeling and control using trailing-edge flaps of wind turbines. *In Proceedings of UKACC, Loughborough*, UK, 2014.
- B. F. Ng, H. Hesse, R. Palacios, J. M. R. Graham, and E. C. Kerrigan. Model-based aeroservoelastic design and load alleviation of large wind turbines. *In AIAA Scitech - 32nd ASME Wind Energy Symposium*, National Harbor, MD, USA, 2014.
- B. P. Van Parys, B. F. Ng, P. J. Goulart, and R. Palacios. Optimal control for load alleviation in wind turbines. *In AIAA Scitech - 32nd ASME Wind Energy Symposium*, National Harbor, MD, USA, 2014.
- B. F. Ng, R. Palacios, J. M. R. Graham, and E. C. Kerrigan. Aeroservoelastic modelling and active control of very large wind turbine blades for gust load alleviation. *In*

Proceedings of the EAWE 9th PhD Seminar on Wind Energy in Europe, Visby, Gotland, Sweden, 2013.

- B. F. Ng, H. Hesse, R. Palacios, J. M. R. Graham, and E. C. Kerrigan. Aeroservoelastic modeling and load alleviation of very large wind turbine blades. *In AWEA Windpower*, Chicago, IL, USA, 2013.

- B. F. Ng, R. Palacios, J. M. R. Graham, and E. C. Kerrigan. Robust control synthesis for gust load alleviation from large aeroelastic models. *In Proceedings of the EAWE 8th PhD Seminar on Wind Energy in Europe*, Zurich, Switzerland, 2012.

- B. F. Ng, R. Palacios, J. M. R. Graham, and E. C. Kerrigan. Robust control synthesis for gust load alleviation from large aeroelastic models with relaxation of spatial discretisation. *In Proceedings of the EWEC*, Copenhagen, Denmark, 2012.

Table 1.2: Table summarising the modelling, control and performance of variable trailing-edge (TE) geometries and rigid flaps in active load alleviation. All land-based configurations. Unless otherwise stated, all loads are referred to as the blade flapwise/out-of-plane root-bending moments.

Reference	**Turbine**	**Flap type / Dimensions**	**Code / Flap modelling**	**Controller**	**Performance**
Andersen et al. [8]	NREL 5MW	Variable TE geometry / Various	HAWC2 [141] / Gaunaa [82]	PID with high-pass filtered flapwise RBM	Using 1 flap, flapwise RBM fatigue loads are reduced by 25%, 2 flaps by 34% and 3 flaps by 37%. Also studied flap locations and controller time lag/delay on performance.
Andersen et al. [6]	Vestas V66 33m blade	Variable TE geometry / 1 flap of 10% chord, Various span	HAWCStab2 (linear version of HAWC2) [141] / Gaunaa [82]	PD from flapwise RBM	Using 1 flap, flapwise RBM fatigue loads are reduced by 14%, 2 flaps by 50% and 3 flaps by 61%. Also studied different flap sizes and locations.
Barlas and van Kuik [17]	NREL 5MW	Rigid flaps / 1 flap of 20% span and 10% chord	DU_SWAMP [20] / Theodorsen [227]	PID from flapwise RBM	Average 5% to 22% reduction in std. dev. of flapwise RBM. Also studied decentralised individual flap control, centralised individual flap control and decentralised multiple flap control.
Barlas et al. [20]	NREL 5MW	Rigid flaps / 3 flaps per blade (10m chord and 4m span each)	DU_SWAMP [20] / Theodorsen [227]	MPC from low-pass filtered blade tip deflection (uses system identification)	Flapwise RBM fatigue load reductions up to 27.3%. Due to low-pass, only targeted low frequency and 1P loads.
Barlas et al. [21]	Experiment on two-bladed turbine, 1.8m diameter	Rigid flaps and variable TE geometry / 50% chord	DU_SWAMP [20] / Theodorsen [227]	$\mathcal{H}_\infty$ loop-shaping from root bending moments	Experiment - 50.5%, simulation - 52% to 55% reduction in flapwise RBM fatigue loads.
Barlas and Madsen [16]	NREL 5MW	Variable TE geometry / 1 flap with 10% chord, 20% span from 75% to 95% span	HAWC2 [141] / Gaunaa [82]	MPC from high-pass filtered flapwise RBM with inflow velocity measurement at flap mid-span	Various reductions in std. dev. of flapwise RBM and fatigue depending on actuator time lag in controller model and simulation model.
Basualdo [23]	Aerofoil	Rigid flaps and variable TE geometry / Various	Vortex method / Vortex method	PD with moving average filter, tuned using ZN	25% rms reduction in aerofoil displacements.

Reference	Turbine	Flap type / Dimensions	Code / Flap modelling	Controller	Performance
Berg et al. [24]	1.5MW and 5MW turbines	Rigid flaps and variable TE geometry / variable TE geometry (Flexsys) - 20% chord and 25% span. Rigid flap - 10% chord	FAST [182] / Lookup table	PD	12% to 24% reduction in flapwise RBM fatigue loads for 5MW case with rigid flaps. 14% to 34% reduction with variable TE geometry.
Bergami and Henriksen [32]	NREL 5MW	Variable TE geometry / 10% chord, 20% span, from 47.7m to 60m	HAWC2 [141] / Gaunaa [82]	Optimisation	Cyclic loads. 75% and 70% reduction in flapwise RBM using cyclic pitch and flaps, respectively. Showed that pitch required 10 to 20 times more energy than flaps.
Bergami and Poulsen [33]	NREL 5MW	Variable TE geometry / 10% chord, 20% span, from 47.7m to 60m	HAWC2 [141] / Gaunaa [82]	LQ	10% reduction of the flapwise RBM, and 14% if periodic loads anticipation is included.
Buhl *et al.* [53]	Aerofoil	Variable TE geometry / 10% chord, various span	Independent / Gaunaa [82]	Optimisation	85% to 95% reduction in std. dev. of normal force in step gust and 75% to 81% reduction in turbulence. Also considered controller time lag.
Castaignet et al. [60, 59]	Experiment on Vestas V27 - 27m diameter	Rigid flaps / 70cm span, between 13% to 18% chord. Flaps can be actuated from 1P to 4P	Linearised Flex5 for controller (but without unsteady aero) / Gaunaa [82]	SISO frequency-weighted MPC with costs on zero-phase bandpass flapwise RBM and bandstop TE flap angles.	Average flapwise RBM fatigue load reduction of 14% during 38min test and 20% flapwise amplitude reduction of 1P loads.
Frederick et al. [78]	Aerofoil (experiment)	Rigid flaps / 4% chord	Vortex particle and analytical / Vortex particle and analytical	PID and LQG	80% reduction in rms loading.
Henriksen et al. [107]	NREL 5MW	Variable TE geometry / 10% chord, 20% span, from 47.7m to 60m	HAWC2 [141] / Gaunaa [82]	MPC from flapwise RBM	Considers cyclic pitch and cyclic flap. Pitch delivers 18% to 20% reduction in flapwise RBM fatigue loads, flaps 15%. Fatigue load alleviation of 30% combining both.

Reference	Turbine	Flap type / Dimensions	Code / Flap modelling	Controller	Performance
Lackner and van Kuik [136]	NREL 5MW	Rigid flaps / 10% chord from 70% to 90% span	Bladed [42] / Xfoil [252] and look-up table	PID from flapwise RBM	Under NTM, 12% to 15% reduction in flapwise RBM fatigue loads. Under ETM, 5% to 13% reduction.
Ng et al. [181] (current report)	NREL 5MW	Rigid flaps / 10% chord, 20% span, from 70-90% span	GNCB+UVLM [170] / UVLM [131]	LQG and $\mathcal{H}_\infty$	13% reduction of the flapwise RBM and fatigue.
Resor et al. [197]	NREL 5MW	Rigid flaps / 10% chord with 25% span from 67% to 91% span	DU_SWAMP [20] / Theodorsen [227]	PD with high-pass tip deflection with inverted notch at 1P	26% to 30% reduction in std. dev of flapwise RBM, 29% to 31% reduction in flapwise RBM fatigue loads.
Riziotis and Voutsinas [198]	Aerofoil and NREL 5MW	Rigid flaps / 10% chord of various spans	2D - FOIL2W, 3D - GENUVP + GAST [198] / Vortex blobs	PI from flapwise RBM signals	30% to 35% reduction in flapwise RBM.
Wilson et al. [249]	NREL 5MW	Variable TE geometry (Flexsys) / 20% chord	FAST [182] / look-up table	PID from tip deflection	Also considers pitch controls. IPC alone gives around 14% to 20% reduction in std. dev. of flapwise RBM. CPC + flaps gives 21% and IPC + flaps gives 27% to 32% reduction in std. dev. of flapwise RBM.
Wilson et al. [248]	NREL 600KW two-bladed turbine, NREL 1.5MW WindPACT, NREL 5MW	Microtabs, variable TE geometry and rigid flaps / Microtabs (1% chord), variable TE geometry (20% chord), rigid flaps (10% chord). All at outer 25% span	FAST [182] / Look-up table	PID using tip deflection and tip deflection rate	Microtabs - 21%, variable TE geometry - 25% to 32%, rigid flap - 20% reduction in std. dev. of flapwise RBM.
Wilson et al. [250]	NREL 5MW	Rigid flaps / 3 flaps of 10% chord, from 67% to 91% span	DU_SWAMP [20] / Look-up table	LQR	15.5% reduction in flapwise RBM fatigue loads and 13.3% reduction in std. dev. of flapwise RBM.
van Wingerden et al. [236]	Experiment of two-bladed rotor	Variable TE geometry (Thunder) / 10.5m span covering half chord	-	$\mathcal{H}_\infty$ loop-shaping with feed-forward control	60% reduction in root strains using feedback alone. 90% reduction in root strains with both feedback and feed-forward control.

Chapter 2

Theoretical Formulation of Aeroelastic Model

The structural model of the turbine will be based on a composite beam description that allows geometrically non-linear effects to be included. It will be coupled to the unsteady vortex-lattice method for the rotor aerodynamics in attached flow conditions. The UVLM allows control surfaces to be modelled directly and accounts for three-dimensional and transient loads resulting from flap actuation. To arrive at a unified aeroelastic description, a fluid-structure coupling between the aerodynamics and structural dynamics has to be defined.

In this chapter, the individual components of the three-dimensional aeroelastic description will be presented. This will include the linearised composite beam formulation (Section 2.1) and the unsteady vortex-lattice method (Section 2.2). The focus will be on their adaptation and implementation on large wind turbines, emphasizing the multi-body structural description in a constrained formulation and the state-space UVLM representation of the rotor. Subsequently, the fluid-structure coupling (Section 2.3) is defined to arrive at the unified aeroelastic framework (Section 2.5). This is accompanied by discussions on model reduction to achieve computation efficiency (Section 2.4). This chapter will be supplemented by Appendix B with the derivations and mathematical representations of the state-space aeroelastic formulation for numerical implementation.

2.1 The Composite Beam Model

Taking advantage of the slenderness of the tower and blades, their structural deformations will be modelled using a composite beam formulation written in a rotating frame of reference [211, 86]. In its original implementation [110, 109, 168], the structural model can account for large static and transient deformations of the blades, which has been reduced to a one-dimensional representation in the three-dimensional space, using an appropriate cross-sectional analysis methodology [188, 72]. For the purpose of efficient controller design, this work will focus

on the linearised approach that provides a compact form of the equations of motion (EoM) around a possibly geometrically non-linear steady-state equilibrium.

2.1.1 Beam Equations of Motion

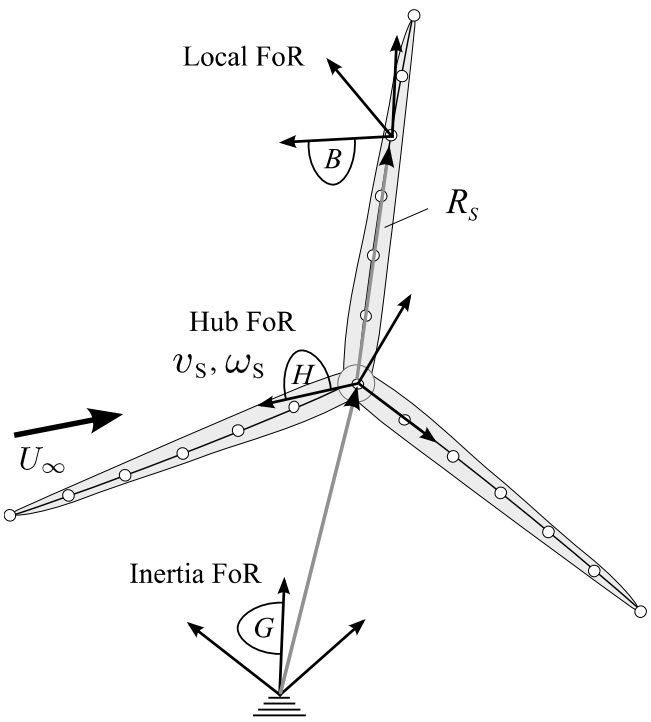


Figure 2.1: Multi-beam configuration with the definition of reference frames for the rotor model.

As shown in Figure 2.1, the deformation of the beam structure (rotor blades) is described in terms of a hub-fixed reference coordinate system H, which is further defined globally to an inertia frame G. The rigid-body translational and angular velocities of the hub H is given by $\boldsymbol{\nu}^\top = \begin{bmatrix}\boldsymbol{v}_S^\top & \boldsymbol{\omega}_S^\top\end{bmatrix}$. To account for large blade deformations, the local orientation of each cross section along the beam reference line is defined by a local coordinate system B and is parametrised at time t by the Cartesian rotation vector $\boldsymbol{\Psi}(s,t)$, where s is the arc-length along the beam reference line [86, 110]. Hence, the nodal positions $\boldsymbol{R}_S(s,t)$, expressed in the hub-fixed frame H, and the cross-sectional orientations, $\boldsymbol{\Psi}(s,t)$, form the independent set of variables for the structural problem.

After a finite-element discretisation, the EoM of the beam are obtained [189, 86], as

$$\boldsymbol{\mathcal{M}}^{SS}(\boldsymbol{\eta})\,\ddot{\boldsymbol{\eta}} + \boldsymbol{\mathcal{M}}^{SR}(\boldsymbol{\eta})\,\dot{\boldsymbol{\nu}} + \boldsymbol{Q}_{gyr}(\boldsymbol{\eta},\dot{\boldsymbol{\eta}},\boldsymbol{\nu}) + \boldsymbol{Q}_{stif}(\boldsymbol{\eta}) = \boldsymbol{Q}_{ext}\,, \tag{2.1}$$

where the matrices $\boldsymbol{\mathcal{M}}^{SS}$ represents the discrete mass, and $\boldsymbol{Q}_{gyr}$, $\boldsymbol{Q}_{stif}$ and $\boldsymbol{Q}_{ext}$ are the gyroscopic, elastic and external generalised forces, respectively, with $\boldsymbol{\eta}$ as the column matrix containing all the nodal displacements and rotations. Eq. (2.1) captures the possibly large

deformations of the blades by balancing the discrete inertial and elastic forces with the external aerodynamic forces. The inertial couplings due to $\boldsymbol{\nu}$ and $\dot{\boldsymbol{\nu}}$, which are functions of time, are incorporated through the coupling mass matrix $\boldsymbol{\mathcal{M}}^{SR}$ and the gyroscopic forces $\boldsymbol{Q}_{gyr}$. The superscripts S and R, denoting structural and rigid-body contributions, respectively, highlight the coupling between the blade structural dynamics and the overall (rigid-body) motion of the rotor.

To arrive at a compact state-space form of the aeroelastic EoM suitable for control synthesis, the structural dynamic equations are linearised around a geometrically non-linear steady-state equilibrium condition $(\boldsymbol{\eta}_0, \dot{\boldsymbol{\eta}}_0 = 0, \boldsymbol{\nu}_0)$. The incremental form of the beam EoM is

$$\begin{aligned}\boldsymbol{\mathcal{M}}^{SS}(\boldsymbol{\eta}_0)\,\Delta\ddot{\boldsymbol{\eta}} + \boldsymbol{\mathcal{M}}^{SR}(\boldsymbol{\eta}_0)\,\Delta\dot{\boldsymbol{\nu}} + \boldsymbol{C}^{SS}_{gyr}(\boldsymbol{\eta}_0,\boldsymbol{\nu}_0)\,\Delta\dot{\boldsymbol{\eta}} + \boldsymbol{C}^{SR}_{gyr}(\boldsymbol{\eta}_0,\boldsymbol{\nu}_0)\,\Delta\boldsymbol{\nu} + \\ + \left[\boldsymbol{K}^{SS}_{gyr}(\boldsymbol{\eta}_0,\boldsymbol{\nu}_0) + \boldsymbol{K}^{SS}_{stif}(\boldsymbol{\eta_0})\right]\Delta\boldsymbol{\eta} = \Delta\boldsymbol{Q}_{ext}\,,\end{aligned} \tag{2.2}$$

where the contribution to the (constant) mass, damping and stiffness matrices has been obtained through direct linearisation of the different generalised forces with respect to $\boldsymbol{\eta}$ and its time derivatives.The effects of tower oscillation on the dynamics of the rotor blades are accounted for in the coupling mass and damping matrices, $\boldsymbol{\mathcal{M}}^{SR}$ and $\boldsymbol{C}^{SR}_{gyr}$, respectively. These linearised beam equations also preserve the rotational effect due to the prescribed angular velocity Ω through the contribution of the linearised gyroscopic forces to the damping and stiffness matrices $\boldsymbol{C}^{SS}_{gyr}$ and $\boldsymbol{K}^{SS}_{gyr}$, respectively. A detailed derivation of Equation (2.2) can be found in Ref. [110].

The resulting linear system can be cast into state-space form, from which we can define an eigenvalue problem that includes rotational effects and geometrically non-linear equilibrium deformations.

2.1.2 Flexible Multi-body Dynamics

The inclusion of tower dynamics in the modelling of large wind turbines constitutes a multi-body dynamics problem. Similar to the modelling of blades, the tower is modelled using beam elements and its structural dynamics are described with respect to global frame A at the tower base. The motion of this frame is further described with respect to the inertia frame G and parametrised through quaternions, to account for any motion of the tower in floating structures. The tower and rotor are connected using Lagrange multipliers, which constrain the nodal velocities of the local frame B_t at the tower top to the translational and angular velocities of frame H fixed to the rotor hub, as shown in Figure 2.2.

Each constraint between two connected bodies (tower and rotor) is enforced through six Lagrange multipliers $\boldsymbol{\lambda}$, for three translational and three rotational constraints. Due to the parametrisation of large rotations in the present geometrically non-linear description of

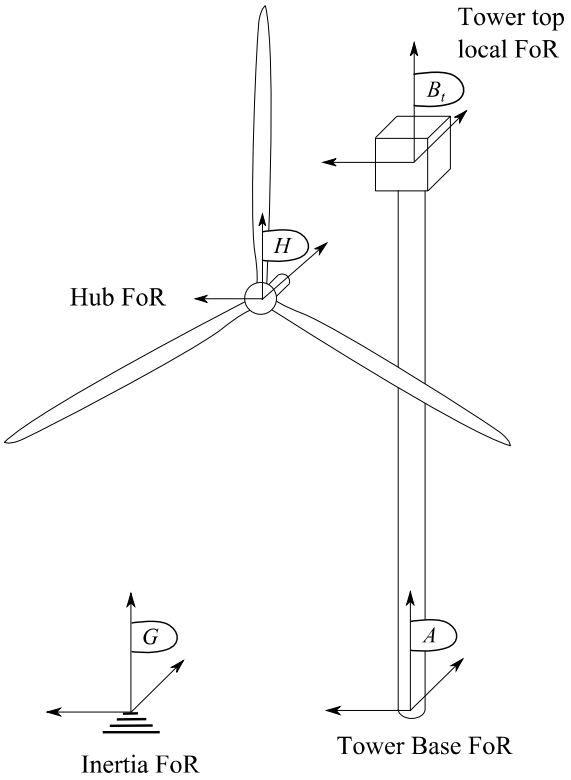


Figure 2.2: Multi-body configuration with the definition of reference frames for the combined rotor and tower model. The abbreviation FoR stands for Frame of Reference.

flexible bodies, it is convenient to enforce the constraints in terms of velocities through

$$\boldsymbol{\Phi}_{ij}(\boldsymbol{\eta}_i) \begin{Bmatrix} \dot{\boldsymbol{\eta}}_i \\ \boldsymbol{\nu}_j \end{Bmatrix} = 0\,, \tag{2.3}$$

where $\boldsymbol{\eta}_i$ are the nodal displacements and rotations at the end of body i. $\boldsymbol{\Phi}$ represents the nonholonomic quantity of all constraints defined between two bodies i and j. In the context of the wind turbine model, i and j denote the tower and rotor degrees of freedom, respectively, and $\boldsymbol{\eta}_i$ corresponds to the displacements and rotations of tower top frame B_t, as defined in Figure 2.2.

From the kinematic description of the beam displacements and velocities [110], we can write the nonholonomic constraints as

$$\boldsymbol{\Phi}_{ij} = \begin{bmatrix} \boldsymbol{\Lambda} & -\boldsymbol{A}_{CC} \end{bmatrix}\,, \tag{2.4}$$

where $\boldsymbol{\Lambda}$ and $\boldsymbol{A}_{CC}$ are transformation matrices to enforce the velocity constraints in the local frame at the end of body i. The resulting change in orientation between the rotor frame H and the tower top frame B_t is accounted for in matrix $\boldsymbol{A}_{CC}$.

The finite element discretisation of the primary variables, the displacements and rotations of all blades, finally leads to the augmented system, given as

$$\boldsymbol{\mathcal{M}}(\boldsymbol{\eta}) \begin{Bmatrix} \ddot{\boldsymbol{\eta}} \\ \dot{\boldsymbol{\nu}} \end{Bmatrix} + \boldsymbol{Q}_{gyr}(\boldsymbol{\eta}, \dot{\boldsymbol{\eta}}, \boldsymbol{\nu}) + \boldsymbol{Q}_{stif}(\boldsymbol{\eta}) = \boldsymbol{Q}_{ext} + \boldsymbol{\Phi}^{\top} \dot{\boldsymbol{\lambda}}, \tag{2.5}$$

where $\boldsymbol{\eta}$ is now the resulting column matrix of all the nodal displacements and rotations of the N bodies and $\boldsymbol{\nu} = \left[\boldsymbol{\nu}_1^{\top}, \cdots, \boldsymbol{\nu}_N^{\top}\right]^{\top}$. Eq. (2.5) extends the original flexible-body dynamics in Eq. (2.1) with the additional constraints. Note that the discrete mass matrix, $\boldsymbol{\mathcal{M}}$, and the discrete generalised forces, $\boldsymbol{Q}_{gyr}$, $\boldsymbol{Q}_{stif}$ and $\boldsymbol{Q}_{ext}$, respectively, now include the structural and rigid-body contributions of all bodies.

2.1.3 Linearised Description

The coupled wind turbine problem, Eq. (2.5) can now be linearised around the steady-state equilibrium with constant rotor velocity leading to a compact form, written as

$$\begin{bmatrix} \boldsymbol{\mathcal{M}}_t^{SS} & \mathbf{0} & \mathbf{0} & -\boldsymbol{\Lambda}^{\top} \\ \mathbf{0} & \boldsymbol{\mathcal{M}}_r^{SS} & \boldsymbol{\mathcal{M}}_r^{SR} & \mathbf{0} \\ \mathbf{0} & \boldsymbol{\mathcal{M}}_r^{RS} & \boldsymbol{\mathcal{M}}_r^{RR} & \boldsymbol{A}_{CC}^{\top}(t) \\ \mathbf{0} & \mathbf{0} & \mathbf{0} & \mathbf{0} \end{bmatrix} \begin{Bmatrix} \Delta\ddot{\boldsymbol{\eta}}_t \\ \Delta\ddot{\boldsymbol{\eta}}_r \\ \Delta\dot{\boldsymbol{\nu}}_r \\ \Delta\dot{\boldsymbol{\lambda}} \end{Bmatrix} + \begin{bmatrix} \boldsymbol{C}_t^{SS} & \mathbf{0} & \mathbf{0} & \mathbf{0} \\ \mathbf{0} & \boldsymbol{C}_r^{SS} & \boldsymbol{C}_r^{SR} & \mathbf{0} \\ \mathbf{0} & \boldsymbol{C}_r^{RS} & \boldsymbol{C}_r^{RR} & \mathbf{0} \\ \boldsymbol{\Lambda} & \mathbf{0} & -\boldsymbol{A}_{CC}(t) & \mathbf{0} \end{bmatrix} \begin{Bmatrix} \Delta\dot{\boldsymbol{\eta}}_t \\ \Delta\dot{\boldsymbol{\eta}}_r \\ \Delta\boldsymbol{\nu}_r \\ \Delta\boldsymbol{\lambda} \end{Bmatrix}$$
$$+ \begin{bmatrix} \boldsymbol{K}_t^{SS} & \mathbf{0} & \mathbf{0} & \mathbf{0} \\ \mathbf{0} & \boldsymbol{K}_r^{SS} & \mathbf{0} & \mathbf{0} \\ \mathbf{0} & \boldsymbol{K}_r^{RS} & \mathbf{0} & \mathbf{0} \\ \mathbf{0} & \mathbf{0} & \mathbf{0} & \mathbf{0} \end{bmatrix} \begin{Bmatrix} \Delta\boldsymbol{\eta}_t \\ \Delta\boldsymbol{\eta}_r \\ \mathbf{0} \\ \mathbf{0} \end{Bmatrix} = \begin{Bmatrix} \mathbf{0} \\ \boldsymbol{Q}_{ext} \\ \int \boldsymbol{Q}_{ext} \\ \mathbf{0} \end{Bmatrix}, \tag{2.6}$$

where the subscripts t and r correspond to the tower and rotor blades, respectively. In the above description, the rigid-body contributions of the tower are removed in the land-based configuration of the turbine. As mentioned, the transformation matrices, $\boldsymbol{\Lambda}$ and $\boldsymbol{A}_{CC}$ enforces the velocity constraints between the rotor hub H and tower top frame B_{t}. The transformation $\boldsymbol{A}_{CC}$ further accounts for changes in orientation between the two frames due to rotation of the rotor. The prescribed rotor velocity and azimuth angles of the rotor blades at steady-state, Ω and $\theta = \Omega t$, respectively, lead to gyroscopic contributions to the damping and stiffness matrices with non-negligible effects on the vibration frequencies of the coupled system [179]. The overall external forces and moments $\int \boldsymbol{Q}_{ext}$ acting at the rotor hub H are included in the third row of the equation to balance the forces due to the tower top motion $\boldsymbol{A}_{CC}^{\top}(t)\Delta\dot{\boldsymbol{\lambda}}$. Additional forcing term to represent losses in loads through the drivetrain and generator can also be included on the right-hand-side of Eq. (2.6) to offset the combined loading $\int \boldsymbol{Q}_{ext}$ at the hub. Finally, the constraint function is included in the last row of Eq. (2.6).

The transformation $\boldsymbol{A}_{CC}$ is defined as

$$\boldsymbol{A}_{CC}(t) = \begin{bmatrix} \boldsymbol{C}_{BS}(t) & \boldsymbol{0} \\ \boldsymbol{0} & \boldsymbol{C}_{BS}(t) \end{bmatrix}, \tag{2.7}$$

where

$$\boldsymbol{C}_{BS}(t) = \begin{bmatrix} \cos\theta(t) & -\sin\theta(t) & 0 \\ \sin\theta(t) & \cos\theta(t) & 0 \\ 0 & 0 & 1 \end{bmatrix}^{\top} \begin{bmatrix} \cos\alpha_{rp} & 0 & -\sin\alpha_{rp} \\ 0 & 1 & 0 \\ \sin\alpha_{rp} & 0 & \cos\alpha_{rp} \end{bmatrix}^{\top}, \tag{2.8}$$

which accounts for the rotation of the turbine $\theta(t)$ and the pitch of the rotor plane α_{rp} with respect to the vertical. $\boldsymbol{\Lambda}$ is an identity matrix. The current description can also be extended to floating concepts in which rigid-body motions of the tower is included in Eq. (2.6). The details are documented in Section 5.

2.2 The Unsteady Vortex-Lattice Method

The basis of the potential-flow theory starts with Laplace's equation (Section 2.2.1), which can be solved using boundary-element methods (Section 2.2.2) with additional physical considerations of wake dynamics (Section 2.2.3). This lays the foundation for the time-domain unsteady vortex-lattice method (UVLM) used in the current description of rotor aerodynamics (Section 2.2.4), which is written in a state-space representation (Section 2.2.5) and for the calculation of aerodynamic forces (Section 2.2.6).

2.2.1 Potential Flow Theory

In potential-flow theory, the velocity field is described as the gradient of a scalar function, known as the velocity potential and given by $\boldsymbol{v} = \nabla\varphi$. This relationship indicates that potential-flow is irrotational as the curl of a gradient is always a zero vector, defined by $\nabla \times \boldsymbol{v} = 0$. Furthermore, for incompressible flows, the divergence of the velocity will be zero, resulting in

$$\nabla\boldsymbol{v} = \nabla^2\varphi = 0\,, \tag{2.9}$$

satisfying Laplace's equation.

The problem statement is accompanied by a pair of boundary conditions. The first boundary condition requires zero flow velocity normal to the surface (Neumann boundary condition) given by

$$\nabla(\boldsymbol{\varphi} + \boldsymbol{\varphi}_{\infty}) \cdot \boldsymbol{n} = 0\,, \tag{2.10}$$

where $\boldsymbol{\varphi}_{\infty}$ is the free-stream velocity potential and $\boldsymbol{n}$ is a vector normal to the body's surface.

The second boundary condition requires that the flow disturbance due to the body's mo-

tion through the fluid, diminishes far from the body. This indicates that the flow approaches free-stream conditions at infinity and can be expressed as

$$\lim_{r\to\infty} |\nabla\boldsymbol{\varphi}| = 0\,, \tag{2.11}$$

where r is the distance to the body.

2.2.2 General Solution based on Boundary-Element Method

In numerical analysis for three-dimensional flows, the Laplace's equation is commonly solved by applying boundary-element methods based on Green's function. This approach involves distributing elementary solutions over the body surface and its wake that satisfies the boundary condition in Eq. (2.11) of having the velocity field decaying to zero as $r \to \infty$. At $r = 0$, the velocity becomes singular and thus the basic elements are also known as singularities. The solution to Laplace's equation is then reduced to finding the unknown singularity distribution subject to the boundary condition in Eq. (2.10).

By applying Green's function, the general solution to Laplace's equation based on elementary solutions of a doublet and a source distributed over the body surface and wake, is given by

$$\boldsymbol{\varphi} = \frac{1}{4\pi}\int_{body+wake} \mu\boldsymbol{n}\cdot\left(\frac{1}{r}\right) dS - \frac{1}{4\pi}\int_{body} \sigma\left(\frac{1}{r}\right) dS\,, \tag{2.12}$$

where μ is the strength of the doublet, σ is the strength of the source and S is the surface boundary. The choice of the elementary solutions is not unique and often, only one type or a linear combination of two singularities are considered. While Eq. (2.12) is based on a distribution of doublets and sources, other elementary solutions such as vortices can be used. For simulating the effect of thickness, source elements are used, whereas for lifting problems, antisymmetric elements such as doublet or vortex elements are used.

Eq. (2.12) can be substituted into the non-penetrating boundary condition Eq. (2.10), and specified at a set of control points (collocation points) on the body surface boundary to solve for the unknown singularities. This reduces the integral equation to a set of algebraic equations. The main advantage of the potential-flow solution is that the three-dimensional field problem defined by Laplace's partial differential equation can be reduced to a two-dimensional equivalent problem through the use of elementary solutions, leading to panel methods [131].

2.2.3 Physical Considerations of Wake Dynamics

For lifting cases, the solution of Laplace's equation through the superposition of elementary solutions is not unique even after fulfilling the non-penetrating boundary condition. This is overcome by imposing additional physical conditions pertaining to the wake model, in particular, defining the strength of the shed wake at trailing-edge and its geometry (shape

and location).

The strength of the wake vortex at trailing-edge can be determined through Kelvin's condition which dictates the conservation of circulation Γ in the fluid surrounding the body and its wake. This is represented by

$$\frac{d\Gamma}{dt} = 0\,. \tag{2.13}$$

Once the wake is shed, it is convected downstream by both the free-steam velocity and the induced velocity from body motion. This is known as the free-wake model and is computationally expensive due to the need to evaluate the induced velocities at all wake points and update their positions at every time-step. Alternatively, prescribed wake shapes can be defined based on observations or experimental flow visualisation results. Likewise, the self-induced velocities on the wake can be neglected and wake shapes are prescribed solely based on the freestream velocity.

2.2.4 Linearised Description of Time-domain UVLM

The time-domain UVLM uses vortex rings as fundamental solutions, which are located in lattices that represent the blades (modelled as a lifting surface) and their wakes. The vortex rings are quadrilateral elements with discrete vortices in closed-loop, with each vortex segment having a constant circulation strength (See Figure 2.3).

As the lifting surface moves through the flow, a row of wake vortices is formed, shed and convected downstream from the trailing-edge. Similar to the element distribution on the lifting surface, the wake is made up of vortex rings. The circulation strength of each shed vortex ring is equal to the strength of the trailing-edge ring at the previous time-step, enforcing Kelvin's circulation theorem in Eq. (2.13).

Once shed, the wake is convected downstream by both the freestream velocity and also velocities induced by all other vortices. This free wake model introduces non-linearities as the locations of the wake vortex rings become a function of time. To obtain linear models for control methods and for computation efficiency, a prescribed wake model that neglects roll-up effects due to self-induced velocities can be implemented.

In the case of the turbine rotor, the shape and position of the prescribed wake is determined by the inflow and rotational velocity of the rotor. This forms a helicoidal shape [61, 1] as shown in Figure 3.5a. A parametric study to understand the effects of wake roll-up showed that models with free and prescribed wake displayed little differences in terms of the computed aerodynamic forces [170]. Other studies comparing the two wake models reported less than 5% difference in power coefficients over a range of tip-speed-ratios (TSR) from 3 to 12 [212].

In the UVLM formulation, the effects of thickness has been neglected. As mentioned, thickness effects can be considered through the use of source elements. However, for wind

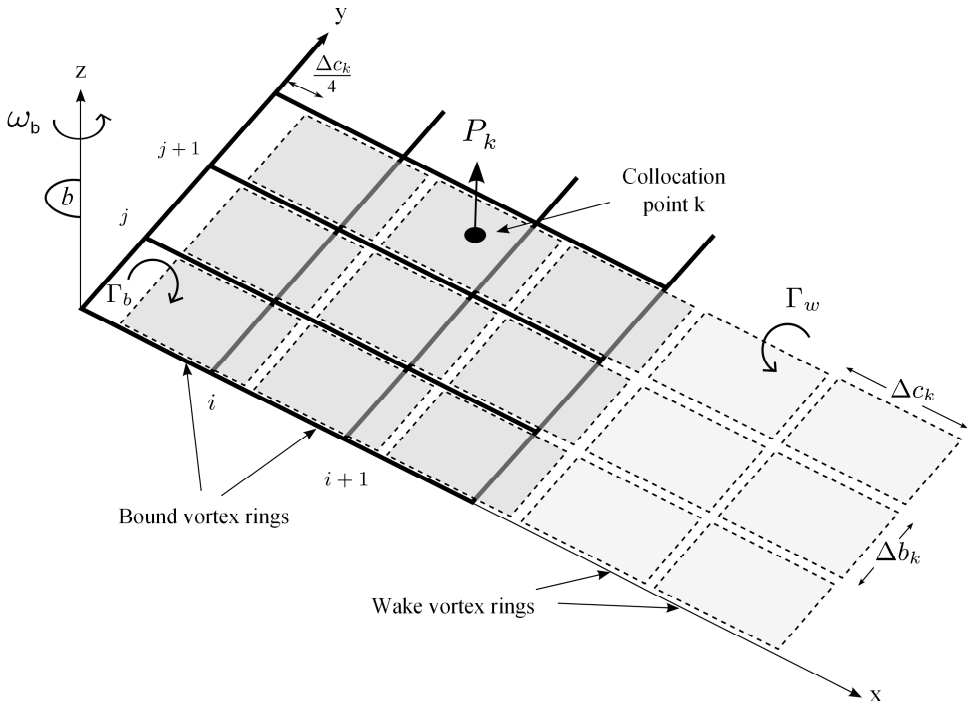


Figure 2.3: Typical thin lifting surface represented by the unsteady vortex-lattice method.

turbines, the effect of thickness in the blades has shown to be negligible when computing aerodynamic forces [34]. Also, the flow along the outer span of the blades, in particular the tip region where the flaps are located, operates in attached flow conditions [35].

The leading segment of the vortex ring on the lifting surface is placed along the quarter chord of each panel, and the collocation points are placed at the three-quarter chord of each panel where boundary conditions are imposed. Flaps are included in the vortex model through additional downwash on the panels covering the flap region.

The vorticity of the blade's bound vortex rings can be determined by imposing the Neumann boundary conditions in Eq. (2.10) at controls (collocation) points distributed over the lifting surface. For multiple lifting surfaces, the relationship for the non-penetrating boundary condition can be expressed as

$$\sum_{p=1}^{N}\left(\sum_{q=1}^{N}\left[\boldsymbol{A}_{b,pq}\boldsymbol{\Gamma}_{b,q}^{n+1}+\boldsymbol{A}_{w,pq}\boldsymbol{\Gamma}_{w,q}^{n+1}\right]+\boldsymbol{w}_{p}^{n+1}\right)=\mathbf{0}\,, \tag{2.14}$$

where N is the number of blades, $\boldsymbol{\Gamma}_b$ and $\boldsymbol{\Gamma}_w$ denote the circulation strengths of the blade's bound and wake vortex rings, respectively. The influence coefficients, $\boldsymbol{A}_b$ and $\boldsymbol{A}_w$, give the induced normal velocity to blade surface at collocation points (resolved using the Biot-Savart law). The last term $\boldsymbol{w}$ is the downwash at collocation points and n is the time-step.

The influence coefficient can be found using the Biot-Savart law, for which the velocity

q_k induced by a vortex segment l on a collocation point k is expressed as

$$\Delta q_{k,l} = \frac{\Gamma_l}{4\pi} \frac{d\mathbf{l}_l \times \mathbf{r}_{k,l}}{|\mathbf{r}_{k,l}|^3} \,, \tag{2.15}$$

and assuming unit circulation (with $\Gamma = 1$), the influence coefficient for a single pair of vortex segment and collocation point is

$$A_{k,l} = \mathbf{n}_k \cdot \Delta q_{l,k} \,, \tag{2.16}$$

where $\mathbf{n}_k$ is a unit vector normal to the surface at collocation point k and $d\mathbf{l}_l$ is a vector representing the length of the vortex segment. The distance between the vortex segment and collocation point is given by $\mathbf{r}_{k,l}$.

Following Katz and Plotkin [131], the Biot-Savart law can be written in a form more suitable for computational purposes as

$$\mathbf{q}_{1,2} = \frac{\Gamma}{4\pi} \frac{\mathbf{r}_1 \times \mathbf{r}_2}{|\mathbf{r}_1 \times \mathbf{r}_2|^2} \mathbf{r}_0 \cdot \left(\frac{\mathbf{r}_1}{|\mathbf{r}_1|} - \frac{\mathbf{r}_2}{|\mathbf{r}_2|} \right) \,, \tag{2.17}$$

where $\mathbf{r}_1$ and $\mathbf{r}_2$ represents the two ends of a vortex segment and $\mathbf{r}_0 = \mathbf{r}_2 - \mathbf{r}_1$. For a rectilinear vortex ring with four segments, Eq. (2.17) is evaluated four times for each of the panel sides and the velocities summed together. From the Biot-Savart law, it is evident that the influence of vortices decays with the square of distance. This allows vortex panels far downstream to be neglected. Biot-Savart law is also singular when $r = 0$, but this can be overcome by vortex core models [246].

The downwash $\boldsymbol{w}$ in Eq. (2.14) is generated by the motion of the lifting surface $\boldsymbol{w}_b$ (the blade), rigid-body motions $\boldsymbol{w}_\nu$ (such as the deflection of the tower), the actuators $\boldsymbol{w}_\beta$ (such as trailing-edge flaps) and external disturbances $\boldsymbol{w}_\delta$ (such as gusts). The downwash are all in the same time-step and the first two contributions $\boldsymbol{w}_b$ and $\boldsymbol{w}_\nu$ are used to couple with the structural and rigid-body dynamics, respectively. The last two contributions $\boldsymbol{w}_\beta$ and $\boldsymbol{w}_\delta$ are inputs to the system. In order for the final EoM to be in explicit form, $\boldsymbol{w}_\beta$ and $\boldsymbol{w}_\delta$ are written in time-step n instead of $n+1$, assuming the effects on the solution to be minimal if the time-step is kept small. The downwash is written as

$$\boldsymbol{w}^{n+1} = \boldsymbol{w}_b^{n+1} + \boldsymbol{w}_\nu^{n+1} + \boldsymbol{w}_\beta^n + \boldsymbol{w}_\delta^n \,. \tag{2.18}$$

The downwash due to motion of the lifting surface $\boldsymbol{w}_b$ is mapped from the structural beam model of the rotor blades and can be represented using

$$\boldsymbol{w}_b^{n+1} = \begin{bmatrix} \boldsymbol{T}_{\Delta\eta_r} & \boldsymbol{T}_{\Delta\dot{\eta}_r} \end{bmatrix} \begin{Bmatrix} \Delta\boldsymbol{\eta}_r \\ \Delta\dot{\boldsymbol{\eta}}_r \end{Bmatrix}^{n+1} \,, \tag{2.19}$$

where $\boldsymbol{T}_{\Delta\eta_r}$ and $\boldsymbol{T}_{\Delta\dot{\eta}_r}$ project the contribution of the nodal displacements $\Delta\boldsymbol{\eta}_r$ and velocities $\Delta\dot{\boldsymbol{\eta}}_r$ onto the aerodynamic lifting surface as downwash.

Finally, the downwash due to rigid-body motion of the rotor (resulting from tower dynamics) is expressed as

$$\boldsymbol{w}_{\nu}^{n+1} = \boldsymbol{T}_{\Delta\dot{\eta}_t}(t)\Delta\dot{\boldsymbol{\eta}}_t^{n+1}\,, \tag{2.20}$$

where $\boldsymbol{T}_{\Delta\dot{\eta}_t}$ is varying with the azimuth location $\theta(t)$ of the rotor blades with respect to the tower.

2.2.5 State-Space UVLM Description

The UVLM description allows the influence coefficients from Eq. (2.14) and wake shedding to be concatenated into a monolithic state-space form. For a three-bladed turbine rotor with equally spaced identical blades, it is written as

$$\begin{bmatrix} \boldsymbol{A}_{c,11} & \boldsymbol{A}_{c,12} & \boldsymbol{A}_{c,13} \\ \boldsymbol{A}_{c,21} & \boldsymbol{A}_{c,22} & \boldsymbol{A}_{c,23} \\ \boldsymbol{A}_{c,31} & \boldsymbol{A}_{c,32} & \boldsymbol{A}_{c,33} \end{bmatrix} \begin{Bmatrix} \boldsymbol{\Gamma}_1 \\ \boldsymbol{\Gamma}_2 \\ \boldsymbol{\Gamma}_3 \end{Bmatrix}^{n+1} = \begin{bmatrix} \boldsymbol{D}_w & \boldsymbol{0} & \boldsymbol{0} \\ \boldsymbol{0} & \boldsymbol{D}_w & \boldsymbol{0} \\ \boldsymbol{0} & \boldsymbol{0} & \boldsymbol{D}_w \end{bmatrix} \begin{Bmatrix} \boldsymbol{\Gamma}_1 \\ \boldsymbol{\Gamma}_2 \\ \boldsymbol{\Gamma}_3 \end{Bmatrix}^{n} + \begin{Bmatrix} \hat{\boldsymbol{w}}_1 \\ \hat{\boldsymbol{w}}_2 \\ \hat{\boldsymbol{w}}_3 \end{Bmatrix}^{n+1}\,, \tag{2.21}$$

where $\boldsymbol{\Gamma} = \begin{Bmatrix} \boldsymbol{\Gamma}_a \\ \boldsymbol{\Gamma}_w \end{Bmatrix}$ and $\hat{\boldsymbol{w}} = \begin{Bmatrix} \boldsymbol{w} \\ \boldsymbol{0} \end{Bmatrix}$. The matrices $\boldsymbol{A}_{c,pq}$ contain the influence coefficient on the bound collocation points of blade p due to both bound and wake vortex rings of blade q, where $p = 1, 2, 3$ and $q = 1, 2, 3$. These matrices also contains rows, together with $\boldsymbol{D}_w$, to impose Kelvin's condition in Eq. (2.13) for the shedding and convection of wake downstream. Due to the symmetry of the equally spaced identical rotor blades, $\boldsymbol{A}_{c,11} = \boldsymbol{A}_{c,22} = \boldsymbol{A}_{c,33}$, $\boldsymbol{A}_{c,12} = \boldsymbol{A}_{c,23} = \boldsymbol{A}_{c,31}$ and $\boldsymbol{A}_{c,13} = \boldsymbol{A}_{c,21} = \boldsymbol{A}_{c,32}$. Note that Eq. (2.21) can be used to represent any number of blades on a rotor.

2.2.6 Computation of Aerodynamic Forces

Pressure distribution across each panel on the lifting surface (rotor blades) is computed using the unsteady Bernoulli equation [131], from which the aerodynamic forces can be obtained. The pressure distribution across each panel k can be expressed in compact form as

$$\Delta P_k^{n+1} = \boldsymbol{\Phi}_k^{n+1}\boldsymbol{\Gamma}_b^{n+1} + \boldsymbol{\Phi}_k^{n}\boldsymbol{\Gamma}_b^{n}\,, \tag{2.22}$$

where $\boldsymbol{\Gamma}_b^{n+1}$ contains circulation strengths of all vortex rings on the lifting surface. Assuming constant pressure acting on the panels, the aerodynamic forces $\boldsymbol{F}_k$ on each panel can be computed as

$$\boldsymbol{F}_k^{n+1} = \Delta P_k^{n+1}\Delta b_k \Delta c_k \cdot \boldsymbol{n}_k\,, \tag{2.23}$$

where Δb_k and Δc_k are the spanwise and chordwise size of bound panel k.

Since the UVLM is based on thin wing theory, special care is needed to obtain the leading-edge suction [213]. In steady flow, pressure forces in the direction of flow are cancelled by

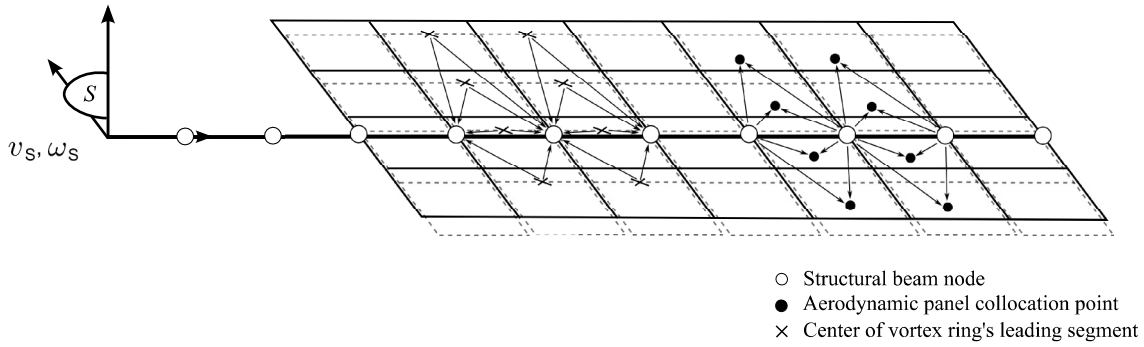


Figure 2.4: Coupling between fluid and structure.

leading-edge suction, leading to zero drag. This is commonly known as the d'Alembert's paradox. In the case of unsteady flow, drag may be present and an approximation given by Katz and Plotkin [131] is used, expressed compactly as

$$D_k^{n+1} = \boldsymbol{\Upsilon}_k^{n+1}\boldsymbol{\Gamma}_b^{n+1} + \boldsymbol{\Upsilon}_k^{n}\boldsymbol{\Gamma}_b^{n}\,. \tag{2.24}$$

The derivation and corresponding matrix entries in Eqs. (2.19) to (2.24) are documented in Appendix B.

2.3 Fluid-Structure Coupling

The continuous-time structural EoM of the wind turbine is discretised using the Newmark-β method and the blades are subsequently coupled with the discrete-time UVLM using coinciding spanwise discretisation.

As each lifting surface is comprised of panels while the structure is modelled using beams that run along the span of the blade, a procedure for mapping the two meshes is required. Firstly, aerodynamic forces at the centre of each bound vortex ring's leading segment are mapped onto the structural nodes. This is under the assumption that the lifting surface remains undeformed such that the spanwise aerodynamic grid coincides with the finite-element description of the beam [170]. Also, it assumes that the aerodynamic forces are approximated as isolated loads at the centre of each bound vortex ring's leading segment. Next, structural displacements, rotations and velocities of the beam are mapped onto aerodynamic collocation points as downwash shown in Figure 2.4.

The computed aerodynamic forces are described in the local frame of each blade. In order to couple with the rigid-body dynamics of the rotor, a further transformation is performed to describe the forces in the rotor hub frame used in Eq. (2.6). Details are found in Appendix B.

The discretised structural dynamics of Eq. (2.6), linear UVLM non-penetrating boundary conditions of Eq. (2.21) and the aerodynamic forces of Eqs. (2.23), (2.24) can symbolically

be expressed, respectively, as

$$\boldsymbol{N}_1(t)\boldsymbol{q}^{n+1} + \boldsymbol{N}_2(t)\boldsymbol{q}^{n} = \boldsymbol{Q}_s^{n+1}\,, \tag{2.25}$$

$$\boldsymbol{A}_1\boldsymbol{\Gamma}^{n+1} = \boldsymbol{A}_2\boldsymbol{\Gamma}^{n} + \boldsymbol{T}(t)\boldsymbol{q}^{n+1} + \boldsymbol{W}^{n}\,, \tag{2.26}$$

$$\boldsymbol{\Psi}_1\boldsymbol{\Gamma}^{n+1} + \boldsymbol{\Psi}_2\boldsymbol{\Gamma}^{n} = \boldsymbol{Q}_a^{n+1}\,, \tag{2.27}$$

where in Eq. (2.25), $\boldsymbol{q}$ contains all the structural and rigid-body degrees of freedom of the tower and rotor blades including the Lagrange multipliers, and $\boldsymbol{Q}_s$ contains the external forces acting on the structural nodes and the combined forces at the rotor hub. The structural beams representing the rotor blades are linearised around a prescribed rotational velocity, and non-linearity enters the system through the constraint equation, which is azimuth dependent in the transformation matrix. As a result, the coefficients $\boldsymbol{N}_1(t)$ and $\boldsymbol{N}_2(t)$ from the Newmark-β discretisation are time-varying.

For the non-penetrating boundary condition in Eq. (2.26), $\boldsymbol{\Gamma}$ contains all the rotor's bound and wake circulations and $\boldsymbol{W}$ is the concatenated vector of downwash due to external perturbations in the flow field (gust) and flap deflections in Eq. (2.18). The additional term $\boldsymbol{T}(t)$ accounts for the downwash acting on the bound collocation points resulting from both structural and rigid-body motions of the rotor and tower, in Eqs. (2.19) and (2.20), respectively. The UVLM is linear in the rotor description but the coupling terms inject an azimuth dependent downwash due to tower deflection onto the panel collocation points.

The last equation (2.27) contains the corresponding forces and moments $\boldsymbol{Q}_a$ computed using the unsteady Bernoulli equation and drag forces. These forces are resolved both at the structural nodes and also summed at the rotor hub. The detailed representation of the matrices can be found in Appendix B.

From the above descriptions of the structure and fluid dynamics, the coupled model can be expressed as

$$\begin{bmatrix} \boldsymbol{A}_1 & -\boldsymbol{T}(t) \\ -\boldsymbol{\Psi}_1 & \boldsymbol{N}_1(t) \end{bmatrix} \begin{Bmatrix} \boldsymbol{\Gamma} \\ \boldsymbol{q} \end{Bmatrix}^{n+1} = \begin{bmatrix} \boldsymbol{A}_2 & \boldsymbol{0} \\ \boldsymbol{\Psi}_2 & -\boldsymbol{N}_2(t) \end{bmatrix} \begin{Bmatrix} \boldsymbol{\Gamma} \\ \boldsymbol{q} \end{Bmatrix}^{n} + \begin{Bmatrix} \boldsymbol{W} \\ \boldsymbol{0} \end{Bmatrix}^{n}\,. \tag{2.28}$$

In the above equation, the first row accounts for the non-penetrating boundary condition of Eq. (2.26). The second row equates Eq. (2.25) to Eq. (2.27).

This aeroelastic formulation accommodates for rotor anisotropy such as imbalance (in conditions of icing) and also external anisotropy pertaining to operating conditions such as wind shear, yaw error and gravity [214]. A block diagram representation of the fluid-structure coupling in the aeroelastic model is shown in Figure 2.5.

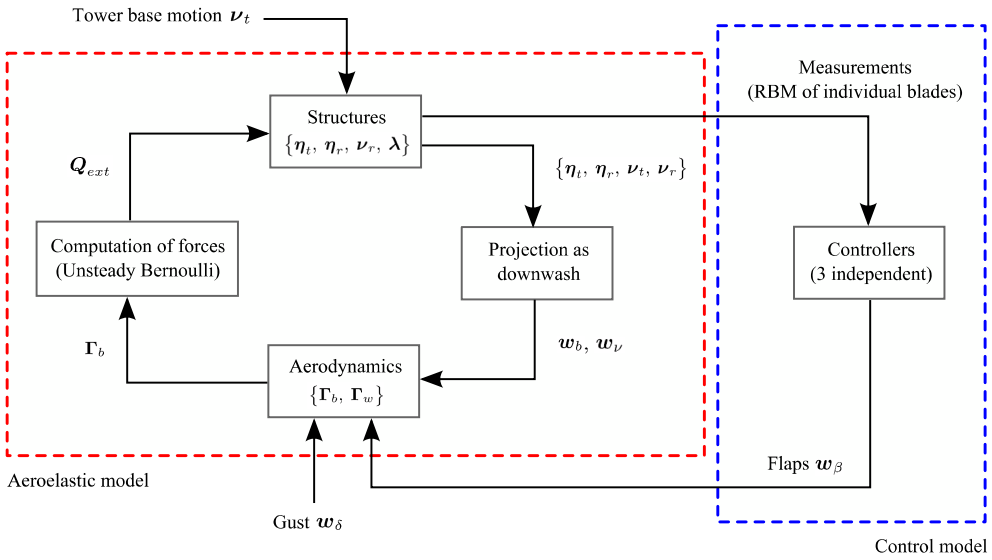


Figure 2.5: Simplified block diagram of fluid-structure coupling in the aeroelastic model and closed-loop configuration with external controllers.

2.4 Model Reduction of the Coupled Aeroelastic Description

With each bound and wake circulation in the UVLM model representing a state, the coupled equations of motion contain a large number of states and direct time-simulation easily becomes computationally prohibitive on a single-processor machine. Furthermore, the rotation of the rotor imposes non-linearity in both the constrained structural EoM and the coupling terms with aerodynamics, rendering standard model-based reduction techniques on the final aeroelastic system infeasible. Hence, the structural and UVLM models are reduced separately prior to coupling. Firstly, the structural degrees of freedom are truncated using classical modal decomposition [87] on individual beams, projecting the dynamic equations onto the natural modes of the system. Next, the UVLM model is reduced through balanced truncation, which has been shown [112] to be effective in reducing large aeroelastic models.

For the structural EoM, classical modal truncation is used to retain only the dominant low frequency modes and details are found in most graduate level structural dynamics textbooks [114]. The key idea is to project the structural dof into its spatial (modes) and temporal (amplitude) parts, thus allowing high frequency modes to be identified and truncated. Here, the modal projection and truncation are performed on the elastic dof of the tower and rotor separately, leading to the modal form of constrained multi-body description (note that the

rigid-body dof can also be included in the modal projection but is not attempted here [109])

$$\begin{aligned}
&\begin{bmatrix} \boldsymbol{\phi}_t^\top \boldsymbol{\mathcal{M}}_t^{SS} \boldsymbol{\phi}_t & \mathbf{0} & \mathbf{0} & -\boldsymbol{\phi}_t \boldsymbol{\Lambda}^\top \\ \mathbf{0} & \boldsymbol{\phi}_{sb}^\top \boldsymbol{\mathcal{M}}_r^{SS} \boldsymbol{\phi}_{sb} & \boldsymbol{\phi}_{sb}^\top \boldsymbol{\mathcal{M}}_r^{SR} & \mathbf{0} \\ \mathbf{0} & \boldsymbol{\mathcal{M}}_r^{RS} \boldsymbol{\phi}_{sb} & \boldsymbol{\mathcal{M}}_r^{RR} & \boldsymbol{A}_{CC}^\top(t) \\ \mathbf{0} & \mathbf{0} & \mathbf{0} & \mathbf{0} \end{bmatrix} \begin{Bmatrix} \Delta\ddot{\boldsymbol{\eta}}_t \\ \Delta\ddot{\boldsymbol{\eta}}_r \\ \Delta\dot{\boldsymbol{\nu}}_r \\ \Delta\dot{\boldsymbol{\lambda}} \end{Bmatrix} \\
&+ \begin{bmatrix} \boldsymbol{\phi}_t^\top \boldsymbol{C}_t^{SS} \boldsymbol{\phi}_t & \mathbf{0} & \mathbf{0} & \mathbf{0} \\ \mathbf{0} & \boldsymbol{\phi}_{sb}^\top \boldsymbol{C}_r^{SS} \boldsymbol{\phi}_{sb} & \boldsymbol{\phi}_{sb}^\top \boldsymbol{C}_r^{SR} & \mathbf{0} \\ \mathbf{0} & \boldsymbol{C}_r^{RS} \boldsymbol{\phi}_{sb} & \boldsymbol{C}_r^{RR} & \mathbf{0} \\ \boldsymbol{\Lambda}\boldsymbol{\phi}_t & \mathbf{0} & -\boldsymbol{A}_{CC}(t) & \mathbf{0} \end{bmatrix} \begin{Bmatrix} \Delta\dot{\hat{\boldsymbol{\eta}}}_t \\ \Delta\dot{\hat{\boldsymbol{\eta}}}_r \\ \Delta\boldsymbol{\nu}_r \\ \Delta\boldsymbol{\lambda} \end{Bmatrix} \\
&+ \begin{bmatrix} \boldsymbol{\phi}_t^\top \boldsymbol{K}_t^{SS} \boldsymbol{\phi}_t & \mathbf{0} & \mathbf{0} & \mathbf{0} \\ \mathbf{0} & \boldsymbol{\phi}_{sb}^\top \boldsymbol{K}_r^{SS} \boldsymbol{\phi}_{sb} & \mathbf{0} & \mathbf{0} \\ \mathbf{0} & \boldsymbol{K}_r^{RS} \boldsymbol{\phi}_{sb} & \mathbf{0} & \mathbf{0} \\ \mathbf{0} & \mathbf{0} & \mathbf{0} & \mathbf{0} \end{bmatrix} \begin{Bmatrix} \Delta\hat{\boldsymbol{\eta}}_t \\ \Delta\hat{\boldsymbol{\eta}}_r \\ \mathbf{0} \\ \mathbf{0} \end{Bmatrix} = \begin{Bmatrix} \mathbf{0} \\ \boldsymbol{\phi}_{sb}^\top \boldsymbol{Q}_{ext} \\ \int \boldsymbol{Q}_{ext} \\ \mathbf{0} \end{Bmatrix},
\end{aligned} \tag{2.29}$$

where $\boldsymbol{\phi}_t$ and $\boldsymbol{\phi}_{sb}$ are the corresponding modes shapes of the tower and rotor, respectively, and $\hat{\boldsymbol{\eta}}$ is now the projected modal co-ordinate.

For the unsteady aerodynamics, balanced model truncation is applied to the linear UVLM description. Balancing methods are based on the concepts of controllability and observability of a linear dynamical system [167, 91]. Consider the system $\{\boldsymbol{A}, \boldsymbol{B}, \boldsymbol{C}, \boldsymbol{D}\}$ with states $\boldsymbol{x}$, balancing involves identifying a transformation $\boldsymbol{x}_b = \boldsymbol{T}_b \boldsymbol{x}$ such that the balanced system $\{\boldsymbol{T}_b \boldsymbol{A} \boldsymbol{T}_b^{-1}, \boldsymbol{T}_b \boldsymbol{B}, \boldsymbol{C} \boldsymbol{T}_b^{-1}, \boldsymbol{D}\}$, is equally controllable and observable. The balancing transformation matrix $\boldsymbol{T}_b$ is obtained using the controllability and observability Gramians $\boldsymbol{P}$ and $\boldsymbol{Q}$, respectively, which are given for stable linear time-invariant systems by the algebraic Lyapunov equations [143, 93]

$$\begin{aligned}
\boldsymbol{A}\boldsymbol{P} + \boldsymbol{P}\boldsymbol{A}^\top + \boldsymbol{B}\boldsymbol{B}^\top &= \mathbf{0}\,, \\
\boldsymbol{A}^\top \boldsymbol{Q} + \boldsymbol{Q}\boldsymbol{A} + \boldsymbol{C}^\top \boldsymbol{C} &= \mathbf{0}\,.
\end{aligned} \tag{2.30}$$

The square-root of the eigenvalues of the Gramian product

$$\boldsymbol{\sigma} = \sqrt{\lambda(\boldsymbol{P}\boldsymbol{Q})}\,,$$

gives the Hankel singular values (HSV) of the system $\sigma_1 \geq \sigma_2 \geq \cdots \geq \sigma_n > 0$. HSV provides a measure of the energy contribution of each state to the input/output behaviour of the system and are invariant through the transformation. For the balanced system, the controllability and observability Gramians, $\boldsymbol{P}_b = \boldsymbol{T}_b \boldsymbol{P} \boldsymbol{T}_b^\top$ and $\boldsymbol{Q}_b = \boldsymbol{T}_b^{-\top} \boldsymbol{Q} \boldsymbol{T}_b^{-1}$, will be the same, diagonal and equal to the HSV. Reduction of the balanced system can then be achieved by removing rows in the transformation matrix $\boldsymbol{T}_b$ corresponding to HSVs of each balanced state [112].

To balance the discrete-time linear UVLM description for model truncation, Eqs. (2.26) and (2.27) are re-arranged into a general state-space realisation, such that the non-linearity

due to downwash from the structural dynamics are expressed as inputs to the system, written as

$$\begin{aligned}\boldsymbol{\Gamma}^{n+1} &= \boldsymbol{A}_1^{-1}\boldsymbol{A}_2\boldsymbol{\Gamma}^n + \begin{bmatrix}\boldsymbol{A}_1^{-1} & \boldsymbol{A}_1^{-1}\end{bmatrix}\begin{Bmatrix}\boldsymbol{T}(t)\boldsymbol{q}^{n+1}\\ \boldsymbol{W}^n\end{Bmatrix},\\ \boldsymbol{Q}_a^{n+1} &= \left(\boldsymbol{\Psi}_1\boldsymbol{A}_1^{-1}\boldsymbol{A}_2 + \boldsymbol{\Psi}_2\right)\boldsymbol{\Gamma}^n + \begin{bmatrix}\boldsymbol{\Psi}_1\boldsymbol{A}_1^{-1} & \boldsymbol{\Psi}_1\boldsymbol{A}_1^{-1}\end{bmatrix}\begin{Bmatrix}\boldsymbol{T}(t)\boldsymbol{q}^{n+1}\\ \boldsymbol{W}^n\end{Bmatrix}.\end{aligned} \tag{2.31}$$

In line with the standard implementation of the balanced reduction, the discrete-time system is then converted to continuous-time using a bilinear transformation, which preserves stability and the system Gramians. Discrete-time counterparts of the balanced reduction exist but are not explored in this work [112, 84]. After model reduction, the system assumes the form

$$\begin{aligned}\boldsymbol{x}_r^{n+1} &= \boldsymbol{A}_r\boldsymbol{x}_r^n + \begin{bmatrix}\boldsymbol{B}_{r,s} & \boldsymbol{B}_{r,g}\end{bmatrix}\begin{Bmatrix}\boldsymbol{T}(t)\boldsymbol{q}^{n+1}\\ \boldsymbol{W}^n\end{Bmatrix},\\ \boldsymbol{Q}_a^{n+1} &= \boldsymbol{C}_r\boldsymbol{x}_r^n + \begin{bmatrix}\boldsymbol{D}_{r,s} & \boldsymbol{D}_{r,g}\end{bmatrix}\begin{Bmatrix}\boldsymbol{T}(t)\boldsymbol{q}^{n+1}\\ \boldsymbol{W}^n\end{Bmatrix},\end{aligned} \tag{2.32}$$

where $\left\{\boldsymbol{A}_r, \begin{bmatrix}\boldsymbol{B}_{r,s} & \boldsymbol{B}_{r,g}\end{bmatrix}, \boldsymbol{C}_r, \begin{bmatrix}\boldsymbol{D}_{r,s} & \boldsymbol{D}_{r,g}\end{bmatrix}\right\}$ are the reduced system matrices, which can be assembled back to the coupled aeroelastic description of Eq. (2.28) and expressed as

$$\begin{bmatrix}\boldsymbol{I} & -\boldsymbol{B}_{r,s}\boldsymbol{T}(t)\boldsymbol{T}_\phi\\ \boldsymbol{0} & \hat{\boldsymbol{N}}_a(t) - \boldsymbol{D}_{r,s}\boldsymbol{T}(t)\end{bmatrix}\begin{Bmatrix}\boldsymbol{x}_r\\ \hat{\boldsymbol{q}}\end{Bmatrix}^{n+1} = \begin{bmatrix}\boldsymbol{A}_r & \boldsymbol{0}\\ \boldsymbol{C}_r & -\hat{\boldsymbol{N}}_b(t)\end{bmatrix}\begin{Bmatrix}\boldsymbol{x}_r\\ \hat{\boldsymbol{q}}\end{Bmatrix}^{n} + \begin{bmatrix}\boldsymbol{B}_{r,g}\\ \boldsymbol{D}_{r,g}\end{bmatrix}\boldsymbol{W}^n, \tag{2.33}$$

where $\hat{\boldsymbol{q}}$, $\hat{\boldsymbol{N}}_a(t)$ and $\hat{\boldsymbol{N}}_b(t)$ are from the discretised structural EoM in modal form in Eq. (2.29), and $\boldsymbol{T}_\phi$ is included to map the projected structural dof to the corresponding aerodynamic downwash.

2.5 Final Aeroelastic Equations

The resulting EoM obtained from combining the constrained structural model and UVLM provide the full aeroelastic system in state-space representation [170]. The equations can be written in the standard form

$$\begin{aligned}\boldsymbol{x}^{n+1} &= \boldsymbol{A}(t)\boldsymbol{x}^n + \boldsymbol{B}\boldsymbol{w}_\beta^n + \boldsymbol{G}\boldsymbol{w}_\delta^n,\\ \boldsymbol{y}^n &= \boldsymbol{C}\boldsymbol{x}^n + \boldsymbol{D}\boldsymbol{w}_\beta^n + \boldsymbol{H}\boldsymbol{w}_\delta^n,\end{aligned} \tag{2.34}$$

where the state matrix $\boldsymbol{A}$ is a function of the azimuth angle $\theta(t)$, which defines the orientations of the rotor blades with respect to the tower at each time-step n. The state vector that

completely defines the aeroelastic system is

$$\boldsymbol{x}^\top = \begin{bmatrix} \Delta\boldsymbol{\Gamma}_b^\top & \Delta\boldsymbol{\Gamma}_w^\top & | & \Delta\boldsymbol{\eta}_t^\top & \Delta\dot{\boldsymbol{\eta}}_t^\top & \Delta\boldsymbol{\eta}_r^\top & \Delta\dot{\boldsymbol{\eta}}_r^\top & | & \Delta\boldsymbol{\nu}_r^\top & \Delta\boldsymbol{\lambda}^\top \end{bmatrix}, \tag{2.35}$$

containing the aerodynamics, structures and rigid-body states. The inputs to Eq. (2.34) are from the downwash terms in Eq. (2.18). Note that the downwash due to motion of lifting surface $\boldsymbol{w}_b$ and rigid-body motion $\boldsymbol{w}_\nu$ do not appear, since they are coupled to the structural dynamics. The control input $\boldsymbol{w}_\beta$ represents the downwash due to flap motion and the external disturbance $\boldsymbol{w}_\delta$ is the downwash due to gust. The output vector, $\boldsymbol{y}$, includes the desired output (e.g., blade root-bending moments, tip deflection, tower top deflection, etc).

Note that in the case of a single blade description, which is assumed to be clamped in a rotating environment, Eq. (2.34) will be linear time-invariant (LTI) as the structural dof of the blade are no longer dependent on its azimuth location with respect to the tower.

Chapter 3

Numerical Verification and Implementation

The three-dimensional methodology presented here comprising of the composite beam model and UVLM was originally explored [168, 109] for flexible aircraft applications under the integrated framework SHARP. The numerical implementation has been verified for static aeroelastic analysis, linear stability analysis, controller design and non-linear open-loop time-marching simulations of flexible aircraft [170, 171, 110].

Given the different operating conditions and modelling requirements between flexible aircraft and wind turbines, in particular the rotating field, only the beam properties of the blades and tower are extracted from SHARP. They are then constrained in a multi-beam configuration, which is subsequently coupled to the rotor aerodynamics following the proven aeroelastic concept.

Prior to establishing the full turbine model, some preliminary studies and numerical verifications are needed to gain confidence in the aeroelastic description. Hence, we begin with a three-dimensional blade description to ensure that gyroscopic effects are correctly captured in the composite beam definition (Section 3.1). Subsequently, the full turbine is modelled. In this dissertation, the land-based NREL 5-MW turbine is chosen as the baseline model (Section 3.2.1) given its publicly available and well-documented structural and aerodynamic properties. The numerical implementation of this NREL turbine using the current aeroelastic formulation will be discussed together with its verification studies (Section 3.2.2). The chapter will conclude with a description of controller implementation for subsequent active load alleviation simulation studies (Section 3.2.3).

Table 3.1: Cantilever beam properties with uniform mass and stiffness distribution. (Verification case)

Span	60 m	Torsional stiffness		4.14×10^8 N·m^2
Elastic axis	0.5·c		(out-of-plane)	(in-plane)
Centre of gravity	0.5·c	Bending stiffness	5.22×10^9 N·m^2	1.32×10^{10} N·m^2
Mass per unit length	2.79×10^2 kg/m	Moment of inertia	1.93×10^2 kg·m	3.22×10^2 kg·m

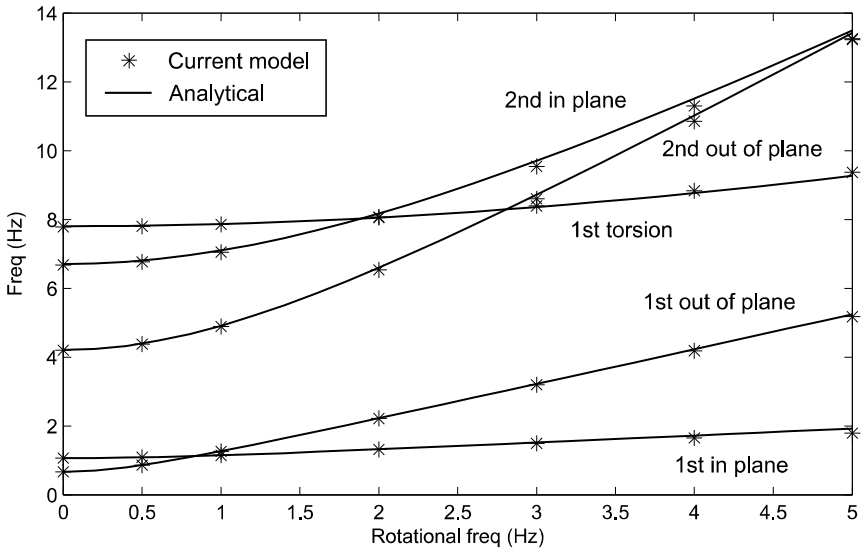


Figure 3.1: Campbell plots comparing fundamental modes of a simple rotating cantilever beam computed using the current model and analytical solutions.

3.1 Numerical Verification of Blade Definition

The main difference between a rotating turbine blade and the wing of an aircraft is the presence of a spanwise tension field resulting from gyroscopic effects. To demonstrate that these effects are correctly captured in the structural description, Campbell plots (showing natural frequencies of the blade as a function of rotational speed) for increasing rotational speeds from SHARP are generated. They are then compared against the analytical solutions in Appendix C for a long rotating cantilever beam with constant properties described in Table 3.1. Figure 3.1 shows the first and second fundamental modes for out-of-plane and in-plane bending as well as the first torsional mode of the rotating beam. It is evident that with increasing rotational speeds, the stiffening effect from gyroscopic forces increases the natural frequencies of all the modes considered. Also, the results from SHARP and the analytical solutions compared well.

Next, the coupling of the structural model to the UVLM is verified on the Goland wing [92], which is a generic lifting surface that is commonly used for numerical verifications in aeroelasticity. This rectangular cantilevered wing has a semi-span of 6.10m and chord of 1.83m [111]. The flutter speeds for the Goland wing in sea-level forward flight has

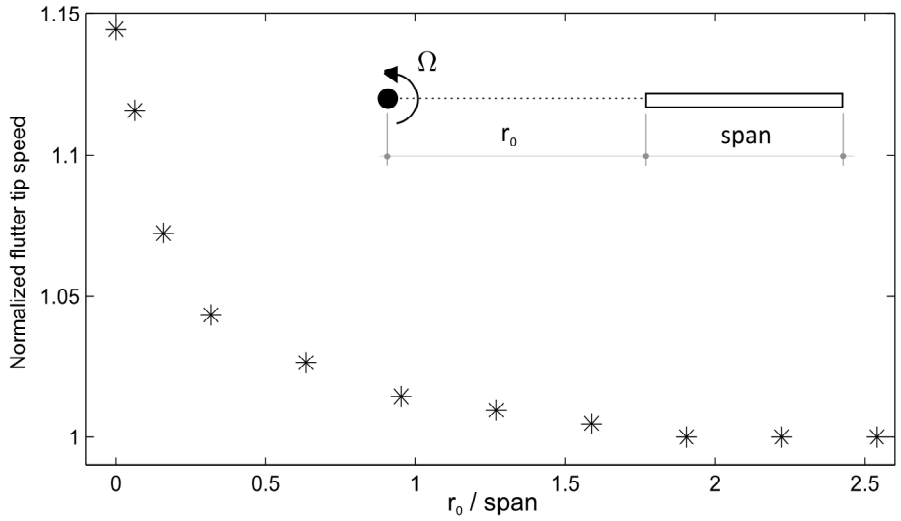


Figure 3.2: Impact of increasing rotational effects on the Goland wing (by varying the distance between the axis of rotation and the root of the wing) on flutter tip speeds. Results are normalised against the forward flight flutter speed.

been reported to be between 163.5 m/s [244] and 169 m/s [111]. For the current model, the flutter speed obtained through an eigenvalue analysis is 166 m/s with a converged solution using 10 chordwise and 15 spanwise panels.

It is interesting at this stage to investigate the influence on flutter speeds with increasing rotational effects. Putting the Goland wing in a rotating frame and varying the distance r_0 from the axis of rotation to the root of the wing, we observe in Figure 3.2 that increasing rotational effects (by bringing axis of rotation closer to the root) causes flutter tip speeds to increase by up to 15%, This gives assurance that it is conservative to set flutter limits using non-rotating conditions. Note that the wake shed by the rotating surface follows the prescribed shape as shown in Figure 3.5a with the curvature of wake shedding depending on the radius of rotation. In the context of wind turbines, flutter has so far not been observed owing to the high torsional stiffness in the blades, and early investigations predicted flutter speeds to be 3.5 to 6 times that of the operating speed [153]. Even for modern MW-sized turbines, their flutter speeds are shown to be more than twice the operating speeds [151, 152, 13, 98, 195].

Next, defining the axis of rotation at the root of the beam, the root locus for the first two modes (out-of-plane bending and torsion) in increasing angular velocities is shown in Figure 3.3. The roots are obtained from converting the eigenvalues of the discrete-time aeroelastic system into continuous-time. Three cases are plotted - the first two corresponding to the Goland wing rotating about its root with tip speeds increasing from 80 m/s to 200 m/s. The difference lies in the structural model where the second case is computed without gyroscopic effects. Also in the plot is the root locus for the Goland wind in straight forward flight from 80 m/s to 170 m/s (without rotational effects). Comparing cases 2 and 3, it is evident that rotational effects in the UVLM, mainly caused by the linear variation of

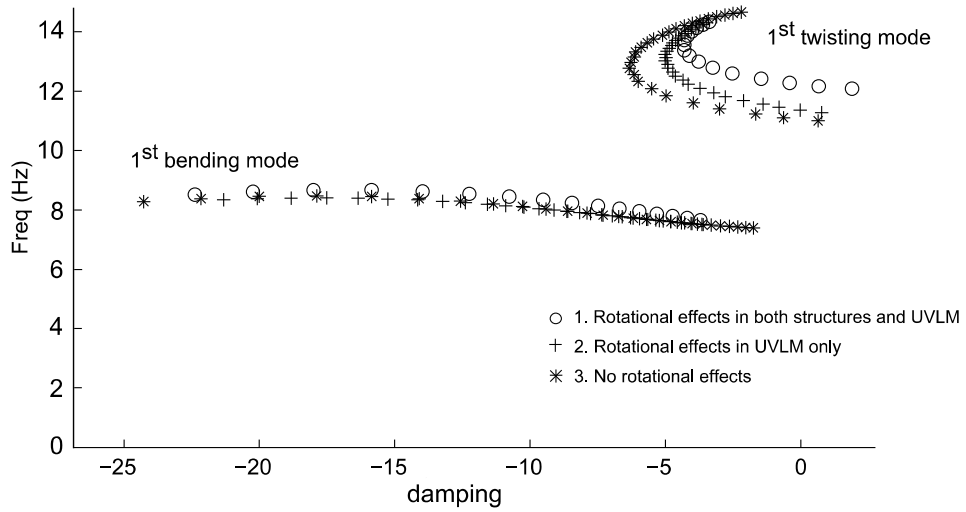


Figure 3.3: Root locus for the first two modes (out-of-plane bending and torsion) of the Goland wing. Case 1 - Rotational effects in both UVLM and structural model (rotational tip speeds from 80 m/s to 200 m/s). Case 2 - Rotational effects accounted for in UVLM only (rotational tip speeds from 80 m/s to 200 m/s). Case 3 - No rotational effects (rotational tip speeds from 80 m/s to 170 m/s).

free-stream from root to tip have a substantial effect in influencing the natural frequency of the torsional mode (the higher-frequency mode), while having a very minor impact on the bending mode. When gyroscopic effects are also included on the structural equations (case 1), the frequency of the torsional mode is pushed even higher. In addition, the first bending mode is also slightly increased.

3.2 Baseline Wind Turbine

This dissertation will adopt the model of the NREL 5MW reference wind turbine [129], which is a publicly available conceptual turbine for benchmark studies of typical utility-scale onshore and offshore multi-megawatt turbines. It is rated 5MW and contains three 61.5m blades with pitch-to-feather capabilities for variable speed regulation. The model parameters rely heavily on the REpower 5MW machine, supplemented with conceptual data from the WindPACT [251, 159], RECOFF [194] and DOWEC [106] projects. In particular, the structural and aerodynamic properties of the turbine blade are adapted from the DOWEC (LM) 64.5m blade [150] with material layup from the UpWind [230] project. To date, it is considered the baseline model for numerical studies of aeroelastic behaviour, controls and components, and serves as the benchmark for comparison of numerical codes [128].

Recently, larger turbine models have also been conceptualised to meet the trends of turbine up-scaling. These include the Sandia's 13.2MW turbine with 100m blades [96, 94, 52] and also DTU's 10MW turbine [15] with 86.4m blades. Both of these conceptual turbines rely on geometric up-scaling from the NREL 5MW according to similarity rules. Their main

focus is on the re-design of composite lay-up to maintain structural integrity. As such, the aeroelastic response and dynamics of these larger turbines are largely similar to that of NREL. In this project, studies on the Sandia blade were also performed but it was seen that the aeroelastic behaviour and flapwise RBM redictions were comparable to the NREL 5MW turbine. Therefore, only the results for the NREL 5MW turbine is presented in this dissertation.

3.2.1 NREL 5MW Reference Wind Turbine

The tower, shaft and blades of the NREL 5MW turbine with cross-sectional properties described in Ref. [129] are modelled as composite beams connected through Lagrange multipliers at the hub. The nacelle and hub are modelled as point masses on the tower top at prescribed offset locations [145]. As for the drivetrain, it is modelled as a torsional rod with a single element connecting the tower to the rotor hub. The rotor and shaft are pitched at 5° as documented. A graphical interpretation of the NREL 5MW wind turbine is shown in Figure 3.4, describing the locations and dimensions of various components [129].

For the aerodynamics, vortex panels are placed on the outer 80% span of the blade and a helicoidal wake profile [61] is prescribed to enable a linear UVLM representation, as shown in Figure 3.5a. The inboard segment of the blade with cylindrical cross-sections is not modelled here but can be included as additional drag forces. The aerodynamic forces arising from pre-twist can be modelled as additional downwash on the lifting surface.

In all the cases that follows, unless otherwise stated, the model of the NREL 5MW wind turbine rotor and tower are used. The operating conditions are under rated inflow of 11 m/s, time step of 0.0035 seconds and tip speed ratio (TSR) of 7. The time-step is chosen based on the discretisation in the UVLM, with the relationship given by $dt = c_m/(v_m d)$, where d is the number of bound chordwise panels, c_m and v_m are the chord length and relative velocity at blade mid-span, respectively.

3.2.2 Numerical Implementation and Verification

Moving from the single lifting surface description in Section 3.1 to the rotor configuration of the NREL turbine, we first investigate the effects of wake interaction on aerodynamic forces due to the presence of multiple surfaces (blades). This is to study the effects of the off-diagonal terms in Eq. (2.21) containing the cross influence coefficients. Next, the Lagrange multipliers are verified to ensure that the constraints between the tower and rotor are implemented correctly. This will be done by comparing the response of the turbine to static flapwise loads as well as matching the natural frequencies of the full wind turbine in parked conditions. Finally, we will study the effects of tower flexibility on the frequency response of the system and the effects of rotation on individual blades. Gravity is not included as it induces edgewise loads, which are not the focus of this study.

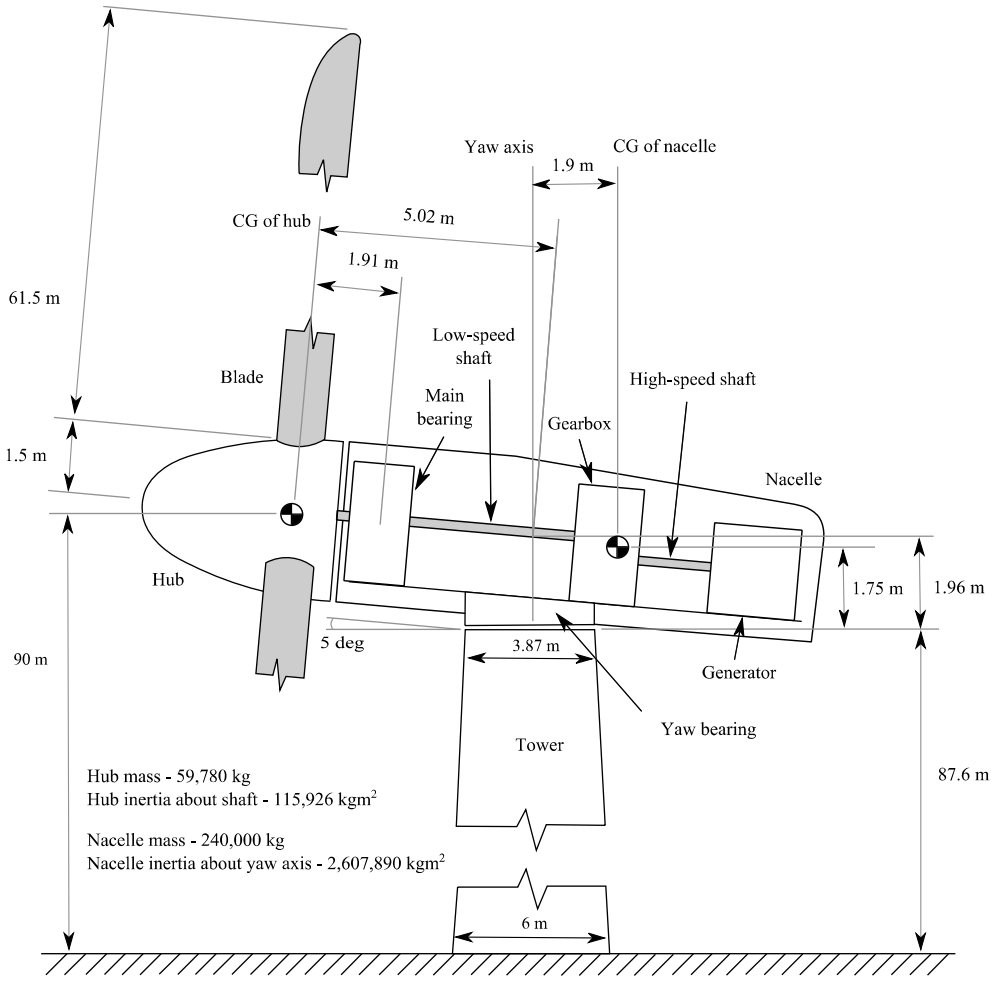
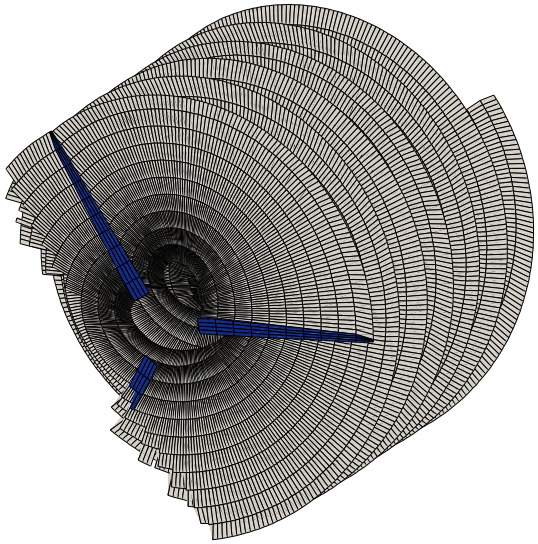


Figure 3.4: Graphical interpretation of the NREL 5MW offshore wind turbine. The gearbox and generator are merged with the nacelle as a single point mass in the modelling, but are shown here for completeness.

Firstly, in modelling the rotor, three similar NREL 5MW blades are placed at 120° azimuth from each other with cross influence of circulation included in the UVLM model. The main effect of the multiple lifting surfaces is to generate additional backflow from the rotating wake, thus reducing flapwise loads on the blades. This is equivalent to the axial induction factor used in BEM theory [102]. Figure 3.6 shows the normalised aerodynamic lift on one of the blades in the full rotor subject to an impulsively started flow and the vertical dotted lines indicate each time the blade has rotated 120°. It is evident that in the transient stage, each time the blade passes through the wake shed by another blade or by itself, the aerodynamic loads are reduced. Also plotted on the same figure is a single rotating blade for comparison, showing a lower reduction in flapwise loads when the blade passes by its own shed wake after a full rotation. In steady state, the flapwise loads in the full rotor configuration are about 15% lower than in a single rotating blade.

Next, the six Lagrange multipliers constraining the tower and rotor in the augmented structural equations of motion are numerically verified, where the kinematic results for the



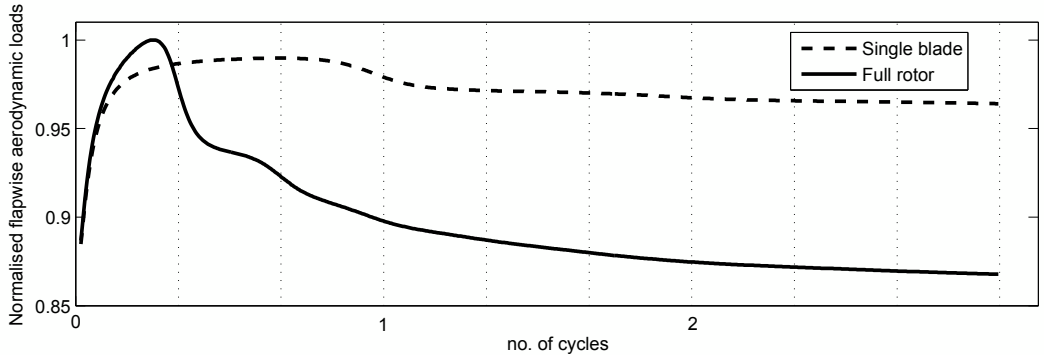


Figure 3.6: Normalised flapwise aerodynamic loads for a single rotating blade and for the full rotor, subjected to an impulsively started gust. (Vertical dotted lines indicate each time a blade has rotated 120°)

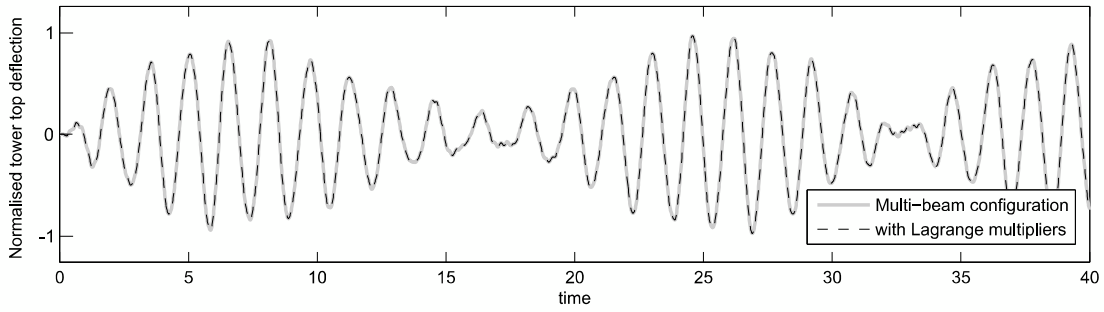
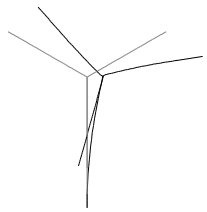


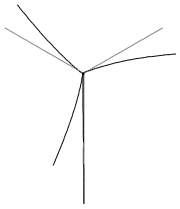
Figure 3.7: Normalised tower top out-of-plane deflection for a stationary (parked) turbine when subject to an out-of-plane force at the blade tip. Comparing a multi-beam configuration with the constrained multi-body description.



(a) 1st Tw SS (0.315Hz)



(b) 1st Tw FA (0.320Hz)



(c) 1st DT Tor (0.611Hz)



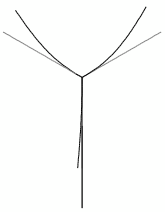
(d) 1st Bl Asym FY (0.641Hz)



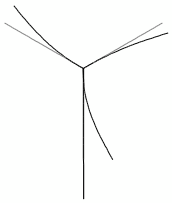
(e) 1st Bl Asym FP (0.670Hz)



(f) 1st Bl Coll Flap (0.703Hz)



(g) 1st Bl Asym EP (1.082Hz)



(h) 1st Bl Asym EY (1.096Hz)



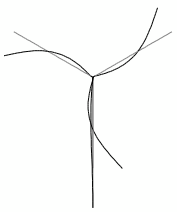
(i) 2nd Bl Asym FY (1.729Hz)



(j) 2nd Bl Asym FP (1.879Hz)



(k) 2nd Bl Coll Flap (1.973Hz)



(l) 2nd DT Tor (2.316Hz)

Figure 3.8: Stationary mode shapes of the NREL 5MW reference wind turbine in parked configuration. The abbreviations are: Bl (Blade), Tw (Tower), SS (Side-Side), FA (Fore-Aft), DT (Drivetrain), Tor (Torsion), Asym (Asymmetric), FY (Flapwise-Yaw), FP (Flapwise-Pitch), Coll (Collective), EP (Edgewise-Pitch), EY (Edgewise-Yaw).

Table 3.2: Full system natural frequencies (Hz) of the NREL 5MW wind turbine (stationary) for structural discretisation of (a) 10 tower elements and 48 elements on each blade (same as documentation [129]) and (b) 10 tower elements and 12 elements on each blade (interpolated blade properties).

Mode	**Description**	**FAST** [129]	**ADAMS** [129]	**SHARP** (10t, 48b)	**SHARP** (10t, 12b)
1	1^{st} Tower Side-to-Side	0.312	0.316	0.315	0.316
2	1^{st} Tower Fore-Aft	0.324	0.320	0.320	0.321
3	1^{st} Drivetrain Torsion	0.621	0.609	0.611	0.617
4	1^{st} Blade Asymmetric Flapwise Yaw	0.667	0.630	0.641	0.662
5	1^{st} Blade Asymmetric Flapwise Pitch	0.668	0.669	0.670	0.693
6	1^{st} Blade Collective Flap	0.699	0.701	0.703	0.726
7	1^{st} Blade Asymmetric Edgewise Pitch	1.080	1.074	1.082	1.091
8	1^{st} Blade Asymmetric Edgewise Yaw	1.090	1.090	1.096	1.105
9	2^{nd} Blade Asymmetric Flapwise Yaw	1.933	1.651	1.729	1.793
10	2^{nd} Blade Asymmetric Flapwise Pitch	1.922	1.856	1.878	1.955
11	2^{nd} Blade Collective Flap	2.021	1.960	1.973	2.061
12	2^{nd} Tower Fore-Aft	2.900	2.860	2.913	2.931
13	2^{nd} Tower Side-to-Side	2.936	2.941	3.029	3.040

tower introduces dynamics around 0.3Hz and 2.9Hz (the first and second tower fore-aft frequencies) and not affecting much of the blade flapwise frequency of around 0.6Hz. Increasing the flexibility of the tower further by reducing the stiffness of the NREL tower by factor of three, we observe that tower frequencies are reduced further as expected. However, the blade flapwise frequency is also shifted to the left.

On the original NREL tower, Figure 3.10 shows flapwise tip deflection of the three blades in rotation when subject to homogeneous gust. Depending on the azimuth location of the blades with respect to the tower during rotation, their tip deflections are altered slightly from one another due to the structural response of the tower.

3.2.3 Controller Description

In the active load alleviation of turbine blades using trailing-edge flaps, a definition of the controller is necessary and the model-based LQG and $\mathcal{H}_\infty$ controllers have been presented in Section 1.4, In subsequent load alleviation studies, Matlab® Robust Control Toolbox™ [228] will be used and the details of formulating the EoM for controller design will be discussed next.

For the two-dimensional model, Eqs. (A.14) provides the linear time-invariant state-space EoM for control design. For the three-dimensional model, Eq. (2.34) is linear time-varying as the turbine dynamics are dependent on the blade's azimuth location with respect to the tower, appearing through the constrained structural EoM and aerodynamics coupling terms.

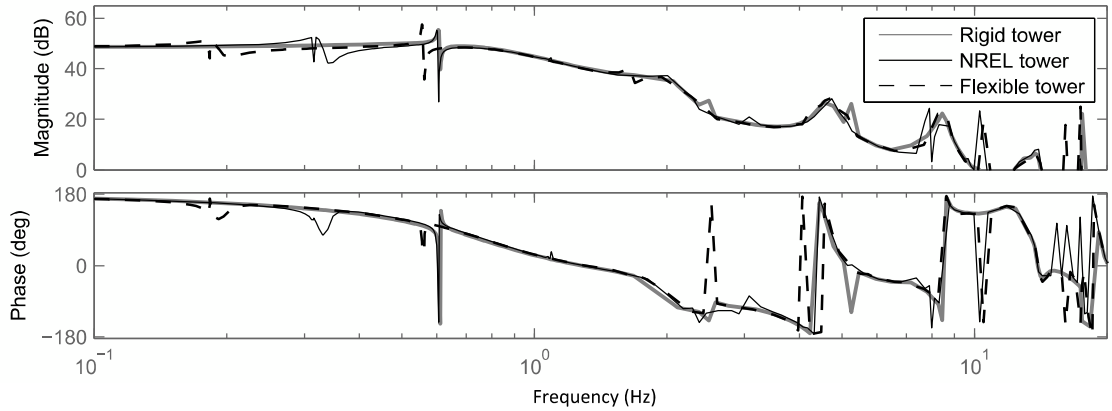


Figure 3.9: Bode plot of full aeroelastic system from gust input to blade flapwise tip deflection on one of the rotor blades (parked). Flexible tower has stiffness in the NREL 5-MW tower reduced by factor of three.

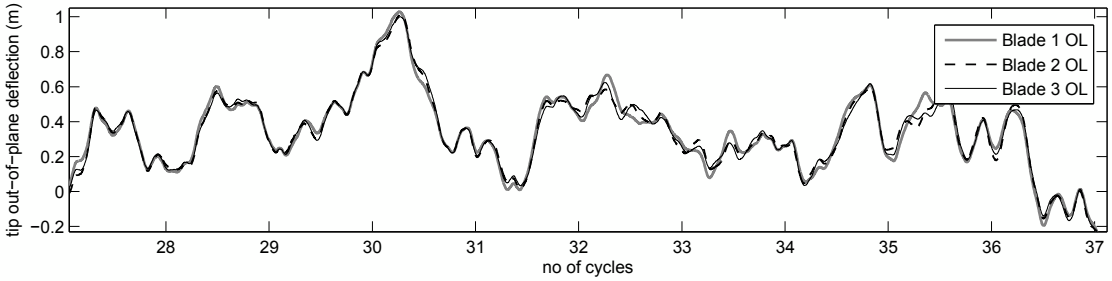


Figure 3.10: Time-series showing the flapwise tip deflection of the three rotor blade in response to homogeneous gust of 10% turbulence intensity (original NREL tower).

However, in the unassembled rotor or rotor blade descriptions, they are linear time-invariant. The two and three dimensional EoM can symbolically be expressed [177, 180] as

$$\begin{aligned} \boldsymbol{x}_c^{n+1} &= \boldsymbol{A}_c\boldsymbol{x}_c^n + \boldsymbol{B}_c\boldsymbol{w}_{\beta,c}^n + \boldsymbol{G}_c\boldsymbol{w}_{\delta,c}^n\,, \\ \boldsymbol{y}_c^n &= \boldsymbol{C}_c\boldsymbol{x}_c^n + \boldsymbol{D}_c\boldsymbol{w}_{\beta,c}^n + \boldsymbol{H}_c\boldsymbol{w}_{\delta,c}^n \end{aligned} \tag{3.1}$$

with subscript c denoting the control model. For the three-dimensional control model, the EoM only contains the structural and aerodynamics dof of the clamped rotor or blade.

The objective function to be minimised is given by:

$$\boldsymbol{z} = \begin{bmatrix} \boldsymbol{Q}^{\frac{1}{2}} & 0 \\ 0 & \boldsymbol{R}^{\frac{1}{2}} \end{bmatrix} \begin{bmatrix} \boldsymbol{y}_c \\ \boldsymbol{w}_{\beta,c} \end{bmatrix} \tag{3.2}$$

containing the weighted measurement $\boldsymbol{y}_c$ and control input $\boldsymbol{w}_{\beta,c}$ from Eq. (3.1). The weights on measurement $\boldsymbol{Q}$ are increased relative to control input weight $\boldsymbol{R}$ until the actuator limits are encountered [24]. A block diagram illustrating the control model is shown in Figure 3.11.

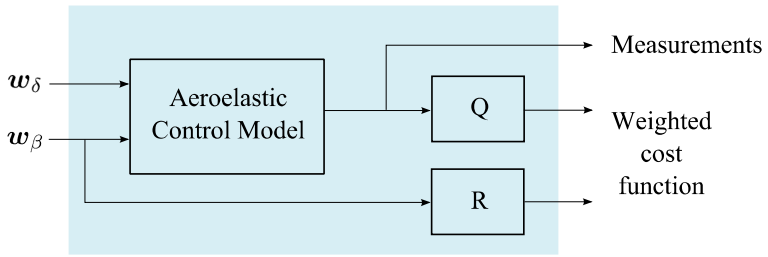


Figure 3.11: Simplified block diagram of control model.

Chapter 4

Numerical Simulations on Land-based NREL 5MW turbine

Numerical simulations of dynamic load alleviation on the land-based NREL 5MW turbine will be presented, starting with a simple two-dimensional model of the blade in Section 4.1, followed by the three-dimensional model of a rotating blade in Section 4.2 and the complete three-bladed turbine with tower in Section 4.3.

The sectional model serves as a starting point to appreciate the effectiveness of active controls in reducing blade flapwise RBM (Section 4.1). It further provides a simple model to carry out initial investigations into controller performance, type and also sensitivity to spatial discretisation that is crucial in vortex methods. These results can be compared to component and full turbine models to assess whether two-dimensional analysis is sufficient for wind turbine active load alleviation studies.

Moving forward from the sectional model, we consider a single rotating blade for parametric study on control surface sizing and investigate the importance of various dof in active load alleviation (Section 4.2). Different spanwise positions and dimensions of the flap are considered to arrive at the final design. The validity of the linearised blade description against its non-linear counterpart and ways of overcoming adverse effects of active load alleviation will be investigated.

Adopting the design parameters and equipped with a deeper understanding of the aeroelastic system from the sectional and blade models, the full turbine is then simulated. This complete model of the turbine allows a comprehensive study on the potential of both passive and active load alleviation mechanisms (Section 4.3). The load reduction performance of active flaps will also be compared to both cyclic and individual pitch controls. This is to identify any potential benefits that flaps can deliver over pitch controls and if a combination of the two mechanisms will be favourable (Section 4.4).

4.1 Sectional Model

The sectional model of a lifting surface (turbine blade) can be described using a plunge-pitch aerofoil coupled with a vortex particle solution to the unsteady aerodynamics. Similar to the three-dimensional aeroelastic formulation, this sectional model can be cast in a state-space realisation for control design and simulation. Details of the mathematical formulation and numerical implementation is found in Appendix A.

This section will examine the potential of active load alleviation in the sectional model (Section 4.1.1), making comparisons between LQG/$\mathcal{H}_\infty$ with PID controllers and eventually discuss the effects of control model spatial discretisation on closed-loop performances (Section 4.1.2).

4.1.1 Load Reduction using Controllers from Converged Models

In all the two-dimensional simulations that follow, the operating conditions are based on the point marked by a triangle Δ on the flutter plot in Figure A.3 in the appendix, with $U/(b\omega_\alpha) = 1$ and $\omega_h/\omega_\alpha = 0.6$. In closed-loop, the measurement feedback is the coefficient of lift C_L and control input is the acceleration of flap deflection $\ddot{\beta}$. The control input in Eq. (A.14) are vectors containing β and it higher derivatives. Hence, a double integrator [11] is introduced such that the control input becomes the flap acceleration

$$\begin{bmatrix} \beta \\ \dot{\beta} \end{bmatrix}^{n+1} = \begin{bmatrix} 1 & dt \\ 0 & 1 \end{bmatrix} \begin{bmatrix} \beta \\ \dot{\beta} \end{bmatrix}^{n} + \begin{bmatrix} 0 \\ dt \end{bmatrix} \ddot{\beta}^n \,. \tag{4.1}$$

The choice for this term is that acceleration is most closely related to forces and it avoids the introduction of a jerk function. The double integrator could be representative of the actuator dynamics but it introduces a time lag that may render poor controller performances. The turbulence is simulated by passing white Gaussian noise through a filter such that the signal output will have the same statistical properties as those measured and verified for atmospheric turbulence [57]. The transfer function of the filter is chosen to generate an output similar to that of the von Kármán turbulence spectrum, which is assumed to be frozen in time as the aerofoil passes through. In the transverse direction, the filter can be expressed as [77, 231]

$$H_{turb}(s) = \frac{\sigma\sqrt{\frac{1}{\pi}\frac{L_s}{U_\infty}}\left(1 + 2.7478\left(\frac{L_s}{U_\infty}\right)s + 0.3398\left(\frac{L_s}{U_\infty}\right)^2 s^2\right)}{1 + 2.9958\left(\frac{L_s}{U_\infty}\right)s + 1.9754\left(\frac{L_s}{U_\infty}\right)^2 s^2 + 0.1539\left(\frac{L_s}{U_\infty}\right)^3 s^3}\,, \tag{4.2}$$

where L_s is the turbulence length scale (given by the altitude for heights below 1000m), $\sigma = 0.1{\cdot}U_{20}$ where U_{20} is wind speed at 20ft / 6.096m and U_∞ is the mean velocity. The turbulence filter can be written in state-space form and combined with the vortex particle aeroelastic model. The turbulence intensity is assumed to be 10% and sampling rate was chosen to be ten times the system bandwidth of 20Hz. A simplified closed-loop block diagram of the aeroelastic

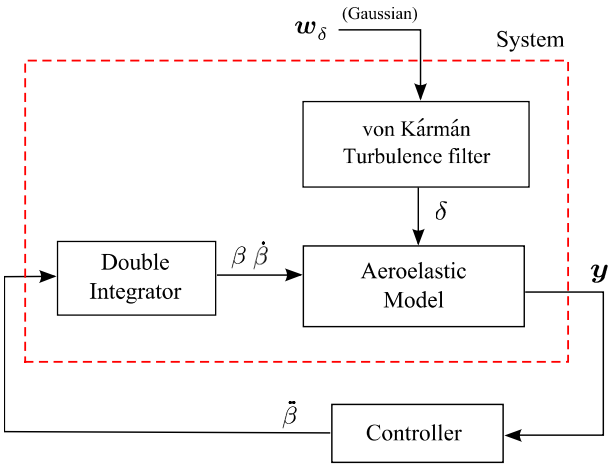


Figure 4.1: Closed-loop block diagram for sectional model, containing turbulence filter and double integrator.

model is illustrated in Figure 4.1 in which the double integrator and turbulence filter are included in the system. In the figure, w_δ represents the external disturbance (Gaussian noise) that is passed through the von Kármán filter to produce the turbulence signal δ.

Performance will be measured based on the percentage reduction in rms of C_L as well as the control energy expenditure, with the latter chosen as

$$E = \frac{1}{T}\int_0^T \ddot{\beta}^2\, dt. \tag{4.3}$$

This measure is selected as flap angular acceleration is proportional to the torque $I_\beta\ddot{\beta}$, and in turn related to the work done, where I_β is the flap moment of inertia about its hinge.

To investigate the flapwise RBM reduction potential of active control surfaces, both the LQG and $\mathcal{H}_\infty$ controllers are designed from the converged vortex aeroelastic model (50 panels per chord and 5 wake chords) and placed in closed-loop with the same model. Using a 10% trailing-edge flap, the achieved reduction in rms(C_L) was around 80% for both the LQG and $\mathcal{H}_\infty$ controllers. The good performance can partly be attributed to the fact that the same model was used for simulation and control. The flap deflection angles were kept within $\pm 5°$ and deflection rates within $\pm 40°/s$ using the controller description in Section 3.2.3. A section of the time-series comparing the open and closed-loop responses is shown in Figure 4.2.

Next, PID controllers are considered. We first looked at the stability margins from control input $\ddot{\beta}$ to output C_L [183]. Since both the gain and phase margins were found to be negative, a proportional-derivative (PD) controller was required to stabilise the system. By sweeping the proportional gain (k_p) and derivative gain (k_d) with a first order low pass filter [11], across possible values in which the system remains stable, we are able to find a set of gains that achieve similar flapwise RBM reductions compared to LQG and $\mathcal{H}_\infty$. Even though all three control methods are capable of delivering the same flapwise RBM reductions, they require different amounts of actuator duty. Computing their respective energy expenditures using

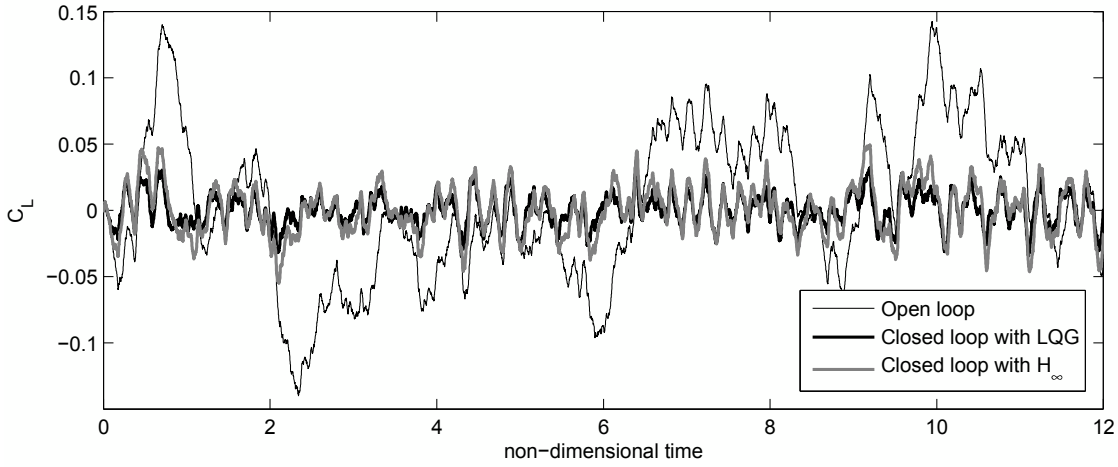


Figure 4.2: Section of time-series for C_L in open and closed-loop using LQG and $\mathcal{H}_\infty$ controllers. Two-dimensional case.

Eq. (4.3), PID controllers expend up to 70% more energy than LQG and $\mathcal{H}_\infty$. The larger energy requirements of PID controllers had also been observed in several studies on active load alleviation in wind turbines [41, 130, 75].

Even though the results indicate that PID control is more energy intensive, there is still some ambiguity in terms of how the power consumption of actuators is being computed. To arrive at conclusive power estimates, one will need experimental data or models that take into account the flap dynamics, mechanical actuators, friction and resistance in a moving fluid. In fact, given the lack of realistic data, almost all the works on active load alleviation in turbines had not considered power requirements. One of the few works that provided a measure was to assume energy consumption to be the same as the hinge moments (due to the same units) [32]. Others considered measuring actuator duty solely by taking the time averaged absolute value of flap deflection rate [130]. Nonetheless, they are all not vigorous treatments of energy measures and not any better than the indicator considered here in Eq. (4.3). More recently, the power requirements of flaps were computed with detailed considerations of gravity, aerodynamics, inertia and friction [191].

4.1.2 Controller design with Spatially Coarse Vortex Aeroelastic Model

Given that LQG and $\mathcal{H}_\infty$ controllers have the same size as the model, controller design using high-order converged vortex aeroelastic models is computationally expensive, and will be especially so in full turbine models. At this stage, one will ask if the control model has to be that fine in order to deliver good performances?

Controllers are known to perform well in the presence of uncertainties depending on the level of model mismatch [121, 241, 139, 65]. To investigate, the number of panels per chord in the vortex aeroelastic model was reduced for controller design, but tested in closed-loop with

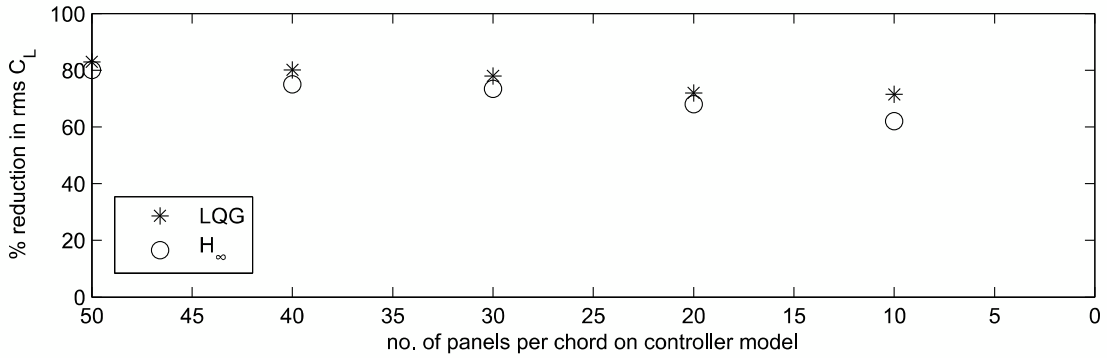


Figure 4.3: Performance of low order panel model for controller design (Figures are plotted with reducing number of panels per chord on horizontal axis).

the converged vortex panel aeroelastic model. This enables us to understand the limits to which controllers developed from spatially coarse models, which had not converged for open-loop predictions, were capable of rejecting disturbances on converged models. As shown in Figure 4.3, a controller developed using just 10 panels per chord was able to achieve good performance when applied in closed-loop with the converged model of 50 panels per chord. The flap deflection angles and rates were kept within $\pm 5^\circ$ and $\pm 60^\circ/\text{s}$ for all cases.

4.2 Single Rotating Blade

In this section, we analyse a single rotating blade for parameter sizing that is necessary for active control design on the complete turbine. The rotating blade is taken from the NREL 5MW turbine and had been numerically verified in Section 3.2.1. By assuming the blade to be clamped in a rotating FoR, rigid-body motion associated with the tower is removed and the resulting EoM is linear. The isolation of the single blade model removes complications from tower interaction to facilitate parametric studies for initial design of active control surfaces.

The influence of three-dimensional effects on flapwise aerodynamic loadings will first be examined and compared against sectional models (Section 4.2.1). Next, using a single rotating NREL 5MW blade model, the configuration of the control surface is determined (Section 4.2.3) by assessing load reduction performances subject to a homogeneous gust input (Section 4.2.4). Finally, the negative effects on torsion resulting from flap actuation will be investigated (Section 4.2.6), and the validity of the linearised aeroelastic description will be compared to its non-linear counterpart (Section 4.2.5).

4.2.1 Aerodynamic Loading

Prior to determining the flap configuration for active load alleviation on the single rotating blade, it is worthwhile to develop an understanding of three-dimensional effects on spanwise load distributions. This allows us to investigate any benefits that the UVLM can deliver as

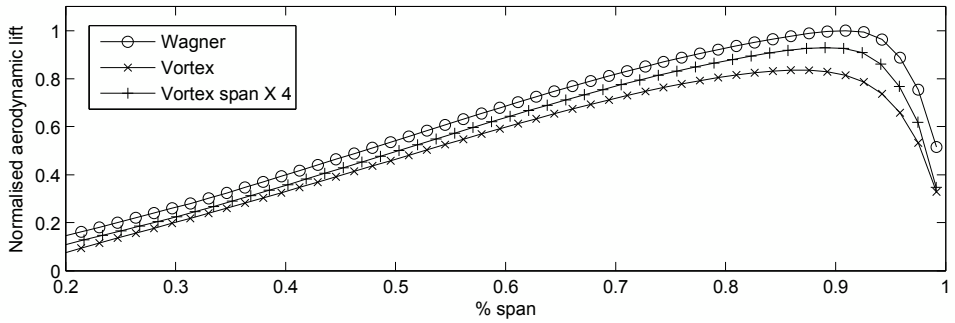


Figure 4.4: Normalised spanwise aerodynamic lift on the rotating NREL 5MW blade resulting from 10° pitch. UVLM has 50 spanwise panels, 10 chordwise panels and 10 wake chords.

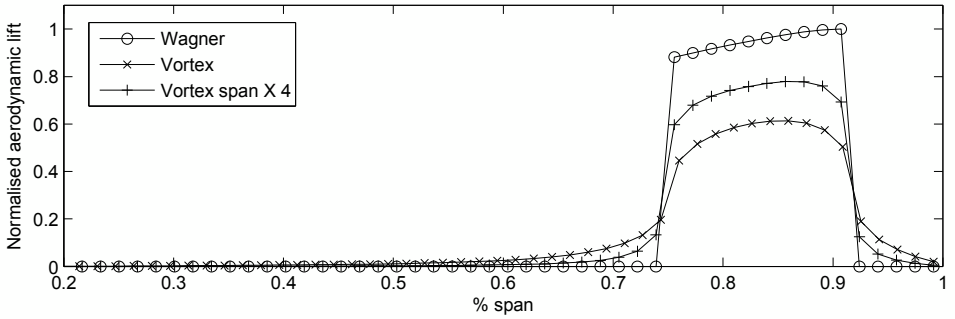


Figure 4.5: Normalised spanwise aerodynamic lift on the rotating NREL 5MW blade resulting from 10° flap actuation. UVLM has 50 spanwise panels, 10 chordwise panels and 10 wake chords. Flap occupies 10% local chord and 20% span.

opposed to most BEM codes that rely on sectional computation of aerodynamic loads.

First, the three-dimensional UVLM of the NREL 5MW blade is modelled and compared against the two-dimensional Wagner solution resolved along spanwise sections of the blade. Comparing the static solution of blade pitch (change in angle-of-attack) in Figure 4.4, we observe a large difference in the computed aerodynamic lift towards the tip region. This is caused by tip loss effects that can only be captured in three-dimensional models such as the UVLM. As BEM is strictly a two-dimensional model, this effect is commonly accounted for using empirical corrections such as the Prandtl's tip loss coefficient. Also plotted on the diagram is the same NREL blade with its span extended by four times, potentially reducing spanwise effects and resulting in computed lift becoming closer to the two-dimensional Wagner's solution.

Next, the static aerodynamic lift from flap actuation in the UVLM and Wagner models are compared in Figure 4.5. Similar to the previous case of pitch, UVLM predicted lower aerodynamic lift (around 35% less than Wagner's). A blade with four times the span is also plotted on the same diagram to illustrate that the computed aerodynamic lift from UVLM can be brought closer to two-dimensional solutions when spanwise effects are reduced. While static aerodynamic lift computed using UVLM are lower compared to analytical solutions, there is better correlation for unsteady aerodynamic lift under harmonic flap actuation. As

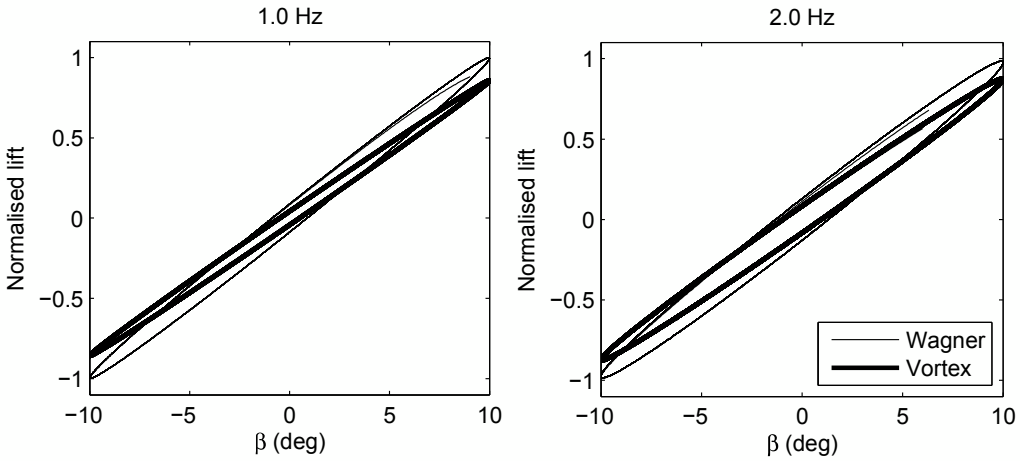


Figure 4.6: Normalised aerodynamic lift with a harmonic 10° flap actuation of 1.0Hz and 2.0Hz.

seen in Figure 4.6, when the frequency of flap actuation is increased, the phase lag predicted by UVLM is relatively close to Wagner's, even though we still see differences in the amplitude due to three-dimensional effects.

4.2.2 Rotating Aerodynamics

As the NREL blade is operating in a rotating environment, the structural dynamics are subject to centrifugal loading and the aerodynamics are determined by a spanwise linearly varying relative velocity from root to tip. Figure 4.7 shows the Bode plot from a homogeneous gust input to blade flapwise RBM for the NREL blade. From the figure, the first flapwise mode is observed at around 0.7 Hz and the edgewise mode slightly above 1 Hz (seen here due to the structural pre-twist of the blade).

Four cases are considered in Figure 4.7. The first case corresponds to a forward motion of the blade without any rotational effects. In the second case, rotational effects are introduced to the structures only and the blade's first flapwise mode is shifted slightly to the right due to stiffening effects. Subsequently in the third case, rotational effects are only introduced to the aerodynamics through spanwise linearly varying velocity from root to tip and several interesting observations can be made - (1) the gain is increased due to the higher flow velocities close to the tip of the rotating blade, (2) the width of influence of the first flapwise mode increases as observed by the wider valley, (3) the gains beyond 1 Hz are maintained and the roll-off is delayed to only occur beyond 4 Hz. This is an indication that the RBM measurements will contain a considerable amount of high frequency noise. In the fourth case, when rotating effects in the structures is further included to rotating aerodynamics, the first flapwise mode is shifted slightly to the right due to stiffening effects.

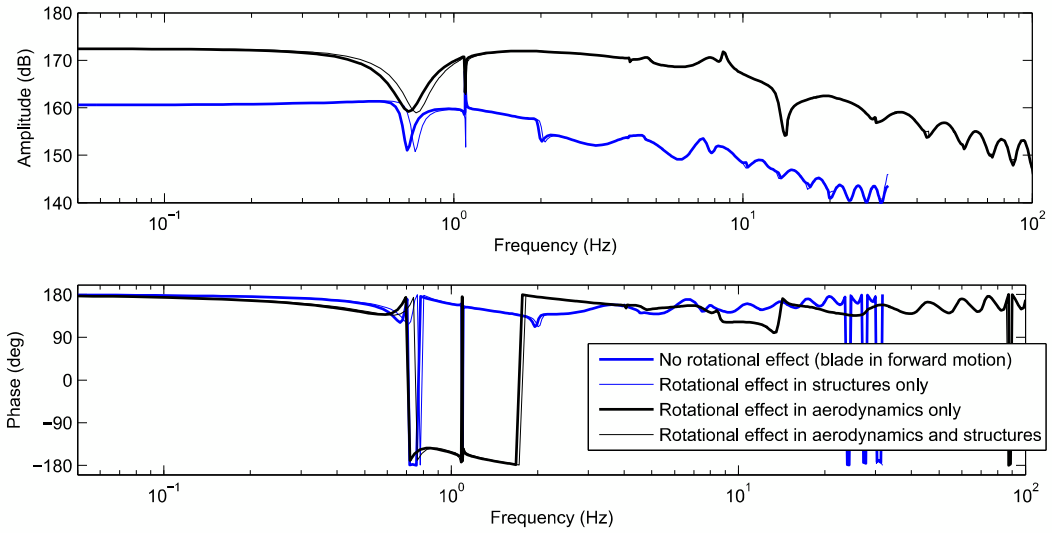


Figure 4.7: Bode plot from a homogeneous gust input to blade flapwise RBM for the NREL blade. Four cases are considered. They include (1) blade in forward motion without rotational effect, (2) rotational effect in structures only, (3) rotational effect in aerodynamics only, (4) rotational effect in both aerodynamics and structures.

4.2.3 Parameter Sizing

In order to identify the location along the blade that maximises the load reduction potential of active flap control, a trailing-edge flap measuring 10% span and 10% of the local chord is moved along the span of the NREL 5MW blade. The rms reduction in blade flapwise RBM and tip deflection is then measured for different flap locations at increasing distances from the root. The results are presented in Figure 4.8. As we move in the spanwise direction away from the root, we observe an exponential increase in the reduction of flapwise RBM. However, when we come close to the tip at around 90% span, rms reductions in blade flapwise RBM dropped as a result of tip effects and also smaller local flap chord due to blade taper. The largest rms reduction in blade flapwise RBM occurs when the flap is placed at 80% span, and similar trends are also observed in Ref. [6].

The reduction in flapwise RBM is obtained by measuring and comparing the areas under the Power Spectral Densities (PSD) of the open and closed-loop models, which gives rms values [184]. According to Parseval's theorem, the total energy of a waveform x in the time domain is equal to the total energy of its transform X in the frequency domain [217]

$$rms = \sqrt{\frac{1}{N}\sum_{i=0}^{N-1} x_i^2} = \sqrt{\frac{2}{N^2}\sum_{k=0}^{N/2} |X_k|^2}, \tag{4.4}$$

where N is the number of samples. The use of PSD provides a more accurate and consistent measure of rms values and avoids long time-stepping simulations of turbulence signals [113]. The operating conditions are under rated inflow of 11 m/s perpendicular to rotor, tip speed

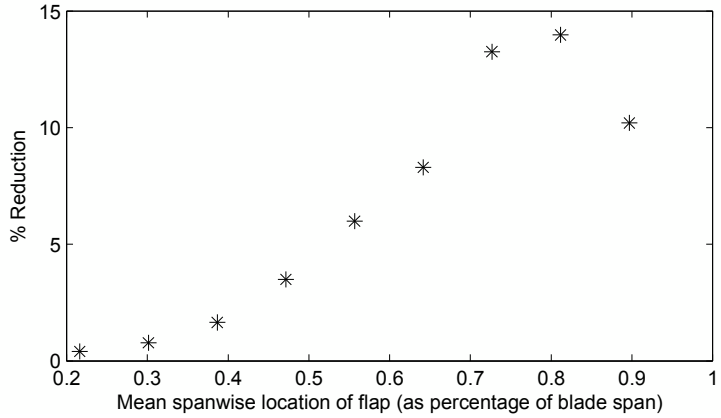


Figure 4.8: Effect of LQG controller on the rms reduction in blade flapwise RBM with varying flap locations along the span of the blade (Flap measures 10% span and 10% chord).

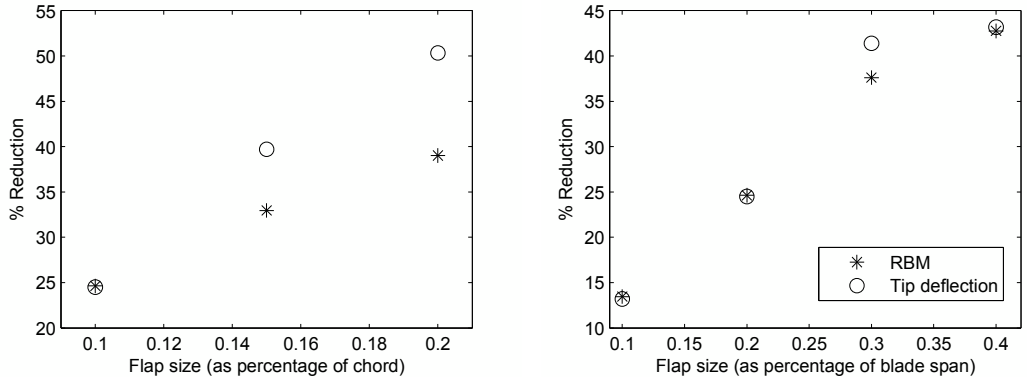
ratio (TSR) of 7.5 and turbulence intensity of 10%.

Note that the closed-loop system here contains an LQG controller with blade flapwise RBM feedback and $\ddot{\beta}$ as the control input, illustrated by the closed-loop block diagram in Figure 4.1. Given the nature of the disturbance input (Gaussian), LQG is considered. The variance for the LQG controller is taken from the turbulence intensity (standard deviation) and the limits of flap deflection angle and rate are $|\beta| \leq 10^\circ$ and $|\dot{\beta}| \leq 100^\circ/\text{s}$ [24], respectively.

The size of the flap is also a parameter for consideration. As we increase the chordwise and spanwise dimensions of the flap in Figures 4.9a and 4.9b, the percentage rms reduction in blade flapwise RBM increases in an almost linear fashion. However, when the flap is increased beyond 30% span in Figure 4.9b, there is a diminishing return in the reduction of flapwise RBM. This observation demonstrates the performance limit that a single flap can achieve with a homogeneous turbulence model, and 30% flap span appears to be a suitable choice delivering good performances. However, having a flap size of 30% span and beyond may be unrealistic for two reasons - too heavy to actuate and the twisting of the blades. There is hence a trade-off between having good performance and limiting the size of the flap, which is designed to be a localised active device capable of actuating at high frequencies. The rms reduction in tip deflection is also plotted on the same figure to show the close relationship between reducing blade flapwise RBM and tip deflection.

4.2.4 Load Reductions in Single Rotating Blade

After the previous parametric study, a flap occupying 20% span of the lifting surface and 10% of the local chord is chosen and located at a mean position of 80% span, as shown in Figure 4.10. Better performances are expected with multiple and distributed flaps [250, 20], and although this can be easily implemented in the existing algorithm, it was not further investigated to complicate the problem.



(a) Varying flap chord, keeping span at 20% of blade.

(b) Varying flap span, keeping chord at 10%.

Figure 4.9: Reduction in rms of blade flapwise RBM and tip deflection with varying flap sizes (Mean position of flap is at 80% span).

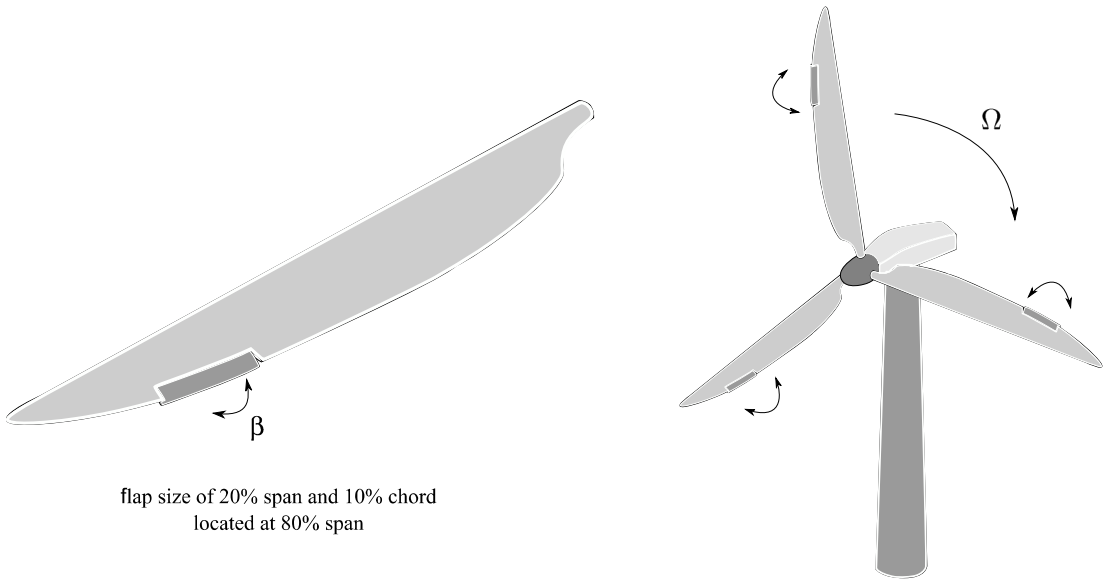
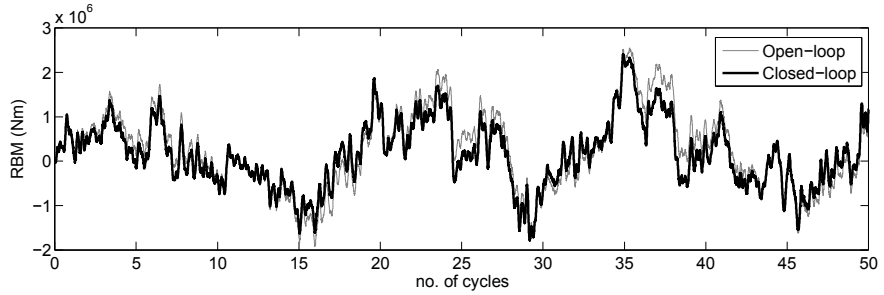
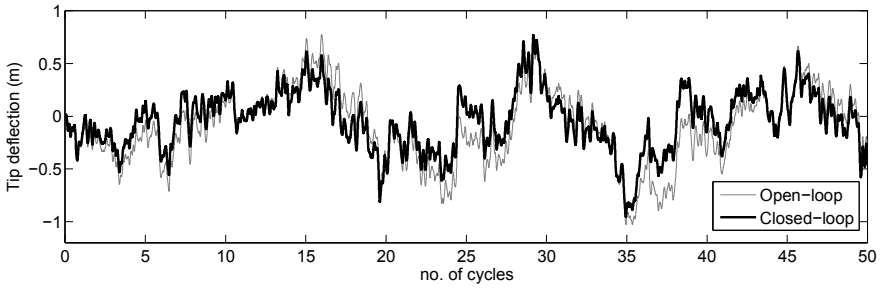


Figure 4.10: Illustration of flap occupying 20% span, 10% of local chord and located at a mean position of 80% span, and the complete turbine model with flaps attached to each blade.

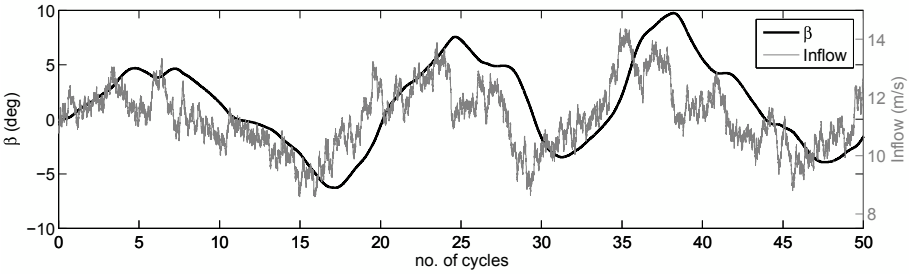
Using this flap configuration and in the presence of a homogeneous gust, we observe an average of around 22% and 26% rms reduction in blade flapwise RBM and tip deflection, respectively. The limit on the flap deflection angle of $\pm 10^\circ$ was met while the limit on flap deflection rate was less of a concern, since it was well below $\pm 100^\circ/\text{s}$. A section of the time-series for the blade flapwise RBM and tip deflection is shown in Figures 4.11a and 4.11b, respectively, where it is evident that peaks in both measures are suppressed in the closed-loop system. The flap deflection angle β is shown in Figure 4.11c, which is within prescribed limits and is actuated at relatively low frequencies given the double integrator on the control input $\ddot{\beta}$. On the same figure, the fluctuation of the inflow is also plotted in which we observe a phase lag in the flap actuation against inflow disturbance.



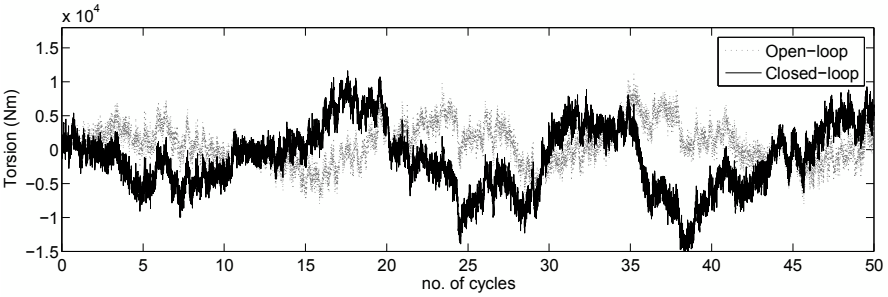
(a) Blade flapwise RBM



(b) Blade flapwise tip deflection



(c) Flap deflection angle (control input) and inflow (disturbance input)



(d) Torsion

Figure 4.11: Section of the time-series for blade flapwise RBM, flapwise tip deflection, flap deflection angle, inflow and torsion.

4.2.5 Non-Linear Comparison

The performance of the controller is then analysed on the non-linear model, where structural deformations and aerodynamic influence coefficient matrices are re-computed at each time instant. Comparing the linear and non-linear open-loop tip deflection responses, shown in

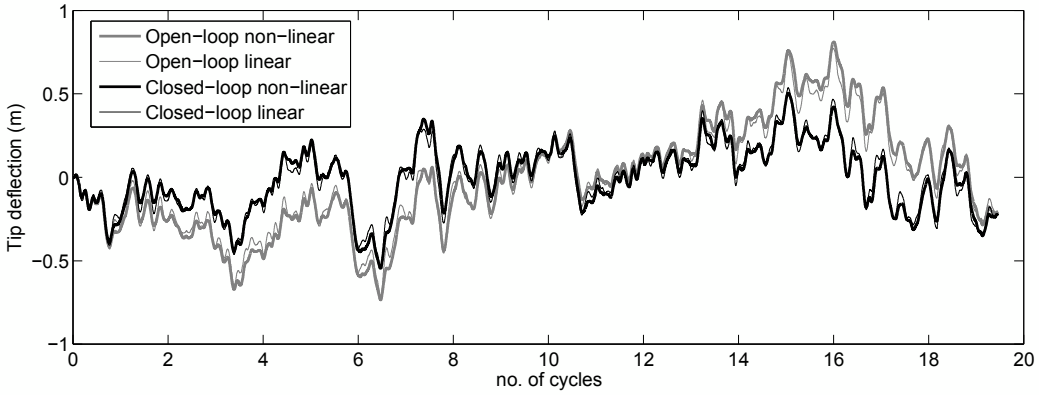


Figure 4.12: Open and closed-loop tip deflection of the linear (thin-lines) and non-linear (thick-lines) models.

Figure 4.12 for the first 20 cycles of tip deflection, we observe little differences, indicating that the linear model is capable of capturing the dynamics present in the non-linear model, and further suggesting that the controller may still perform well in the non-linear case. To illustrate this, on the same figure, the LQG controller designed from the linear model is placed in closed-loop with the non-linear model, where it is evident that peaks are suppressed by the control action, in a manner that is very similar to the linear closed-loop system. (For this single blade model of 20 cycles simulation time, the non-linear model took an approximate 8 weeks to compute, while the linear model took less than 15 minutes.)

4.2.6 Torsional Effects

While the use of flap delivers benefits in terms of suppressing blade flapwise RBM and tip deflection, the concentration of lift in the flap region generates a moment arm about the elastic axis that increases torsion. As shown in Figure 4.11d, the torsional loads are magnified significantly through flap deflection. A straightforward method to overcome this is to reduce the weight $\boldsymbol{Q}$ in Eq. (3.2), so that a bigger penalty is placed on the control input leading to lower adverse torsional effects.

Alternatively, as LQG is a Multiple-Input-Multiple-Output (MIMO) controller, torsion can also be included in the objective function to be minimised. Setting the weight corresponding to blade flapwise RBM to unity and gradually increasing the weight on torsion from 10^{-3} to 10^{3}, we obtain in Figure 4.13 the trade-off between blade flapwise RBM and root torsion when using active flap controls. Also plotted is the trade-off obtained from reducing the weight $\boldsymbol{Q}$ on flapwise RBM alone without considering torsion in the objective function. Both plots coincide at the top left corner when torsion is not considered, with the corresponding values indicating the minimum rms of flapwise RBM achievable and the resulting rms of torsion using controllers tuned to satisfy the limits on β and $\dot{\beta}$. As we move from left to right in the plot, we are sacrificing reductions in rms of flapwise RBM (hence an increase in the

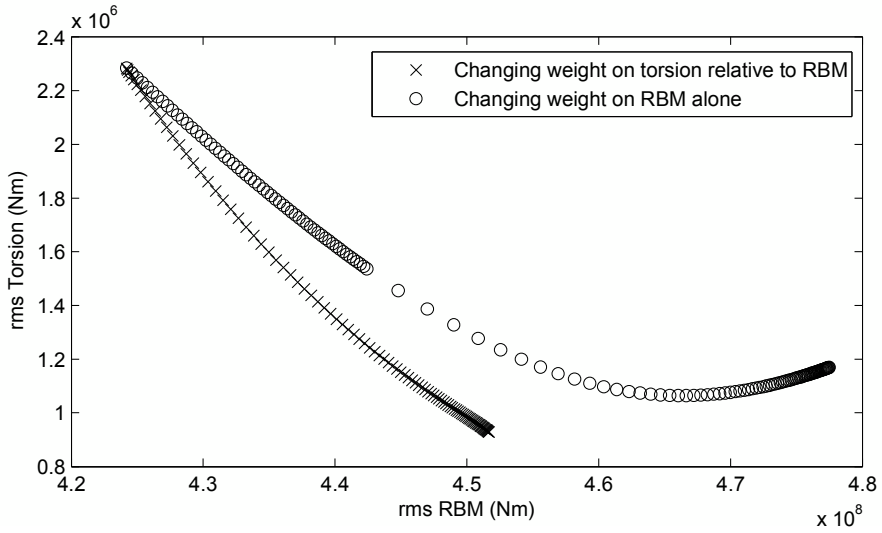


Figure 4.13: Trade-off between blade flapwise RBM and torsion in using active flap controls.

value of rms of flapwise RBM) for reduced torsional effects.

Three observations can be made. Firstly, there is diminishing return on the reduction in torsion as more flapwise RBM reduction is sacrificed. Secondly, if we were to consider the scale of trade-off, we could achieve a larger reduction in torsion with a given amount of blade flapwise RBM reduction we sacrifice. For instance, in the case of increasing weight on torsion, a 5% sacrifice in flapwise RBM reduction from the leftmost point on the plot is able to achieve close to 50% reduction in torsion. Lastly, we see better returns through increasing the weight on torsion from the steeper slope compared to changing weights on flapwise RBM alone, meaning that we can get more reduction in torsion for a given sacrifice in flapwise RBM reduction.

4.3 Land-Based NREL 5MW Turbine

With a deeper understanding of the aeroelastic system and design parameters from the sectional and blade models, the full turbine is now simulated. Instead of the homogeneous gust input, a realistic wind field is considered (Section 4.3.1), including tower shadow effects that contribute to inflow blockage (Section 4.3.2). Given the large number of states in the complete turbine model, due mainly to the UVLM description, model reductions are performed prior to the simulations (Section 4.3.3). Subsequently, using the monolithic aeroelastic description, both passive (Section 4.3.4) and active (Sections 4.3.5 and 4.3.7) load alleviations in large wind turbines are examined in detail, including their combined effects (Section 4.3.6). A flow-chart is shown in Figure 4.14 to illustrate the major steps adopted in the simulation of the full turbine model.

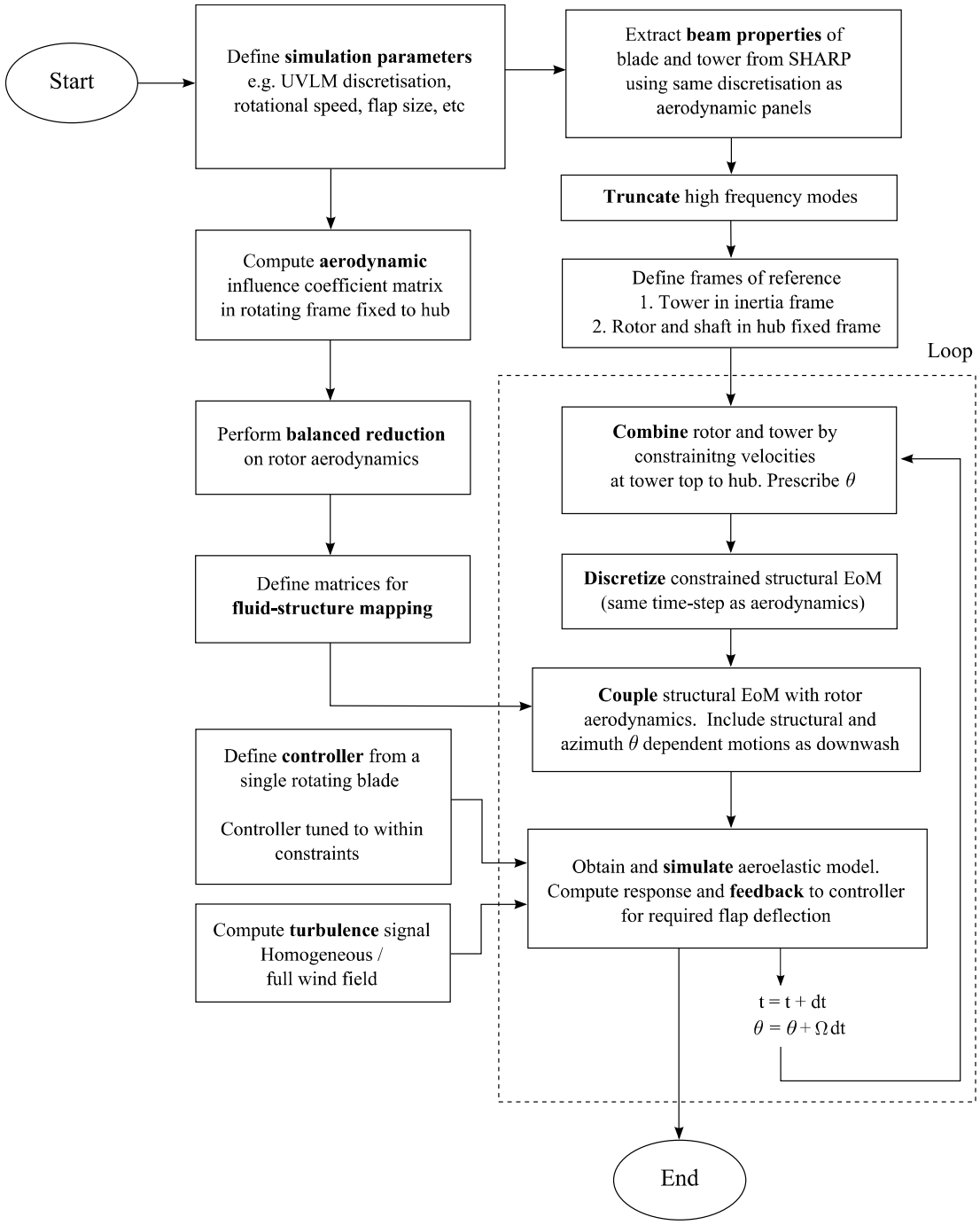


Figure 4.14: Flow-chart to illustrate the major steps adopted in the simulation of the full turbine model.

4.3.1 Wind Field

Wind conditions are most critical in the design of wind turbines, and having a realistic wind field in numerical simulations will provide a huge benefit to predicting loads in an operating environment that is as close as possible to the actual conditions. The IEC 61400-1 [117] is the international standard providing sets of design requirements to ensure turbines are properly engineered to withstand the operating conditions throughout their lifetime of 20 years. It

stipulates different load cases that the turbine is expected to operate in, ranging from normal to extreme wind conditions.

In order to simulate the full wind field in accordance to the IEC guidelines for the NREL 5MW turbine, the open-source tool, Turbsim, developed by the US National Renewable Energy Laboratory is used [122]. Within the IEC, the NREL 5MW turbine falls under class 1B and the normal turbulence model (NTM) for fatigue analysis is considered.

Turbsim is an inflow turbulence code to provide numerical simulations of full field flow in a user-defined grid that covers the rotor swept area [123, 132, 237]. Having a refined grid naturally improves resolution of the turbulence field but it also requires large amount of data storage and long computation times. Hence, the number of grid points is selected based on a trade-off between resolution and computation power/storage. The duration of simulation time is ten minutes as stipulated by the IEC, and a total of 31×31 grid points are selected for the NREL 5MW turbine based on the recommendation by Turbsim [122]. As the turbulence code only generates winds speeds at the grid points, we have developed a code for linear interpolation and rotational sampling of wind speeds to be used as inputs to the simulation model.

The turbulence spectrum available in Turbsim includes the IEC Kaimal and von Kármán turbulence models, and various system identified characteristic models derived from measurements taken from wind farms. The Mann turbulence model stipulated within the IEC is not yet available in Turbsim [160]. To be consistent with the simulations for sectional and homogeneous gust, the von Kármán spectrum is selected.

Under normal operating conditions, the wind profile $U_\infty(z)$ varies with height z above ground and this is commonly known as the wind shear effects. Turbsim incorporates various wind shear models and the IEC recommended is the power law with an exponent of 0.2. The power law has the basic form [9]:

$$U_\infty(z) = U_\infty(z_r)\left(\frac{z}{z_r}\right)^\alpha, \tag{4.5}$$

where $U_\infty(z_r)$ is the reference wind speed at height z_r, and α is the power law exponent.

A full field spectrum generated from Turbsim with 11 m/s hub height wind speed and grid size of 31×31 at an instant in time is shown in Figure 4.15, along with an overlay of the turbine rotor and tower. It is immediately apparent that the effects of the wind shear is significant, with close to 10 m/s difference between the top and bottom of the wind field. The wind shear generates once-per-revolution (1P) flapwise loads on the turbine blades and 3P loads on other fixed components (tower). Note that Turbsim does not account for the blockage effect due to the presence of the tower.

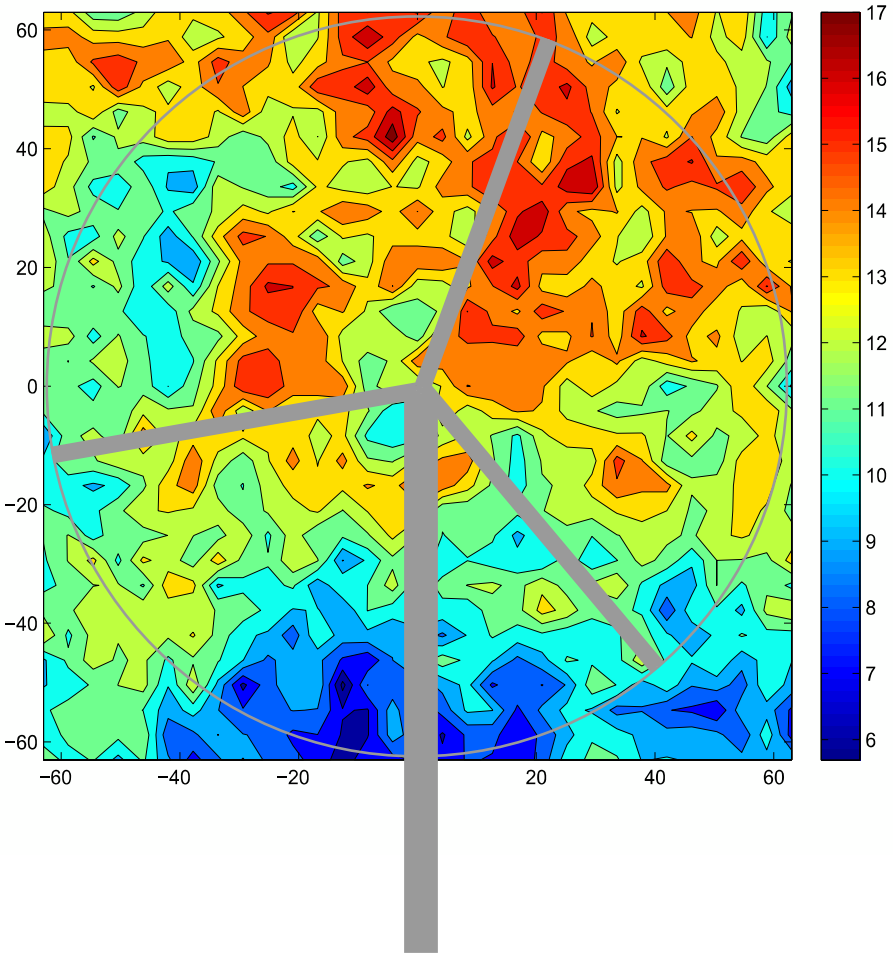


Figure 4.15: Sample wind field from Turbsim with overlaying turbine rotor and tower.

4.3.2 Tower Shadow

The effect of tower shadow on a turbine is accounted for by the reduced wind speeds upwind of the tower. It is often modelled using two-dimensional potential flow theory by superimposing a doublet to a uniform flow in a horizontal plane [55], expressed as

$$\psi = U_\infty y \left(1 - \frac{(D/2)^2}{x^2 + y^2}\right) , \tag{4.6}$$

where ψ is the stream function, D is the tower diameter, and x and y are the longitudinal and lateral coordinates with respect to tower centre (See Figure 4.16). Differentiating the stream function with respect to y yields the flow velocity

$$U = U_\infty \left(1 - \frac{(D/2)^2(x^2 - y^2)}{(x^2 + y^2)^2}\right) , \tag{4.7}$$

with the term in brackets known as the *velocity deficit*. For the NREL 5MW turbine, the *velocity deficit* as a function of y is plotted in Figure 4.17 at the hub and bottom of the rotor

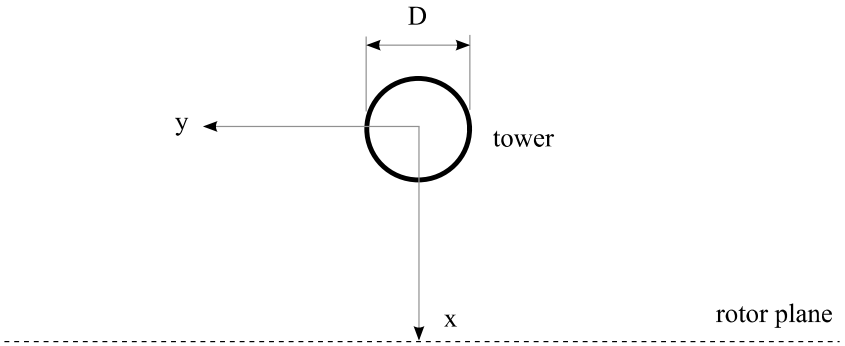


Figure 4.16: Tower shadow.

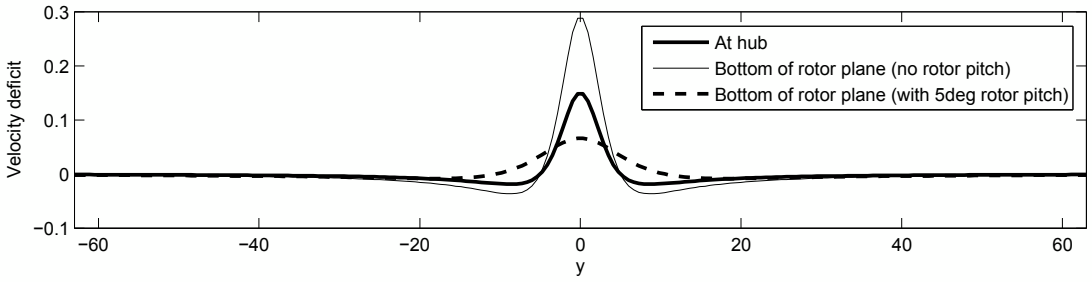


Figure 4.17: Tower deficit close to hub and at bottom of rotor plane for the NREL 5-MW turbine. For deficit at bottom of rotor plane (vertical), the rotor plane is vertical and at 5m ahead from the tower centreline ($x = 5$). For deficit at bottom of rotor plane (with pitch), rotor plane is pitched at 5° as per the NREL 5-MW configuration.

plane. With 5° rotor pitch and assuming undeformed blade configurations, the *velocity deficit* experienced by the blades ranges between 0.15 to 0.07 from root to tip. Even though the tower may have a larger circumference towards its base, the effect of blockage in this region is smaller than at the tower top due to the 5° pitch of the rotor plane.

The PSD of blade flapwise RBM for one of the rotating blades on the full turbine is shown in Figure 4.18 to compare the RBM with and without tower shadow (and with and without 5° rotor pitch). The tower shadow will impose 1P flapwise loads on the rotating blades, as it does in the wind shear of a full wind field. From the plots, it is evident that there are little differences in the 1P peak with and without tower shadow, clearly indicating that 1P flapwise loads are dominated by wind shear effects. However, we do observe differences in the 3P flapwise loads, which are due to the combined effect of the blades on fixed components such as the tower. Nonetheless, it should be noted that the influence of tower shadow on blade flapwise loads is small but may become significant in cases of large blade deformations.

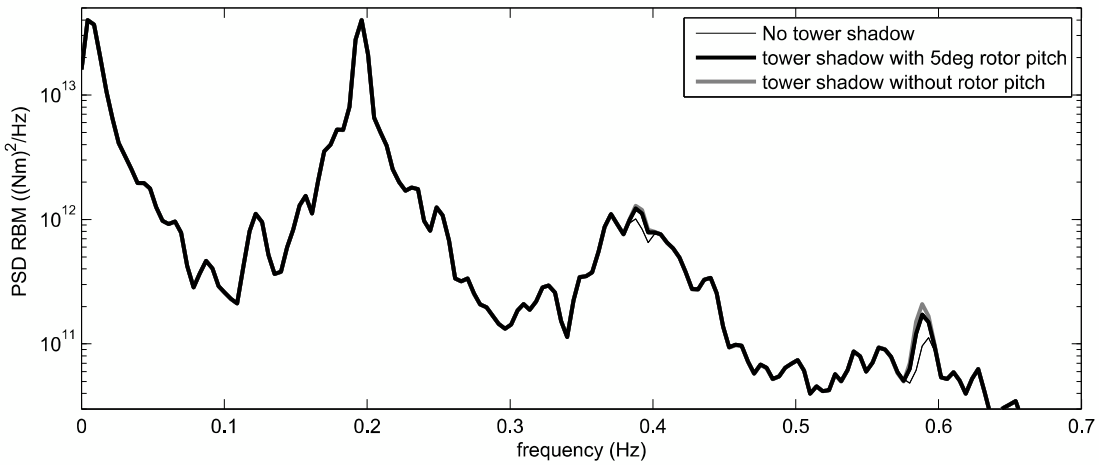


Figure 4.18: PSD of flapwise RBM for one of the rotor blades on the full turbine when subject to full wind field, including wind shear effects, and (1) no tower shadow, (2) tower shadow with a 5° rotor pitch and (3) tower shadow without rotor pitch.

4.3.3 Model Reduction

The convergence of UVLM relies closely on the discretisation of both bound and wake panels for convergence. In particular, the number of wake panels determines the ability to capture unsteadiness in the aerodynamics and wake interaction among the blades. A convergence study revealed that an equal spanwise discretisation of 10 panels, equal chordwise discretisation of 20 panels and keeping a wake profile of a quarter rotor diameter downstream is sufficient to capture the unsteady aerodynamics.

As shown in Figure 3.5b, the finite element discretisation of the beam model coincides with the spanwise panel discretisation of the UVLM to facilitate fluid-structure mapping. Including the inner span of the blade with cylindrical cross section in the structural beam model with no accompanying aerodynamics, and maintaining regular discretisation, a total of 12 beam elements for each blade is used. The beam properties are obtained using a linear interpolation on the documented structural properties [129], which had 48 elements for the blades. The natural frequencies for the turbine with 12 elements on each blade and 10 tower elements are listed in the last column of Table 3.2, showing only a marginal difference from the baseline model. The resulting coupled aeroelastic system in Eq. (2.34) using this discretisation contains a total of over 30,000 states. As mentioned in Section 2.4, the number of states is reduced by performing modal decomposition on the structural module and model truncation on the aerodynamics prior to coupling.

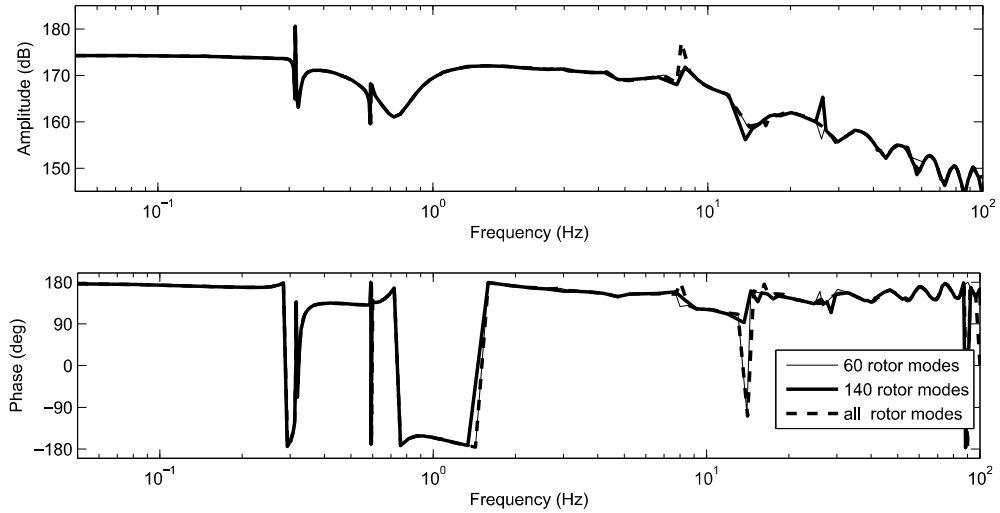
The reduction of the structural model through modal decomposition is achieved through a parametric study on the full aeroelastic system suggesting that it is sufficient to keep only the lowest 10 tower modes and 140 blades modes. This was carried out by looking at the frequency response on snapshots of Eq. (2.34) at various instantaneous azimuth values of θ.

As an illustration, we consider the case of setting $\theta = 0°$ and look at the Bode diagram from a homogeneous gust input to various outputs on one of the rotor blades. In Figure 4.19a, the spikes at around 0.3 Hz is due to the first tower fore-aft and 0.6 Hz is due to the first drivetrain torsion. Slightly to the right, the local minimum of a valley is observed at 0.75 Hz, which corresponds to the first flapwise mode of the blade. This first blade flapwise frequency is slightly higher than the stationary 0.68 Hz reported in Table 3.2 due to the structural stiffening effect from rotation. As the first flapwise frequency is the dominant mode in the response of RBM, its resonating effect is also felt in its surrounding and the width of influence is widened by the rotating aerodynamics (linearly varying spanwise velocity). In fact, the rotating aerodynamics is also the primary cause of the high gains above 1 Hz and delaying the roll-off to higher frequencies. These trends are also observed previously in Section 4.2.2.

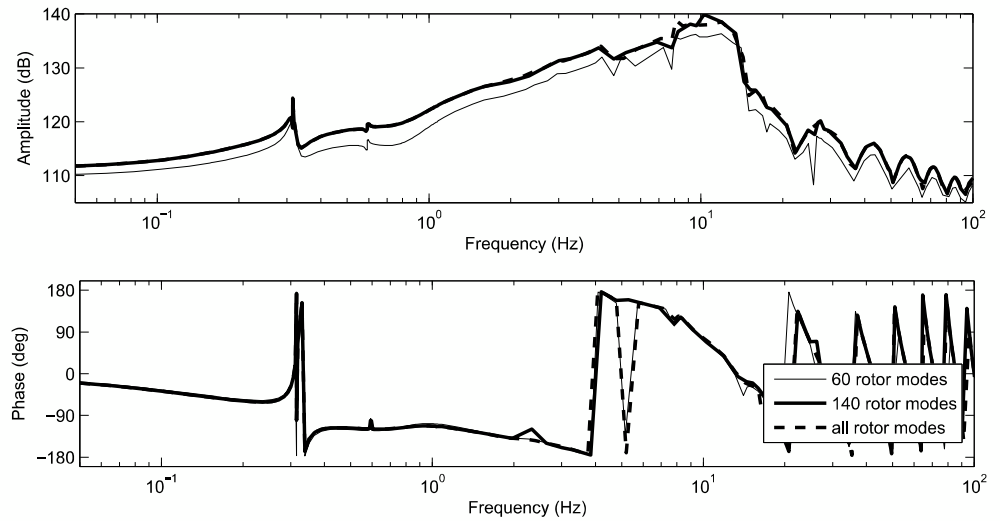
Figure 4.19a shows that the dominant low frequency dynamics for blade flapwise RBM can be captured relatively well using just 60 of the lowest rotor modes. However, this is insufficient for blade root torsion where we will need at least 140 rotor modes to match the amplitude. The reason is that for torsion, the superposition of higher frequency mode shapes is essential in obtaining the resulting quasi-static torsional amplitudes that are crucial in fluid-structure mapping. It should also be noted that the rise in torsional gain with frequency is due to the location of the elastic axis at quarter chord, resulting in moments being dominated by non-circulatory lift from the perspective of classical unsteady aerodynamics solutions. As frequency increases further, the magnitude eventually falls off due to structural damping. Note that the first torsional mode is around 8 Hz.

As the modal truncation here is based on a frequency cut-out of the lowest 140 rotor modes, it unavoidably also retains a considerable amount of high frequency modes that are not necessary in capturing blade torsion. An alternative is to identify each mode and retain only those needed to capture the required dynamics, such as blade flapwise RBM and torsion. However, difficulties arise as the nature of each mode is not clearly distinguishable from one another at higher frequencies with significant interaction between the modes. Since the size of the structural model is not the determining factor for computational speed compared to the size of the UVLM model, the lowest 140 rotor modes were retained. In the above cases, all tower modes are kept. A further study identified that only 10 tower modes are needed to capture the tower fore-aft deflection.

The reduction of the aerodynamics is performed using balanced truncation. The Hankel singular values (HSV) [215] of the balanced UVLM model with respect to the largest HSV are shown in Figure 4.20. In the current balanced UVLM model, relative states that are smaller than three orders of magnitude are truncated. The reduced UVLM model is then coupled with the truncated structural EoM and simulated using turbulent input signals. The time marching solutions of the reduced order system compared well with those of the full order system, providing confidence that the reduced UVLM model retains key dynamical characteristics of the full aeroelastic model. We have analysed the solution of the truncated UVLM in the fully coupled system to avoid truncating states that appear insignificant in the aerodynamics



(a) Homogeneous gust input to blade flapwise RBM.



(b) Homogeneous gust input to blade root torsion.

Figure 4.19: Bode plot from homogeneous gust input to flapwise RBM and root torsion on one of the rotor blades at an instantaneous azimuth angle $\theta = 0°$. Comparing the effects of truncating structural modes on rotor by keeping the lowest (i) 60 rotor modes, (ii) 140 rotor modes and (iii) all rotor modes. In the above cases, all tower structural modes and aerodynamic states are kept.

model but may still be crucial in the coupling process. Similar to modal truncation, the Bode plots from homogeneous gust input to blade flapwise RBM and torsion are shown in Figure 4.21 and it is evident that the reduced model of keeping 350 aerodynamic states, 10 tower and 140 blade structural modes is able to capture the dominant lower frequency responses for blade flapwise RBM and root torsion. The full model in the figure has all the structural modes and aerodynamic states.

The reduced aeroelastic model has close to 900 states and with the rotor blades returning

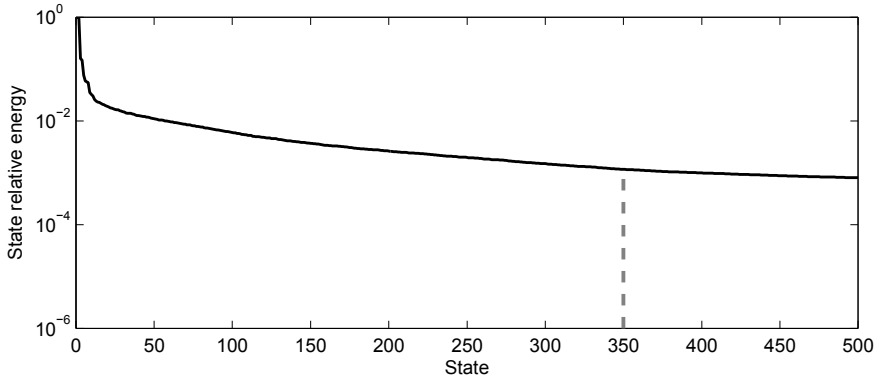


Figure 4.20: Normalised Hankel Singular Values of the balanced UVLM model with respect to the largest HSV.

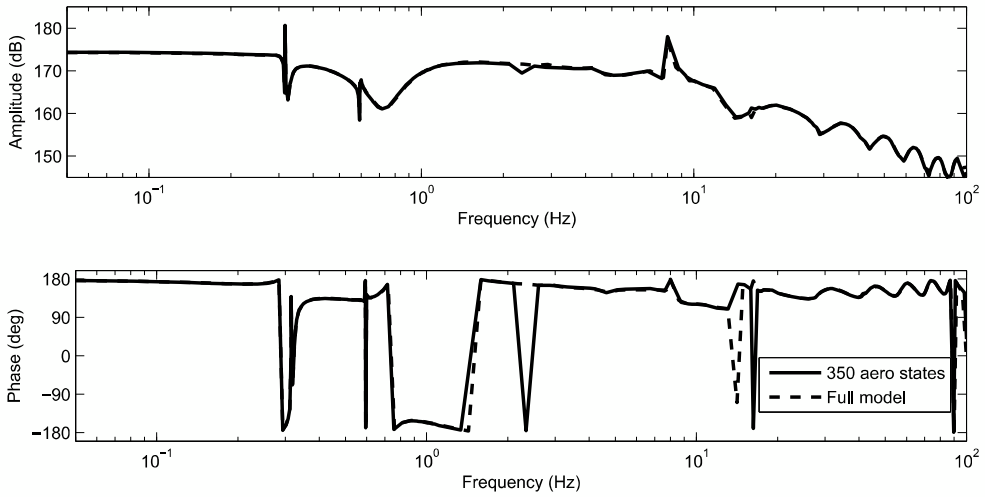
to the same azimuth location after each round of rotation, all the state matrices in the first rotation can be stored and extracted for use in subsequent loops. These methods, including model reductions in the structures and aerodynamics as described, helped to save computation time by more than two orders of magnitude with minimal impact on the accuracy of the simulations. (For each 600 seconds of simulation, the computation took approximately 30 minutes on a single processor machine.)

Instead of reducing the structures and aerodynamics separately prior to coupling as described above, an alternative is to define and reduce the aeroelastic description of the rotor prior to coupling with the tower structural dynamics, as described in Appendix E. As nonlinearity in the complete turbine stems from the tower, the aeroelastic description of the rotor alone will be linear. By reducing the rotor as a whole, the fluid-structure mapping is preserved within the aeroelastic model, and model reduction can be performed using less input/output channels defined by the overall simulation, hence requiring less states to be retained. However, using this method, the number of states required is still relatively large (at least 500) and not much smaller than the separate reduction of structural and aerodynamic modules. As the split procedure provides a better insight into the system dynamics, it is preferred and will be adopted in the simulations that follow.

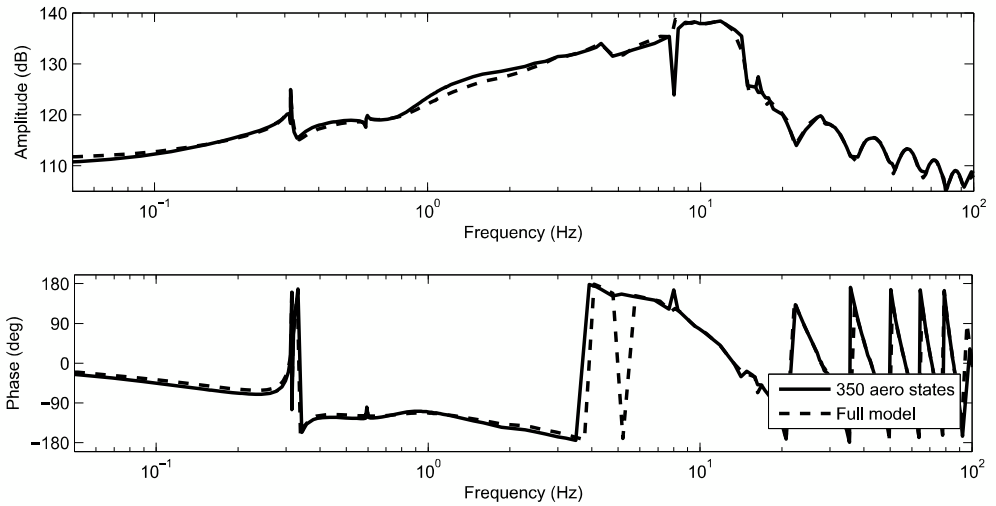
4.3.4 Passive Load Alleviation

Fibre-reinforced plastics are characterised by anisotropic behaviour and can be used to tailor the elastic response of the structure [114]. For wind turbine blades where out-of-plane bending is the dominant load, coupling between flapwise bending and torsion have shown to be beneficial for load alleviation [154]. Here, we will demonstrate the concept of bend-twist coupling on the NREL 5MW blade using the existing aeroelastic description, which will subsequently be integrated with active flaps in Section 4.3.6.

If EI is the bending stiffness and GJ is the torsional stiffness, bend-twist coupling can be introduced to the linearised beam equation through an off-diagonal term in the sectional



(a) Homogeneous gust input to blade flapwise RBM.



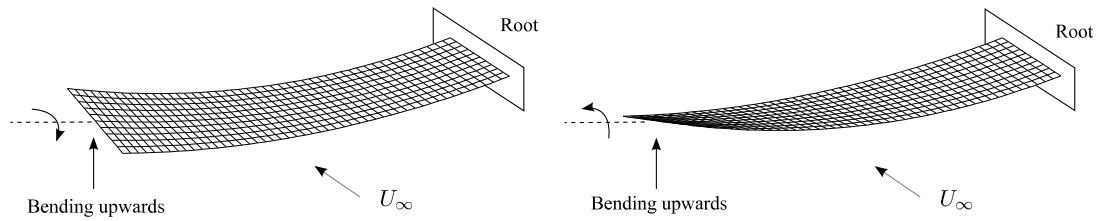
(b) Homogeneous gust input to blade root torsion.

Figure 4.21: Bode plot from homogeneous gust input to blade flapwise RBM and root torsion on one of the rotor blades at an instantaneous azimuth angle $\theta = 0°$. Comparing the effect of keeping 350 aerodynamic states (with 10 tower and 140 rotor structural modes). Full model has all structural modes and aerodynamic states.

stiffness matrix. This bend-twist coupling will be defined as

$$\alpha\sqrt{GJ \times EI}, \tag{4.8}$$

with $-1 < \alpha < 1$ [114] such that the stiffness matrix remains positive definite (with real and positive eigenvalues). To simplify comparisons, we assume that the values of EI and GJ are kept constant. However, in actual practice, when fibres are oriented away from their principal axes, the stiffness values in their original directions will be lower, unless more fibre plies are added.



(a) Twist-towards-feather ($\alpha < 0$). (b) Twist-towards-stall ($\alpha > 0$).

Figure 4.22: Illustration of twist-towards-feather and twist-towards-stall using a simple rectangular surface that is clamped on its right end and bending upwards.

Different signs of α results in different bend-twist coupled responses

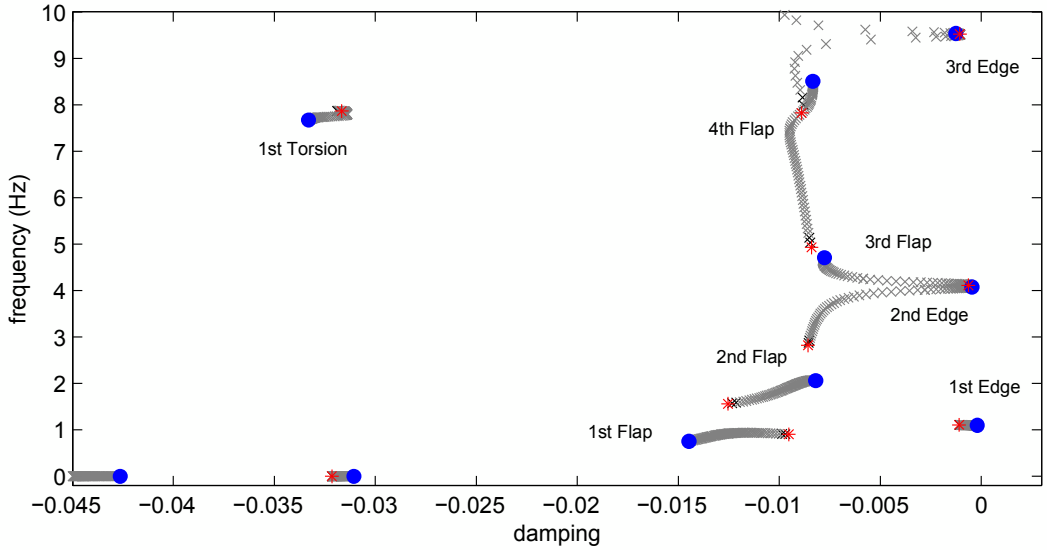
$$\alpha = \begin{cases} 0 & \text{for no elastic coupling,} \\ < 0 & \text{for twist-towards-feather,} \\ > 0 & \text{for twist-towards-stall.} \end{cases}$$

For twist-towards-feather, the blade twists in a direction such that the AoA generates aerodynamic forces that reduce bending. For twist-towards-stall, the response is reversed such that the blade twists in a direction that generates aerodynamic forces to increase bending. An illustration of both behaviours is shown in Figure 4.22.

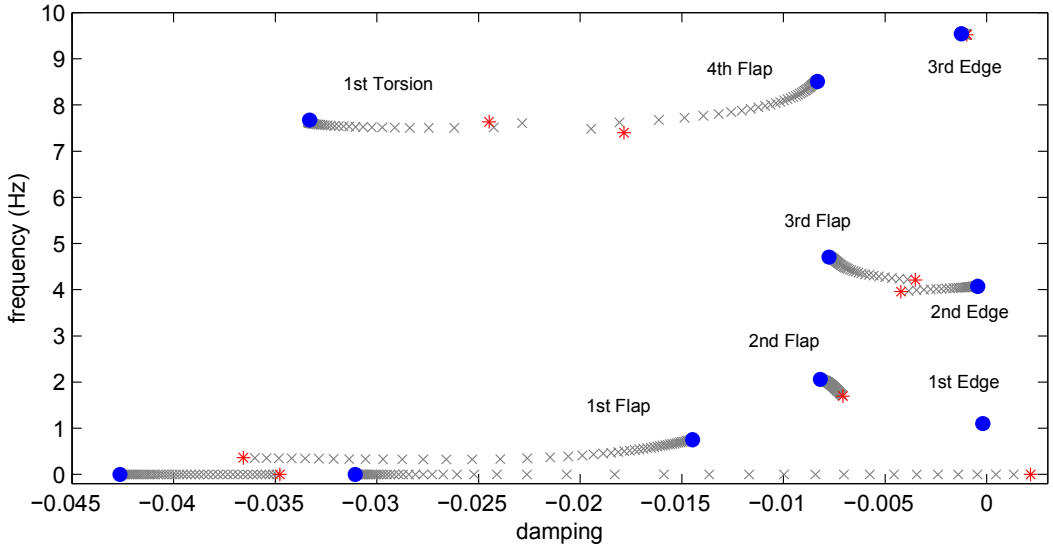
To begin, consider a single rotating NREL blade with the aeroelastic stability plot shown in Figure 4.23 for varying amounts of elastic coupling. For ease of visualisation, the stability plot is separated into negative and positive elastic couplings. With increasing negative coupling (twist-towards-feather) from 0.0 to -0.8 in Figure 4.23a, the torsional and first flapwise modes become less damped as their roots are shifted to the right. The fourth flap mode (with significant torsion) moves down with increasing negative coupling, indicating that higher frequency flap/torsion modes are more easily excited. Due to the structural pre-twist in the blade, edgewise modes are also affected through the flapwise bending component in the coupling. These trends indicate that even though twist-towards-feather delivers benefits in terms of load alleviation, it comes at the cost of increased excitation of higher frequency modes in the elastically coupled blades.

The root locus for varying α from 0.0 to 0.5 is shown in Figure 4.23b. With increasing positive coupling (twist-towards-stall), the torsional mode shifts to the right and approaches the fourth flap mode, with potential interaction. The first flapwise mode becomes highly damped and the edgewise modes are left relatively stagnant, except for the second edge that becomes more damped. As α is increased to 0.5, one of the real aerodynamic roots becomes positive, indicating instability through divergence.

The effect of elastic coupling on passive load alleviation on the full wind turbine is demon-



(a) Twist-towards-feather with negative elastic coupling parameter α varied from 0.0 (blue circle) to -0.8 (red star) in increments of -0.01.



(b) Twist-towards-stall with positive elastic coupling parameter α varied from 0.0 (blue circle) to 0.5 (red star) in increments of 0.01.

Figure 4.23: Root locus of the NREL blade for varying degrees of elastic coupling.

strated in Figure 4.24. The values of blade flapwise RBM, torsion and tower fore-aft deflection are averaged across six turbulence seeds and normalised against their respective rms values at $\alpha = 0$. Note that rms values and standard deviation are the same when zero mean is used. With twist-towards-feather, the rms of blade flapwise RBM is reduced significantly and is almost halved with large amounts of negative coupling. The reductions reported in literature are at least 20% (with maximum up to 80%) [154]. Even though there is an accompanying rise in rms of torsion, the increase is relatively moderate. On the other hand, with positive elastic coupling, both the rms of flapwise RBM and torsion rises very quickly as a result of

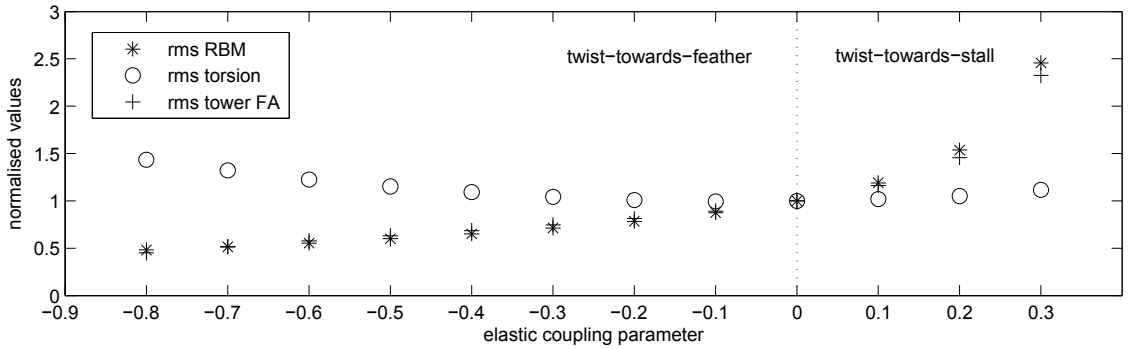


Figure 4.24: Open-loop flapwise RBM, torsion and tower fore-aft deflection with varying degrees of elastic coupling α for the NREL wind turbine. Results are averaged across six turbulence seeds and normalised against their respective rms values at $\alpha = 0$.

twist-towards-stall.

4.3.5 Active Load Alleviation

Next, the turbine is fitted with one flap on each blade to investigate their effectiveness in load reduction. Based on the previous study in Section 4.2.3, a flap occupying 20% span of the lifting surface and 10% of the local chord is chosen and located at a mean position of 80% span. In all the cases that follow, unless otherwise stated, the NREL 5MW wind turbine rotor and tower are used. The operating conditions are rated inflow of 11 m/s and TSR of 7. Each simulation is performed on 6×600 seconds of wind field with characteristic hub height turbulence intensity of 17.5%.

Here, $\mathcal{H}_\infty$ controls are adopted as the inflow contains wind shear effects on top of a turbulence field (no longer Gaussian). Also, to avoid the time lag in controller response observed when using $\ddot{\beta}$ as the control input shown in Figure 4.11c, the control input is now β. As explained in Section 4.1.1, due to the lack of available data for flap models, the dynamics of actuator response is not included. However, there are some works that examine the effects of controller time-lag on closed-loop performances [8, 53]. In the $\mathcal{H}_\infty$ formulation, the weights on the states (measurement output) are increased relative to the control inputs (flap deflection angle β) until either the flap deflection angle or rate limits of $|\beta| \leq 10°$ and $|\dot{\beta}| \leq 100°/\text{s}$ are encountered [24] (see Section 3.2.3).

The controller is designed from a single NREL blade in clamped configuration described in a rotating FoR and written in linear state-space representation [179]. The chordwise UVLM discretization of the control model is the same as the discretization on the rotor blades of the full turbine model to enable the same time step in the discrete-time $\mathcal{H}_\infty$ controller. The number of spanwise and wake panels in the control model is also the same as those on the rotor blades. When the controller is placed in closed-loop with the full turbine model, a decentralised system is formed in which three independent controllers act on each of the flaps. As before, the feedback to the controllers is chosen to be the flapwise RBM of the

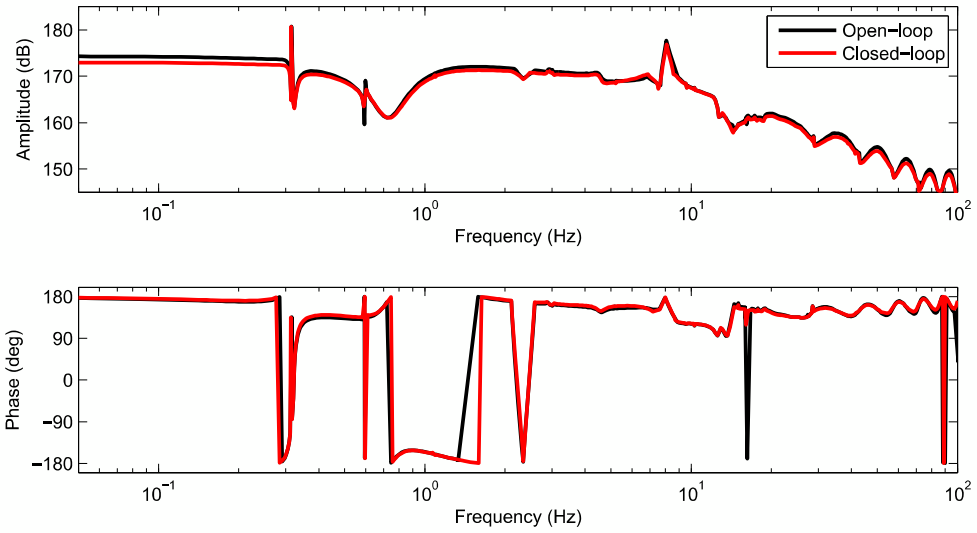


Figure 4.25: Open and closed-loop Bode plots from homogeneous gust input to flapwise RBM on one of the rotor blades at an instantaneous azimuth angle $\theta = 0°$. Using $\mathcal{H}_\infty$ controlled trailing-edge flaps.

Table 4.1: Closed-loop performance of the NREL 5MW turbine using active flap controls across six different turbulence seeds. Negative sign implies an increase. The abbreviation %rd stands for percentage reduction.

%rd rms flapwise RBM	12.9 ± 0.1	%rd max flapwise tip deflection	16.0 ± 2.2
%rd rms torsion	-97.9 ± 5.3	%rd rms tower fore-aft deflection	11.1 ± 0.2
%rd max flapwise RBM	12.6 ± 0.6	max β (°)	9.01 ± 0.99
%rd max torsion	-84.4 ± 17.2	max $\dot{\beta}$ (°/s)	34.9 ± 2.6
%rd DEL flapwise RBM	13.3 ± 0.89		

individual blades (See Figure 2.5).

On average, we are observing around 13% rms reduction in blade flapwise RBM on the reference turbine as shown in Table 4.1 for the six turbulence seeds. There is also a positive effect on reducing stationary component loads such as the tower fore-aft deflection. However, there is a significant increase in torsion as a result of additional moments generated about the elastic axis due to flap deflections (negative percentage reductions in the table). This can be overcome by including torsion in the objective function of the controller to be minimised, as demonstrated in Section 4.2.6 but will not be explored here. The open and closed-loop Bode diagram from a homogeneous gust input to flapwise RBM on one of the rotor blades at $\theta = 0°$ is shown in Figure 4.25 where the reduction in amplitude through the action of the flaps is across most frequencies.

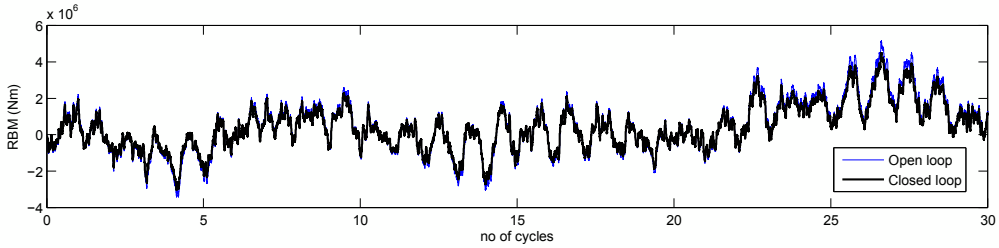
The fatigue analysis involves a rainflow counting algorithm on stresses and for an assumed stress-number of cycles to failure (S-N) curve (also known as Wöhler curve), Palmgren-Miner's linear damage rule is applied to determine the damage. Following which, an overall

damage load that is equivalent to the fluctuating load spectrum can be computed [117, 10, 105, 79]. For the current analysis, a S-N slope of 10, typical for composite materials is chosen. The tabulated results consider only the time-series of the flapwise RBM from the simulation without weighting of wind speeds. Hence, the average damage equivalent load (DEL) reduction of around 13% does not indicate lifetime damage but is an estimate of the fatigue loads. Details for computing the DEL used here in fatigue analysis can be found in Appendix D.

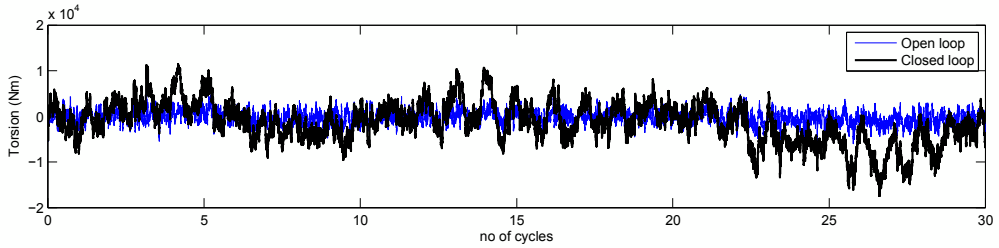
Sections of the time-series for blade flapwise RBM and tip deflection on one of the three blades in operation are shown in Figures 4.26a and 4.26c, respectively. Comparing the open and closed-loop responses, it is apparent that important reductions are obtained in the 1P loads. Yet, when the power-spectral-density (PSD) of flapwise RBM is plotted in Figure 4.27, the reduction is observed across most frequencies. The PSD is computed with Welch's method to smoothen the power spectrum using eight segments of 50% overlap [245]. The Welch's method smoothens periodogram by reducing noise in the estimated power spectrum at the expense of frequency resolution. The algorithm splits a given set of data into overlapping segments, computes modified periodograms of the overlapping segments, and averages the resulting periodograms to produce the power spectral density estimate. This averaging of periodograms reduces the variance, hence smoothing the estimated power spectrum. It is based upon the idea of Barlett [22] but allows segments to overlap. The overlapping segments are windowed (using a Hamming window) to reduce the importance of end samples such that the effects of leakages are minimised.

In the full turbine model, saturation limits of $\pm 10°$and $\pm 100°/s$ were placed on β and $\dot{\beta}$, respectively. However, these limits were seldom reached. In an effort to improve performance that could potentially be achieved through higher flap deflection angles and rates, the controller from the single blade was tuned such that the limit on β was exceeded. When implemented on the full turbine model, the saturation on β at $\pm 10°$ was activated using controllers tuned to $|\beta| \leq 30°$, as shown in Figure 4.28. The closed-loop results are shown in Table 4.2 and it is clear that the rms of flapwise RBM can be increased to over 30% using a more aggressive controller. While the limit on β is met, $\dot{\beta}$ was continuously increasing before saturating ($100°/s$) and levelling out. However, accompanying this is a large increase in rms torsion, which may outweigh the potential benefits in rms flapwise RBM. For the maximum values (blade flapwise RBM and tip deflection), their percentage reductions were less substantial, indicating that maximum values are more highly affected by the bounds on β. On the other hand, rms values are bounded by $\dot{\beta}$ limits. The improvement in fatigue follows the same trend as maximum flapwise RBM (this is expected as fatigue calculations are highly affected by peak events [30]). The PSD for the closed-loop blade flapwise RBM is included in Figure 4.27 for controller tuned to $|\beta| \leq 30°$, showing a further reduction across most frequencies compared to the default case of $|\beta| \leq 10°$ tuned controller.

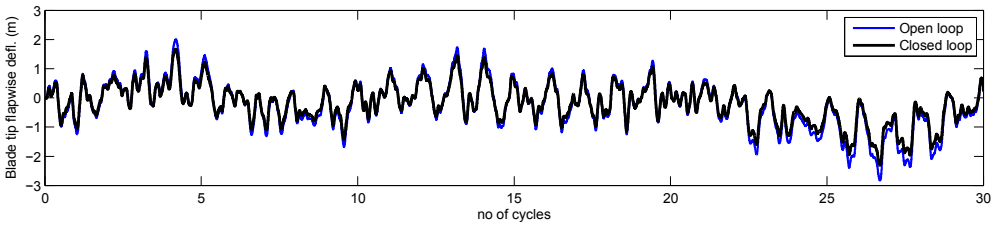
The previous study has been based on 'lift-flaps' in which a downward deflection of the flap generates aerodynamic lift that is in the opposite direction. A question arose as to whether



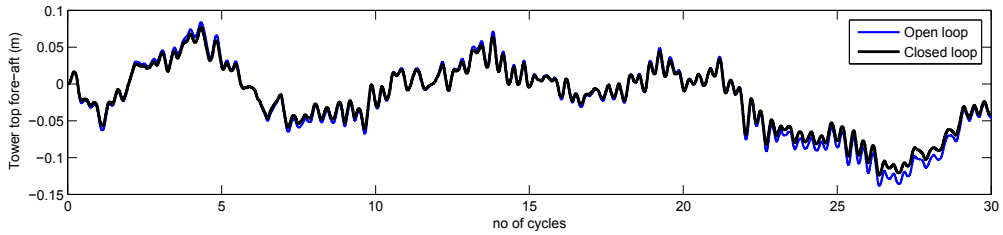
(a) Section of time-series for blade flapwise RBM.



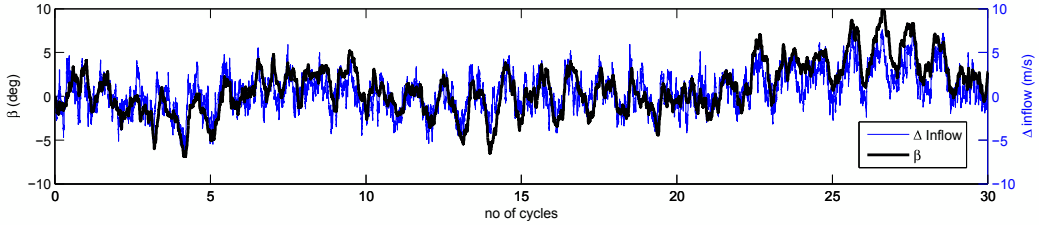
(b) Section of time-series for blade root torsion.



(c) Section of time-series for blade tip flapwise deflection.



(d) Section of time-series for tower top fore-aft deflection.



(e) Section of time-series for flap deflection angle and change in inflow at the blade tip during rotation.

Figure 4.26: Section of time-series for the full wind turbine configuration without elastic coupling.

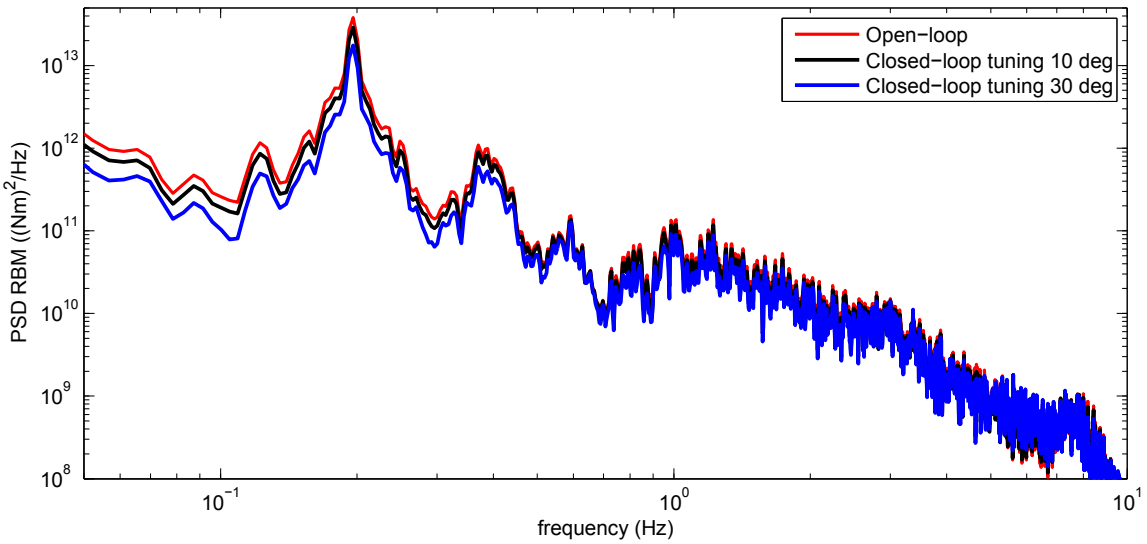


Figure 4.27: PSD of flapwise RBM on one of the rotor blades in open/closed-loop without elastic coupling. Comparing controllers tuned to 10° and 30°.

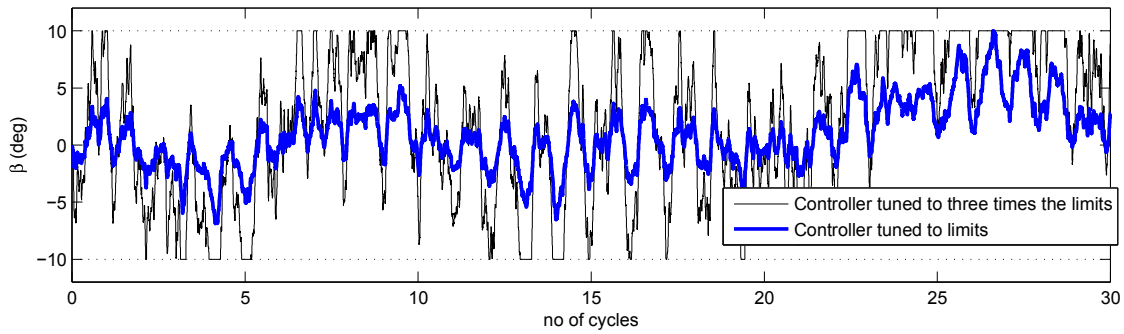


Figure 4.28: Closed-loop flap deflection angle using different controllers with tuning on maximum $|\beta|$ to the limits of 10° and 30°.

Table 4.2: Closed-loop performance using different controllers with tuning on maximum $|\beta|$ varied from 10° to 35°. For percentages, they are averaged across six turbulence seeds and for $\dot{\beta}$, the maximum values among the seeds are shown. The abbreviations are: Cont (Controller), %rd (percentage reduction), bl (blade), tw (tower), FA (Fore-Aft), def (deflection).

Cont tuning	**%rd rms RBM**	**%rd rms torsion**	**%rd max RBM**	**%rd max torsion**	**%rd DEL RBM**	**%rd max bl tip def**	**%rd rms tw FA def**	**max $\dot{\beta}$** (°/s)
10°	13.0	-97.9	12.6	-84.4	13.3	16.0	11.1	37.0
12°	15.9	-127	14.5	-104	15.4	18.6	13.6	62.1
15°	19.6	-165	15.5	-115	16.5	20.3	16.7	65.8
20°	24.8	-222	16.2	-123	17.3	20.7	21.1	82.9
25°	28.6	-268	16.3	-126	17.6	20.6	24.3	96.5
30°	31.1	-304	16.4	-127	17.7	20.4	26.5	99.6
35°	32.1	-331	16.3	-127	17.5	19.1	27.4	100

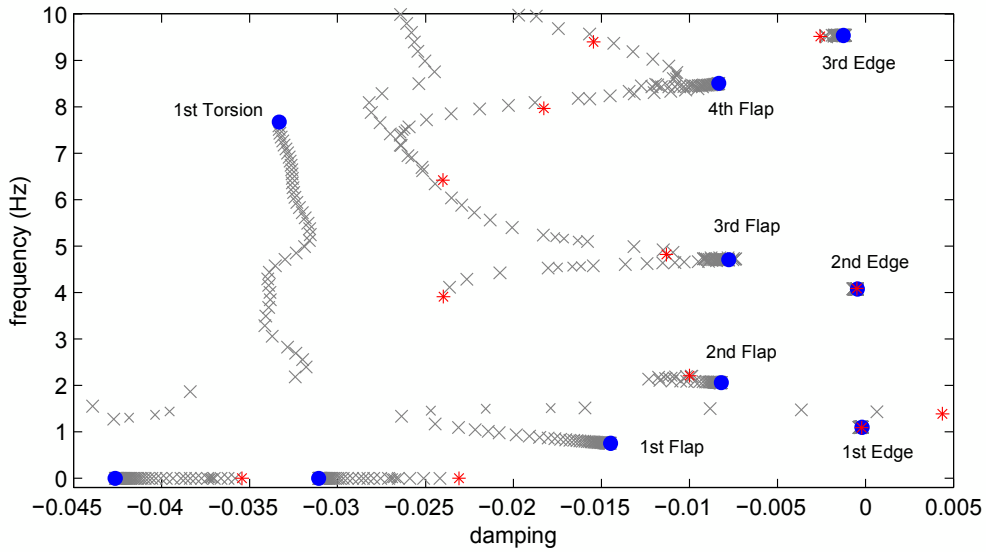


Figure 4.29: Root locus on a single NREL blade as torsional stiffness is reduced from its original value (blue circle) to 14% stiffness (red star) in intervals of 2%.

'moment flaps', such as those used in helicopter vibration control, could be beneficial in the context of the NREL blade [63]. The change in aerodynamic lift in 'moment flaps' is in the same direction as flap deflection, which is a result of the control reversal phenomenon. This normally occurs when the blade is highly-flexible in torsion, such that the moments created about the elastic-axis due to flap deflection results in large changes in angle-of-attack, thereby generating additional lift that overshadows the effect of flap deflection. There is also the advantage of weight reduction in the blade. To investigate, the torsional stiffness of the NREL blade was reduced from its original value to 14% stiffness, and the corresponding aeroelastic stability plot is shown in Figure 4.29. A single rotating blade in clamped configuration is considered here as the focus is to analyse the use of 'moment flaps' as a concept and if feasible, apply it to the complete turbine. As expected, torsional frequency falls with reduced torsional stiffness, and each time it bypasses a flap mode, it gets 'repelled' slightly until it encounters the first flap mode and the aeroelastic system becomes unstable. Before that, we observe an increase in damping of the flapwise modes as torsional stiffness is reduced, which could be beneficial in reducing flapwise fatigue loads. The edgewise modes with the least damping also becomes slightly more damped. Note that the mass of the blade is assumed to remain constant.

From the bode plot of homogeneous gust input to blade flapwise RBM in Figure 4.30, control reversal was observed to occur between 40% to 30% of the original torsional stiffness (where the phase undergoes a 180° change at low frequencies). The closed-loop performance using an $\mathcal{H}_\infty$ controller subject to six turbulence seeds is shown in Figure 4.31. Here, a different controller is designed for each value of reduced torsional stiffness. As torsional stiffness is reduced, the closed-loop performance falls due to moments created by the flap that modifies the angle-of-attack of the blade. Performance reaches a minimum at around

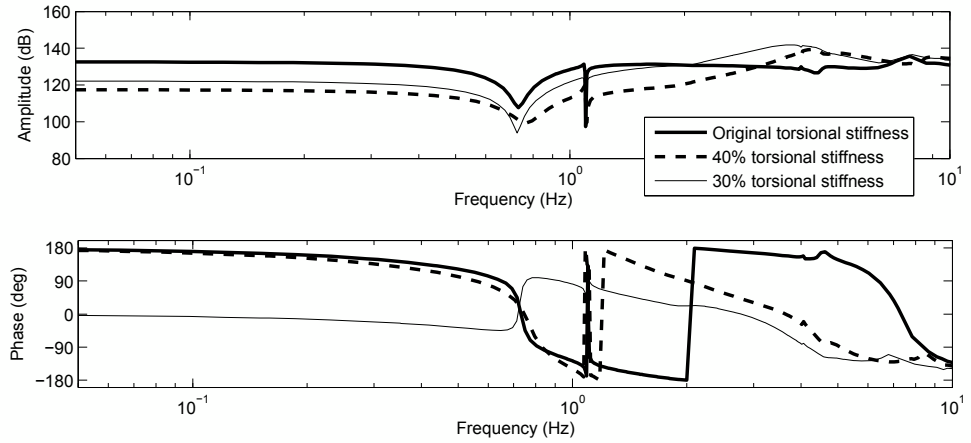


Figure 4.30: Bode plot from flap input to blade flapwise RBM on the NREL blade as torsional stiffness is reduced.

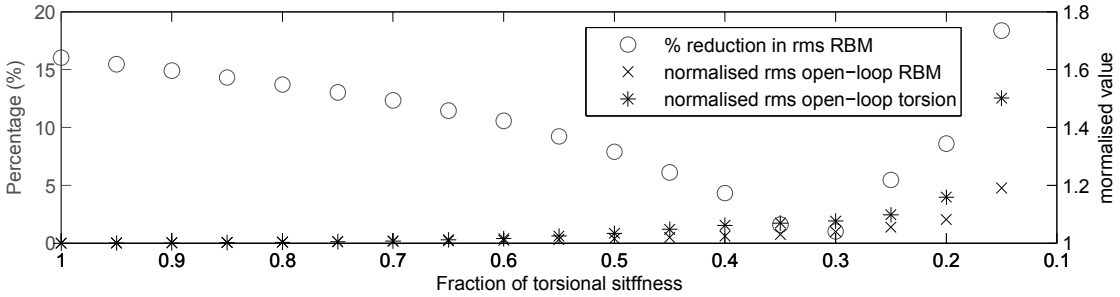


Figure 4.31: Percentage reduction in flapwise RBM and open-loop rms values as torsional stiffness is reduced on a single rotating blade.

30% torsional stiffness (control reversal point) and then rises sharply. Also plotted on the same figure are the rms values of blade flapwise RBM and torsion, which increase at an exponential rate as torsional stiffness is reduced. To conclude, it is clear that the use of 'moment flaps' on the NREL blade is not a possible solution given the large reduction in torsional stiffness required before aeroelastic amplification on the control input is observed.

In all the simulations considered here, a single blade was used for controller design. The results were similar when a centralised control method was adopted in which the control model was a rotor with three blades rigidly clamped at the hub. This now includes aerodynamic cross-influences due to multiple lifting surfaces but does not have any structural interaction between the blades due to the rigid joint. Hence, the closed-loop performance was similar to the original case, except for a smaller amplitude of loads due to the wake induction effect.

A final study compared the results with a controller designed from the full wind turbine model at an instantaneous arbitrary azimuth location. As observed previously in Figure 3.10, the response of the three blades in rotation is relatively similar, despite the non-linearity imposed through different azimuth locations of the rotor blades with respect to the tower. The resulting closed-loop performance was of less than 5% difference from previous cases,

further demonstrating the dominance of gust disturbance and that it is sufficient to use a single rotating blade for control design.

4.3.6 Combined Passive and Active Load Alleviation

In the previous two sections, bend-twist coupling and flap control have separately demonstrated potential in load alleviation for the NREL 5MW turbine, raising the question of any synergies that can be derived from integrating the two mechanisms. This is achieved by attaching flaps to an elastically coupled blade, providing a combination of active and passive load alleviation capabilities. Table 4.3 shows the load reduction performances for varying degrees of elastic coupling (for α between -0.5 to 0.3 at intervals of 0.1). Performances without parenthesis are closed-loop percentage reductions by the action of active flaps alone on top of the reductions delivered by the individually bend-twist coupled blades. Percentage reductions in parenthesis are for the combined action of active flap control and bend-twist coupling.

We observe that when active flaps are used, percentage reductions in rms and maximum flapwise RBM decrease with negative coupling despite an increased use of $\dot{\beta}$. This is likely due to the lower damping of the dominant first flapwise mode in Figure 4.23a, rendering the blade more flexible in the out-of-plane direction. However, when the closed-loop flapwise RBM values of the combined active flap with bend-twist coupling are compared against an uncoupled blade in open-loop (percentages in parenthesis), the combined load reductions are very significant. Flapwise RBM are reduced almost by half, and the corresponding percentage increase in torsional loads are kept relatively unchanged.

The trend is completely reversed with positive elastic coupling where we observe larger reductions in flapwise RBM from active flap controls due mainly to the increased damping of the dominant first flapwise mode in Figure 4.23b. However, this larger reduction in flapwise RBM brought about by the active flaps is insufficient to overcome the increase in flapwise RBM due to the twist-towards-stall action of the elastic coupling, resulting in negative flapwise RBM reductions (percentages in parenthesis). In all the cases, a different controller is designed for each value of elastic coupling. In Table 4.3, the performances in percentages are averaged across six turbulence seeds, while the values of $\dot{\beta}$ are the maximum values across the seeds.

As an illustration, consider the case of α = -0.4, the twist-towards-feather effect reduces open-loop rms and maximum values of flapwise RBM by around 35% and 30%, respectively. Adding active flaps to this configuration adds a further 10% reduction, and despite having a larger $\dot{\beta}$, this is still lower than the 13% in the uncoupled case. The combined effect of the two mechanisms is able to deliver about 40% flapwise RBM reduction when compared to an uncoupled blade with relatively small changes to the increase in torsional loads. When it comes to flapwise fatigue loads, it follows similar trends as the maximum values.

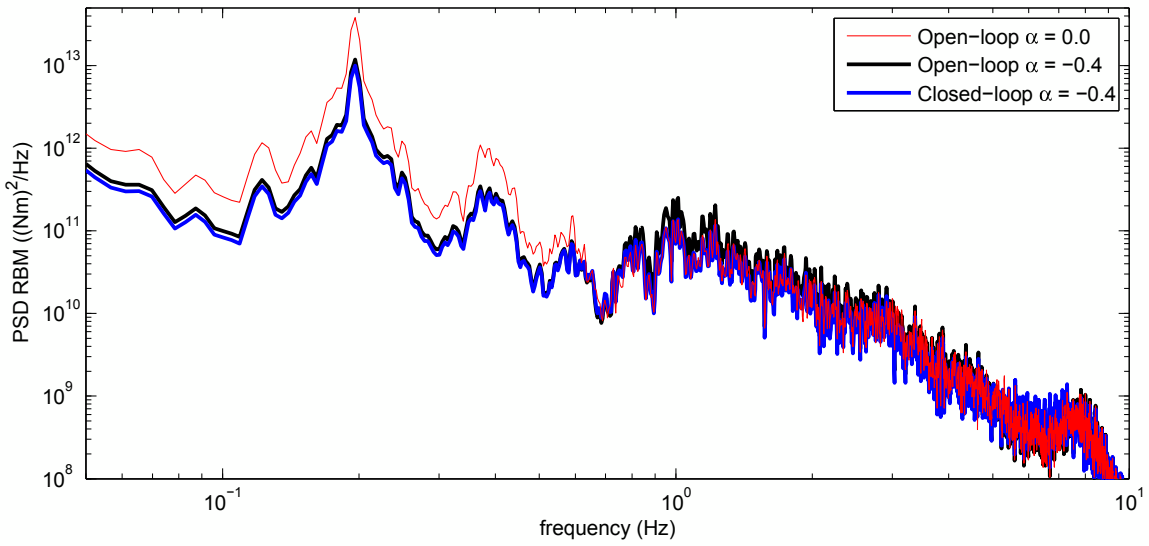


Figure 4.32: PSD of flapwise RBM on one of the rotor blades in open/closed-loop with and without elastic coupling.

Looking at the PSD of flapwise RBM for the coupled case of α = -0.4, Figure 4.32 shows that the effect of the elastic coupling is focused on the lower frequency flapwise loads (3P and below), but amplifies the higher frequencies (0.7 Hz to 2.0 Hz). This amplification of higher frequency loads is also observed when we analysed the stability plot of a single blade in Figure 4.23a. When the flaps are actuated, the attenuation was in the higher frequency range, which also happens to be the region where elastic coupling had the flapwise loads amplified. The flaps are capable of bringing the high frequency flapwise RBM back to values similar to the uncoupled case. This is in contrast to the action of the flaps in the uncoupled blade which acted on all frequencies in Figure 4.27. It also explains why $\dot{\beta}$ increases in cases of twist-towards-feather blades (negative coupling) in Table 4.3.

Table 4.3: Closed-loop performance of the NREL 5MW turbine with different degrees of bend-twist coupling α from Eq. (4.8). Note that the percentage reductions without parenthesis are the additional reductions due to flaps on top of the reductions delivered by the individually bend-twist coupled blades. The percentage reductions in parenthesis (*total*) represent the performance of combined active flap control and bend-twist coupling. The abbreviation %rd represents percentage reduction.

a	**OL rms RBM (Nm)**	**OL rms torsion (Nm)**	**%rd rms RBM** Active (*total*)	**%rd rms torsion** Active (*total*)	**%rd max RBM** Active (*total*)	**%rd max torsion** Active (*total*)	**%rd DEL RBM** Active (*total*)	**max $\dot{\beta}$** (°/s)
0.3	3.10×10^6	2.75×10^3	19.0 (*-98.5)*	-104 (*-130)*	18.1 (*-88.5)*	-80.2 (*-113)*	19.0 (*-85.7)*	19.8
0.2	1.94×10^6	2.57×10^3	15.8 (*-29.3)*	-100 (*-111)*	14.9 (*-25.1)*	-80.8 (*-93.2)*	15.7 (*–24.1)*	26.0
0.1	1.44×10^6	2.46×10^3	13.7 (*1.82)*	-96.2 (*-98.2)*	12.8 (*4.28)*	-77.4 (*-81.0)*	14.1 (*-7.08)*	30.4
0.0	1.26×10^6	2.43×10^3	13.0 (*13.0)*	-97.9 (*-97.9)*	12.6 (*12.6)*	-84.4 (*-84.4)*	13.2 (*13.2)*	37.0
-0.1	1.11×10^6	2.41×10^3	12.3 (*23.2)*	-100 (*-98.4)*	11.8 (*21.7)*	-88.4 (*-85.8)*	12.5 (*22.3)*	66.8
-0.2	9.93×10^5	2.41×10^3	11.5 (*30.5)*	-102 (*-100)*	11.2 (*28.6)*	-90.9 (*-86.7)*	11.5 (*28.8)*	78.4
-0.3	9.02×10^5	2.42×10^3	10.8 (*36.4)*	-106 (*-105)*	10.7 (*34.2)*	-95.6 (*-91.0)*	11.4 (*34.5)*	85.8
-0.4	8.26×10^5	2.43×10^3	9.89 (*41.1)*	-105 (*-105)*	9.74 (*38.6)*	-97.2 (*-91.7)*	10.3 (*38.8)*	85.2
-0.5	7.60×10^5	2.45×10^3	8.93 (*45.3)*	-105 (*-106)*	8.55 (*42.6)*	-98.4 (*-93.3)*	9.07 (*42.5)*	79.8

4.3.7 Frequency Targeted Load Reduction

Figure 4.27 shows that in the presence of a full wind field, the dynamics of the turbine are dominated by 1P flapwise loads. Separately, the intention of active flaps is to target the higher frequency loadings, leaving any static effects to existing pitch mechanisms. Hence, the question arose as to whether targeting specific frequency regions will have any beneficial effects on flapwise RBM reductions? To investigate, different low, high and band-pass filters are included in the measurement output (blade flapwise RBM) of the simulation model [20, 59]. The same filters are also applied to the control model such that the controller design will have knowledge of the filtered signal.

Filters are commonly used in signal processing to remove unwanted noise or retain frequency range of interest. The main parameters in filter design are the selection of the cut-off frequency and order of polynomial, defining the boundary of the frequency response and the roll-off rates, respectively. The simplest filter can be assembled in first or second order form. For second-order, the standard form is given by

$$H(s) = \frac{N(s)}{\frac{s^2}{\omega_c^2} + \frac{s}{Q\omega_c} + 1}\,, \tag{4.9}$$

where ω_c is the cut-off frequency and s is the Laplace variable [54]. The quality factor is given by $Q = \frac{1}{2\zeta}$ with damping ratio ζ and

$$N(s) = \begin{cases} k & \text{for low-pass filter with gain } k, \\ k\frac{s^2}{\omega_c^2} & \text{for high-pass filter with gain } k, \\ k\frac{s}{Q\omega_c} & \text{for band-pass filter with gain } k, \\ k\left(1 - \frac{s^2}{\omega_c^2}\right) & \text{for notch filter with gain } k. \end{cases}$$

Note that the notations k and s used here have different definitions from the rest of the document.

To achieve sharper roll-off at the cut-off frequencies, higher-order filters can be used. Filters can be further classified by the approximating polynomial used to define the transfer function, delivering different characteristics in the frequency response. These include the Chebyshev, Butterworth, Bessel and elliptic filters, among others. The interested reader is referred to Refs. [208, 186] on filter design. For instance, Butterworth filters have as flat a frequency response as possible in the band-pass region, and Chebyshev filters are characterised by ripples and have a steeper roll-off than Butterworth. In this report, for the band-pass filter, a second-order filter is considered and the coefficient of the polynomial is taken from Butterworth with $\frac{1}{Q} = \sqrt{2}$ [20]. A larger quality factor Q can be selected for a sharper peak in the frequency response to better isolate the band-pass frequency. The frequency response of the second-order low, high and band-pass Butterworth filter is shown in Figure 4.33 with

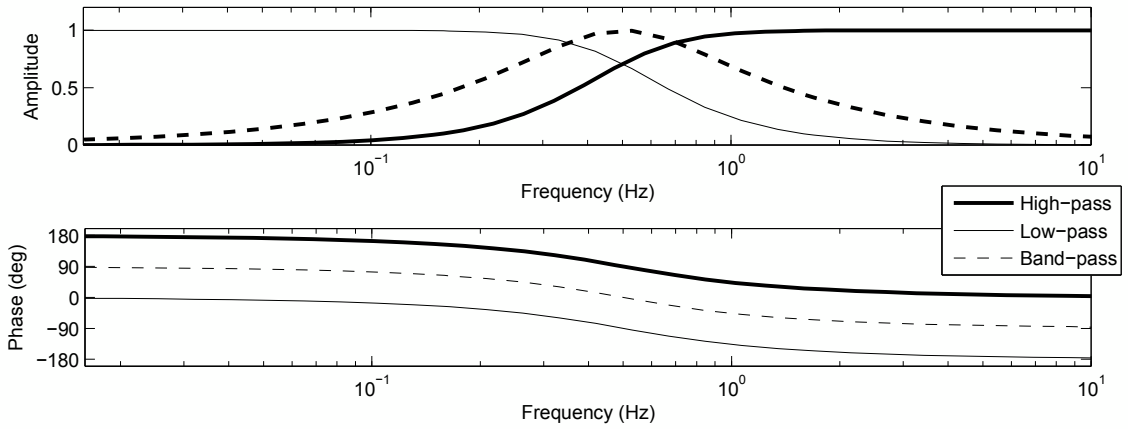


Figure 4.33: Frequency responses of the second-order low, high and band-pass filters (ω_c = 0.5Hz, $Q = \frac{1}{\sqrt{2}}$, $k = 1$).

a cut-off frequency of 0.5Hz.

The effects of having different filters in the measurement output (blade flapwise RBM) is shown in Table 4.4. For each case, an $\mathcal{H}_\infty$ controller is designed from a single rotating blade with the same output filter as the full turbine simulation model. The limits of 10° and 100°/s flap deflection angles and rates, respectively, are used to tune the controller.

It is evident that the best performance is achieved without any filter. With high-pass, performances across rms, maximum and DEL values fall as the cut-off frequency is increased. This goes to negative (a rise in flapwise RBM values) when the controller is designed to only target loads above 0.4Hz. Undoubtedly, this is an indication that high frequency loads above 0.4Hz are of relatively little influence over maximum and fatigue loadings. When we look at the PSD for high-pass of 0.5Hz in Figure 4.34a, it is interesting to see that even though reductions above 0.5Hz are more substantial than the unfiltered case, it is not delivering any load reductions. If we were to analyse the plot more closely, for high-pass of 0.5Hz, there is actually a slight intensification of frequencies below 0.5Hz. This somewhat cancels out any advantage that may be present from the attenuation of high-frequency loads. Also, it should be noted that with high-pass, the flap deflection rates are amplified to within close proximity of the bounds

When we look into the low-pass filtered cases in Table 4.4, the performance does not vary much between the unfiltered case or when we cut-off frequencies above 0.1Hz or 0.7Hz, indicating that the low frequency regions have significant contributions to rms, maximum and fatigue loads. Furthermore, the flap deflection rates for low pass filtered control action is almost half that of the unfiltered case, meaning less actuator duty for almost the same amount of load reduction. The PSD for low-pass of 0.2Hz is shown in Figure 4.34b where the low frequency loads are relatively similar to the unfiltered case.

The band-pass filtered cases are more straightforward. The 1P flapwise loads have the

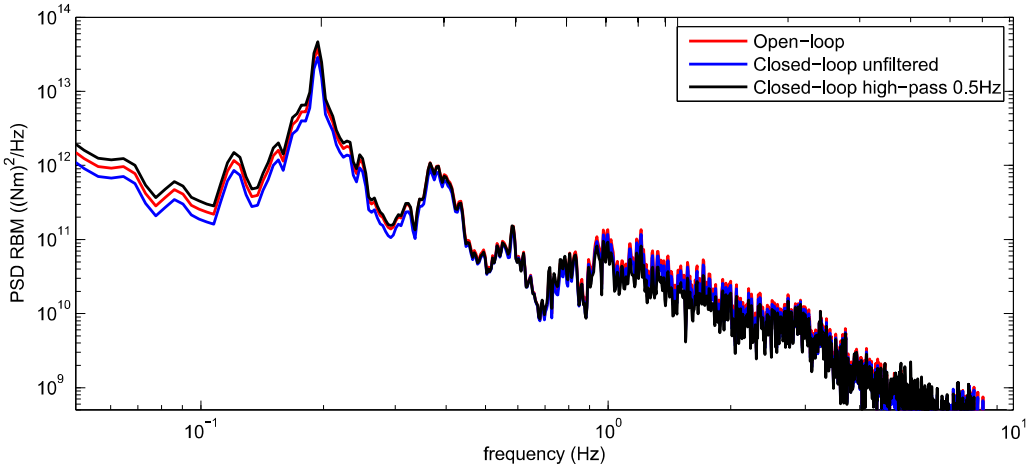
Table 4.4: Performances with high, low and band-pass filters in measurement output. The abbreviations are: %rd (percentage reduction) and tor (torsion).

ω_c **(Hz)**	**%rd rms RBM**	**%rd rms tor**	**%rd max RBM**	**%rd max tor**	**%rd DEL RBM**	**max** $\dot{\beta}$ **(°/s)**
No filter						
	13.0	-97.9	12.6	-84.4	13.2	37.0
High-pass						
0.1	8.78	-86.5	9.01	-67.5	9.62	67.4
0.2	7.40	-86.8	7.66	-73.2	8.22	95.5
0.3	-1.01	-70.4	0.08	-58.8	0.10	99.2
0.4	-5.31	-69.1	-3.98	-63.2	-4.24	99.7
0.5	-5.89	-64.8	-4.58	-59.8	-4.87	99.6
Low-pass						
0.1	11.5	-131	11.3	-108	11.8	12.3
0.2	11.9	-109	11.4	-90.1	12.0	15.2
0.3	12.4	-103	11.7	-85.5	12.3	17.4
0.4	12.7	-102	12.0	-85.8	12.6	19.0
0.5	12.7	-101	12.0	-85.0	12.6	19.8
0.6	12.9	-102	12.2	-86.1	12.9	20.6
0.7	12.9	-102	12.2	-85.8	12.9	20.9
Band-pass						
0.2	8.61	-107	8.39	-80.3	8.97	23.5
0.4	4.68	-76.3	4.98	-63.5	5.33	29.0
0.6	2.43	-68.8	3.18	-62.5	3.40	37.8

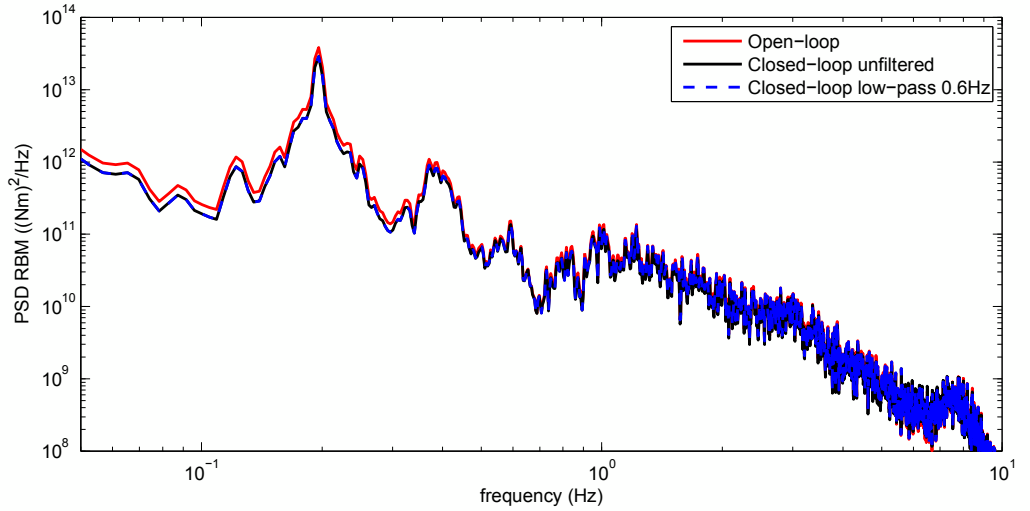
dominant effect over the 2P and 3P flapwise loads. However, concentrating all the control energy on the 1P flapwise load is still not as good as the unfiltered case. The PSD for the different cases of band-pass is shown in Figure 4.34a, clearly demonstrating the suppression of flapwise RBM in the targeted frequency regions. However, it should be noted that both band-pass of 0.4Hz and 0.6Hz gave the same suppression in the region of 0.4Hz, with the latter's PSD slightly below the rest as we go close to 0.6Hz. As we are using only a second-order filter, better isolation of frequencies should be observed if high-order filters are used, giving steeper roll-off at the edges. Also, a larger quality factor Q would give better isolation of band-pass frequencies.

4.4 Pitch Controls

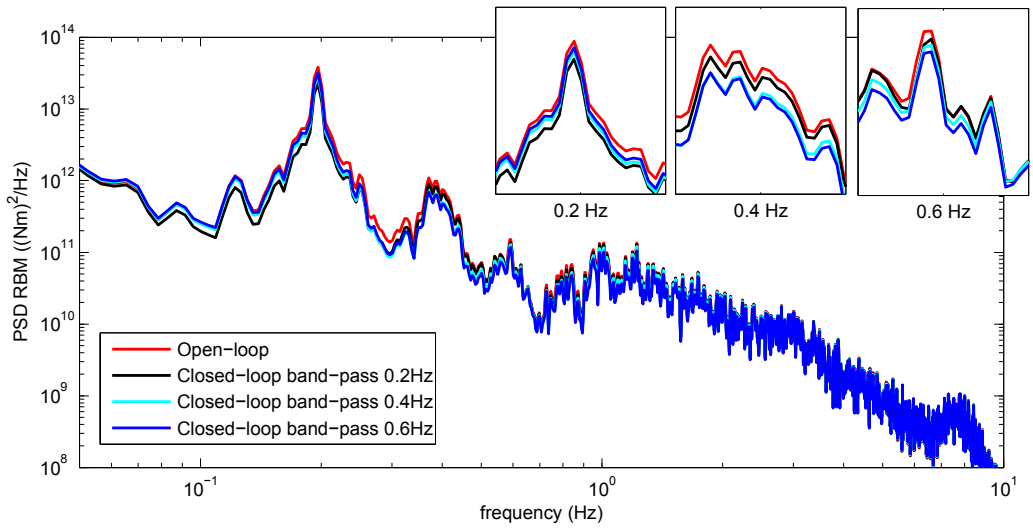
Pitch controls currently exist on variable speed wind turbines for speed regulation and there have been calls for its adaptation to load alleviation [42]. It involves actuating the entire blade, changing AoA to modify aerodynamic lift and drag forces to counteract fluctuations in loading. The limit to which pitch controls is capable of reducing loads on the turbine



(a) Comparing open-loop, closed-loop unfiltered and high-pass with 0.5Hz cut-off.



(b) Comparing open-loop, closed-loop unfiltered and low-pass with 0.2Hz cut-off.



(c) Comparing open-loop, band-pass with 0.2Hz, 0.4Hz and 0.6Hz cut-off.

Figure 4.34: PSD of RBM for comparing different closed-loop models with controller targeting specific frequency regions.

blade is dependent on the actuator constraints, and for the NREL 5MW turbine, the pitch actuator limit is taken to be ±8°/s [129].

We will consider the following cases for pitch controls, namely individual pitch controls (IPC) in Section 4.4.1, cyclic pitch controls (CPC) and a combination of CPC and flap in Section 4.4.2. The intention is to critically assess the potential benefits and drawbacks that pitch may have over flap controls. We will also explore the possibility of combining CPC with flaps, with the former targeting specific 1P flapwise loads through a prescribed harmonic pitch actuation and leaving the remaining frequencies to the latter.

4.4.1 Individual Pitch Control

In the present framework for the aeroelastic description of the turbine, IPC is modelled by imposing a change in downwash on all the UVLM panels resulting from the change in AoA due to pitch. Similar to flaps, the controller is designed from a single rotating blade and placed in closed-loop with the full turbine, tuned to the pitch rate limits of ±8°/s. The load reduction performance of IPC is shown in the first row of Table 4.5, which are significantly higher than the reductions obtained using flaps. This is not surprising as the pitch actuation is across the entire blade, and it results in larger aerodynamic forces than those achieved through the actuation of flaps. Moreover, the increase in torsional loads from pitch is not as large as in the case of flaps. This is due to higher balancing of moments fore and aft of the elastic axis (quarter chord) as compared to flaps where there is a larger moment arm due to the peak in forces at the flap hinge. The open and closed-loop Bode diagram from a homogeneous gust input to flapwise RBM on one of the rotor blades at $\theta = 0°$ is shown in Figure 4.35 where the reduction in amplitude through the action of the IPC is across most of the low frequencies. On the same figure, the closed-loop Bode digram due to flaps is also included, showing less reductions of amplitude. If we were to look at the PSD for the open and closed-loop IPC (Figure 4.36), the same trends can be observed.

In longer and more flexible blades where torsional stiffness is potentially lowered, we further observe in Table 4.5 that performance initially increases for IPC as torsional stiffness is reduced. Below a point in which torsional stiffness is 70% of the original value, IPC appears to have lost its ability for flapwise load alleviation in the highly flexible blade. In comparison, flaps remained working below 70% stiffness. In all the cases for IPC, the pitch rate limit in the full turbine model was within ±8°/s.

4.4.2 Cyclic Pitch Control

To reduce the actuator duty of IPC, a possible solution is to use cyclic pitch controls (CPC) to actuate at a single frequency. This can be tuned to target the 1P flapwise loads that have the highest impact on loadings. For the power law wind shear exponent of 0.2 considered here, the maximum achievable performance was obtained when CPC amplitude was tuned to

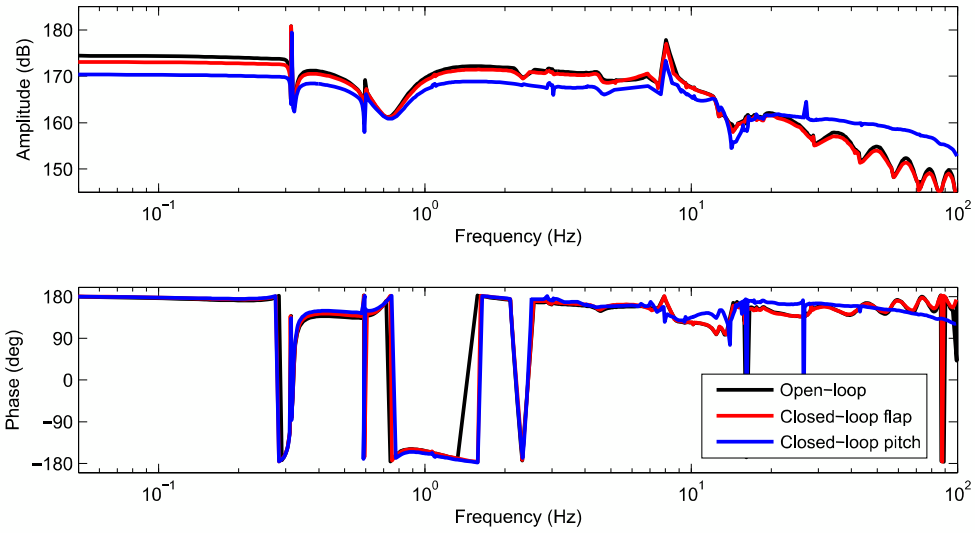


Figure 4.35: Open and closed-loop Bode plots from homogeneous gust input to flapwise RBM on one of the rotor blades at an instantaneous azimuth angle $\theta = 0°$. Using $\mathcal{H}_\infty$ controlled IPC and flap.

Table 4.5: Performances of individual pitch control against flaps (IPC/flaps). The abbreviations are: %rd (percentage reduction) and tor (torsion).

Fraction of torsional stiffness	**%rd rms RBM IPC / flaps**	**%rd rms tor IPC / flaps**	**%rd DEL RBM IPC / flaps**
1.0	35.8 / 13.0	-3.33 / -97.9	35.8 / 13.3
0.9	34.5 / 12.3	-3.18 / -102	34.4 / 12.3
0.8	36.6 / 11.4	-3.2 / -102	38.2 / 10.5
0.7	41.9 / 10.2	-3.43 / -107	41.3 / 8.41
0.6	-1.73 / 8.57	-43.5 / -99.0	-2.55 / 6.18
0.5	-5.51 / 6.17	-38.6 / -96.2	-6.01 / 3.58
0.4	-9.69 / 9.52	-24.9 / -93.3	-5.12 / -1.64

1.2°. Considering a rotating speed of the rotor of 0.2Hz, the pitch rate is 1.5°/s and is within limits. Table 4.6 shows that the reduction through CPC alone is around 12.5% and is almost similar to using flaps alone. However, there is an insignificant change in torsional loads using CPC. When CPC is used in conjunction with flaps, performance can be more than doubled, but at the expense of higher flap actuator duty. The PSD for cyclic pitch alone is shown in Figure 4.37 where the 1P flapwise load is significantly suppressed. When combined with flaps, the further flapwise load reduction is across all the remaining frequencies.

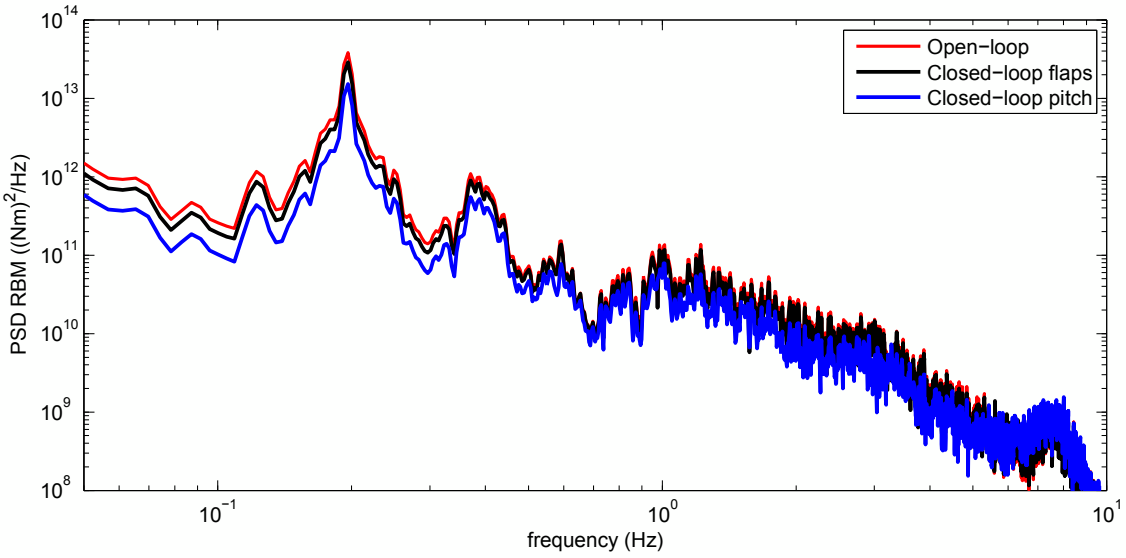


Figure 4.36: Open and closed-loop PSD of flap and individual pitch controls.

Table 4.6: Performances of cyclic pitch controls alone and with flaps. The abbreviations are: %rd (percentage reduction) and tor (torsion).

	%rd rms RBM	**%rd rms tor**	**%rd max RBM**	**%rd max tor**	**%rd DEL RBM**	**max $\dot{\beta}$ (°/s)**
Cyclic pitch alone	12.6	1.39	15.3	1.74	9.45	-
Flap alone	13.0	-97.9	12.6	-84.4	13.2	37.0
Cyclic + flaps	26.7	-102.1	28.6	-69.9	19.1	84.0

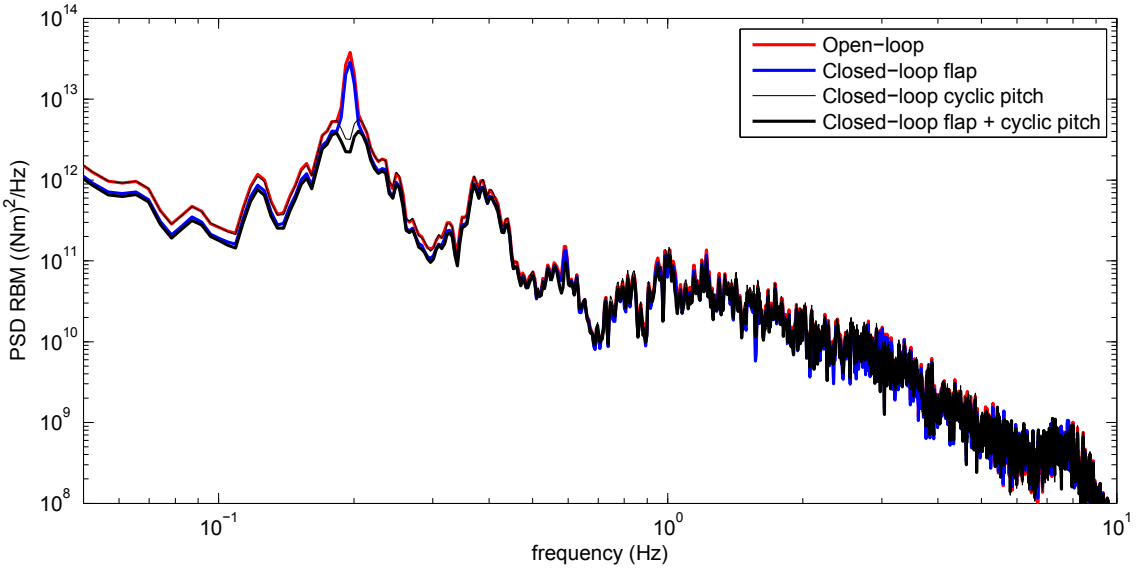


Figure 4.37: Open and closed-loop PSD of cyclic pitch control alone and with flaps.

4.5 Summary

The use of trailing-edge flaps for active load alleviation without elastic coupling has delivered close to 13% reduction in flapwise RBM. Separately, it has also been shown that both IPC and CPC are able to deliver slightly higher reductions in flapwise RBM than flaps. However, there are limitations to IPC and CPC worth considering:

- The power required for pitch controls is expected to be much higher with the pitch mechanism having to overcome the inertia of the entire blade. In Ref. [32], pitch control was shown to require above 20% more energy than flaps (comparing torsion with flap hinge moments) to achieve the same level of performance in simple cyclic loadings.
- There will be increased wear and tear that the pitch bearings have to overcome [191].
- IPC may interfere with other control objectives that uses the same pitch mechanism (such as for speed control), even though there are existing methods to distinguish commands for load alleviation and speed [42].
- In longer and more flexible blades, the propagation of pitch may not be instantaneous along the span of the blade.
- We will need to account for increase in blade mass as they are elongated. This will not only increase actuation energy, but also limit the maximum pitch rate that the mechanisms can achieve, thus limiting its load reduction performance.

In comparison, flaps may still be preferred in longer and more flexible blade as they are localised mechanisms with the capability of faster actuation speeds, lighter in weight and provides a large moment arm to mitigate the dominant flapwise root-bending loads.

Chapter 5

Floating NREL 5MW Turbine with Spar Buoy

The development of offshore wind turbines has been gaining momentum to take advantage of vast wind energy resources in open waters where there are less turbulent winds and more predictable power generation [172]. There are also less constraints in terms of turbine size, noise and also visual impact [124]. At the point of writing, offshore installations are dominated by fixed-bottom structures, such as monopile, tripod, gravity and suction bucket foundations [173]. However, beyond a depth of approximately 50m, these support structures are no longer commercially viable and floating concepts may be needed [135]. The development of floating turbines is still in its infancy and the ones built so far are for research purposes. They are attractive in their ability to access uncharted territories and avoid protected offshore regions and shipping lanes [205]. Much of the technology for the floating structures are derived from oil platforms and can be classified based on the mooring systems, tanks and ballast options [39]. With proven track record in oil and gas explorations, the long-term survivability of these floating structures is not of concern. The main challenge is in their adaptation to HAWT specific operational conditions and developing cost-effective floating concepts that are attractive to the wind industry [125].

Offshore floating turbines operate in different conditions compared to its fixed-bottom counterparts [39]. Most importantly, there is more significant skewed flow due to the motion of the platform, resulting in rapid local velocity changes and greater unsteady effects that could violate the fundamental assumptions underpinning momentum based approaches. Hence, more rigorous modelling techniques, such as UVLM, could provide insights and better prediction of the dynamic loadings [204].

The study of passive and active flap controls in floating wind turbines have so far not been explored. Using the aeroelastic tool developed in this study, a floating turbine is modelled as shown in Figure 5.1. It is based on the work of Jonkman [124], who developed a semi-conceptual floating turbine with parameters based on the NREL 5MW turbine and support

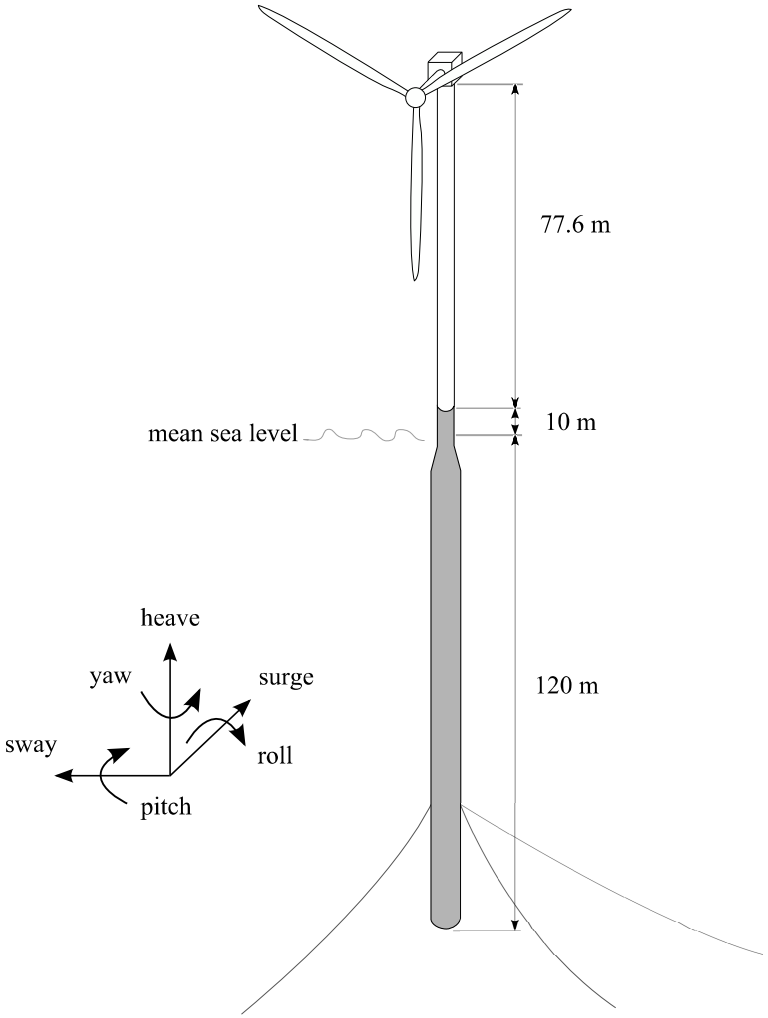


Figure 5.1: Floating turbine with spar buoy and mooring system.

foundations from the Statoil's 'Hywind' project [126].

The original spar-buoy support structure adopted from 'Hywind' requires slight adaptation for use with the NREL 5MW turbine. This is to accommodate for differences in weight and structural properties between the two [126, 128]. Some key properties of the floating platform will be reviewed (Section 5.1), including the wave kinematics used in the excitation of the platform (Section 5.2). The approach to incorporate all the floating components, wave input and wind-wave interaction into the current aeroelastic description will be described in Section 5.3. Numerical verifications and closed-loop performances using active and passive methods will be presented in Sections 5.4 and 5.5, respectively.

5.1 Floating Platform and Ballast

The floating NREL 5MW turbine has a slightly shorter tower compared to its land-based counterpart. All other components such as rotor, nacelle and hub are kept the same. Ne-

Table 5.1: Full system natural frequencies (Hz) of the NREL 5MW wind turbine in stationary configuration, comparing land-based and floating tower configurations (fixed-bottom without floating platform).

Mode	**Description**	**SHARP (Hz) land-based tower**	**SHARP (Hz) floating tower**
1	1st Tower Fore-Aft	0.320	0.372
2	1st Tower Side-to-Side	0.315	0.364
3	1st Drivetrain Torsion	0.611	0.619
4	1st Blade Asymmetric Flapwise Yaw	0.641	0.640
5	1st Blade Asymmetric Flapwise Pitch	0.670	0.672
6	1st Blade Collective Flap	0.703	0.707
7	1st Blade Asymmetric Edgewise Pitch	1.082	1.082
8	1st Blade Asymmetric Edgewise Yaw	1.096	1.098
9	2nd Blade Asymmetric Flapwise Yaw	1.729	1.723
10	2nd Blade Asymmetric Flapwise Pitch	1.878	1.886
11	2nd Blade Collective Flap	1.973	1.975
	3rd Flapwise Yaw		3.107
12	2nd Tower Fore-Aft	2.913	3.559
13	2nd Tower Side-to-Side	3.029	3.707

glecting the floating platform and considering the shorter tower in a stationary fixed-bottom configuration, the computed natural frequencies of the turbine are significantly higher for the tower modes, and a slight increase in other component modes are also observed (Table 5.1).

The tower base is elevated at 10m above sea-level and the draft is 120m below sea-level, as shown in Figure 5.2. The mass of the platform, including ballast, is calculated so that the combined weight of the rotor-nacelle assembly, tower, and platform, plus the weight of the mooring system in water (not including the small portion resting on the sea floor), balances the buoyancy of the undisplaced platform in still water (i.e. weight of the displaced fluid).

The detailed description for the hydrostatics modelling of the floating platform and mooring system is found in Refs. [126, 128]. These are made publicly available through the offshore code collaboration comparison (OC3) project [128, 68] involving several research institutes to develop and benchmark offshore turbine codes. In these publications, a hydrodynamics model based on sanitised properties of the Statoil 'Hywind' floating turbine was furnished using Morison's equation [137].

Morisons representation is valid for slender, vertical surface-piercing cylinders that extend to the sea floor, and accounts for relative kinematics between the fluid and substructure. It is a semi-empirical equation for the in-line force acting on a body in oscillatory flow, and is applicable when the effects of diffraction and radiation damping are negligible. The relative form of Morison's equation accounts for the loading from incident-wave-induced excitation, radiation-induced added mass, and flow-separation-induced viscous drag in the directions of the surge, sway, roll, and pitch dof. Hydrodynamic heave forces are neglected and yaw

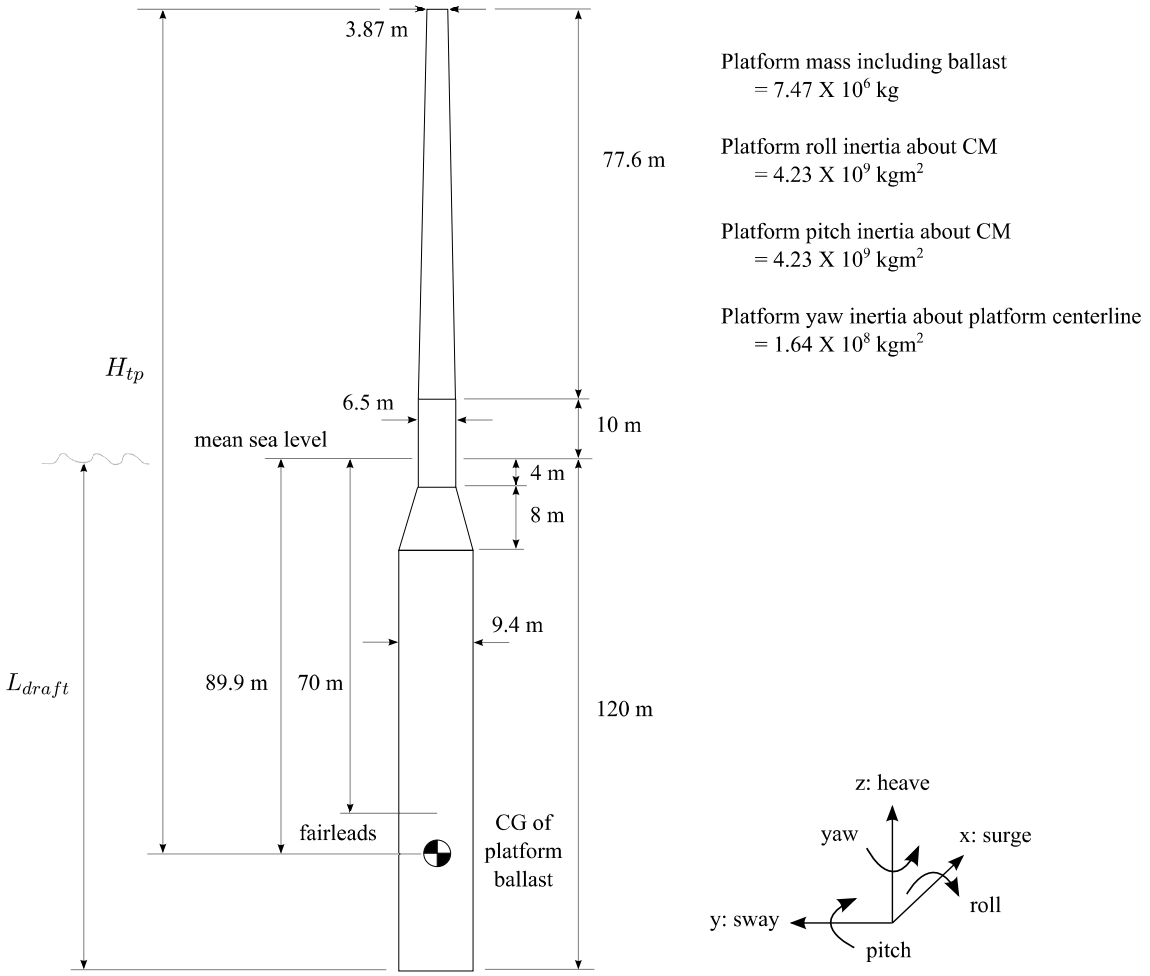


Figure 5.2: Configuration of floating platform (including ballast).

moments are zero for cylindrical structures [124]. The Morison's equation is given by

$$f_{ms} = \frac{1}{4}\rho\pi D^2 \left(1 + C_A\right)\dot{u} + \frac{1}{2}\rho D C_D |u| u \,, \tag{5.1}$$

where f_{ms} is the fluid force per unit length of cylinder at a given time, D is the diameter and u the flow velocity perpendicular to the cylinder. Both the diameter and flow velocity varies along the length of the floating structure and the latter is further dependent on the time-varying wave elevation. The added-mass coefficient, $C_A = 0.970$, is selected to give the same added mass in surge as found in linear potential flow theory. The viscous-drag coefficient is empirically determined as $C_D = 0.6$. To obtain the total in-line force acting on the structure, Eq. (5.1) is integrated over the entire length of submerged platform L_{draft} that is dependent on the wave elevation, giving

$$\boldsymbol{F}_{ms} = \int_{L_{\text{draft}}} f_{ms} dz. \tag{5.2}$$

The hydrodynamic heave forces must be added separately and can be approximated as the change in buoyancy brought about by direct integration of the hydrostatic pressure, given

by

$$\boldsymbol{F}_{buo} = \begin{bmatrix} 0 & 0 & \rho_w g L_{\text{draft}} & 0 & 0 & 0 \end{bmatrix}^\top . \tag{5.3}$$

An additional linear damping is also proposed based on the actual 'Hywind' project findings and is expressed as

$$\boldsymbol{F}_{\text{damp}} = -\boldsymbol{B}_f \Delta\boldsymbol{\nu}_t \,, \tag{5.4}$$

where

$$\boldsymbol{B}_f = diag \begin{bmatrix} 1.0 \times 10^5 & 1.0 \times 10^5 & 1.3 \times 10^5 & 0 & 0 & 1.3 \times 10^7 \end{bmatrix} ,$$

and $\Delta\boldsymbol{\nu}_t$ contains the rigid-body dof of the platform defined in Eq. (5.12).

The mooring system is used to hold the floating platform in place to prevent it from drifting. For the current floating turbine, the mooring system consist of three lines and are distributed 120° apart. They are attached to the ballast through the fairleads located 70m below mean sea-level. A simplified model of the mooring system for small displacements was provided based on several assumptions [126]. These include (1) the elimination of the delta connection and augmenting the system with yaw stiffness in compensation, (2) replacing the multi-segmented mooring lines with an equivalent homogeneous line of weighted-average properties, and (3) neglecting mooring system damping, hydrodynamic drag and line-to-seabed drag.

The total load $\boldsymbol{F}_{\text{ml}}$ from all the mooring lines acting at the cente of gravity (C.G.) of the support platform is given by

$$\boldsymbol{F}_{\text{ml}} = \boldsymbol{F}_{\text{ml,0}} - \boldsymbol{C}_{\text{ml}} \int \Delta\boldsymbol{\nu}_t dt \,, \tag{5.5}$$

where

$$\boldsymbol{F}_{\text{ml,0}} = \begin{bmatrix} 0 & 0 & -1.61 \times 10^6 & 0 & 0 & 0 \end{bmatrix}^\top ,$$

and

$$\boldsymbol{C}_{\text{ml}} = \begin{bmatrix} 4.12 \times 10^4 & 0 & 0 & 0 & -2.82 \times 10^6 & 0 \\ 0 & 4.12 \times 10^4 & 0 & 2.82 \times 10^6 & 0 & 0 \\ 0 & 0 & 1.19 \times 10^4 & 0 & 0 & 0 \\ 0 & 2.82 \times 10^6 & 0 & 3.11 \times 10^8 & 0 & 0 \\ -2.82 \times 10^6 & 0 & 0 & 0 & 3.11 \times 10^8 & 0 \\ 0 & 0 & 0 & 0 & 0 & 1.16 \times 10^7 \end{bmatrix} .$$

$\boldsymbol{F}_{\text{ml,0}}$ represents the pre-tension at the fairleads from the weight of the mooring lines not resting on the sea floor in water. $\boldsymbol{C}_{\text{ml}}$ is the combined result of the stiffness of the mooring lines and the effective geometric stiffness brought about by the weight of the lines in water, depending on the layout of the mooring system.

The equations for the damping and mooring lines (5.4) (5.5) are defined in the conventional

Table 5.2: Horizontal and vertical particle velocity and acceleration for deep seas [166].

Horizontal particle velocity	$u = \omega_w a e^{kz} \sin(\omega_w t - kx)$
Vertical particle velocity	$w = \omega_w a e^{kz} \cos(\omega_w t - kx)$
Horizontal particle acceleration	$\dot{u} = \omega_w^2 a e^{kz} \cos(\omega_w t - kx)$
Vertical particle acceleration	$\dot{w} = -\omega_w^2 a e^{kz} \sin(\omega_w t - kx)$

floating axis shown in Figure 5.2. Attaching the platform to the tower, which is in a different definition of coordinate system, a transformation matrix is required to map the forces

$$\boldsymbol{T}_f = \begin{bmatrix} 0 & 0 & 1 & 0 & 0 & 0 \\ 0 & 1 & 0 & 0 & 0 & 0 \\ -1 & 0 & 0 & 0 & 0 & 0 \\ 0 & 0 & 0 & 0 & 0 & 1 \\ 0 & 0 & 0 & 0 & 1 & 0 \\ 0 & 0 & 0 & -1 & 0 & 0 \end{bmatrix} . \tag{5.6}$$

5.2 Wave Kinematics

The kinematics of incident-wave in irregular seas is determined using a wave spectrum combined with linear Airy wave theory. The fundamental assumption in Airy (linear) wave theory [4, 137] is that the fluid is inviscid, incompressible and irrotational, allowing the use of potential flow solutions to model the motion of gravity waves on the surface of a fluid.

Airy wave theory describes the elevation e_v of the wave as a harmonic motion, given by

$$e_v = a \sin(\omega_w t - kx) , \tag{5.7}$$

where a is the amplitude (given by half the wave height), $k = 2\pi/\lambda$ is the angular wave number, λ is the wavelength, ω_w is the wave frequency and x is the horizontal position of the wave particle (to describe the time lag) [166].

Wave kinematics can be divided mainly into shallow, intermediate and deep waters. For the case of the floating platform considered here, it is situated in deep waters, with velocities and accelerations given in Table 5.2 where z is the depth of the wave particle, measured from the mean sea-level.

For irregular waves, either the Pierson-Moskowitz or JONSWAP (JOint North Sea WAve Project) spectrum are commonly used to combine with Airy wave, to define a and ω_w in Eq. (5.7). Both spectrum are documented in the IEC 61400-3 [118] for offshore wind turbine standards and requirements. Here, the Pierson-Moskowitz spectrum is adopted as it caters for fully developed sea and for wind blowing over a large area for a long time. Hence, it is more representative than JONSWAP, which is for seas that are never developed and based on data collected in the North Sea. Both spectrum will be briefly discussed next.

The one-sided Pierson-Moskowitz spectrum is defined as [222]

$$S(\omega_w)_{PM} = \frac{\alpha g^2}{\omega_w^5} \exp\left(-\beta(\omega_{w,0}/\omega_w)^4\right) ,$$

where $\alpha = 8.1 \times 10^{-3}$, $\beta = 0.74$, $\omega_{w,0} = g/U_{19.5}$ with $U_{19.5}$ the wind speed at height of 19.5m above the sea surface. Another relation for the Pierson-Moskowitz spectrum (one-sided) is given by [124]

$$S(\omega_w)_{PM} = \frac{1}{2\pi}\frac{5}{16} H_s^2 T_p \left(\frac{\omega_w T_p}{2\pi}\right)^{-5} \exp\left[-\frac{5}{4}\left(\frac{\omega_w T_p}{2\pi}\right)^{-4}\right] , \tag{5.8}$$

where H_s is the significant wave height and T_p is the peak spectral period.

For JONSWAP, the one-sided spectrum [222] is given by

$$S(\omega_w)_{JS} = S(\omega_w)_{PM}\left[1 - 0.287\,\ln(\gamma)\right]\gamma^{\exp\left(-0.5\left(\frac{\frac{\omega_w T_p}{2\pi}-1}{\sigma(\omega_w)}\right)^2\right)} , \tag{5.9}$$

where γ is the peak shape parameter of the irregular sea state and σ is the scaling factor, which are functions of the wave height and period given by

$$\gamma = \begin{cases} 5 & \text{for } \frac{T_p}{\sqrt{H_s}} \leq 3.6 m^{-\frac{1}{2}} s \\ \exp\left(5.75 - 1.15\frac{T_p}{\sqrt{H_s}}\right) & \text{for } 3.6 < \frac{T_p}{\sqrt{H_s}} \leq 5 m^{-\frac{1}{2}} s \\ 1 & \text{for } \frac{T_p}{\sqrt{H_s}} > 5 m^{-\frac{1}{2}} s \end{cases} . \tag{5.10}$$

$$\sigma(\omega_w) = \begin{cases} 0.07 & \text{for } \omega_w \leq \frac{2\pi}{T_p} \\ 0.09 & \text{for } \omega_w > \frac{2\pi}{T_p} \end{cases} , \tag{5.11}$$

A comparison of the Pierson-Moskowitz and JONSWAP spectra are shown in Figure 5.3 for $H_s = 6$m and $T_p = 10$s, where JONSWAP has a narrower and higher peak compared to Pierson-Moskowitz.

5.3 Aeroelastic Offshore Turbine Formulation

In the structural description of the floating turbine, the platform (including ballast) and tower are modelled together as a single beam. The platform is represented by a massless rigid beam element spanning from the base of the tower to the C.G. location of the platform in Figure 5.2. A point mass including inertia is then added to the C.G. location. The finite element discretisation of the floating tower is the same as those documented in Ref. [126].

The motion of the floating platform constitutes a rigid-body motion at the base of the entire system. It will be referred to as $\boldsymbol{\nu}_t^\top = \begin{bmatrix} \nu_t^\top & \omega_t^\top \end{bmatrix}$ and it is included in Eq. (2.6) to

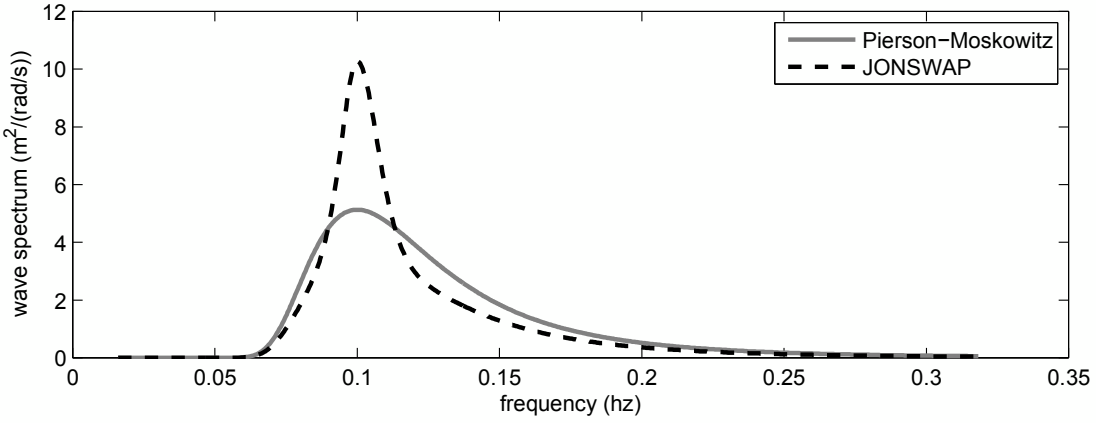


Figure 5.3: Comparing the Pierson-Moskowitz and JONSWAP spectrums.

arrive at

$$
\begin{bmatrix}
\boldsymbol{\mathcal{M}}_t^{SS} & \boldsymbol{\mathcal{M}}_t^{SR} & \mathbf{0} & \mathbf{0} & -\boldsymbol{\Lambda}^\top \\
\boldsymbol{\mathcal{M}}_t^{RS} & \boldsymbol{\mathcal{M}}_t^{RR} & \mathbf{0} & \mathbf{0} & \mathbf{0} \\
\mathbf{0} & \boldsymbol{\mathcal{M}}_r^{SR}\boldsymbol{A}_{CC}(t)\boldsymbol{T}_{tr} & \boldsymbol{\mathcal{M}}_r^{SS} & \boldsymbol{\mathcal{M}}_r^{SR} & \mathbf{0} \\
\mathbf{0} & \boldsymbol{\mathcal{M}}_r^{RR}\boldsymbol{A}_{CC}(t)\boldsymbol{T}_{tr} & \boldsymbol{\mathcal{M}}_r^{RS} & \boldsymbol{\mathcal{M}}_r^{RR} & \boldsymbol{A}_{CC}^\top(t) \\
\mathbf{0} & \mathbf{0} & \mathbf{0} & \mathbf{0} &
\end{bmatrix}
\begin{Bmatrix}
\Delta\ddot{\boldsymbol{\eta}}_t \\ \Delta\dot{\boldsymbol{\nu}}_t \\ \Delta\ddot{\boldsymbol{\eta}}_r \\ \Delta\dot{\boldsymbol{\nu}}_r \\ \Delta\dot{\boldsymbol{\lambda}}
\end{Bmatrix}
$$

$$
+
\begin{bmatrix}
\boldsymbol{C}_t^{SS} & \boldsymbol{C}_t^{SR} & \mathbf{0} & \mathbf{0} & \mathbf{0} \\
\boldsymbol{C}_t^{RS} & \boldsymbol{C}_t^{RR} + \boldsymbol{T}_f\boldsymbol{B}_f\boldsymbol{T}_f^\top & \mathbf{0} & \mathbf{0} & \mathbf{0} \\
\mathbf{0} & \boldsymbol{\mathcal{C}}_r^{SR}\boldsymbol{A}_{CC}(t)\boldsymbol{T}_{tr} & \boldsymbol{\mathcal{C}}_r^{SS} & \boldsymbol{\mathcal{C}}_r^{SR} & \mathbf{0} \\
\mathbf{0} & \boldsymbol{\mathcal{C}}_r^{RR}\boldsymbol{A}_{CC}(t)\boldsymbol{T}_{tr} & \boldsymbol{\mathcal{C}}_r^{RS} & \boldsymbol{\mathcal{C}}_r^{RR} & \mathbf{0} \\
\boldsymbol{\Lambda} & \mathbf{0} & \mathbf{0} & -\boldsymbol{A}_{CC}(t) & \mathbf{0}
\end{bmatrix}
\begin{Bmatrix}
\Delta\dot{\boldsymbol{\eta}}_t \\ \Delta\boldsymbol{\nu}_t \\ \Delta\dot{\boldsymbol{\eta}}_r \\ \Delta\boldsymbol{\nu}_r \\ \Delta\boldsymbol{\lambda}
\end{Bmatrix}
$$

$$
+
\begin{bmatrix}
\boldsymbol{K}_t^{SS} & \mathbf{0} & \mathbf{0} & \mathbf{0} & \mathbf{0} \\
\boldsymbol{K}_t^{SS} & \boldsymbol{T}_f\boldsymbol{C}_{lines}\boldsymbol{T}_f^\top & \mathbf{0} & \mathbf{0} & \mathbf{0} \\
\mathbf{0} & \mathbf{0} & \boldsymbol{K}_r^{SS} & \mathbf{0} & \mathbf{0} \\
\mathbf{0} & \mathbf{0} & \boldsymbol{K}_r^{RS} & \mathbf{0} & \mathbf{0} \\
\mathbf{0} & \mathbf{0} & \mathbf{0} & \mathbf{0} & \mathbf{0}
\end{bmatrix}
\begin{Bmatrix}
\Delta\boldsymbol{\eta}_t \\ \int\Delta\boldsymbol{\nu}_t dt \\ \Delta\boldsymbol{\eta}_r \\ \mathbf{0} \\ \mathbf{0}
\end{Bmatrix}
=
\begin{Bmatrix}
\mathbf{0} \\ \boldsymbol{T}_f\left(\boldsymbol{F}_{buo} + \boldsymbol{F}_{ms} + \boldsymbol{F}_{ml,0}\right) \\ \boldsymbol{Q}_{ext} \\ \int\boldsymbol{Q}_{ext} \\ \mathbf{0}
\end{Bmatrix},
\tag{5.12}
$$

where $\Delta\boldsymbol{\nu}_t$ is the rigid-body motion of the tower/platform and $\boldsymbol{T}_{tr}$ is used to map the base motion to the tower top. Note that the Lagrange multiplier only couples the elastic deformations of the tower (in A frame) to the rotor hub (H frame). It does not capture the rigid-body motions of the tower/platform assembly in the G frame, which will also excite dynamics in the rotor. Hence, $\boldsymbol{A}_{CC}(t)\boldsymbol{T}_{tr}$ includes the direct mapping of the kinematics of base motion and the additional kinematics due to rotation of tower moment arm. Using small angle approximations and assuming small vertical motion of the tower top resulting from tower base

rotations (pitch and roll), $\boldsymbol{T}_{tr}$ can be expressed as

$$\boldsymbol{T}_{tr} = \begin{bmatrix} 1 & 0 & 0 & 0 & 0 & 0 \\ 0 & 1 & 0 & 0 & 0 & H_{tp} \\ 0 & 0 & 1 & 0 & -H_{tp} & 0 \\ 0 & 0 & 0 & 1 & 0 & 0 \\ 0 & 0 & 0 & 0 & 1 & 0 \\ 0 & 0 & 0 & 0 & 0 & 1 \end{bmatrix}, \tag{5.13}$$

where H_{tp} is the total length of the beam used to model the tower and platform (i.e. from C.G. of ballast to tower top) in Figure 5.2.

The motion of the platform induces additional aerodynamic downwash on the rotor blades that is azimuth dependent. The relationship is similar to the downwash contribution from the tower top motion as described in Section B.2 of the appendix. Hence, the same transformation matrix from Eq. (B.6) is used to map rigid-body motions of the tower/platform as downwash on the rotor blades. An additional term is hence added to the right-hand-side of Eq. (B.25) in the form

$$\begin{bmatrix} \boldsymbol{T}_{\Delta\dot{\eta}_{t,1}}(t)\boldsymbol{T}_{tr} \\ \mathbf{0} \\ \boldsymbol{T}_{\Delta\dot{\eta}_{t,2}}(t)\boldsymbol{T}_{tr} \\ \mathbf{0} \\ \boldsymbol{T}_{\Delta\dot{\eta}_{t,3}}(t)\boldsymbol{T}_{tr} \\ \mathbf{0} \end{bmatrix} \Delta\boldsymbol{\nu}_t^{n+1}\,. \tag{5.14}$$

5.4 Numerical Verification

As a parametric study, the floating wind turbine in Ref. [128] is modelled, and a regular Airy wave of height 6m and period 10s is then simulated on the floating platform. To avoid exciting high frequency dynamics, the wave is input into the system gradually using a ramp function for the first 100s. The surge and pitch motions of the platform are shown in Figure 5.4. The amplitudes reported [128] (FAST/ADAMS) for heave, surge and pitch are 0.25m, 1.5m and 0.8°, respectively, and are very close to those attained through the current model. For the comparison, the turbine is in a stationary configuration with rigid rotor. The elastic tower fore-aft motion is shown in Figure 5.5 and also agrees well with literature [128], which reported an amplitude of 0.23m. This provide confidence that the dynamics of the free-floating platform and tower are captured through the structural model and the wave kinematics is implemented correctly.

In actual sea conditions, wave kinematics is irregular. Hence, for illustration, the stationary turbine is subjected to Pierson-Moskowitz wave spectrum ($H_s = 6$m, $T_p = 10$s) and sections of time-series for the platform, tower top and blade tip deflections are plotted in Figures 5.6, 5.7 and 5.8. Here, the irregular wave is ramped up for the first 50s of simulation and

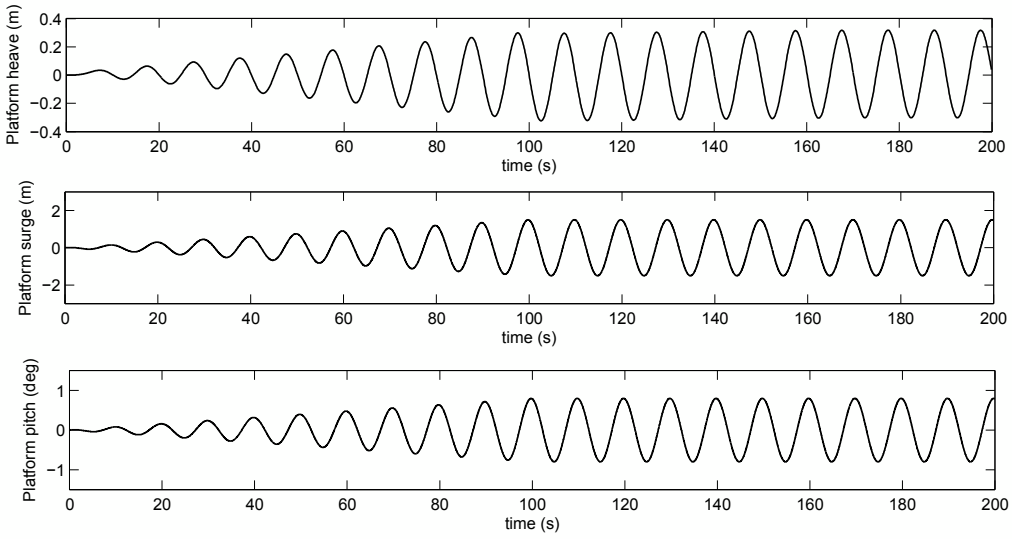


Figure 5.4: Resulting platform motion of the stationary floating turbine with a regular Airy wave of height 6m and period 10s. To avoid exciting high frequency dynamics, a ramp function is prescribed for the first 100s of wave input.

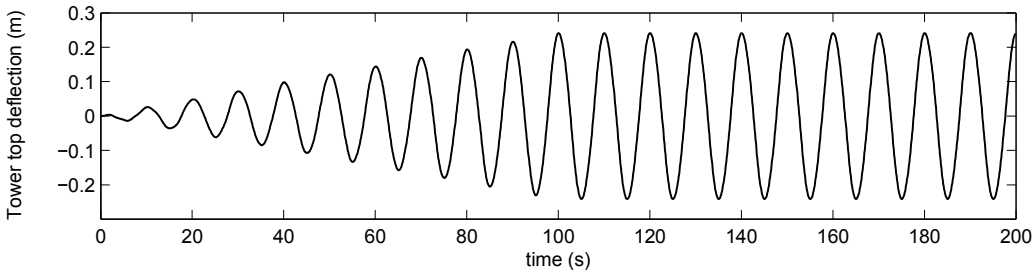


Figure 5.5: Resulting tower-top fore-aft elastic deformation of the stationary floating turbine with a regular Airy wave of height 6m and period 10s.

both the tower and rotor are fully flexible. Note that the tower top and blade tip deflections are all expressed in their local FoR. It is evident that the response is characterised by low frequency loads from the wave spectrum, and the dominant motion is in the platform surge and pitch, resulting in significant impacts on blade and tower top out-of-plane oscillations.

5.5 Closed-Loop Performance

The inclusion of regular or irregular wave kinematics introduces low frequency content on the loading of turbine components. This is evident through Figure 5.9 which compares blade flapwise RBM on the land-based and floating turbine subjected to regular and irregular waves. In all the cases, the turbines are also subjected to a full wind field.

As an initial study of active load alleviation on floating turbines, the same controllers used for the land-based turbine that were designed on a single rotating blade are applied. Table 5.3

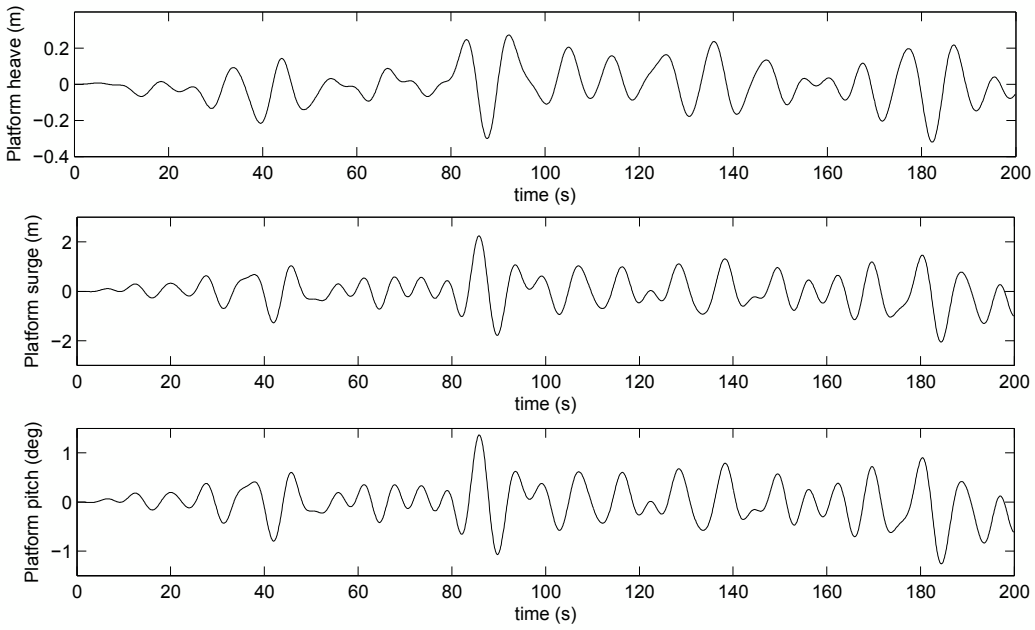


Figure 5.6: Resulting platform motion of the stationary floating turbine subjected to Pierson-Moskowitz wave. To avoid exciting high frequency dynamics, a ramp function is prescribed for the first 50s of wave input.

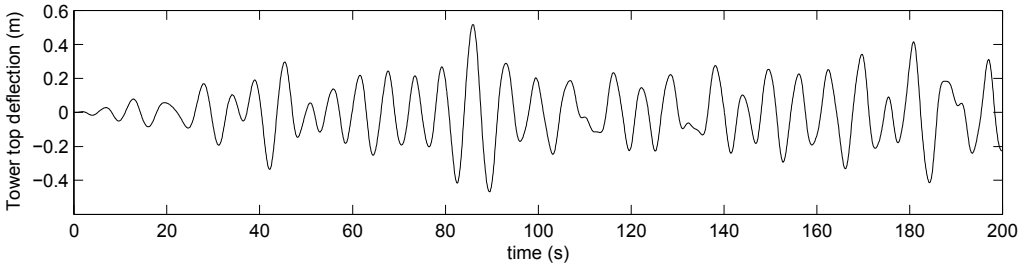


Figure 5.7: Resulting tower-top fore-aft elastic deformation of the stationary floating turbine subjected to Pierson-Moskowitz wave.

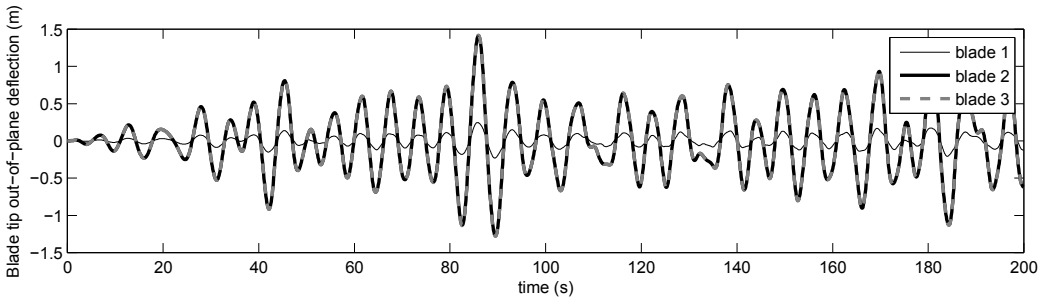


Figure 5.8: Resulting blade tip out-of-plane deflections of the stationary floating turbine subjected to Pierson-Moskowitz wave.

shows the closed-loop performances of the land-based and floating turbines with regular and irregular waves. While the percentage reductions are relatively similar, the open-loop rms values of the floating turbine are much larger than the land-based due to the presence of

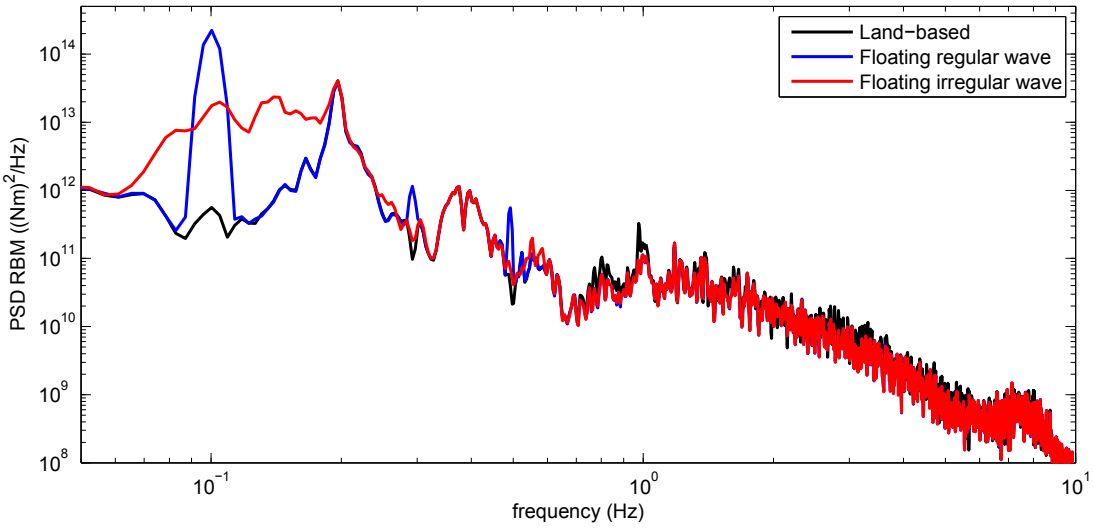


Figure 5.9: PSD of flapwise RBM on one of the rotor blades in open-loop, comparing the land-based and floating turbine with regular and irregular waves (all in the presence of full wind field).

low frequency wave signal. The PSD for the floating turbine with irregular wave is shown in Figure 5.10 for which the reduction is across all frequencies.

Specific frequency bands can be targeted by filtering the measurement signal prior to the feedback to controller. The results for low-pass 0.2Hz and 0.4Hz are included in Table 5.3, where the load reductions in rms, maximum and fatigue are almost similar to the unfiltered case. However, the actuator duty in terms of $\dot{\beta}$ is reduced by more than three times. Note that the controller is designed from the single rotating blade with knowledge of the filter.

The use of passive and active load reduction mechanisms is also considered. Based on the findings from the land-based turbine in Section 4.3.6, an elastic coupling of $\alpha = -0.4$ is chosen and the results are further tabulated in Table 5.3. For the floating turbine, the open-loop rms values are much larger than the land-based turbine. Percentage reductions from active, passive and the combined action are slightly smaller in the floating turbine as compared to the land-based version. The performances with regular and irregular waves are largely similar, although the latter is having smaller reductions.

The PSD for the floating turbine with irregular wave is shown in Figure 5.11. With passive load alleviation through elastic coupling alone, the reductions are focused in the low frequency region, in particular those introduced by the wave kinematics. There is also an amplification of flapwise RBM in the higher frequency range above 0.8Hz. When active load alleviation is included, the suppression was focused on these high frequency bands and to bring them close to the open-loop response.

For all the load alleviation cases considered here for the floating turbine, with either active controls alone or a combination of active and passive load alleviation, there is a very slight

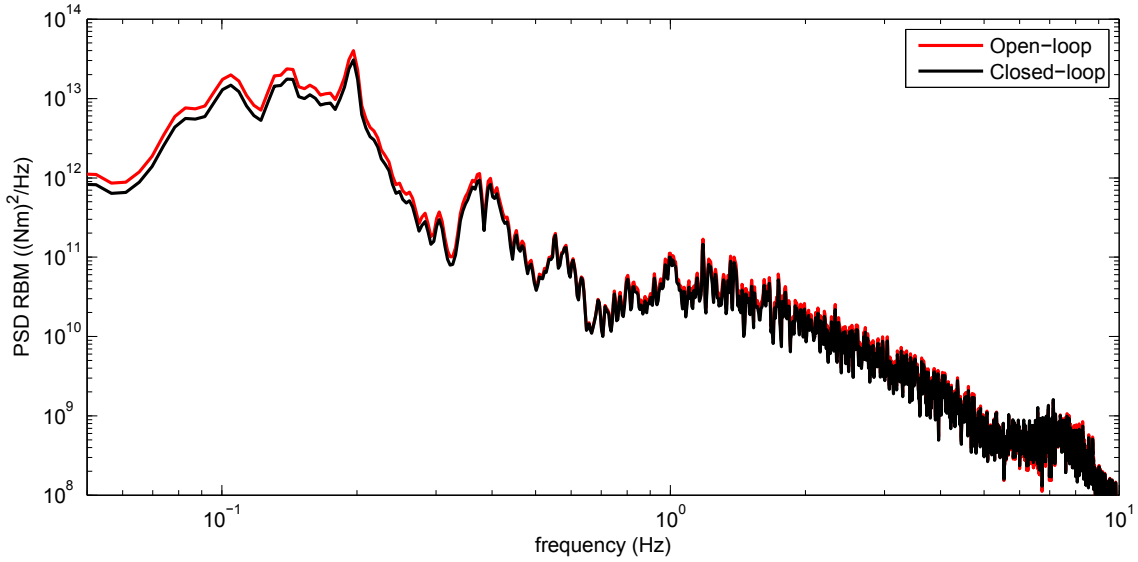


Figure 5.10: PSD of flapwise RBM on one of the floating wind turbine rotor blades in open and closed-loop with active load alleviation alone. In the presence of irregular wave, wind shear and turbulence inflow.

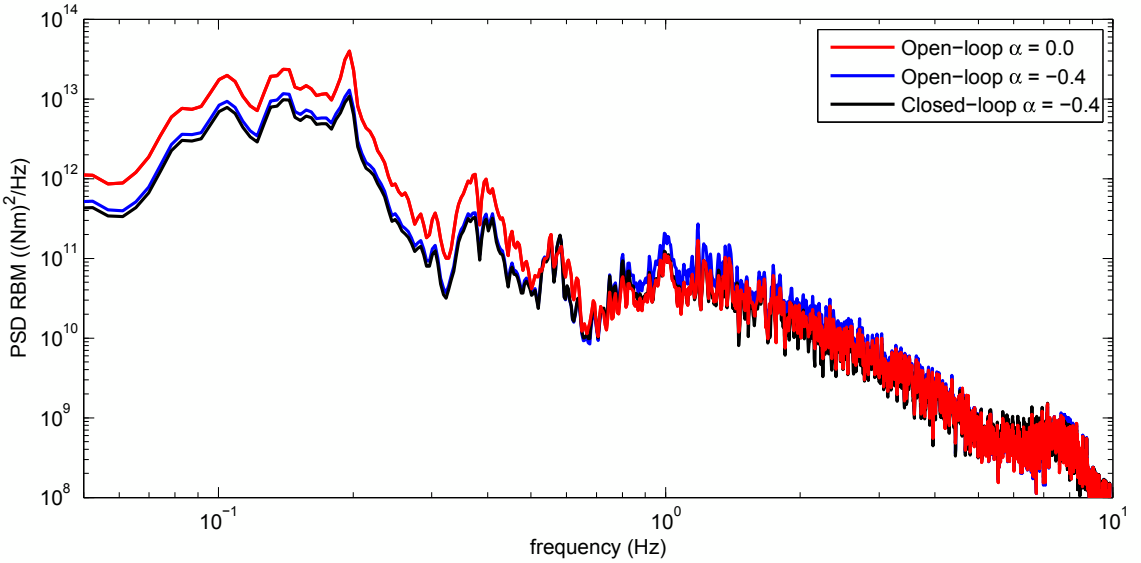


Figure 5.11: PSD of flapwise RBM on one of the floating wind turbine rotor blades in open and closed-loop with passive and active load alleviation. In the presence of irregular wave, wind shear and turbulence inflow.

increase in platform motions (surge, heave and pitch) that is below 1%. Further to that, for the tower top fore-aft deflection in Table 5.4, the reduction in rms and maximum values are relatively small with active controls alone. Even when passive load alleviation is included, the reduction in tower loads is also not as large as the reduction in blade loads. Looking at the PSD for the tower fore-aft deflection in Figure 5.12, we see that the tower deflections have a strong low frequency content due to the platform motion from wave kinematics. These are not acted on by either the passive or active mechanisms, which had been designed to target blade loads.

Table 5.3: Closed-loop alleviation of blade loads on the floating NREL 5MW wind turbine under the action of a full wind field in combination with regular and irregular waves. Comparing (1) active flaps alone (2) active flaps with filtered measurements (3) combined passive ($\alpha = -0.4$) and active mechanisms. The percentage reductions in parenthesis (*total*) represent the performance of the combined active flap control and bend-twist coupling. The abbreviations are: Config (Configuration), %rd (percentage reduction), tor (torsion), Fl (Floating), reg (regular wave), irr (irregular wave), lp (low-pass).

Config	α	**OL rms RBM (Nm)**	**OL rms tor (Nm)**	**%rd rms RBM**	**%rd rms tor**	**%rd max RBM**	**%rd max tor**	**%rd DEL RBM**	**max $\dot{\beta}$** ($^\circ$/s)
Active									
Land	-	1.26×10^6	2.43×10^3	13.0	-97.9	12.6	-84.4	13.2	37.0
Fl reg	-	1.96×10^6	2.80×10^3	13.5	-147	11.2	-88.0	12.1	66.8
Fl reg (lp 0.2Hz)	-	1.96×10^6	2.80×10^3	13.9	-169	10.8	-93.0	11.6	16.4
Fl reg (lp 0.4Hz)	-	1.96×10^6	2.80×10^3	13.4	-151	11.0	-90.0	11.5	20.1
Fl irr	-	1.78×10^6	2.93×10^3	13.2	-120	10.8	-73.1	11.3	99.6
Fl irr (lp 0.2Hz)	-	1.78×10^6	2.93×10^3	13.1	-144	10.3	-76.9	10.7	18.9
Fl irr (lp 0.4Hz)	-	1.78×10^6	2.93×10^3	13.2	-126	10.6	-74.4	10.8	24.5
Passive/Active				Active (*total*)					
Land	-0.4	8.26×10^5	2.43×10^3	9.89 (*41.1*)	-105 (*-105*)	9.74 (*38.6*)	-97.2 (*-91.7*)	10.3 (*38.8*)	85.2
Fl reg	-0.4	1.32×10^6	2.66×10^3	8.88 (*39.0*)	-156 (*-143*)	6.80 (*36.4*)	-90.0 (*-82.1*)	7.51 (*35.0*)	99.9
Fl irr	-0.4	1.20×10^6	2.76×10^3	8.83 (*38.6*)	-129 (*-116*)	6.14 (*32.9*)	-67.1 (*-60.4*)	6.50 (*33.6*)	100

Table 5.4: Closed-loop passive ($\alpha = -0.4$) and active load alleviation of the tower top fore-aft deflection on the floating NREL 5MW wind turbine. In the presence of full wind field in combination with regular or irregular waves. The abbreviations are: Config (Configuration), %rd (percentage reduction), Fl (Floating), reg (regular wave), irr (irregular wave), lp (low-pass), FA (fore-aft motion).

Config	**Elastic coupling (α)**	**%rd rms tower FA**	**%rd max tower FA**
Active			
Fl reg	-	0.0328	2.97
Fl reg (lp 0.2Hz)	-	0.346	3.19
Fl reg (lp 0.4Hz)	-	0.0935	2.92
Fl irr	-	0.793	1.11
Fl irr (lp 0.2Hz)	-	1.58	1.59
Fl irr (lp 0.4Hz)	-	0.950	1.13
Passive/Active		Active (*total*)	Active (*total*)
Fl reg	-0.4	-0.609 (*0.653*)	0.909 (*9.57*)
Fl irr	-0.4	-0.301 (*3.47*)	0.289 (*4.76*)

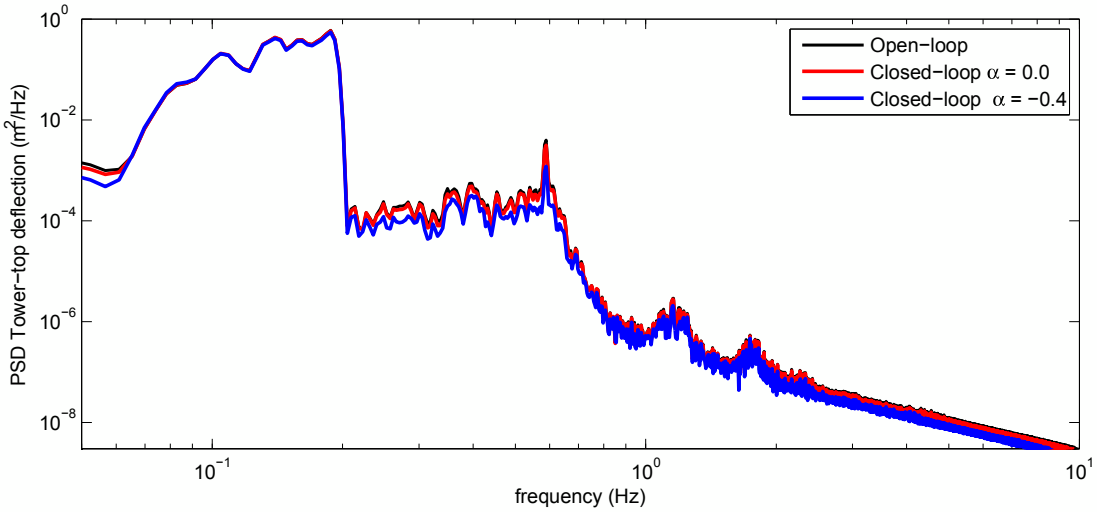


Figure 5.12: PSD at low frequencies of tower top fore-aft deflection in open and closed-loop with passive and active load alleviation. In the presence of an irregular wave and a full wind field.

From the above analysis, it is evident that the current aeroelastic formulation is capable of modelling floating turbines that are subjected to arbitrary platform motion. Also, the use of both active and passive mechanisms are capable to alleviate blade loadings resulting from both the wind and wave kinematics. Even though the controllers are designed on a single clamped rotating blade, they have shown to work well in both the land-based and floating turbine configurations.

Chapter 6

Conclusions

This chapter will conclude the dissertation with a summary on the outcomes of this work in Section 6.1. It will re-assess the problem statement set out at the beginning and evaluate the challenges in both the aeroeservoelastic modelling and load alleviation in wind turbines. The key contributions in this project are subsequently outlined in Section 6.2 to distinguish itself from other works and highlight the novelty that is involved. The chapter will draw to a close with recommendations for future works in Section 6.3, discussing the pending issues and potential for further applications resulting from the main findings.

6.1 Summary

We have seen that the increase in size of wind turbines for larger energy capture requires a multi-disciplinary approach to understand the dynamics of the larger rotor blades and to tackle the accompanying rise in loads on the structure. This requires improvements in the existing modelling techniques to better capture turbine dynamics for structural design, reduction in component weight and material savings. It also calls for methods of load control to maintain or even extend the fatigue lives of blades in the higher loading environment.

With most existing turbines equipped with pitch control mechanisms for speed regulation, a vast amount of literature has recommended their adaptation to load alleviation through cyclic or individual pitch controls. However, the responses of these pitch actuators may be sluggish from the inertia of the more heavy and longer blades. Hence, innovative blade designs with sophisticated active control techniques, such as *smart rotor* concepts have been proposed for faster and localised load alleviation. They combine the use of sensors, actuators and controls in a holistic approach to active load alleviation. Most of these concepts are adopted from air vehicles where there is a proven track record. Even so, it is still a relatively young subject in wind energy with numerous challenges to overcome, mainly the modelling, implementation and finally gaining confidence and acceptance from blade manufacturers.

In this dissertation, the problem of having *a higher-fidelity aeroelastic framework with*

proposed smart rotor concept for load alleviation has been addressed. The challenge is to seek an enhancement to existing modelling techniques for improved capture of turbine dynamics, yet retaining numerical efficiency and control design capabilities. The solution adopted here is to resolve the aerodynamics using the UVLM to administer better characterisations of three-dimensional flows across the rotor. With a prescribed helicoidal wake, a linear state-space description of the UVLM can be formulated to allow reduced-order modelling and also controller design.

The state-space UVLM is easily coupled to any linearised structural description and here, a geometrically non-linear composite beam has been used to represent the rotor blades and tower. The unified aeroelastic framework enables a comprehensive understanding of the aeroelastic behaviour in large wind turbines and to discover the potential advantages of *smart rotor* concepts. As opposed to most works in active load alleviation that have used PID controllers, the control-orientated modelling approach here enables a linear state-space description to apply model-based robust control methods. Finally, the aeroelastic description has also been extended to floating concepts.

In terms of the numerical simulations, this thesis was structured in a bottom-up approach - starting with a two-dimensional aeroelastic description and moved on to the full three-dimensional model of the NREL 5MW blade and turbine. The two-dimensional aeroelastic description was first introduced to allow fundamental studies on active load alleviation. This provided a simple model to carry out initial investigations into controller performance, type and sensitivity to spatial discretisation, which is crucial in vortex methods. Moving on to a single rotating blade using the three-dimensional aeroelastic description, parametric studies into control surface sizing, adverse torsional loads and non-linear numerical verifications were performed. Spanwise effects on the aerodynamics were also scrutinised to highlight the importance of using three-dimensional models in aeroservoelastic modelling. In the full turbine model, the separate and combined use of active flap control and passive load alleviation were explored. Using an $\mathcal{H}_\infty$ controller with blade flapwise RBM feedback, a reduction of 13% in blade root bending loads was achieved with flap deflections angles kept within the limits of $\pm 10^\circ$. When coupled with passive load alleviation through bend-twist coupling, the performance was as high as 40%. Some of the other key results will be highlighted in the next section.

6.2 Key Contributions

The main contribution of this work is a new approach for medium fidelity, physics-based and control-oriented aeroservoelastic modelling. Using a monolithic aeroelastic description, closed-loop full turbine simulations were explored in detail and some of the significant findings will be highlighted here. The essential contributions of this thesis are:

- Methodology

  - Physics-based aeroservoelastic modelling using the unsteady vortex-lattice method
  - Control-oriented approach
- Results
  - Spatial discretisation of controller model
  - Adverse torsional effects
  - Combined passive load alleviation and active flap control
  - Frequency targeted load alleviation
  - Control reversal
  - Floating concepts

6.2.1 Methodology

Physics-based Aeroservoelastic Modelling

The application of *smart rotor* concepts on turbines for load alleviation is topical, and in recent years, received intensive treatment within the wind energy literature. However, there are many missing gaps in the approach to modelling and controls, in particular the description of the aerodynamics and the unified aeroelastic model for control design. Furthermore, with the increase in size of wind turbines for larger energy capture, a high-fidelity and efficient aeroservoelastic numerical tool is needed to predict the dynamics in the longer and more flexible rotor blades. The key to capturing these dynamics is to deliver a physics-based approach to not just the simulation model but also to arrive at linear models for controller design.

The common approach to aeroservoelastic modelling of wind turbines is through BEM coupled with a linearised beam description for the structural dynamics. However, BEM is essentially a two-dimensional analysis of the aerodynamics, and it fails to capture spanwise effects that can only be treated through full three-dimensional models. BEM is also overly dependent on empirical relationships to complement its shortfalls. For instance, BEM is often accompanied with corrections for tip-loss as well as the unsteady and wake aerodynamics. For dynamic load alleviation in large wind turbines with trailing-edge aerodynamic surfaces, a more physics-based approach is essential to allow better estimates of aeroelastic responses under attached flow conditions and direct modelling of lifting surfaces. This is given by the time-domain UVLM presented in this dissertation. The method does not rely on empirical corrections and is essentially a three-dimensional tool. In Section 4.2.1, the importance of three-dimensional effects in capturing aerodynamics loading has been emphasised by comparing the results to an equivalent two-dimensional strip-based counterpart.

Adopting a prescribed wake model, the UVLM can be presented in a state-space description to be coupled with any linearised structural module. Here for the wind turbine, the rotor and tower are represented using geometrically non-linear composite beams that allow

arbitrarily-large structural displacements. While this unified aeroelastic concept has been applied and proven in flexible aircraft application, it is the adaptation and implementation on wind turbines that has been explored here. In Sections 2 and Appendix B, a detailed description of the mathematical representations is furnished to allow the reader to duplicate the presented results using the existing numerical implementation.

The concept of model reduction is a relatively well-established subject in control literature. To effectively formulate a large aeroelastic model that is suitable for model reductions is an area that requires specific treatment as shown in this dissertation. We further demonstrated the use of balanced truncation on the aerodynamics and modal decomposition on the structural dynamics to arrive at a reduced-order model for simulation. The aeroelastic model can be reduced from its original 30,000 states to just 900 states, and computational speed increased by more than two orders of magnitude with minimal impact on the accuracy of the simulations.

Control-oriented Approach

In active load alleviation, controller design plays an important role in the overall performance of the system. Most of the existing research and commercial codes are designed for simulations, with control surfaces added in at a later stage. To obtain a control model, numerical linearisation is often used but the resulting dynamics are different from the true system. Sometimes, certain dynamics such as the unsteady aerodynamics of flap actuation have to be explicitly neglected to obtain linear models. An alternative is to use system identification to build approximate mathematical models using input/output data. While this is an effective way to obtain linear models for control, its accuracy is dependent on the input signals used in the excitation of system dynamics; in wind turbine applications the identification is further complicated by the periodic behaviour of the system. As such, the proposed control-oriented physics-based approach provides an efficient control model for load alleviation studies.

Due to the varying azimuth location of the rotor blades with respect to the tower, the unified aeroelastic description of the turbine is time-varying. However, when tower dynamics are removed, the single rotating blade and rotor descriptions are linear time-invariant and can be used for controller design. Here, the linear state-space model of the single rotating blade is used to design the controller and placed in closed-loop with the full non-linear turbine model. The advantage of having a linear time-invariant blade model for control design is to avoid Coleman transformations or complex control methods for periodic disturbance rejection on full models. Most models are developed with little knowledge of the dynamics and hence designers work on the overall time-varying turbine model for control design. However, with a physics-based approach, we are able to use the blade description.

A large portion of the existing literature in active load alleviation had relied on PID controllers, and it is only recently that robust controllers are sought as an alternative solution. Given the higher actuator duty and the possibility of poor stability margins observed in PID methods, the motivation was to explore further into LQG or $\mathcal{H}_\infty$ controllers for active load

alleviation. This is facilitated by the linear state-space description of the single blade to allow the use of model-based control methods easily. It was also demonstrated that PID controllers expended 70% more energy than LQG and $\mathcal{H}_\infty$ controllers for the same level of load reduction.

6.2.2 Results

Spatial Discretisation of Controller Model

The use of vortex methods requires dense spatial discretisation for convergence, and the challenge is in designing controllers from these increasingly-large computational models. In particular, for model-based control methods such as LQG and $\mathcal{H}_\infty$, the resulting controllers are at least as large as the control model. Given that the size of the aeroelastic model is highly dependent on the spatial discretisation of the vortex panels, the question is whether spatially coarse models that have not converged are able to deliver control models with good performances. Hence, using the two-dimensional model, our study indicated that spatially coarse models that are five times smaller in size are capable of displaying comparable performance to controllers designed from converged models. Further investigations could also be performed to determine controller robustness in closed-loop systems through the gap metric [121, 241, 139, 65].

Adverse Torsional Effects

While the use of flaps deliver benefits in terms of suppressing blade flapwise RBM and tip deflection, it has an adverse effect on torsional loads. Most works that rely on PID controls classified this as an unavoidable situation, which can only be overcome by having tighter bounds on flap deflection limits. However, with a multiple-input-multiple-output controller, this dissertation have demonstrated that adverse torsion can be measured and included in the objective function to be minimised along with flapwise RBM. Balancing the weights between torsion and flapwise RBM, the immediate observation was that the scale of torsional load increase was close to ten times that of flapwise RBM. This indicates that we could achieve a large reduction in adverse torsion for a small amount of flapwise RBM reduction that we sacrifice.

Combined Passive Load Alleviation and Active Flap Control

The use of bend-twist coupling in turbine blades had been extensively studied and even integrated with individual pitch controls for combined passive and active load alleviation. However, bend-twist coupling has not been considered with active flaps. In this dissertation, detailed analysis of the combined behaviour indicated that the performance is beyond those achievable with either mechanism alone. The combined flapwise RBM reduction was more than 40%, out of which three quarters of the performance was contributed by the passive mechanism. Critically to our goals, the target region of both mechanisms is complementary, with the bend-twist coupling providing alleviation on lower frequency flapwise loads (below

3P) and the active flaps concentrated on the remaining higher frequencies. This is a very promising solution that could render further investigations.

Frequency Targeted Load Alleviation

Active load alleviation alone (without elastic coupling) was found to deliver close to 13% reduction in flapwise RBM. However, the reduction was acting across all frequencies and may not be very efficient, considering that blade flapwise RBM are dominated by low frequencies. We have demonstrated that by low-pass filtering the signal, we are able to achieve the same performance with less actuator duty. Targeting specific frequency bands alone (such as the 1P) delivered only half of the performance.

Control Reversal

Previous works in active load alleviation in wind turbines have considered 'lift flaps' in which the downward deflection of flap generates aerodynamic lift that is in the opposite direction. However, as rotor size increases with longer and more flexible blades, the effectiveness of these flaps is shown to deteriorate. For the NREL 5MW turbine blade, if torsional stiffness was reduced to 30% of the original value, control reversal sets in and the change in aerodynamic lift was in the same direction as flap deflection. Once we bypassed this value with even lower torsional stiffness, performance was seen to increase at an exponential rate. It should be noted that a torsional stiffness of 30% may not be sufficient to ensure structural integrity of the turbine blades.

Floating Concepts

The analysis of dynamics in floating wind turbines have in recent years gained interest due to the vast wind energy resources available in deeper open waters. There is still much more to be done in understanding of wind-wave interaction that could yield an increase in component loads. While active load alleviation is relatively well-covered for land-based turbines, it is not yet implemented on floating concepts. Here, our aeroelastic description was extended to include a conceptual floating platform with the NREL 5MW turbine, and load alleviation studies using passive and active mechanisms were performed. The reduction in blade loads was largely similar to its land-based counterpart but tower fore-aft deflection (dominated by platform motion) was left relatively unchanged. The same controllers are used for both land-based and floating turbines, which are designed from a single clamped rotating blade.

6.3 Recommendations for Future Work

The aeroservoelastic formulation considered here provided a comprehensive simulation tool and an efficient control model for large wind turbine fatigue and load alleviation analysis. It is capable of capturing dynamics that are not possible in traditional two-dimensional models. Even though a number of test cases, concepts and extensions to the existing model have been explored, there are limitations and much more can be done to improve the aeroelastic

modelling, controls and also numerical test cases.

6.3.1 Improvements/Additions to Existing Simulation Framework

UVLM Panel Discretisation

In the UVLM, a regular chordwise distribution of vortex panels was adopted and as a result, a considerably large number of panels was needed for convergence. If however, the panels are concentrated at the leading edge and flap hinge, where there are peaks in pressure distributions, the total number of panels can potentially be reduced. The same can be said for the use of spanwise distribution of panels such that we have more panels towards to the tip where roll-up effects are dominant.

UVLM Wake Shedding

Free-wake models are known to give better predictions of aerodynamic loads than the helicoidal model adopted here [145]. However, free-wake models are computationally more demanding in having to resolve the Biot-Savart law at every time step [131]. Instead of the prescribed helicoidal shape, a fixed wake based on results from free-wake models or flow visualisation in tunnel experiments can be used to enhance the solution to unsteady aerodynamics and also wake interactions.

Gravity

Gravity has been omitted from the model as it is thought to generate edgewise loads that are not the focus of the current study. However, due to the structural-twist of the blade, there would be interactions between edgewise and flapwise loads. Since gravity generates 1P loads similar to wind shear, the load alleviation performance is not expected to vary much from the current study. Gravity could nonetheless be included in the model to provide a more accurate description of turbine loads.

Inclusion of Thickness

It has been shown that for wind turbines, the effect of thickness in the blades is negligible when computing loads [34]. The effects of thickness are second order on the lift and can generally be ignored without significant loss of accuracy. However, they can be included through the use of source elements to increase the fidelity of the model, assuming attached flow conditions. If however, viscous effects and flow separation are to be included, the methods by Riziotis and Voutsinas can be adopted [198]. These effects are especially important close to the root of the turbine blades, which have cylindrical cross-sections. Viscous effects can be introduced through surface velocity transpiration to represent mass flow differences on the boundary layer between real viscous and the equivalent inviscid flow, and flow separation is introduced through double wake shedding [35].

Operating Conditions

In the simulations, the inflow is assumed to be perpendicular to the the rotor plane. However, in actual operation, the direction of incoming flow varies [71]. Further to that, the incoming flow field will also contain wake turbulence from turbines upstream in a wind farm configuration [162]. The wake emitted by an upstream turbine exhibits a stochastic pattern known as wake meandering. It is different from traditional turbulence and may be considered as a turbulence field with intermittent characteristics, with a significantly modified turbulence structure and increased turbulence intensity [140]. All these could be taken in account as external disturbances to the aeroelastic model.

Potential Uses of Active Control Devices

The flaps are designed to operate when the turbine is in power production under rated and above rated conditions; although flaps have been claimed to be more effective in above-rated conditions [30]. During other operating regimes, the flaps could potentially be used for other purposes, such as increasing power output in below-rated conditions [216]. Even during rated and above rated conditions, flaps could double up as means of increasing and avoiding fluctuations in power output. At the current stage, the simulation tool may not be capable of power and load predictions below rated wind speeds as the turbine blades operate at high angles of attack. Until viscous and flow separation effects are incorporated in the aerodynamic model, the current tool will be restricted to attached flow conditions.

Rotor Speed Variation and Gain Scheduling

In the numerical simulations, the EoM is linearised about a constant rotor speed with a predefined helicoidal shed wake. However, in actual operation, rotor speed varies by about 10% and the controllers designed based on a constant wind speed may not perform well across the variable operating conditions. Hence, gain scheduling may be required using a family of controllers designed from control models of different rotor speeds.

Drivetrain Modelling

The drivetrain plays a crucial role in the transmission of aerodynamics loads to stationary components such as the tower. In the current model, the drivetrain is modelled as a torsional rod connecting the rotor hub to the tower top and the overall mass and inertia of the nacelle is included as a point mass at the tower top. It neglects individual component dynamics within the drivetrain (main bearing, gearbox and generator) that have an effect on the transmission of loads and ignores flexibility that can introduce additional dof. A model of the drivetrain is hence required at the interface between the hub and tower top [89, 104, 55].

Experimental Validation

The main challenge in aeroelastic modelling and load alleviation study is in complementing numerical solutions with experimental measurements to gain confidence in predictions and to better understand the limits of modelling techniques. To validate aeroelastic responses, the aeroelastic formulation can be used to model experimental turbines, such as those of Barlas et al. [21] or Castaignet et al. [58, 60], and compare static and dynamic responses

using experimental test-cases. For load alleviation performances, as shown in the tabulated performances in Table 1.2 and the comparisons in Section 1.7.4, the only full-scale experiment is that conducted by Castaignet et al. [58, 60] where 14% fatigue reduction had been reported. This is close to the 13% reported in this study. However, it should be noted that there are differences in the operating conditions and model specifications, in particular, the experimental turbine blade is shorter and more rigid as compared to the NREL 5MW conceptual turbine. Further and more rigorous validations against experiments will be required to compare load reduction performance in larger and flexible turbine blades, in both land-based and floating configurations, when they become available.

Comparison with Blade-Element Momentum Methods

The numerical cost of simulations involving the UVLM is still considerably large compared to BEM. Even though studies have demonstrated the shortcomings of BEM, there is a lack of comparison between the accuracy of BEM and UVLM in wind turbine applications. Hence, a comparison between the two methods, in particular the prediction of unsteady aerodynamic loads due to inflow and control surfaces, is needed to justify for the additional computation burden with using the UVLM.

Rotating Aerodynamics

It is observed in Figure 4.7 that rotating aerodynamics have a considerable effect on the dynamical response of the aeroelastic system. The spanwise linearly varying velocity on the blade increases the sphere of influence of dominant modes and also amplifies high frequency responses. Further investigations is hence suggested to understand the cause of rotating aerodynamics on the response of the NREL blade and also determine the detrimental effects that the observed high frequency gains have on fatigue loadings.

6.3.2 Improvements to Control Methodology

Control Objectives

In the numerical simulations, the control objective had been to reduce the blade flapwise RBM, with the assumption that RBM can be measured using strain gauges attached to the root of the blades. However, other measurement feedback can be considered in the objective function. For instance, blade tip deflections or accelerations could be detected using accelerometers attached to the blade tips and then fed back to the controller. In fact, blade flapwise tip deflection feedback was explored in the single rotating blade analysis and was shown to give comparable performances to flapwise RBM feedback.

The adverse torsional load due to flap deflection can be suppressed by including it as a control objective to be minimised. This has been demonstrated for the single rotating blade and can be extended to the full turbine. Apart from torsion, edgewise loads can also be included to access any potential benefits this could deliver, considering that the structural-twist in the

rotor blades brings about a coupling of edgewise and flapwise dofs.

Three similar controllers designed on a single rotating blade is used to control the flaps on the three rotor blades in a decentralised configuration. As such, the overall objective is to reduce the loadings on individual blades without regard to the overall rotor loads as a whole. We could alternatively design the controller to tackle the overall loads on the full rotor through the d-q transformation [42] (Coleman transformation [64]) such that measurement outputs from the three blades are projected onto two orthogonal tilt and yaw axes. These projected measurements are then fed into the controller to minimise the out-of-plane tilt and yaw, for which the control signals are inverse transformed before being fed back to the system. The use of d-q transformation for flap actuation had been shown to deliver slightly better load reductions than a decentralised control system [191].

Actuator Modelling

The control inputs to the turbine are defined as the deflection angles β of the flaps and are assumed to be 100% efficient. This, in general is not the case in actual implementations where one will need to account for flap dynamics, mechanical actuators, friction and resistance in a moving fluid, among others. Hence, it would be beneficial to add a model of the actuator to account for uncertainties in the flap mechanism. Such a model can be obtained through wind tunnel or bench test results.

Refinement to Controller Design

The action of the flap controller is seen to be acting across most frequencies (See Figure 4.27) and when specific frequencies are targeted in Table 4.4, similar load reductions could be obtained with lower actuator duty. This is a indication that the design task undertaken in this study could have been improved through an initial assessment of the fatigue contributions within the loading frequency spectrum, in particular the per-revolution loads. Once the dominant fatigue contributor is identified, all the effort in controller design for subsequent load alleviation investigations can be focused to target this contributor.

Furthermore, the flap and pitch controllers are seen to be acting at frequencies below 0.2Hz (See Figure 4.27 and 4.36), which could be interfering with the turbine full envelope controller (typically 0.16Hz) that is used to maintain the correct operating state as the wind speed varies. It is crucial that this full envelope controller is not affected by the active flap/pitch controls as the objective of the latter is for load reductions without posing obstructions to normal turbine operation or energy production. In addition, the flap and pitch controllers are seen to be acting at frequencies above 0.6Hz (3P), which have minimal contribution to fatigue loadings, yet increasing actuator duty and amplifying noise. Hence, the controller should effectively be designed to only target the 1P and 2P, such as to avoid high frequency signal noise interference and low frequency interference with the turbine full envelope controller.

Other Control Methods

In the design of LQG and $\mathcal{H}_\infty$ controllers, the weights are adjusted such that the bounds on

actuator limits are not exceeded. However, this is not optimal and better performance can be obtained through optimisation-based control methods, such as model predictive control, that allows constraints to be explicitly defined [59]. Through the course of the project, MPC was attempted on the unified aeroelastic description. However, given the large size of the system, even after model reduction, MPC was found to be computationally unaffordable even for small horizons lengths. It was hence not pursued further. Nonetheless, MPC could still potentially be explored if small control models from aggressive reduction of states or sparse spatial discretisation in the UVLM are considered. Inevitably, there will be large amount of uncertainties in these smaller models for which the limits of MPC can be tested.

The time-varying unified aeroelastic system is periodic in nature given the rotor blades return to its original azimuth location after each rotation. The treatment of periodic systems has been considered in a handful of references, which exploit knowledge of periodicity for potential advantage in developing the control algorithm. These methods could be applied to active load alleviation in wind turbines [56, 40, 119], for instance, periodic LQR.

Lidar can also be considered for sensing the incoming velocity wind field for speed and load alleviation control on turbines. This is particularly beneficial to provide a preview of the incoming disturbance to improve performances through feed-forward and model predictive control [50]. It also avoids possible delays in conventional feedback compensation by allowing the controller to act in anticipation of the disturbance [201]. Apart from lidar, sonic detection and ranging (sodar) can also provide preview information through the use of sound waves [138]. However, these methods are affected by environmental conditions such as precipitation and some form of estimation is needed to account for changes in the velocity field between where it is being detected and when it finally encounters the rotor. Other sensors can also be considered to improve the performance of feedback control, such as the use of pitot tubes at the blade leading-edge, fibre wires to give more accurate measurements of the disturbances close to rotor plane. Also, sensor optimization strategies [25] can be adopted to find the best combination of sensor types and location to maximise performance. As it can be seen, there are many challenges in sensor technology and applications that are open for explorations.

Appendix A

Two-dimensional Vortex Particle State-Space Aeroelastic Implementation

The two-dimensional modelling of an aerofoil will be presented in this appendix. The structural model is first described in Section A.1 followed by the vortex particle method in Section A.2. They are then coupled in a unified aeroelastic description in Section A.3 with the numerical verifications presented in Section A.4.

A.1 Two Degrees-of-Freedom Aerofoil

The structural model contains a simple two degrees-of-freedom (2-dof) plunge-pitch aerofoil restrained by a pair of springs as shown in Figure A.1. The spring constants, k_h and k_α, restrains the plunge and pitch motions, respectively. The model has a half chord length of b, with the distance from mid-chord to elastic axis and flap hinge denoted by ab and eb, respectively. Free-stream velocity is denoted by U_∞, pitch angle by α, plunge by h and flap deflection angle by β. The convention taken for h is positive downwards, α is positive nose up about the elastic axis and β is positive flap down about the hinge. Lift L is positive upwards and moment M_α about the elastic axis is positive when the aerofoil pitches nose up.

The dynamic Equations of Motion (EoM) are written in non-dimensional form as

$$\boldsymbol{\mathcal{M}}\ddot{\boldsymbol{q}} + \boldsymbol{\mathcal{K}}\boldsymbol{q} = \boldsymbol{Q}_s\,, \tag{A.1}$$

such that

$$\boldsymbol{\mathcal{M}} = \begin{bmatrix} 1 & x_\alpha \\ x_\alpha & r_\alpha^2 \end{bmatrix},\ \boldsymbol{q} = \begin{bmatrix} \frac{h}{b} \\ \alpha \end{bmatrix},\ \boldsymbol{\mathcal{K}} = \begin{bmatrix} \omega_h^2 & 0 \\ 0 & \omega_\alpha^2 r_\alpha^2 \end{bmatrix},\ \boldsymbol{Q}_s = \begin{bmatrix} -\frac{L}{Mb} \\ \frac{M_\alpha}{Mb^2} \end{bmatrix},$$

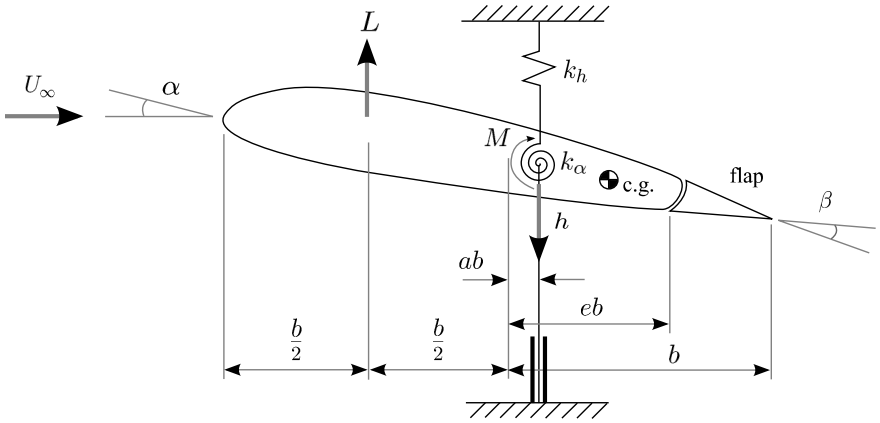


Figure A.1: 2-dof Structural Model.

In the equation, $x_\alpha = \frac{S_\alpha}{Mb}$ is the distance between centre of gravity and elastic axis and $r_\alpha^2 = \frac{I_\alpha}{Mb^2}$ is the aerofoil's radius of gyration (both normalised by b). The terms $\omega_h = \sqrt{\frac{k_h}{M}}$ and $\omega_\alpha = \sqrt{\frac{k_\alpha}{I_\alpha}}$ represent uncoupled natural frequency of plunge and pitch modes, respectively. M is the mass per unit span, S_α is the static moment of aerofoil section about the elastic axis and I_α is the aerofoil moment of inertia per unit span about the elastic axis. $\ddot{h}$ and $\ddot{\alpha}$ are the second derivatives of plunge and pitch, respectively. The flaps are assumed to have a rigid link. Also, their masses are considered to be small and any inertial effects from flap deflections are ignored.

A.2 Unsteady Aerofoil Aerodynamics

The classical method for solving two-dimensional unsteady aerodynamics is provided by Theodorsen [227]. This closed form solution is obtained by considering a two-dimensional flat plate undergoing harmonic motion in an inviscid and incompressible flow with infinite wake [80]

$$C_L = C_{L(nc)} + C_{L(c)} \,. \tag{A.2}$$

The equation contains a non-circulatory part $C_{L(nc)}$ to account for the inertia forces in accelerating an apparent mass of fluid as the aerofoil moves through, and a circulatory part $C_{L(c)}$ to account for circulation around the aerofoil. A physical explanation for the circulatory lift is that aerodynamic forces will need a finite amount of time to develop and reach its final value when subject to perturbations. The unsteady aerodynamics from flap actuation is also provided by Theodorsen [227].

An equivalent solution in the time domain is provided by Wagner [243] through the superposition of indicial responses using the Duhamel integral for the circulatory part of the flow. To account for the unsteady aerodynamics in a sharp edge travelling gust, the time domain solution is given by Küssner [134]. For a detailed description of the above methods, the interested reader may refer to the cited references, or the text by Leishman [146]. To

enable aerofoil thickness, cambered shapes and allow for free or prescribed wake shapes, the time domain vortex particle method is used. This concept is similar to the three-dimensional vortex panel method described in Section 2.2.

The two-dimensional aeroelastic description involving the plunge-pitch aerofoil and the analytical solution of Wagner is well-established and will not be elaborated in this dissertation. The interested reader is referred to Refs. [176, 177, 178, 114, 80, 187], which provide details of the mathematical formulation tailored for numerical implementation. It is however the aeroelastic description involving the plunge-pitch aerofoil and vortex particle method that requires further explanation, in particular the state-space representation.

The two-dimensional vortex particle method can be written in a state-space representation in terms of aerofoil vorticity $\boldsymbol{\Gamma}_a \in \mathbb{R}^{m_a \times 1}$ and wake vorticity $\boldsymbol{\Gamma}_w \in \mathbb{R}^{m_w \times 1}$

$$\begin{bmatrix} \boldsymbol{A}_a & \boldsymbol{A}_w \\ \boldsymbol{A}_{wa} & \boldsymbol{A}_{ww} \end{bmatrix} \begin{Bmatrix} \boldsymbol{\Gamma}_a \\ \boldsymbol{\Gamma}_w \end{Bmatrix}^{n+1} = \begin{bmatrix} \boldsymbol{0} & \boldsymbol{0} \\ \boldsymbol{B}_{wa} & \boldsymbol{B}_{ww} \end{bmatrix} \begin{Bmatrix} \boldsymbol{\Gamma}_a \\ \boldsymbol{\Gamma}_w \end{Bmatrix}^{n} + \begin{Bmatrix} \boldsymbol{w}_a \\ \boldsymbol{0} \end{Bmatrix}^{n+1}, \tag{A.3}$$

where $\boldsymbol{w}_a \in \mathbb{R}^{m_a \times 1}$ is the downwash due to the motion of the aerofoil and incident gust. The total number of vortex particles on the aerofoil and wake are denoted m_a and m_w, respectively. The first row in the above equation imposes the Neumann boundary condition from Eq. (2.17) with $\boldsymbol{A}_a \in \mathbb{R}^{m_a \times m_a}$ and $\boldsymbol{A}_w \in \mathbb{R}^{m_a \times m_w}$. The second row containing $\boldsymbol{A}_{wa} \in \mathbb{R}^{m_w \times m_a}$, $\boldsymbol{A}_{ww} \in \mathbb{R}^{m_w \times m_w}$, $\boldsymbol{B}_{wa} \in \mathbb{R}^{m_w \times m_a}$ and $\boldsymbol{B}_{ww} \in \mathbb{R}^{m_w \times m_w}$ imposes Kelvin's condition from Eq. (2.13).

Rewriting Eq. (A.3)

$$\boldsymbol{\Gamma}^{n+1} = \boldsymbol{A}_1 \boldsymbol{\Gamma}^n + \boldsymbol{A}_2 \boldsymbol{w}^{n+1}, \tag{A.4}$$

where $\boldsymbol{\Gamma} = \begin{Bmatrix} \boldsymbol{\Gamma}_a \\ \boldsymbol{\Gamma}_w \end{Bmatrix}$.

Assuming small angles of attack with grouping of variables, the downwash can be written as

$$\boldsymbol{w}^{n+1} = \boldsymbol{W}_q \boldsymbol{q}^{n+1} + \boldsymbol{W}_\beta \boldsymbol{\beta}^n + \boldsymbol{W}_\delta \boldsymbol{\delta}^n, \tag{A.5}$$

where $\boldsymbol{q} = \begin{bmatrix} h & \alpha & \dot{h} & \dot{\alpha} \end{bmatrix}^\top$, $\boldsymbol{\beta} = \begin{bmatrix} \beta & \dot{\beta} \end{bmatrix}^\top$ and $\boldsymbol{\delta} = \begin{bmatrix} \delta_1 & \cdots & \delta_{m_a} \end{bmatrix}^\top$, such that δ is the induced gust angle. Note that $\boldsymbol{\beta}$ and $\boldsymbol{\delta}$ are written in time-steps n such that the final EoM is in explicit form.

The matrices $\boldsymbol{W}_q \in \mathbb{R}^{m_a \times 4}$, $\boldsymbol{W}_\beta \in \mathbb{R}^{m_a \times 2}$ and $\boldsymbol{W}_\delta \in \mathbb{R}^{m_a \times m_a}$ are expressed as

$$\boldsymbol{W}_{q,kj} = \begin{cases} 0 & \text{if } j = 1, \\ n_{z,k} U_\infty & \text{if } j = 2, \\ n_{z,k} & \text{if } j = 3, \\ n_{z,k} x_{c,k}^{ea} & \text{if } j = 4, \end{cases}$$

$$\boldsymbol{W}_{\beta,kj} = \begin{cases} 0 & \text{if } k < k_f \text{ and } j = 1\,, \\ n_{z,k}U_\infty & \text{if } k \geq k_f \text{ and } j = 1\,, \\ 0 & \text{if } k < k_f \text{ and } j = 2\,, \\ n_{z,k}x^h_{c,k} & \text{if } k \geq k_f \text{ and } j = 2\,, \end{cases}$$

$$\boldsymbol{W}_\delta = diag\left(n_{z,1}U_\infty,\, n_{z,2}U_\infty,\, \ldots,\, n_{z,m_a}U_\infty\right),$$

where $k \in [1 \ldots m_a]$. The normal to the aerofoil surface is given by n_z, the free-stream velocity by U_∞ and the distance between the k^{th} collocation point and the elastic axis by $x^{ea}_{c,k}$. The collocation points covering the trailing-edge flaps starts from k_f to m_a where $k_f \leq m_a$, and $x^h_{c,k}$ is the distance from collocation point k in the flap region to the hinge axis. Note that the plunge h has no bearing on the aerodynamic downwash.

In computing the pressures and loads on the aerofoil, we make use of the two-dimensional unsteady Bernoulli equation [131]. In continuous time, the pressure difference Δp_k across the lower and upper surfaces of the k^{th} vortex particle at distance x from the leading edge is

$$\Delta p_k(t) = \rho\left[U_\infty(t)\Gamma_a(x,t) + \frac{\partial}{\partial t}\int_0^x \Gamma_a(x,t)dx\right], \tag{A.6}$$

where ρ is density of air.

Integrating Eq. (A.6) over the entire aerofoil and writing in discrete-time state-space non-dimensional form, we obtain for the coefficient of lift

$$C_L^{n+1} = \begin{bmatrix} \frac{2}{U^{n+1}c} + \frac{2(c-x_{v,1})}{(U^{n+1})^2 c\Delta t} \\ \frac{2}{U^{n+1}c} + \frac{2(c-x_{v,2})}{(U^{n+1})^2 c\Delta t} \\ \vdots \\ \frac{2}{U^{n+1}c} + \frac{2(c-x_{v,m_a})}{(U^{n+1})^2 c\Delta t} \end{bmatrix}^\top \begin{Bmatrix} \Gamma_{a,1} \\ \Gamma_{a,2} \\ \vdots \\ \Gamma_{a,m_a} \end{Bmatrix}^{n+1} + \begin{bmatrix} \frac{2(-c+x_{v,1})}{(U^{n+1})^2 c\Delta t} \\ \frac{2(-c+x_{v,2})}{(U^{n+1})^2 c\Delta t} \\ \vdots \\ \frac{2(-c+x_{v,m_a})}{(U^{n+1})^2 c\Delta t} \end{bmatrix}^\top \begin{Bmatrix} \Gamma_{a,1} \\ \Gamma_{a,2} \\ \vdots \\ \Gamma_{a,m_a} \end{Bmatrix}^{n}. \tag{A.7}$$

A similar expression can be obtained for the coefficient of moment about the elastic axis

$$C_M^{n+1} = -\begin{bmatrix} \frac{2(x_{v,1}-x_{ea})}{U^{n+1}c^2} + \frac{2}{(U^{n+1})^2 c^2\Delta t}\Pi_1 \\ \frac{2(x_{v,2}-x_{ea})}{U^{n+1}c^2} + \frac{2}{(U^{n+1})^2 c^2\Delta t}\Pi_2 \\ \vdots \\ \frac{2(x_{v,m_a}-x_{ea})}{U^{n+1}c^2} + \frac{2}{(U^{n+1})^2 c^2\Delta t}\Pi_{m_a} \end{bmatrix}^\top \begin{Bmatrix} \Gamma_{a,1} \\ \Gamma_{a,2} \\ \vdots \\ \Gamma_{a,m_a} \end{Bmatrix}^{n+1} + \begin{bmatrix} \frac{2}{(U^{n+1})^2 c^2\Delta t}\Pi_1 \\ \frac{2}{(U^{n+1})^2 c^2\Delta t}\Pi_2 \\ \vdots \\ \frac{2}{(U^{n+1})^2 c^2\Delta t}\Pi_{m_a} \end{bmatrix}^\top \begin{Bmatrix} \Gamma_{a,1} \\ \Gamma_{a,2} \\ \vdots \\ \Gamma_{a,m_a} \end{Bmatrix}^{n}, \tag{A.8}$$

where $\Pi_k = \left(\frac{c^2}{2} - c\,x_{ea}\right) - \left(\frac{x_{v,k}^2}{2} - x_{v,k}\,x_{ea}\right)$ and $k \in [1 \ldots m_a]$. x_v and x_{ea} are the locations of the vortex point and elastic axis from the leading edge, respectively.

Combining the equations for lift and moment about the elastic axis, we obtain

$$\boldsymbol{Q}_a^{n+1} = \boldsymbol{F}_1\boldsymbol{\Gamma}^{n+1} + \boldsymbol{F}_2\boldsymbol{\Gamma}^n\,, \tag{A.9}$$

where $\boldsymbol{Q}_a^{n+1} = \begin{bmatrix} C_L^{n+1} \\ C_M^{n+1} \end{bmatrix}$ and $\boldsymbol{\Gamma} = \begin{Bmatrix} \boldsymbol{\Gamma}_a \\ \boldsymbol{\Gamma}_w \end{Bmatrix}$. Both $\boldsymbol{F}_1$ and $\boldsymbol{F}_2$ contains additional columns of zeros corresponding to the wake vortex particles.

To have an understanding of load distribution along the aerofoil resulting from AoA changes and flap deflection, the normalised pressure distribution across the aerofoil is shown in Figure A.2. A pitch of 1° is found to deliver the same integrated aerodynamic force acting on the aerofoil (area under plot) as 2.6° of flap deflection. The flap occupies 10% chord. It is also evident that with pitch, pressure is concentrated towards the leading edge, while for flaps, pressure peaks are distributed between the leading edge and flap hinge.

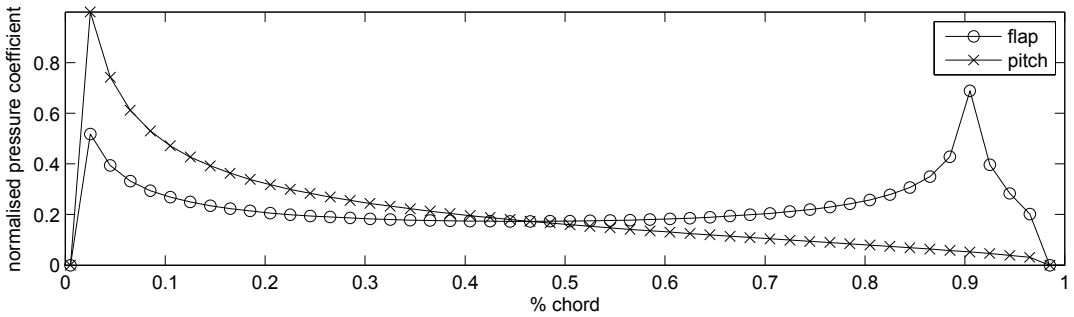


Figure A.2: Normalised pressure distribution across aerofoil in pitch and flap actuation, both delivering the same amount of aerodynamic lift force (Using 50 equally distributed vortex particles on the aerofoil and keeping a wake of 5 chord lengths).

A.3 Fluid-Structure Coupling

In order to couple the discrete vortex particle model to the structural model, Eq. (A.1) is discretised using the backward Euler method [87] to give

$$\boldsymbol{Q}_s^{n+1} = \boldsymbol{N}_1 \boldsymbol{q}^{n+1} + \boldsymbol{N}_2 \boldsymbol{q}^n \,, \tag{A.10}$$

where $\boldsymbol{N}_1 \in \mathbb{R}^{4\times4}$ and $\boldsymbol{N}_2 \in \mathbb{R}^{4\times4}$ are matrices from the discretised structural model.

Equating Eq. (A.9) to (A.10), we obtain

$$\boldsymbol{T}\boldsymbol{Q}_a^{n+1} = \boldsymbol{Q}_s^{n+1}$$

$$-\boldsymbol{T}\boldsymbol{F}_1\boldsymbol{\Gamma}^{n+1} + \boldsymbol{N}_1\boldsymbol{q}^{n+1} = \boldsymbol{T}\boldsymbol{F}_2\boldsymbol{\Gamma}^n - \boldsymbol{N}_2\boldsymbol{q}^n \,, \tag{A.11}$$

where $\boldsymbol{T}$ is a transformation matrix to account for difference in size and dimensions, given by

$$\boldsymbol{T} = \begin{bmatrix} -\frac{\rho U_\infty^2}{M} & 0 \\ 0 & \frac{2\rho U_\infty^2}{M} \\ 0 & 0 \\ 0 & 0 \end{bmatrix}, \tag{A.12}$$

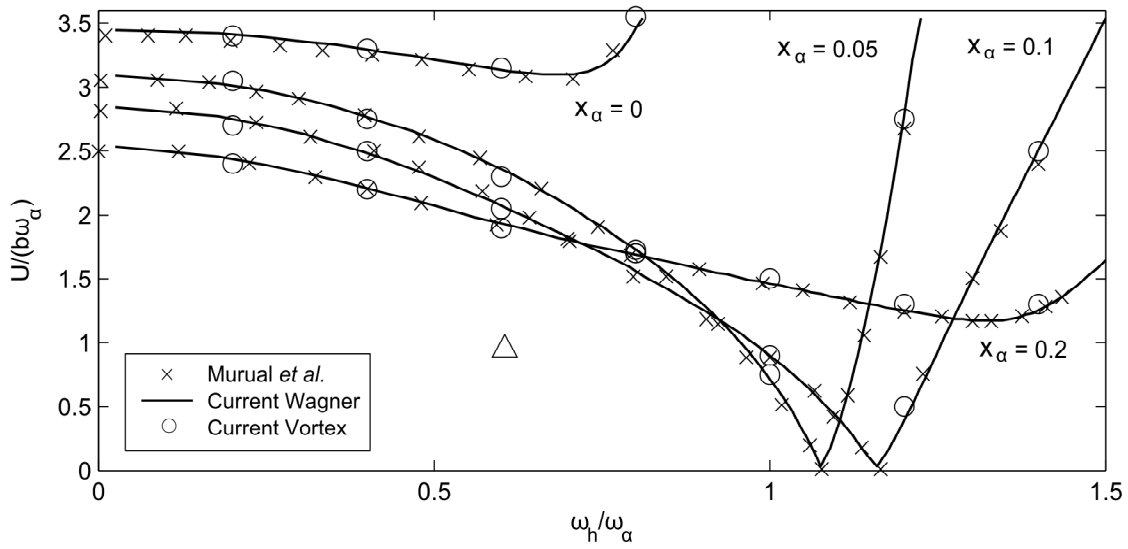


Figure A.3: Flutter boundaries of 2-dof aerofoil. Verifying current Wagner and vortex aeroelastic descriptions with Murua et al. [169]. ($a = -0.3$, $\kappa = \frac{\pi\rho b^2}{M} = 0.05$, $r_\alpha^2 = 0.25$, $b = 1.0$)

where M is the mass.

Consolidating Eqs. (A.3), (A.5), (A.11) and expressing in matrix form, we obtain

$$\begin{bmatrix} \boldsymbol{I} & -\boldsymbol{A}_2\boldsymbol{W}_q \\ -\boldsymbol{T}\boldsymbol{F}_1 & \boldsymbol{N}_1 \end{bmatrix} \begin{Bmatrix} \boldsymbol{\Gamma} \\ \boldsymbol{q} \end{Bmatrix}^{n+1} = \begin{bmatrix} \boldsymbol{A}_1 & \boldsymbol{0} \\ \boldsymbol{T}\boldsymbol{F}_2 & -\boldsymbol{N}_2 \end{bmatrix} \begin{Bmatrix} \boldsymbol{\Gamma} \\ \boldsymbol{q} \end{Bmatrix}^{n} + \begin{bmatrix} \boldsymbol{A}_2\boldsymbol{W}_\beta \\ \boldsymbol{0} \end{bmatrix} \boldsymbol{\beta}^n + \begin{bmatrix} \boldsymbol{A}_2\boldsymbol{W}_\delta \\ \boldsymbol{0} \end{bmatrix} \boldsymbol{\delta}^n. \tag{A.13}$$

Finally, by introducing a new state variable $\boldsymbol{x} = \begin{bmatrix} \boldsymbol{\Gamma}^\top & \boldsymbol{q}^\top \end{bmatrix}^\top$, the above is written as

$$\boldsymbol{x}^{n+1} = \boldsymbol{A}\boldsymbol{x}^n + \boldsymbol{B}\boldsymbol{\beta}^n + \boldsymbol{G}\boldsymbol{\delta}^n \,. \tag{A.14}$$

giving us the state equation defining the coupled aeroelastic description of the sectional model.

A.4 Sectional Model Numerical Verification

The aeroelastic model presented in previous sections of this appendix is verified against Murua et al. [169] for flutter speeds shown in Figure A.3. Also included in the flutter plot is a Wagner aeroelastic model developed using Wagner's indicial step response for the unsteady aerodynamics and coupled with the same structural model. In general, there is good agreement for all the three models considered. Similar results were also reported by Refs. [254, 29]. Note that a parametric study on the unsteady aerodynamics indicated that convergence on the unsteady aerodynamics was achieved using 50 equally distributed vortex particles on the aerofoil and keeping a wake of 5 chord lengths.

Appendix B

Three-dimensional Vortex-Panel State-Space Aeroelastic Implementation

The linearised description of the UVLM in Section 2.2.4 is further elaborated in this Appendix. Details of the state-space formulation (Section B.1), downwash computation (Section B.2), pressure calculations (Section B.3), rotor assembly (Section B.4) and coupling (Section B.5) are presented to facilitate any reader who wishes to adopt a numerical implementation of the described model.

B.1 System Matrices

The influence coefficients, $\boldsymbol{A}_b$ and $\boldsymbol{A}_w$ in Eq. (2.14), give the induced normal velocity to lifting surface (blade) at collocation points due to both the blade's bound and wake vortices, respectively (resolved using the Biot-Savart law in Eq. (2.17)). The shedding of the wake vortices requires further explanation, in particular, to be concatenated in the state matrix of the UVLM.

As the blade moves through the fluid, a row of wake vortex rings are formed, shed and convected downstream. From Kelvin's theorem in Eq. (2.13), the circulation strength of this row of wake vortex rings is equal to the circulation of the respective trailing-edge vortex rings in the previous time-step, written as

$$(\Gamma_w)^{n+1}_{m_c+1,j} = (\Gamma_b)^{n}_{m_c,j} \ , \tag{B.1}$$

where $(\Gamma_w)_{m_c+1,j}$ represents the wake vortex ring shed from the trailing-edge at each time instance and $(\Gamma_b)_{m_c,j}$ represents the vortex ring on the trailing-edge of the lifting surface. The subscript (i,j) are the indices of the bound chordwise and spanwise panels, $i \in [1 \dots m_c]$

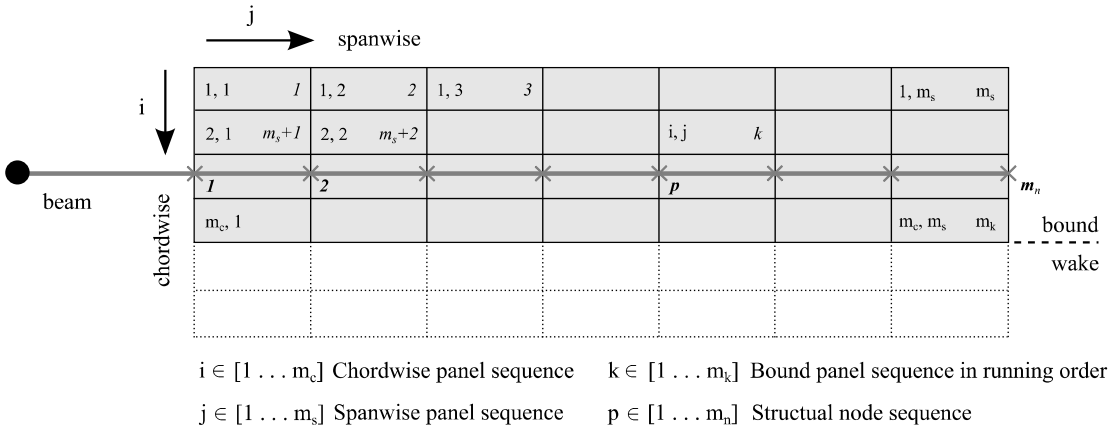


Figure B.1: Simplified model definition of panel distribution.

and $j \in [1 \dots m_s]$. See Figure B.1. Note that $m_k = m_c \times m_s$.

Once shed, the wake vortex rings are convected downstream such that their circulation strengths remains the same

$$(\Gamma_w)^{n+2}_{m_c+2,j} = (\Gamma_w)^{n+1}_{m_c+1,j} \ . \tag{B.2}$$

The cornerpoint locations of the wake vortex rings are determined by the free-stream velocity and the downwash induced by all other vortex rings. This introduces non-linearity as the location of the wake has to be re-computed at each time-step. As discussed in Section 2.2.4, a helicoidal wake is prescribed to arrive at a linear UVLM description.

The influence coefficients in Eq. (2.14), and wake shedding in Eqs. (B.1) and (B.2) can be combined into a state-space expression in terms of bound and wake circulation strengths

$$\begin{bmatrix} \boldsymbol{A}_b & \boldsymbol{A}_w \\ \boldsymbol{A}_{wb} & \boldsymbol{A}_{ww} \end{bmatrix} \begin{Bmatrix} \boldsymbol{\Gamma}_b \\ \boldsymbol{\Gamma}_w \end{Bmatrix}^{n+1} = \begin{bmatrix} \boldsymbol{0} & \boldsymbol{0} \\ \boldsymbol{B}_{wb} & \boldsymbol{B}_{ww} \end{bmatrix} \begin{Bmatrix} \boldsymbol{\Gamma}_a \\ \boldsymbol{\Gamma}_w \end{Bmatrix}^{n} + \begin{Bmatrix} \boldsymbol{w} \\ \boldsymbol{0} \end{Bmatrix}^{n+1} , \tag{B.3}$$

where $\boldsymbol{A}_b \in \mathbb{R}^{m_k \times m_k}$, $\boldsymbol{A}_w \in \mathbb{R}^{m_k \times m_w}$. The total number of the blade's bound and wake vortex rings are denoted m_k and m_w, respectively. $\boldsymbol{\Gamma}_b \in \mathbb{R}^{m_k \times 1}$ and $\boldsymbol{\Gamma}_w \in \mathbb{R}^{m_w \times 1}$ are vectors containing the bound and wake circulation strengths, respectively. The second row of Eq. (B.3) accounts for the wake convection from Eqs. (B.1) and (B.2).

B.2 Downwash Computation

The last term $\boldsymbol{w}$ in Eq. (B.3) is the downwash at collocation points due to the elastic dof, rigid-body dof, actuators and external disturbances. It is defined in Eqs. (2.18) to (2.20) as

$$\boldsymbol{w}^{n+1} = \begin{bmatrix} \boldsymbol{T}_{\Delta\eta_r} & \boldsymbol{T}_{\Delta\dot{\eta}_r} \end{bmatrix} \begin{Bmatrix} \Delta\boldsymbol{\eta}_r \\ \Delta\dot{\boldsymbol{\eta}}_r \end{Bmatrix}^{n+1} + \boldsymbol{T}_{\Delta\dot{\eta}_t}(t) {\Delta\dot{\boldsymbol{\eta}}_t}^{n+1} + \boldsymbol{w}^n_\beta + \boldsymbol{w}^n_\delta \, . \tag{B.4}$$

The first term in Eq. (B.4) superimposes the structural displacements/rotations and their first time derivatives at the beam nodes, onto the panel collocation points as downwash (expressed in the aerodynamic grid frame b in Figure 2.3).

Referring to Figure 2.4, the finite element discretisation of the beam is such that it coincides with the spanwise aerodynamic grid to facilitate mapping. This allows the dof at beam nodes to be projected onto adjacent spanwise distributed aerodynamic grids. Both $\boldsymbol{T}_{\Delta\eta_r}$ and $\boldsymbol{T}_{\Delta\dot{\eta}_r}$ are of size $\mathbb{R}^{m_k\times 6m_n}$, where $k\in[1\dots m_k]$ denote the collocation points in running sequence and $p\in[1\dots m_n]$ is the sequence of beam nodes that lie on the aerodynamic gird, with each node defined by its $6\times$ dof (see Figure B.1). Note that $k=(i-1)m_s+j$ and the axis of rotation of the beam is assumed to lie outside the aerodynamic grid for proper shedding of wake in the rotating aerodynamic grid. This avoids singularities in the UVLM close to the axis of rotation. The first node is assumed to start where it first coincides with the edge of the aerodynamic grid and $m_n=m_s+1$. Note that $\boldsymbol{w}_\beta$ and $\boldsymbol{w}_\delta$ are written in time-steps n such that the final EoM is in explicit form.

In general, both $\boldsymbol{T}_{\Delta\eta_r}$ and $\boldsymbol{T}_{\Delta\dot{\eta}_r}$ are sparse and populated with block entries corresponding to

$$(\boldsymbol{T}_{\Delta\eta_r})_{k,m}=(\boldsymbol{T}_{\Delta\dot{\eta}_r})_{k,m}=\begin{cases}\boldsymbol{\chi}_{k,m}, & \text{if } \mathrm{mod}(k-1,m_s)+1=m\,,\\ \boldsymbol{\chi}_{k,m}, & \text{if } \mathrm{mod}(k-1,m_s)+1=m-1\,,\\ \boldsymbol{0}_{1\times 6}, & \text{elsewhere}\,,\end{cases} \tag{B.5}$$

where m_s is the total number of spanwise aerodynamic panels and $\mathrm{mod}(\bullet)$ is the modulus after division.

For $\boldsymbol{T}_{\Delta\eta_r}$:

$$\boldsymbol{\chi}_{k,m}=\left(\frac{1}{2}\right)Q_{\infty,k}\begin{bmatrix}0 & 0 & 0 & n_z & 0 & 0\end{bmatrix}_k\,,$$

and for $\boldsymbol{T}_{\Delta\dot{\eta}_r}$

$$\boldsymbol{\chi}_{k,m}=\left(\frac{1}{2}\right)\begin{bmatrix}0 & \tau_{i,z} & -n_z & x_c^{ea}n_z & 0 & 0\end{bmatrix}_k\,,$$

where $Q_{\infty,k}=U_\infty+\Omega\, y_{c,k}$ is the resultant velocity at the k^{th} collocation point due to both free-stream and also rotation of the lifting surface, and $y_{c,k}$ is the radial distance of the k^{th} collocation point to axis of rotation. The vectors $\boldsymbol{\tau}_{i,k}=\begin{bmatrix}\tau_{i,x} & \tau_{i,y} & \tau_{i,z}\end{bmatrix}_k$ and $\boldsymbol{n}_k=\begin{bmatrix}n_x & n_y & n_z\end{bmatrix}_k$ are the tangent in chordwise direction and normal to the panel surface containing the k^{th} collocation point, defined in the b frame in Figure 2.3. The chordwise distance between elastic axis and the k^{th} collocation point is denoted $x_{c,k}^{ea}$.

If there are structural nodes defined outside the aerodynamic grid, additional columns of zeros will be included in matrices $\boldsymbol{T}_{\Delta\eta_r}$ and $\boldsymbol{T}_{\Delta\dot{\eta}_r}$ to account for the nodes that do not generate any corresponding downwash on collocation points. This is typically the case at the root of the blades, where the aerodynamics of the inner section are not modelled. For each node that falls outside the aerodynamic grid, six columns of zeros are added in front of the

transformation matrices.

The transformation $\boldsymbol{T}_{\Delta\dot{\eta}_t}(t) \in \mathbb{R}^{m_k \times 6m_t}$ in Eq. (B.4) extracts the relevant tower top velocities and rotations (expressed in global frame A of Figure 2.2) as additional downwash on the rotor blades in the constrained multi-body definition of the turbine containing the rotor and tower. m_t is the total number of tower elements. The influence of the tower top motion on the downwash are dependent on the azimuth location of the blades with respect to the tower at each time-step. Note that only the last six columns of $\boldsymbol{T}_{\Delta\dot{\eta}_t}(t)$ are populated and given by

$$\boldsymbol{T}_{\Delta\dot{\eta}_t}(t) = \begin{bmatrix} \cdots & \boldsymbol{T}_{\Delta\dot{\eta}_t,x}(t) & \boldsymbol{T}_{\Delta\dot{\eta}_t,y}(t) & \boldsymbol{T}_{\Delta\dot{\eta}_t,z} & \boldsymbol{T}_{\Delta\dot{\eta}_t,\theta_x}(t) & \boldsymbol{T}_{\Delta\dot{\eta}_t,\theta_y}(t) & \boldsymbol{T}_{\Delta\dot{\eta}_t,\theta_z} \end{bmatrix}, \tag{B.6}$$

where

$$\boldsymbol{T}_{\Delta\dot{\eta}_t,x}(t) = -\begin{bmatrix} (\tau_{i,z})_1 \sin(\theta(t)+\Theta) \\ \vdots \\ (\tau_{i,z})_k \sin(\theta(t)+\Theta) \end{bmatrix}_{m_k\times 1}, \quad \boldsymbol{T}_{\Delta\dot{\eta}_t,y}(t) = -\begin{bmatrix} (\tau_{i,z})_1 \cos(\theta(t)+\Theta) \\ \vdots \\ (\tau_{i,z})_k \cos(\theta(t)+\Theta) \end{bmatrix}_{m_k\times 1},$$

$$\boldsymbol{T}_{\Delta\dot{\eta}_t,z} = \begin{bmatrix} n_{z,1} \\ \vdots \\ n_{z,k} \end{bmatrix}_{m_k\times 1}, \quad \boldsymbol{T}_{\Delta\dot{\eta}_t,\theta_x}(t) = -\begin{bmatrix} n_{z,1}\, y_{c,1} \sin(\theta(t)+\Theta) \\ \vdots \\ n_{z,k}\, y_{c,k} \sin(\theta(t)+\Theta) \end{bmatrix}_{m_k\times 1},$$

$$\boldsymbol{T}_{\Delta\dot{\eta}_t,\theta_y}(t) = -\begin{bmatrix} n_{z,1}\, y_{c,1} \cos(\theta(t)+\Theta) \\ \vdots \\ n_{z,k}\, y_{c,k} \cos(\theta(t)+\Theta) \end{bmatrix}_{m_k\times 1}, \quad \boldsymbol{T}_{\Delta\dot{\eta}_t,\theta_z} = \begin{bmatrix} (\tau_{i,z})_1\, y_{c,1} \\ \vdots \\ (\tau_{i,z})_k\, y_{c,k} \end{bmatrix}_{m_k\times 1}.$$

The azimuth location of the stationary blade with respect to the vertical is given by Θ. For a three-bladed rotor in park configuration (one blade vertically down), Θ = -60°, +60°, +180°. The column vectors appears only in the last six columns of $\boldsymbol{T}_{\Delta\dot{\eta}_t}$ to map tower top axial, side-side, fore-aft, yaw, pitch and roll motions as downwash on the rotor. The tower-top fore-aft and roll motions $\boldsymbol{T}_{\Delta\dot{\eta}_t,z}$ and $\boldsymbol{T}_{\Delta\dot{\eta}_t,\theta_z}$ are assumed to be time independent as they are about the axis perpendicular to the rotor plane.

Additional in-plane motion due to shaft flexibility, expressed in the local shaft frame, can be included

$$\boldsymbol{T}_{\Delta\dot{\eta}_s} = \begin{bmatrix} \cdots & \mathbf{0} & \mathbf{0} & \mathbf{0} & \boldsymbol{T}_{\Delta\dot{\eta}_s,4} & \mathbf{0} & \mathbf{0} \end{bmatrix}_{m_k\times 6m_h}, \tag{B.7}$$

where m_h is the number of shaft elements and $\boldsymbol{T}_{\Delta\dot{\eta}_s,4}$ maps the torsional dof of the shaft as downwash on the rotor. It has the same form as $\boldsymbol{T}_{\Delta\dot{\eta}_t,\theta_z}$. The shaft is assumed to be stiff in all the other dofs.

The downwash due to gust $\boldsymbol{w}_\delta$ in Eq. (B.4) has its elements defined as

$$w_{\delta,k} = \mathbf{n}_k \cdot \begin{bmatrix} Q_{\infty,k} \cos\delta_k \\ 0 \\ Q_{\infty,k} \sin\delta_k \end{bmatrix}, \tag{B.8}$$

where δ_k is the additional angle of attack due to disturbance in the wind field (gust). The downwash due to flaps $\boldsymbol{w}_\beta$ has its elements defined as

$$w_{\beta,k} = \begin{cases} w_{flap} & \text{if } k = k_f, \\ 0 & otherwise, \end{cases} \tag{B.9}$$

where

$$w_{flap} = \mathbf{n}_k \cdot \begin{bmatrix} Q_{\infty,k} \cos\beta_k \\ 0 \\ Q_{\infty,k} \sin\beta_k + x^h_{c,k}\dot{\beta}_k \end{bmatrix}. \tag{B.10}$$

The flap deflection angle β_k defines the additional downwash imposed on panels in the flap region (positive for flap deflection downwards). The subscript k_f contain the indices of panels covering the flaps, and $x^h_{c,k}$ is the chordwise distance from the flap collocation point to the hinge location.

Assuming small angles of attack such that $\sin(\theta) = \theta$ and $\cos(\theta) = 1$ where θ is small

$$w_{\delta,k} = n_{x,k}Q_{\infty,k} + n_{z,k}Q_{\infty,k}\delta_k\,,$$

$$w_{\beta,k} = \begin{cases} n_{x,k}Q_{\infty,k} + n_{z,k}Q_{\infty,k}\beta_k + n_{z,k}x^h_{c,k}\dot{\beta}_k & \text{if } k = k_f, \\ 0 & otherwise. \end{cases}$$

Further assuming that the camber in the blade is small such that n_x is negligible, the downwash due to gust can be assembled as

$$\boldsymbol{w}_\delta = \mathbf{W}_\delta \boldsymbol{\delta}\,, \tag{B.11}$$

where $\boldsymbol{W}_\delta \in \mathbb{R}^{m_k \times m_k}$ is a diagonal matrix with entries corresponding to $n_{z,k}Q_{\infty,k}$ and $\boldsymbol{\delta} \in \mathbb{R}^{m_k \times 1}$ is a vector containing the downwash on individual panels due to gust.

The downwash due to flaps can be assembled as

$$\boldsymbol{w}_\beta = \boldsymbol{W}_\beta \boldsymbol{\beta} + \boldsymbol{W}_{\dot{\beta}}\dot{\boldsymbol{\beta}}\,, \tag{B.12}$$

where $\boldsymbol{W}_{\beta} \in \mathbb{R}^{m_k \times m_k}$ and $\boldsymbol{W}_{\dot{\beta}} \in \mathbb{R}^{m_k \times m_k}$ are diagonal matrices with entries

$$W_{\beta,k} = \begin{cases} n_{z,k} Q_{\infty,k} & \text{if } k = k_f\,, \\ 0 & \text{otherwise}\,, \end{cases}$$

$$W_{\dot{\beta},k} = \begin{cases} n_{z,k} x^h_{c,k} & \text{if } k = k_f\,, \\ 0 & \text{otherwise}\,, \end{cases}$$

and both $\boldsymbol{\beta} \in \mathbb{R}^{m_k \times 1}$ and $\dot{\boldsymbol{\beta}} \in \mathbb{R}^{m_k \times 1}$ are column vectors containing the flap deflection angles and rates in the corresponding k_f entries. The description allows for multiple flaps of any dimension provided they coincide with the size of the panels representing them.

B.3 Pressure Distribution

The aerodynamic loads are obtained from the pressure distribution using the unsteady Bernoulli equation

$$\begin{aligned} \Delta p_k^{n+1} = &\left(\frac{\rho \hat{\boldsymbol{v}}_k \cdot \boldsymbol{\tau}_{i,k}}{\Delta c_k} + \frac{\rho}{\Delta t} + \frac{\rho \hat{\boldsymbol{v}}_k \cdot \boldsymbol{\tau}_{j,k}}{\Delta b_k} \right) (\Gamma_b)^{n+1}_{i,j} + \left(-\frac{\rho \hat{\boldsymbol{v}}_k \cdot \boldsymbol{\tau}_{i,k}}{\Delta c_k} \right) (\Gamma_b)^{n+1}_{i-1,j} \\ &+ \left(-\frac{\rho \hat{\boldsymbol{v}}_k \cdot \boldsymbol{\tau}_{j,k}}{\Delta b_k} \right) (\Gamma_b)^{n+1}_{i,j-1} + \left(-\frac{\rho}{\Delta t} \right) (\Gamma_b)^{n}_{i,j}\,, \end{aligned} \tag{B.13}$$

where Δc_k and Δb_k are the chordwise and spanwise lengths of the vortex panel belonging to the k^{th} collocation point (see Figure 2.3). $\boldsymbol{\tau}_{i,k}$ and $\boldsymbol{\tau}_{j,k}$ are the tangential vectors in the i and j directions at the k^{th} collocation point, respectively. $(\Gamma_b)_{i,j}$ is the circulation of the (i,j) vortex ring on the lifting surface that shares the same panel as the k^{th} collocation point.

Eq. (B.13) can be expressed as

$$\Delta p_k^{n+1} = \Phi^{n+1}_{1,k} (\Gamma_b)^{n+1}_{i,j} + \Phi^{n+1}_{2,k} (\Gamma_b)^{n+1}_{i-1,j} + \Phi^{n+1}_{3,k} (\Gamma_b)^{n+1}_{i,j-1} + \Phi^{n}_{4,k} (\Gamma_b)^{n}_{i,j}\,, \tag{B.14}$$

and for panels along the leading edge

$$\Delta p_k^{n+1} = \Phi^{n+1}_{1,k} (\Gamma_b)^{n+1}_{i,j} + \Phi^{n+1}_{3,k} (\Gamma_b)^{n+1}_{i,j-1} + \Phi^{n}_{4,k} (\Gamma_b)^{n}_{i,j}\,, \tag{B.15}$$

The pressure distribution from Eqs. (B.14) and (B.15) can be assembled into a vector $\Delta \boldsymbol{P} \in \mathbb{R}^{m_k \times 1}$, given by

$$\Delta \boldsymbol{P}^{n+1} = \boldsymbol{\Phi}^{n+1}_a \boldsymbol{\Gamma}^{n+1} + \boldsymbol{\Phi}^{n}_b \boldsymbol{\Gamma}^{n}, \tag{B.16}$$

where $\boldsymbol{\Gamma} = \begin{Bmatrix} \boldsymbol{\Gamma}_b \\ \boldsymbol{\Gamma}_w \end{Bmatrix}$. The terms $\boldsymbol{\Phi}_a \in \mathbb{R}^{m_k \times (m_k + m_w)}$ and $\boldsymbol{\Phi}_b \in \mathbb{R}^{m_k \times (m_k + m_w)}$ contains the coefficients of $\boldsymbol{\Gamma}_b$ and rows of zeros to account for $\boldsymbol{\Gamma}_w$.

Assuming no side-slip, the lift acting on the centre of the vortex rings' leading segment can be computed using

$$\boldsymbol{L}^{n+1} = \boldsymbol{n}_\infty \Delta \boldsymbol{S} \Delta \boldsymbol{P}^{n+1}, \tag{B.17}$$

where

$$\boldsymbol{n}_\infty = diag\left(\cos\alpha_1,\, \cos\alpha_2,\, \ldots,\, \cos\alpha_{m_k}\right),$$

$$\Delta \boldsymbol{S} = diag\left(\Delta c_1\, \Delta b_1,\, \Delta c_2\, \Delta b_2,\, \ldots,\, \Delta c_{m_k}\, \Delta b_{m_k}\right).$$

Note that α_k is the angle of attack between each panel and the free-stream, and $\Delta \boldsymbol{S} \in \mathbb{R}^{m_k \times m_k}$ contains the area of each panel along its diagonal.

B.3.1 Drag

The induced drag is parallel to the free-stream velocity and can be expressed as [131, 213]

$$\begin{aligned} D_k^{n+1} = &\left(\rho(w_{ind} + w_w)_k \Delta b_k + \frac{\rho}{\Delta t}\Delta b_k \Delta c_k \sin\alpha_k\right)(\Gamma_b)_{i,j}^{n+1} \\ &+ \left(-\rho(w_{ind} + w_w)_k \Delta b_k\right)(\Gamma_b)_{i-1,j}^{n+1} \\ &+ \left(-\frac{\rho}{\Delta t}\Delta b_k \Delta c_k \sin\alpha_k\right)(\Gamma_b)_{i,j}^{n}, \end{aligned} \tag{B.18}$$

where w_{ind} and w_w are the downwash induced by the streamwise vortex lines on the lifting surface and the wake, respectively. These terms are computed using the Biot-Savart law.

Eq. (B.18) can be expressed as

$$D_k^{n+1} = \Upsilon_{1,k}^{n+1}\Gamma_{i,j}^{n+1} + \Upsilon_{2,k}^{n+1}\Gamma_{i-1,j}^{n+1} + \Upsilon_{3,k}^{n}\Gamma_{i,j}^{n}, \tag{B.19}$$

and for panels along the leading edge

$$D_k^{n+1} = \Upsilon_{1,k}^{n+1}\Gamma_{i,j}^{n+1} + \Upsilon_{3,k}^{n}\Gamma_{i,j}^{n}. \tag{B.20}$$

The induced drag in Eqs. (B.19) and (B.20) can be assembled into a vector $\boldsymbol{D} \in \mathbb{R}^{m_k \times 1}$, given by

$$\boldsymbol{D}^{n+1} = \tilde{\boldsymbol{\Upsilon}}_a^{n+1}\tilde{\boldsymbol{\Gamma}}^{n+1} + \tilde{\boldsymbol{\Upsilon}}_b^{n}\tilde{\boldsymbol{\Gamma}}^{n}. \tag{B.21}$$

The terms $\boldsymbol{\Upsilon}_a \in \mathbb{R}^{m_k \times (m_k + m_w)}$ and $\boldsymbol{\Upsilon}_b \in \mathbb{R}^{m_k \times (m_k + m_w)}$ contains the coefficients of $\boldsymbol{\Gamma}_b$ and rows of zeros to account for $\boldsymbol{\Gamma}_w$.

B.3.2 Forces and Moments

The forces in the aerodynamics frame b can be resolved from lift and drag forces using simple geometry

$$\begin{aligned} \boldsymbol{F}_z^{n+1} &= \boldsymbol{s}_\alpha \boldsymbol{D}^{n+1} + \boldsymbol{c}_\alpha \boldsymbol{L}^{n+1}, \\ \boldsymbol{F}_x^{n+1} &= \boldsymbol{c}_\alpha \boldsymbol{D}^{n+1} - \boldsymbol{s}_\alpha \boldsymbol{L}^{n+1}, \end{aligned} \tag{B.22}$$

where

$$\boldsymbol{s}_\alpha = diag\left(\sin\alpha_1,\, \sin\alpha_2,\, \ldots,\, \sin\alpha_{m_k}\right),$$

$$\boldsymbol{s}_\alpha = diag\left(\cos\alpha_1,\, \cos\alpha_2,\, \ldots,\, \cos\alpha_{m_k}\right),$$

The moments about any point with directional vector $\boldsymbol{r}_k = \begin{bmatrix} r_{x,k} & r_{y,k} & r_{z,k} \end{bmatrix}^\top$ to the centre of the k^{th} vortex ring's leading segment can be resolved using

$$\begin{bmatrix} M_{x,k} \\ M_{y,k} \\ M_{z,k} \end{bmatrix}^{n+1} = \begin{bmatrix} r_{x,k} \\ r_{y,k} \\ r_{z,k} \end{bmatrix}^{n+1} \times \begin{bmatrix} F_{x,k} \\ F_{y,k} \\ F_{z,k} \end{bmatrix}^{n+1} , = \begin{bmatrix} r_{y,k}F_{z,k} - r_{z,k}F_{y,k} \\ -r_{x,k}F_{z,k} + r_{z,k}F_{x,k} \\ r_{x,k}F_{y,k} - r_{y,k}F_{x,k} \end{bmatrix}^{n+1} , \tag{B.23}$$

and for the moments about each axis, it can be assembled into vectors $\boldsymbol{M}_x \in \mathbb{R}^{m_k \times 1}$, $\boldsymbol{M}_y \in \mathbb{R}^{m_k \times 1}$ and $\boldsymbol{M}_z \in \mathbb{R}^{m_k \times 1}$, given by

$$\begin{aligned} \boldsymbol{M}_x^{n+1} &= \boldsymbol{r}_y \boldsymbol{F}_z^{n+1} - \boldsymbol{r}_z \boldsymbol{F}_y^{n+1}, \\ \boldsymbol{M}_y^{n+1} &= -\boldsymbol{r}_x \boldsymbol{F}_z^{n+1} + \boldsymbol{r}_z \boldsymbol{F}_x^{n+1}, \\ \boldsymbol{M}_z^{n+1} &= \boldsymbol{r}_x \boldsymbol{F}_y^{n+1} - \boldsymbol{r}_y \boldsymbol{F}_x^{n+1}, \end{aligned} \tag{B.24}$$

where

$$\boldsymbol{r}_x = diag\left(r_{x,1},\, r_{x,2},\, \ldots,\, r_{x,m_k}\right),$$

$$\boldsymbol{r}_y = diag\left(r_{y,1},\, r_{y,2},\, \ldots,\, r_{y,m_k}\right),$$

$$\boldsymbol{r}_z = diag\left(r_{z,1},\, r_{z,2},\, \ldots,\, r_{z,m_k}\right).$$

B.4 Multiple Lifting Surfaces in Full Rotor Configuration

For each blade in the three-bladed rotor, the influence coefficients in Eq. (2.14) include downwash contributions from the bound and wake vortex rings of other lifting surfaces. Including the shedding and convection of wake vortex rings in the state matrix and following the state-space structure of Eq. (B.3), we arrive at Eq. (2.21), and as an illustration, the

augmented form is

$$
\begin{aligned}
&\begin{bmatrix}
\boldsymbol{A}_{b,11} & \boldsymbol{A}_{w,11} & \boldsymbol{A}_{b,12} & \boldsymbol{A}_{w,12} & \boldsymbol{A}_{b,13} & \boldsymbol{A}_{w,13} \\
\boldsymbol{0} & \boldsymbol{I} & \boldsymbol{0} & \boldsymbol{0} & \boldsymbol{0} & \boldsymbol{0} \\
\boldsymbol{A}_{b,21} & \boldsymbol{A}_{w,21} & \boldsymbol{A}_{b,22} & \boldsymbol{A}_{w,22} & \boldsymbol{A}_{b,23} & \boldsymbol{A}_{w,23} \\
\boldsymbol{0} & \boldsymbol{0} & \boldsymbol{0} & \boldsymbol{I} & \boldsymbol{0} & \boldsymbol{0} \\
\boldsymbol{A}_{b,31} & \boldsymbol{A}_{w,31} & \boldsymbol{A}_{b,32} & \boldsymbol{A}_{w,32} & \boldsymbol{A}_{b,33} & \boldsymbol{A}_{w,33} \\
\boldsymbol{0} & \boldsymbol{0} & \boldsymbol{0} & \boldsymbol{0} & \boldsymbol{0} & \boldsymbol{I}
\end{bmatrix}
\begin{Bmatrix}
\boldsymbol{\Gamma}_{b,1} \\ \boldsymbol{\Gamma}_{w,1} \\ \boldsymbol{\Gamma}_{b,2} \\ \boldsymbol{\Gamma}_{w,2} \\ \boldsymbol{\Gamma}_{b,3} \\ \boldsymbol{\Gamma}_{w,3}
\end{Bmatrix}^{n+1} \\
&= \begin{bmatrix}
\boldsymbol{0} & \boldsymbol{0} & \boldsymbol{0} & \boldsymbol{0} & \boldsymbol{0} & \boldsymbol{0} \\
\boldsymbol{A}_{wb} & \boldsymbol{A}_{ww} & \boldsymbol{0} & \boldsymbol{0} & \boldsymbol{0} & \boldsymbol{0} \\
\boldsymbol{0} & \boldsymbol{0} & \boldsymbol{0} & \boldsymbol{0} & \boldsymbol{0} & \boldsymbol{0} \\
\boldsymbol{0} & \boldsymbol{0} & \boldsymbol{A}_{wb} & \boldsymbol{A}_{ww} & \boldsymbol{0} & \boldsymbol{0} \\
\boldsymbol{0} & \boldsymbol{0} & \boldsymbol{0} & \boldsymbol{0} & \boldsymbol{0} & \boldsymbol{0} \\
\boldsymbol{0} & \boldsymbol{0} & \boldsymbol{0} & \boldsymbol{0} & \boldsymbol{A}_{wb} & \boldsymbol{A}_{ww}
\end{bmatrix}
\begin{Bmatrix}
\boldsymbol{\Gamma}_{b,1} \\ \boldsymbol{\Gamma}_{w,1} \\ \boldsymbol{\Gamma}_{b,2} \\ \boldsymbol{\Gamma}_{w,2} \\ \boldsymbol{\Gamma}_{b,3} \\ \boldsymbol{\Gamma}_{w,3}
\end{Bmatrix}^{n}
+ \begin{bmatrix}
\boldsymbol{0} & \boldsymbol{T}_{\Delta\dot{\eta}_{t,1}}(t) & \boldsymbol{T}_{\Delta\eta_{sr,1}} & \boldsymbol{T}_{\Delta\dot{\eta}_{sr,1}} \\
\boldsymbol{0} & \boldsymbol{0} & \boldsymbol{0} & \boldsymbol{0} \\
\boldsymbol{0} & \boldsymbol{T}_{\Delta\dot{\eta}_{t,2}}(t) & \boldsymbol{T}_{\Delta\eta_{sr,2}} & \boldsymbol{T}_{\Delta\dot{\eta}_{sr,2}} \\
\boldsymbol{0} & \boldsymbol{0} & \boldsymbol{0} & \boldsymbol{0} \\
\boldsymbol{0} & \boldsymbol{T}_{\Delta\dot{\eta}_{t,3}}(t) & \boldsymbol{T}_{\Delta\eta_{sr,3}} & \boldsymbol{T}_{\Delta\dot{\eta}_{sr,3}} \\
\boldsymbol{0} & \boldsymbol{0} & \boldsymbol{0} & \boldsymbol{0}
\end{bmatrix}
\begin{Bmatrix}
\Delta\boldsymbol{\eta}_t \\ \Delta\dot{\boldsymbol{\eta}}_t \\ \Delta\boldsymbol{\eta}_r \\ \Delta\dot{\boldsymbol{\eta}}_r
\end{Bmatrix}^{n+1} \\
&+ \begin{bmatrix}
\boldsymbol{W}_\beta & \boldsymbol{W}_{\dot{\beta}} & \boldsymbol{0} & \boldsymbol{0} & \boldsymbol{0} & \boldsymbol{0} \\
\boldsymbol{0} & \boldsymbol{0} & \boldsymbol{0} & \boldsymbol{0} & \boldsymbol{0} & \boldsymbol{0} \\
\boldsymbol{0} & \boldsymbol{0} & \boldsymbol{W}_\beta & \boldsymbol{W}_{\dot{\beta}} & \boldsymbol{0} & \boldsymbol{0} \\
\boldsymbol{0} & \boldsymbol{0} & \boldsymbol{0} & \boldsymbol{0} & \boldsymbol{0} & \boldsymbol{0} \\
\boldsymbol{0} & \boldsymbol{0} & \boldsymbol{0} & \boldsymbol{0} & \boldsymbol{W}_\beta & \boldsymbol{W}_{\dot{\beta}} \\
\boldsymbol{0} & \boldsymbol{0} & \boldsymbol{0} & \boldsymbol{0} & \boldsymbol{0} & \boldsymbol{0}
\end{bmatrix}
\begin{Bmatrix}
\boldsymbol{\beta}_1 \\ \dot{\boldsymbol{\beta}}_1 \\ \boldsymbol{\beta}_2 \\ \dot{\boldsymbol{\beta}}_2 \\ \boldsymbol{\beta}_3 \\ \dot{\boldsymbol{\beta}}_3
\end{Bmatrix}^{n}
+ \begin{bmatrix}
\boldsymbol{W}_\delta & \boldsymbol{0} & \boldsymbol{0} \\
\boldsymbol{0} & \boldsymbol{0} & \boldsymbol{0} \\
\boldsymbol{0} & \boldsymbol{W}_\delta & \boldsymbol{0} \\
\boldsymbol{0} & \boldsymbol{0} & \boldsymbol{0} \\
\boldsymbol{0} & \boldsymbol{0} & \boldsymbol{W}_\delta \\
\boldsymbol{0} & \boldsymbol{0} & \boldsymbol{0}
\end{bmatrix}
\begin{Bmatrix}
\boldsymbol{\delta}_1 \\ \boldsymbol{\delta}_2 \\ \boldsymbol{\delta}_3
\end{Bmatrix}^{n},
\end{aligned}
\tag{B.25}
$$

where $\Delta\boldsymbol{\eta}_r^\top = \begin{Bmatrix} \Delta\boldsymbol{\eta}_s^\top & \Delta\boldsymbol{\eta}_{b,1}^\top & \Delta\boldsymbol{\eta}_{b,2}^\top & \Delta\boldsymbol{\eta}_{b,3}^\top \end{Bmatrix} \in \mathbb{R}^{(6m_s+3(6m_n))\times 1}$ are the combined elastic dof of the shaft and rotor blades, and $\Delta\boldsymbol{\eta}_t \in \mathbb{R}^{6m_t\times 1}$ contains the tower elastic dof.

The transformation matrices for the rotor contain

$$
\begin{aligned}
\boldsymbol{T}_{\Delta\eta_{sr,1}} &= \begin{bmatrix} \boldsymbol{0} & \boldsymbol{T}_{\Delta\eta_r} & \boldsymbol{0} & \boldsymbol{0} \end{bmatrix}, \\
\boldsymbol{T}_{\Delta\eta_{sr,2}} &= \begin{bmatrix} \boldsymbol{0} & \boldsymbol{0} & \boldsymbol{T}_{\Delta\eta_r} & \boldsymbol{0} \end{bmatrix}, \\
\boldsymbol{T}_{\Delta\eta_{sr,3}} &= \begin{bmatrix} \boldsymbol{0} & \boldsymbol{0} & \boldsymbol{0} & \boldsymbol{T}_{\Delta\eta_r} \end{bmatrix}, \\
\boldsymbol{T}_{\Delta\dot{\eta}_{sr,1}} &= \begin{bmatrix} \boldsymbol{T}_{\Delta\dot{\eta}_s} & \boldsymbol{T}_{\Delta\dot{\eta}_r} & \boldsymbol{0} & \boldsymbol{0} \end{bmatrix}, \\
\boldsymbol{T}_{\Delta\dot{\eta}_{sr,2}} &= \begin{bmatrix} \boldsymbol{T}_{\Delta\dot{\eta}_s} & \boldsymbol{0} & \boldsymbol{T}_{\Delta\dot{\eta}_r} & \boldsymbol{0} \end{bmatrix}, \\
\boldsymbol{T}_{\Delta\dot{\eta}_{sr,3}} &= \begin{bmatrix} \boldsymbol{T}_{\Delta\dot{\eta}_s} & \boldsymbol{0} & \boldsymbol{0} & \boldsymbol{T}_{\Delta\dot{\eta}_r} \end{bmatrix},
\end{aligned}
\tag{B.26}
$$

for which the entries are from Eqs. (B.5) and (B.7). These transformations are defined in the local blade frame and hence independent of the azimuth location.

The transformation matrices for the tower motion $\boldsymbol{T}_{\Delta\dot{\eta}_{t,i}}(t) : i \in [1,2,3]$ is the same as $\boldsymbol{T}_{\Delta\dot{\eta}_t}(t)$ in Eq. (B.6), with Θ = -60°, +60°, +180° to account for the equal distribution of the blades around the rotor. The last two terms in Eq. (B.25) account for the downwash from flap deflection and gust in Eqs. (B.12) and (B.11), respectively.

If the blades are identical and equally spaced on the rotor

$$\begin{aligned}
\boldsymbol{A}_{b,11} &= \boldsymbol{A}_{b,22} = \boldsymbol{A}_{b,33}\,, \\
\boldsymbol{A}_{w,11} &= \boldsymbol{A}_{w,22} = \boldsymbol{A}_{w,33}\,, \\
\boldsymbol{A}_{b,12} &= \boldsymbol{A}_{b,23} = \boldsymbol{A}_{b,31}\,, \\
\boldsymbol{A}_{w,12} &= \boldsymbol{A}_{w,23} = \boldsymbol{A}_{w,31}\,, \\
\boldsymbol{A}_{b,13} &= \boldsymbol{A}_{b,21} = \boldsymbol{A}_{b,32}\,, \\
\boldsymbol{A}_{w,13} &= \boldsymbol{A}_{w,21} = \boldsymbol{A}_{w,32}\,.
\end{aligned} \tag{B.27}$$

Eq. (B.25) can be expressed symbolically as

$$\boldsymbol{A}_1\boldsymbol{\Gamma}^{n+1} = \boldsymbol{A}_2\boldsymbol{\Gamma}^{n} + \boldsymbol{T}(t)\boldsymbol{q}^{n+1} + \boldsymbol{W}^{n}\,, \tag{B.28}$$

in which $\boldsymbol{W}$ contains both the downwash due to flaps and gust.

B.5 State-Space Coupling

The fluid-structure coupling involves the mapping of downwash and forces between the structural beam model and UVLM. The continuous-time structural EoM is first discretised using the Newmark-β scheme (Section B.5.1) with the same time-step as the discrete-time UVLM. With the finite-element discretisation of the beam coinciding with the spanwise aerodynamic grid, the mapping of structural dof as downwash on the collocation points is performed through the transformation matrices in Eq. (B.26). The mapping of forces will involve the assembly of aerodynamic forces and moments about the structural nodes (Sections B.5.2 and B.5.3).

B.5.1 Discretisation of Structural Dynamics

The Newmark-β method is commonly used in structural dynamics as a numerical integration tool to solve differential equations. It is a one-step method specialised to second-order systems and can be obtained from the first-order Taylor expansion of displacements and velocities [86]. With the intention to retain the state-space structure of the linearised structural dynamics in Eq. (2.6) after discretisation, and considering a standard form of $\boldsymbol{M}\Delta\ddot{\boldsymbol{q}}+\boldsymbol{C}\Delta\dot{\boldsymbol{q}}+\boldsymbol{K}\Delta\boldsymbol{q}=\hat{\boldsymbol{Q}}_s$, the Newmark-$\beta$ scheme in this work is assembled as

$$\begin{bmatrix} \boldsymbol{0} & \boldsymbol{0} & \boldsymbol{S}_1 \\ \boldsymbol{0} & -\boldsymbol{I} & \Delta t\hat{\phi} \\ -\boldsymbol{I} & \boldsymbol{0} & \Delta t^2\beta \end{bmatrix} \begin{bmatrix} \Delta\boldsymbol{q} \\ \Delta\dot{\boldsymbol{q}} \\ \Delta\ddot{\boldsymbol{q}} \end{bmatrix}^{n+1} + \begin{bmatrix} \boldsymbol{K} & \boldsymbol{C}+\boldsymbol{K}\Delta t & \boldsymbol{S}_2 \\ \boldsymbol{0} & \boldsymbol{I} & (1-\hat{\phi})\Delta t \\ \boldsymbol{I} & \Delta t & \left(\frac{1}{2}-\beta\right)\Delta t^2 \end{bmatrix} \begin{bmatrix} \Delta\boldsymbol{q} \\ \Delta\dot{\boldsymbol{q}} \\ \Delta\ddot{\boldsymbol{q}} \end{bmatrix}^{n} = \begin{bmatrix} \hat{\boldsymbol{Q}}_s^{n+1} \\ \boldsymbol{0} \\ \boldsymbol{0} \end{bmatrix}, \tag{B.29}$$

where $\boldsymbol{S}_1 = \boldsymbol{M} + \hat{\phi}\Delta t\boldsymbol{C} + \Delta t^2\beta\boldsymbol{K}$ and $\boldsymbol{S}_2 = \boldsymbol{C}(1-\hat{\phi})\Delta t + \boldsymbol{K}\Delta t^2\left(\frac{1}{2}-\beta\right)$. For ease of representation in subsequent analysis, we express Eq. (B.29) as

$$\boldsymbol{N}_1\Delta\boldsymbol{s}^{n+1} + \boldsymbol{N}_2\Delta\boldsymbol{s}^n = \boldsymbol{Q}_s^{n+1}\,, \tag{B.30}$$

with $\Delta\boldsymbol{s} = \begin{bmatrix}\Delta\boldsymbol{q} & \Delta\dot{\boldsymbol{q}} & \Delta\ddot{\boldsymbol{q}}\end{bmatrix}^\top$ and $\boldsymbol{Q}_s = \begin{bmatrix}\hat{\boldsymbol{Q}}_s^{n+1} & \boldsymbol{0} & \boldsymbol{0}\end{bmatrix}^\top$.

The parameters β and $\hat{\phi}$ associated with the quadrature scheme are suggested as $\beta = \frac{1}{4}$ and $\hat{\phi} = \frac{1}{2}$ which leads to an unconditionally stable integration operator of maximum accuracy. Numerical damping can also be introduced through a third parameter α [87]:

$$\hat{\phi} = \frac{1}{2} + \alpha\,, \quad \beta = \frac{1}{4}\left(\hat{\phi} + \frac{1}{2}\right)^2\,,$$

with $\alpha > 0$.

B.5.2 Aerodynamic Force Mapping

The aerodynamic forces and moments resolved at the centre of each vortex ring's leading segment is mapped equally between the closest adjacent spanwise nodes as shown in Figure 2.4. The aerodynamic forces and moments about each node in Eqs. (B.22) and (B.24) is first sorted and assembled into a column vector

$$\boldsymbol{F}_a = \begin{Bmatrix}\boldsymbol{F}_{a,1}\\ \vdots \\ \boldsymbol{F}_{a,m_k}\,,\end{Bmatrix}, \tag{B.31}$$

where $\boldsymbol{F}_a \in \mathbb{R}^{6m_k}$ with entries $\boldsymbol{F}_{a,k} = \begin{bmatrix}F_{y,k} & -F_{x,k} & F_{z,k} & M_{y,k} & -M_{x,k} & M_{z,k}\end{bmatrix}^\top$ with $k \in [1 \ldots m_k]$. The assembly sorts the forces and moments by their respective panels, and accounts for the different definitions of body fixed frames in the aerodynamic grid b and structural beam S in Figures 2.3 and 2.4, respectively.

Next, a transformation matrix $\boldsymbol{T}_F \in \mathbb{R}^{6m_n \times 6m_k}$ is used to map the forces and moments onto the structural nodes such that

$$\boldsymbol{Q}_a = \begin{Bmatrix}\boldsymbol{T}_F\boldsymbol{F}_a\\ [\boldsymbol{0}]_{6m_n\times 1}\\ [\boldsymbol{0}]_{6m_n\times 1}\end{Bmatrix}\,, \tag{B.32}$$

where

$$T_{F,ij} = \begin{cases}\frac{1}{2} & \text{if } \mathrm{mod}(j-1, 6m_s)+1 = i \;\&\; i < 6m_s+1\,,\\ \frac{1}{2} & \text{if } \mathrm{mod}(j-1, 6m_s)+1 = i-6 \;\&\; i > m_n\,,\\ 0 & \text{otherwise}\,,\end{cases}$$

for $i \in [1 \dots 6m_n]$ and $j \in [1 \dots 6m_k]$.

B.5.3 Fluid Structure Coupling

The equations for the UVLM in Eq. (B.28), structural forces in Eq. (B.30) and aerodynamic forces in Eq. (B.32) can be consolidated to arrive at the coupled EoM

$$\begin{bmatrix} \boldsymbol{A}_1 & -\boldsymbol{T}(t) \\ -\boldsymbol{\Psi}_1 & \boldsymbol{N}_1(t) \end{bmatrix} \begin{Bmatrix} \boldsymbol{\Gamma} \\ \boldsymbol{q} \end{Bmatrix}^{n+1} = \begin{bmatrix} \boldsymbol{A}_2 & \boldsymbol{0} \\ \boldsymbol{\Psi}_2 & -\boldsymbol{N}_2(t) \end{bmatrix} \begin{Bmatrix} \boldsymbol{\Gamma} \\ \boldsymbol{q} \end{Bmatrix}^{n} + \begin{Bmatrix} \boldsymbol{W} \\ \boldsymbol{0} \end{Bmatrix}^{n} . \tag{2.28}$$

Appendix C

Analytical Solution to Rotating Beam

The analytical solution to a rotating beam in pure bending and pure torsion are presented in this appendix, which had been used to verify the gyroscopic implementation in the structural EoM. The key components of deformations are the out-of-plane bending (Section C.1), in-plane bending (Section C.2) and torsion (Section C.3).

C.1 Out-of-plane Bending

The distinguishing factor between a rotating beam from a conventional beam is the presence of a spanwise varying tension field. The starting point to describe the EoM is to consider an infinitesimal spanwise element. For the out-of-plane bending

$$m\ddot{z}(r,t) + \left(EI_z z''(r,t)\right)'' - \Omega^2 \left(z'(r,t) \int_r^R mrdr\right)' = f_z(r,t)\,, \tag{C.1}$$

where m is the mass per unit segment, E is the elastic modulus and I_z is the second moment of area. $(\dot{\bullet})$ represents the derivative with respect to time, and $(\bullet)'$ is the derivative with respect to spanwise location of the element r. The distributed force (per unit segment) acting on the element is represented on the right-hand-side by f_z. The derivation is left out and the interested reader is referred to Refs. [37, 51].

Using Galerkin's method, the solution to Eq. (C.1) is assumed to be

$$z(r,t) = \sum_{j=1}^{\infty} \phi_{z,j}(r) q_{z,j}(t)\,, \tag{C.2}$$

where $\phi_{z,j}(r)$ is the j^{th} out-of-plane natural mode shape and $q_{z,j}(t)$ is the j^{th} generalised out-of-plane co-ordinate.

Substituting Eq. (C.2) into (C.1) and pre-multiplying by mode shape $\phi_{z,i}(r)$, we integrate over the entire beam to obtain

$$\boldsymbol{M}\ddot{\boldsymbol{q}}_z + \left[\boldsymbol{K}_S + \Omega^2 \boldsymbol{K}_{CF}\right] \boldsymbol{q}_z = \boldsymbol{F}_z \,, \tag{C.3}$$

where

$$\begin{aligned}
M_{i,j} &= \int_0^R m\phi_{z,i}(r)\phi_{z,j}(r)dr \,, \\
K_{S,i,j} &= \int_0^R EI_z\phi''_{z,i}(r)\phi''_{z,j}(r)dr \,, \\
K_{CF,i,j} &= \int_0^R \left(\phi'_{z,i}(r)\phi'_{z,j}(r)\int_{r_1}^R mr\,dr\right)dr \,, \\
F_{z,i} &= \int_0^R \phi_{z,i}(r)f_z(r,t)dr \,,
\end{aligned}$$

such that i and j represents the index of element on the i^{th} row and j^{th} column in the matrices, respectively. Using the property of orthogonality where

$$\int_0^R \phi_{z,i}(r)\phi_{z,j}(r)dr_1 \begin{cases} = 0 & \text{if } i \neq j \,, \\ \neq 0 & \text{if } i = j \,, \end{cases}$$

the matrices $\boldsymbol{M}$ and $\boldsymbol{K}_S$ are diagonal. However, $\boldsymbol{K}_{CF}$ will not be diagonal as it is multiplied with an integral term.

In general, for rotating beams, the modes shapes ϕ_z are weak functions of rotor speed. Hence, the quantities, $\boldsymbol{M}$, $\boldsymbol{K}_s$ and $\boldsymbol{K}_{CF}$ are also weak function of rotor speed but can be approximated as constants. For free vibration, we set $\boldsymbol{F}_z = 0$ in Eq. (C.3) and assuming harmonic motion $\boldsymbol{q}_z = \boldsymbol{q}_{z,0}e^{i\omega_z t}$, we obtain

$$\boldsymbol{\omega}_z^2 = \left[\frac{\boldsymbol{K}_{S,j}}{\boldsymbol{M}} + \Omega^2\frac{\boldsymbol{K}_{CF}}{\boldsymbol{M}}\right] = \boldsymbol{\omega}_{z,NR}^2 + \Omega^2\boldsymbol{K}_z \,, \tag{C.4}$$

where Ω is rotational speed of the rotor, $\boldsymbol{\omega}_z$ and $\boldsymbol{\omega}_{z,NR}$ are vectors containing the frequencies of the different modes for rotating and non-rotating blades, respectively. $\boldsymbol{K}_z$ is to account for centrifugal stiffening, also known as the rise factor or Southwell coefficient. It is a measure of how fast the frequency of the modes increases with rotor speed. In general, the rise factor is not constant and varies with rotational speed. However, the effect of the rotational speed on mode shapes is minimal and hence the rise factor can be considered a constant, taken at zero rotational speed [37]. The reader is also referred to Refs. [74, 192] for effects of rotor speed on Southwell coefficient and its approximations.

C.2 In-plane Bending

For in-plane bending, an additional term $\Omega^2 my$ is included in Eq. (C.1) to account for the contribution of centrifugal force in the direction of in-plane deformation. The element bending equation for in-plane motion is hence

$$m\ddot{y}(r,t) + \left(EI_y y''(r,t)\right)'' - \Omega^2 \left(y'(r,t)\int_r^R mrdr\right)' - \Omega^2 my(r,t) = f_y(r,t)\,. \tag{C.5}$$

Following the method used in out-of-plane bending motion, we arrive at

$$\hat{\boldsymbol{M}}\ddot{\boldsymbol{q}}_y + \left[\hat{\boldsymbol{K}}_S + \Omega^2\hat{\boldsymbol{K}}_{CF}\right]\boldsymbol{q}_y = \boldsymbol{F}_y\,, \tag{C.6}$$

where

$$\begin{aligned}
\hat{M}_{i,j} &= \int_0^R m\phi_{y,i}(r)\phi_{y,j}(r)dr\,,\\
\hat{K}_{S,i,j} &= \int_0^R EI_y\phi''_{y,i}(r)\phi''_{y,j}(r)dr\,,\\
\hat{K}_{CF,i,j} &= \int_0^R \left(\phi'_{y,i}(r)\phi'_{y,j}(r)\int_{r_1}^R mr\,dr\right)dr - \int_0^R m\phi_{y,i}(r)\phi_{y,j}(r)dr\,,\\
F_{y,i} &= \int_0^R \phi_{y,i}(r)f_y(r,t)dr\,,
\end{aligned}$$

such that $\phi_y(r)$ is the in-plane natural mode shape and $q_y(t)$ is the generalised in-plane co-ordinate. For free vibration, we set $\boldsymbol{F}_y = 0$ in Eq. (C.6) and assuming harmonic motion $\boldsymbol{q}_y = \boldsymbol{q}_{y,0}e^{i\omega_y t}$, we obtain

$$\boldsymbol{\omega}_y^2 = \left[\frac{\hat{\boldsymbol{K}}_S}{\hat{\boldsymbol{M}}} + \Omega^2\frac{\hat{\boldsymbol{K}}_{CF}}{\hat{\boldsymbol{M}}}\right] = \boldsymbol{\omega}_{y,NR}^2 + \Omega^2\boldsymbol{K}_y\,, \tag{C.7}$$

where Ω is rotational speed of the rotor, $\boldsymbol{\omega}_y$ and $\boldsymbol{\omega}_{y,NR}$ are vectors containing the frequencies of the different modes for rotating and non-rotating blade, respectively. $\boldsymbol{K}_y$ is to account for centrifugal stiffening and $\boldsymbol{K}_y = \boldsymbol{K}_z - \boldsymbol{I}$.

C.3 Torsion

Consider a blade segment under pure torsion (uncoupled from bending) by assuming the elastic axis to be a straight line and coincides with the shear axis. The EoM can be written as

$$-\left(GJ\theta'(r,t)\right)' + \rho I_p\ddot{\theta}(r,t) + \rho I_p\Omega^2\theta(r,t) = f_\theta(r,t)\,, \tag{C.8}$$

where ρ is the density and I_p is the polar area moment of inertia per unit length about elastic axis. The term $\rho\bar{I}_p\Omega^2\theta$ is present due to feathering (pitching) motion during rotation of the blade. It is caused by additional moment resulting from a component of the centrifugal force acting on the leading and trailing-edges of the blade. G is the modulus of rigidity (shear modulus) and J is the torsion stiffness. Making use of the Galerkin's projection in previous bending cases, we obtain

$$\tilde{\boldsymbol{M}}\ddot{\boldsymbol{q}}_\theta + \left[\tilde{\boldsymbol{K}}_S + \Omega^2\tilde{\boldsymbol{K}}_{CF}\right]\boldsymbol{q}_\theta = \boldsymbol{F}_\theta\,, \tag{C.9}$$

where

$$\begin{aligned}
\tilde{M}_{i,j} &= \int_0^R \rho I_p \phi_{\theta,i}(r)\phi_{\theta,j}(r)dr\,,\\
\tilde{K}_{S,i,j} &= -\int_0^R GJ\phi'_{\theta,i}(r)\phi'_{\theta,j}(r)dr\,,\\
\tilde{K}_{CF,i,j} &= \int_0^R \rho I_p \phi_{\theta,i}(r)\phi_{\theta,j}(r)dr\,,\\
F_{\theta,i} &= \int_0^R \phi_{\theta,i}(r) f_\theta(r,t)dr\,,
\end{aligned}$$

such that $\phi_\theta(r)$ is the in-plane natural mode shape and $q_\theta(t)$ is the generalised in-plane co-ordinate. For free vibration, we set $\boldsymbol{F}_\theta = 0$ in Eq. (C.8) and assuming harmonic motion $\boldsymbol{q}_\theta = \boldsymbol{q}_{\theta,0}e^{i\omega_\theta t}$, we obtain

$$\boldsymbol{\omega}_\theta^2 = \left[\frac{\tilde{\boldsymbol{K}}_S}{\tilde{\boldsymbol{M}}} + \Omega^2\frac{\tilde{\boldsymbol{K}}_{CF}}{\tilde{\boldsymbol{M}}}\right] = \boldsymbol{\omega}_{\theta,NR}^2 + \Omega^2\boldsymbol{K}_\theta\,. \tag{C.10}$$

where Ω is rotational speed of the rotor, $\boldsymbol{\omega}_\theta$ and $\boldsymbol{\omega}_{\theta,NR}$ are vectors containing the frequencies of the different modes for rotating and non-rotating blades, respectively. $\boldsymbol{K}_\theta = \boldsymbol{I}$ is the rise factor to account for centrifugal stiffening.

Appendix D

Damage Equivalent Loads

Fatigue is a major driver for the structural design of wind turbines to maintain structural integrity. In Ref. [130], fatigue is quantified by the rms value of flapwise, edgewise and torsional velocities. A more common approach to compare two or more fatigue load spectrum in wind turbines is the use of an equivalent load range [60, 248, 5, 136]. It analyses fatigue due to fluctuating loads that are broken down into local extremes in the time domain and is a technique outlined in Annex G of IEC 61400-1 Edition 3 [117]. This commonly involves a rainflow counting algorithm [10] on loads and for an assumed Stress-Number of cycles to failure (S-N) curve (also known as Wöhler curve) or Moment-Number of cycles to failure (M-N) curve, Palmgren-Miner's linear damage rule is applied to determine the damage. Following which, the Damage Equivalent Loads (DEL) can be computed.

Rainflow counting is a method for the counting of fatigue cycles in a given time-series and is commonly used in wind turbine fatigue analysis. It is among a variety of counting methods such as peak counting, simple range counting, level crossing counting, etc. [10]. The method computes the number of cycles and sorts them (into bins) by their amplitudes and means, for which cumulative damage theories such as the Palmgren-Miner's rule can be applied to assess the fatigue life of a structure. The rainflow counting algorithm is widely documented and will not be elaborated. The interested reader is referred to Refs. [10, 73].

Using the binned amplitudes, means and number of cycles from the rainflow counting algorithm, the equivalent load cycle is computed. To begin, a Moment-Number of cycles to failure (M-N) curve is assumed [79] (Figure D.1) with the relationship defined as

$$M_a = M_u N^{-\frac{1}{m}}, \tag{D.1}$$

where M_a is the amplitude moment in one load cycle, M_u is the ultimate moment of the blade, N is the number of cycles to failure and m is the slope of the M-N curve. A range of M_u can be defined and is expressed in terms of M_{max}, which is the maximum moments observed in the spectrum. This can range from the more extreme case of $M_u = 1.5M_{max}$ to a conservative value of $M_u = 4.5M_{max}$. The slope m is determined by the material properties

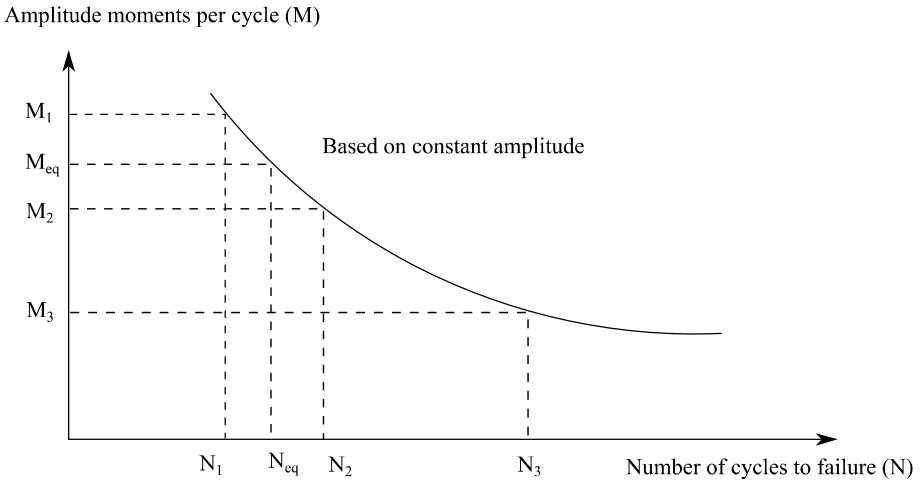


Figure D.1: M-N curve (Note that if plotted on log-log scale, this will be a straight line).

and is chosen to be between 6 and 12. For steel and composites (carbon fibre), m is often taken to be 4 and 10, respectively [42]. For fibreglass, it is assumed that $m = 12$ [60].

Most available fatigue calculation methods are based on constant amplitude loads. However, in an actual loading spectrum, the load amplitudes are not constant and the Palmgren-Miner rule (linear damage rule) is employed. According to the Palmgren-Miner rule, the damage fraction D_i at any load level is linearly proportional to the ratio between the number of cycles of operation n_i and the total number of cycles to failure N_i at the i^{th} amplitude load level. This is given by

$$D_i = \frac{n_i}{N_i}\,. \tag{D.2}$$

Normally the number of cycles of operation n_i is computed for a specific duration depending on the simulation, T_{sim}. For wind turbine applications where the operating life is for 20 to 25 years, this value can be extrapolated using a simple relationship

$$n_i = n_{i,sim}\frac{T_{20}}{T_{sim}}\,, \tag{D.3}$$

where $n_{i,sim}$ is the number of cycles counted in the simulation time and n_i is now the number of cycles in the operation lifetime of the wind turbine [95]. Note however, that if ratios between DEL are to be taken, it will be independent of this extrapolation.

For k number of load amplitudes in a spectrum, failure will occur if

$$\sum_{i=1}^{k} D_i \geq 1.0\,, \tag{D.4}$$

and in other words, total damage can be defined as

$$D = \sum_{i=1}^{k} \frac{n_i}{N_i}\,, \tag{D.5}$$

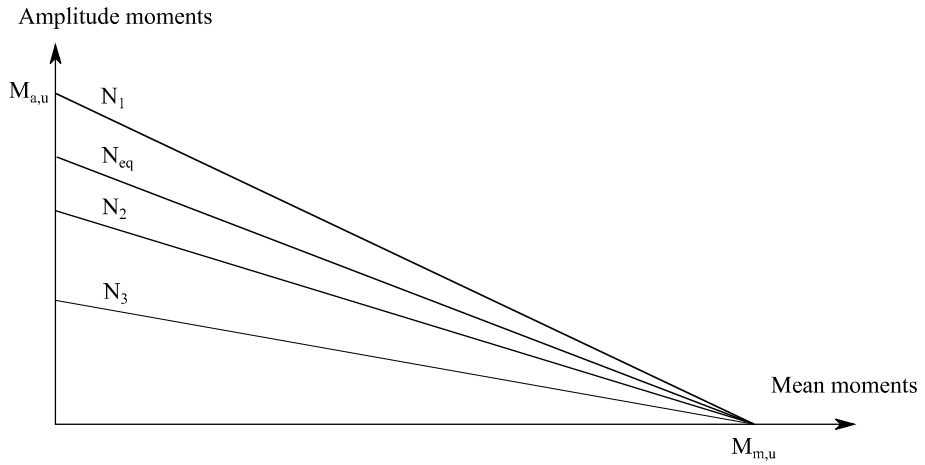


Figure D.2: Goodman relationship.

and failure occurs when $D \geq 1.0$. From the description, it is clear that the Palmgren-Miner rule employs some assumption, which could also be seen as its limitations. The main assumptions are that cycles of the same amplitude causes the same damage, regardless of when they occur. Also, damage caused by individual cycles are assumed to be independent of one another, and all cycles follow the same damage relationships.

A load spectrum will not only have cycles of different amplitudes, the mean values of the cycles will also be different and not necessarily zero. Hence, a method is proposed [105, 79] to extrapolate the equivalent damages using a Goodman relationship, which is used to quantify the interaction between the mean and alternating load amplitude on the fatigue life of a material. The Goodman relationship, as shown in Figure D.2, is for a specified number of cycles to failure and assumes a linear decrease in the alternating load amplitudes with increasing mean loads.

For each cycle of a specific amplitude and non-zero mean, we can find an equivalent loading amplitude of zero mean by defining

$$\begin{aligned} \frac{M_{a,R=-1}}{M_u - M_{m,R=-1}} &= \frac{M_a}{M_u - M_m}\,, \\ M_{a,R=-1} &= \frac{M_a(M_u - M_{m,R=-1})}{M_u - M_m}\,, \end{aligned} \tag{D.6}$$

where $M_{a,R=-1}$ is the equivalent amplitude for load cycle of zero mean and $M_{m,R=-1} = 0$ corresponding to zero mean.

Substituting Eq. (D.6) into (D.1), and combining with Eq. (D.5), we obtain,

$$D = \sum_{i=1}^{k} n_i \left(\frac{M_{a,i}(M_u - M_{m,R=-1})}{M_u(M_u - M_{m,i})} \right)^m . \tag{D.7}$$

With the computed damage D in Eq. (D.7), we can assume an equivalent loading with

constant moment amplitude $M_{a,eq}$ and number of cycles to fatigue N_{eq} that causes the same amount of damage. Hence, we can relate

$$\begin{aligned} N_{eq}\left(\frac{M_{a,eq}(M_u - M_{m,R=-1})}{M_u(M_u - M_{m,eq})}\right)^m &= \sum_{i=1}^{k} n_i \left(\frac{M_{a,i}(M_u - M_{m,R=-1})}{M_u(M_u - M_{m,i})}\right)^m , \\ M_{a,eq} &= \sum_{i=1}^{k}\left(\frac{n_i}{N_{eq}}\right)^{\frac{1}{m}} \frac{M_{a,i}(M_u - M_{m,eq})}{(M_u - M_{m,i})} . \end{aligned} \tag{D.8}$$

It is evident that if the ratio of two equivalent load spectra is to be taken, it will be independent of the chosen N_{eq} and $M_{m,eq}$. Note that this method is to find an equivalent load of constant amplitude for a load spectrum with cycles of different amplitudes and zero mean.

In practice, the lifetime damage of a wind turbine is estimated using a set of shorter time-series and hence the computed load spectra has to be extrapolated over the entire lifetime. Most wind turbines have a design life of 20 to 25 years. To compute the time to failure t_{fail}, we take the ratio between the design life t_{life} of the turbine against the computed damage over the lifetime D_{life}

$$t_{fail} = \frac{t_{life}}{D_{life}} . \tag{D.9}$$

For the wind turbine application, we make use of root-bending moments to calculate the equivalent load. This is done for a specific wind speed. As wind turbines operate across different wind speeds through its lifetime, we are able to sum up the equivalent loads computed for different wind speeds [70]. For instance, we compute equivalent loads for wind speeds at intervals of 1 m/s ranging from 10 m/s to 24 m/s and subsequently sum up the computed equivalent loads. This is done through a weighing factor $R_{w,j}$ which scales the equivalent loads to account for the fact wind turbines operate at a variety of wind speeds with a certain probability distribution throughout its entire lifetime

$$M_{a,eq} = \sum_{j=1}^{b} R_{w,j} M_{a,eq,j} , \tag{D.10}$$

where b is the number of wind speed bins simulated.

The weight $R_{w,j}$ can be computed by assuming a Rayleigh distribution of wind speeds given by the IEC [117]

$$P_R(V_j) = 1 - exp\left[-\pi\left(\frac{V_j}{2V_{ave}}\right)^2\right] , \tag{D.11}$$

where P_R gives the cumulative probability function, i.e. the probability that $V < V_j$ and $V_{ave} = 0.2V_{rel}$, which defines the mode (centre) of the distribution, with V_{rel} taken from the IEC table [117]. Subsequently, the weights/probability of wind speed V_j occurring can be computed using

$$R_{w,j} = P_R(V_j) - P_R(V_{j-1}) . \tag{D.12}$$

Appendix E

Model Reduction on Combined Rotor Description

Instead of reducing the structures and aerodynamics separately prior to coupling, an alternative is to define and reduce the aeroelastic description of the rotor prior to coupling with the tower structural dynamics. The coupled aeroelastic description of the system is given by Eq. 2.28 and restated here

$$\begin{bmatrix} \boldsymbol{A}_1 & -\boldsymbol{T}(t) \\ -\boldsymbol{\Psi}_1 & \boldsymbol{N}_1(t) \end{bmatrix} \begin{Bmatrix} \boldsymbol{\Gamma} \\ \boldsymbol{q} \end{Bmatrix}^{n+1} = \begin{bmatrix} \boldsymbol{A}_2 & \boldsymbol{0} \\ \boldsymbol{\Psi}_2 & -\boldsymbol{N}_2(t) \end{bmatrix} \begin{Bmatrix} \boldsymbol{\Gamma} \\ \boldsymbol{q} \end{Bmatrix}^{n} + \begin{Bmatrix} \boldsymbol{W} \\ \boldsymbol{0} \end{Bmatrix}^{n}, \tag{2.28}$$

where

$$\boldsymbol{q}^\top = \begin{bmatrix} \Delta\boldsymbol{\eta}_t^\top & \Delta\dot{\boldsymbol{\eta}}_t^\top & | & \Delta\boldsymbol{\eta}_r^\top & \Delta\dot{\boldsymbol{\eta}}_r^\top & | & \Delta\boldsymbol{\nu}_r^\top & \Delta\boldsymbol{\lambda}^\top \end{bmatrix} = \begin{bmatrix} \bar{\boldsymbol{q}}_t^\top & | & \bar{\boldsymbol{q}}_r^\top & | & \tilde{\boldsymbol{q}}_i^\top \end{bmatrix}. \tag{E.1}$$

If however, we express the downwash contribution from tower motion as a function of the rigid-body dof $\Delta\boldsymbol{\nu}_r$ of the rotor instead of the structural dof at tower top, the transformation matrix $\boldsymbol{T}$ will be time-invariant. The rigid-body dof of the rotor $\Delta\boldsymbol{\nu}_r$ is in the rotating frame. As a result, Eq. (2.28) becomes

$$\begin{bmatrix} \boldsymbol{A}_1 & -\boldsymbol{T} \\ -\boldsymbol{\Psi}_1 & \boldsymbol{N}_1(t) \end{bmatrix} \begin{Bmatrix} \boldsymbol{\Gamma} \\ \boldsymbol{q} \end{Bmatrix}^{n+1} = \begin{bmatrix} \boldsymbol{A}_2 & \boldsymbol{0} \\ \boldsymbol{\Psi}_2 & -\boldsymbol{N}_2(t) \end{bmatrix} \begin{Bmatrix} \boldsymbol{\Gamma} \\ \boldsymbol{q} \end{Bmatrix}^{n} + \begin{Bmatrix} \boldsymbol{W} \\ \boldsymbol{0} \end{Bmatrix}^{n}. \tag{E.2}$$

We identify the time-varying components of the matrices and rearrange them in the last row and columns. These are associated with the rigid-body rotor motion and Lagrange multipliers. Eq. (E.2) can be expressed as

$$\begin{bmatrix} \boldsymbol{L}_{11} & \boldsymbol{L}_{12} \\ \boldsymbol{L}_{21} & \boldsymbol{L}_{22}(t) \end{bmatrix} \begin{Bmatrix} \bar{\boldsymbol{x}} \\ \tilde{\boldsymbol{x}} \end{Bmatrix}^{n+1} = \begin{bmatrix} \boldsymbol{A}_{11} & \boldsymbol{A}_{12} \\ \boldsymbol{A}_{21} & \boldsymbol{A}_{22}(t) \end{bmatrix} \begin{Bmatrix} \bar{\boldsymbol{x}} \\ \tilde{\boldsymbol{x}} \end{Bmatrix}^{n} + \begin{Bmatrix} \boldsymbol{B}_{11} \\ \boldsymbol{B}_{21} \end{Bmatrix} \boldsymbol{u}^n, \tag{E.3}$$

where the time-invariant components are indicated with $(\bar{\bullet})$ and time-varying with $(\tilde{\bullet})$. The state $\bar{\boldsymbol{x}} = \begin{bmatrix}\boldsymbol{\Gamma}^\top & \bar{\boldsymbol{q}}_r^\top\end{bmatrix}^\top$ and $\tilde{\boldsymbol{x}} = \begin{bmatrix}\bar{\boldsymbol{q}}_t^\top & \tilde{\boldsymbol{q}}_i^\top\end{bmatrix}^\top$. The input $\boldsymbol{u}^n = \boldsymbol{W}^n$. Note that the tower dof $\bar{\boldsymbol{q}}_t$ are also included in the time-varying component of Eq. E.3 to avoid truncation in the model reduction process due to their small HSVs. The tower dof can be reduced through modal decomposition prior to the coupling.

From the first row

$$\boldsymbol{L}_{11}\bar{\boldsymbol{x}}^{n+1} + \boldsymbol{L}_{12}\tilde{\boldsymbol{x}}^{n+1} = \boldsymbol{A}_{11}\bar{\boldsymbol{x}}^{n} + \boldsymbol{A}_{12}\tilde{\boldsymbol{x}}^{n} + \boldsymbol{B}_{11}\boldsymbol{u}^{n}\,,$$

we express the time-varying component as inputs to the system

$$\bar{\boldsymbol{x}}^{n+1} = \boldsymbol{L}_{11}^{-1}\boldsymbol{A}_{11}\bar{\boldsymbol{x}}^{n} + \boldsymbol{L}_{11}^{-1}\begin{bmatrix}\boldsymbol{B}_{11} & -\boldsymbol{L}_{12} & \boldsymbol{A}_{12}\end{bmatrix}\begin{Bmatrix}\boldsymbol{u}^n\\ \tilde{\boldsymbol{x}}^{n+1}\\ \tilde{\boldsymbol{x}}^{n}\end{Bmatrix}. \tag{E.4}$$

The output is given by Eq. 2.25 as

$$\boldsymbol{y}^{n+1} = \bar{\boldsymbol{N}}_1\bar{\boldsymbol{x}}^{n+1} + \tilde{\boldsymbol{N}}_1\tilde{\boldsymbol{x}}^{n+1} + \bar{\boldsymbol{N}}_2\bar{\boldsymbol{x}}^{n} + \tilde{\boldsymbol{N}}_2\tilde{\boldsymbol{x}}^{n}\,,$$

and substituting Eq. (E.4)

$$\boldsymbol{y}^{n+1} = \bar{\boldsymbol{N}}_1\left(\boldsymbol{L}_{11}^{-1}\boldsymbol{A}_{11}\bar{\boldsymbol{x}}^{n} + \boldsymbol{L}_{11}^{-1}\begin{bmatrix}\boldsymbol{B}_{11} & -\boldsymbol{L}_{12} & \boldsymbol{A}_{12}\end{bmatrix}\begin{Bmatrix}\boldsymbol{u}^n\\ \tilde{\boldsymbol{x}}^{n+1}\\ \tilde{\boldsymbol{x}}^{n}\end{Bmatrix}\right) + \tilde{\boldsymbol{N}}_1\tilde{\boldsymbol{x}}^{n+1} + \bar{\boldsymbol{N}}_2\bar{\boldsymbol{x}}^{n} + \tilde{\boldsymbol{N}}_2\tilde{\boldsymbol{x}}^{n}\,,$$

$$\boldsymbol{y}^{n+1} = \left(\bar{\boldsymbol{N}}_1\boldsymbol{L}_{11}^{-1}\boldsymbol{A}_{11} + \bar{\boldsymbol{N}}_2\right)\bar{\boldsymbol{x}}^{n} + \left(\bar{\boldsymbol{N}}_1\boldsymbol{L}_{11}^{-1}\begin{bmatrix}\boldsymbol{B}_{11} & -\boldsymbol{L}_{12} & \boldsymbol{A}_{12}\end{bmatrix} + \begin{bmatrix}\boldsymbol{0} & \tilde{\boldsymbol{N}}_1 & \tilde{\boldsymbol{N}}_2\end{bmatrix}\right)\begin{Bmatrix}\boldsymbol{u}^n\\ \tilde{\boldsymbol{x}}^{n+1}\\ \tilde{\boldsymbol{x}}^{n}\end{Bmatrix}. \tag{E.5}$$

Eqs. (E.4) and (E.5) forms the linear state-space realisation to be reduced. Through balanced realisation, the transformed states can be expressed as the original states through $\boldsymbol{x}_r = \boldsymbol{T}_b\bar{\boldsymbol{x}}$, and truncation can be performed on $\boldsymbol{T}_b$ to remove rows that are insignificant in the input-output process.

The reduced system is assumed to be of the form

$$\boldsymbol{x}_r^{n+1} = \boldsymbol{A}_r\boldsymbol{x}_r^{n} + \begin{bmatrix}\boldsymbol{B}_{r,1} & \boldsymbol{B}_{r,2} & \boldsymbol{B}_{r,3}\end{bmatrix}\begin{Bmatrix}\boldsymbol{u}^n\\ \tilde{\boldsymbol{x}}^{n+1}\\ \tilde{\boldsymbol{x}}^{n}\end{Bmatrix}, \tag{E.6}$$

$$\boldsymbol{y}^{n+1} = \boldsymbol{C}_r\boldsymbol{x}_r^{n} + \begin{bmatrix}\boldsymbol{D}_{r,1} & \boldsymbol{D}_{r,2} & \boldsymbol{D}_{r,3}\end{bmatrix}\begin{Bmatrix}\boldsymbol{u}^n\\ \tilde{\boldsymbol{x}}^{n+1}\\ \tilde{\boldsymbol{x}}^{n}\end{Bmatrix}. \tag{E.7}$$

From the reduced state Eq. (E.6),

$$\begin{bmatrix} \boldsymbol{I} & \boldsymbol{B}_{r,2} \end{bmatrix} \begin{Bmatrix} \boldsymbol{x}_r^{n+1} \\ \tilde{\boldsymbol{x}}^{n+1} \end{Bmatrix} = \begin{bmatrix} \boldsymbol{A}_r & \boldsymbol{B}_{r,3} \end{bmatrix} \begin{Bmatrix} \boldsymbol{x}_r^{n} \\ \tilde{\boldsymbol{x}}^{n} \end{Bmatrix} + \boldsymbol{B}_{r,1} \boldsymbol{u}^n \,,$$

and concatenating with the second row of Eq. (E.3), we obtain

$$\begin{bmatrix} \boldsymbol{I} & \boldsymbol{B}_{r,2} \\ \boldsymbol{L}_{21} \boldsymbol{T}_b^{-1} & \boldsymbol{L}_{22}(t) \end{bmatrix} \begin{Bmatrix} \boldsymbol{x}_r^{n+1} \\ \tilde{\boldsymbol{x}}^{n+1} \end{Bmatrix} = \begin{bmatrix} \boldsymbol{A}_r & \boldsymbol{B}_{r,3} \\ \boldsymbol{A}_{21} \boldsymbol{T}_b^{-1} & \boldsymbol{A}_{22}(t) \end{bmatrix} \begin{Bmatrix} \boldsymbol{x}_r^{n} \\ \tilde{\boldsymbol{x}}^{n} \end{Bmatrix} + \begin{Bmatrix} \boldsymbol{B}_{r,1} \\ \boldsymbol{B}_{21} \end{Bmatrix} \boldsymbol{u}^n \,,$$

which can be expressed as

$$\begin{Bmatrix} \boldsymbol{x}_r^{n+1} \\ \tilde{\boldsymbol{x}}^{n+1} \end{Bmatrix} = \begin{bmatrix} \hat{\boldsymbol{A}}_{11} & \hat{\boldsymbol{A}}_{12} \\ \hat{\boldsymbol{A}}_{21} & \hat{\boldsymbol{A}}_{22} \end{bmatrix} \begin{Bmatrix} \boldsymbol{x}_r^{n} \\ \tilde{\boldsymbol{x}}^{n} \end{Bmatrix} + \begin{Bmatrix} \hat{\boldsymbol{B}}_{11} \\ \hat{\boldsymbol{B}}_{21} \end{Bmatrix} \boldsymbol{u}^n \,. \tag{E.8}$$

From the reduced output Eq. (E.7),

$$\boldsymbol{y}^{n+1} = \begin{bmatrix} \boldsymbol{C}_r & \boldsymbol{D}_{r,3} \end{bmatrix} \begin{Bmatrix} \boldsymbol{x}_r^{n} \\ \tilde{\boldsymbol{x}}^{n} \end{Bmatrix} + \boldsymbol{D}_{r,1} \boldsymbol{u}^n + \boldsymbol{D}_{r,2} \tilde{\boldsymbol{x}}^{n+1} \,,$$

and substituting the second row of Eq. (E.8)

$$\boldsymbol{y}^{n+1} = \begin{bmatrix} \boldsymbol{C}_r & \boldsymbol{D}_{r,3} \end{bmatrix} \begin{Bmatrix} \boldsymbol{x}_r^{n} \\ \tilde{\boldsymbol{x}}^{n} \end{Bmatrix} + \boldsymbol{D}_{r,1} \boldsymbol{u}^n + \boldsymbol{D}_{r,2} \left(\begin{bmatrix} \hat{\boldsymbol{A}}_{21} & \hat{\boldsymbol{A}}_{22} \end{bmatrix} \begin{Bmatrix} \boldsymbol{x}_r^{n} \\ \tilde{\boldsymbol{x}}^{n} \end{Bmatrix} + \hat{\boldsymbol{B}}_{21} \boldsymbol{u}^n \right) \,,$$

$$\boldsymbol{y}^{n+1} = \begin{bmatrix} \boldsymbol{C}_r + \boldsymbol{D}_{r,2} \hat{\boldsymbol{A}}_{21} & \boldsymbol{D}_{r,3} + \boldsymbol{D}_{r,2} \hat{\boldsymbol{A}}_{22} \end{bmatrix} \begin{Bmatrix} \boldsymbol{x}_r^{n} \\ \tilde{\boldsymbol{x}}^{n} \end{Bmatrix} + \left(\boldsymbol{D}_{r,1} + \boldsymbol{D}_{r,2} \hat{\boldsymbol{B}}_{21} \right) \boldsymbol{u}^n \,. \tag{E.9}$$

Bibliography

[1] H. Abedi, L. Davidson, and S. Voutsinas. Vortex method application for aerodynamic loads on rotor blades. In *Proceedings of the EWEC*, Vienna, Austria, 2013.

[2] International Energy Agency. Long-term research and development needs for wind energy for the time frame 2012 to 2030. Technical report, IEA, 2013.

[3] A. Ahlström. *Aeroelastic simulation of wind turbine dynamics.* PhD thesis, Royal Institute of Technology, Sweden, 2005.

[4] G. B. Airy. Tides and waves. *Encyclopaedia Metropolitana. Mixed Sciences*, 3, 1845.

[5] P. B. Andersen. *Advanced load alleviation for wind turbines using adaptive trailing edge flaps: Sensoring and control.* PhD thesis, Technical University of Denmark, 2010.

[6] P. B. Andersen, M. Gaunaa, C. Bak, and T. Buhl. Load alleviation on wind turbine blades using variable airfoil geometry. In *Proceedings of the EWEC*, Athens, Greece, 2006.

[7] P. B Andersen, M. Gaunaa, C. Bak, and M. H. Hansen. A dynamic stall model for airfoils with deformable trailing edges. *Journal of Physics Conference Series: The Science of Making Torque from Wind*, 78:012028, 2007. doi: 10.1088/1742-6596/75/1/012028.

[8] P. B. Andersen, L. Henriksen, M. Gaunaa, C. Bak, and T. Buhl. Deformable trailing edge flaps for modern megawatt wind turbine controllers using strain gauge sensors. *Wind Energy*, 13(2-3):193–206, 2010. doi: 10.1002/we.371.

[9] K. Argyriadis. Wind conditions for offshore wind turbine design, RECOFF, comparison of standards and regulations. Technical report, Recommendations for Design of Offshore Wind Turbines ENK5-CT-2000-00322, 2005.

[10] S. Ariduru. *Fatigue life calculation by rainflow counting method.* PhD thesis, Middle East Technical University, Turkey, 2004.

[11] K. J. Åström and R. M. Murray. *Feedback systems: An introduction for scientists and engineers.* Princeton University Press, Princeton; Oxford, UK, 2008.

[12] A. B. Bach, M. Lennie, G. Pechlivanoglou, C. N. Nayeri, and C. O. Paschereit. Finite micro-tab system for load control on a wind turbine. *Journal of Physics Conference*

Series: The Science of Making Torque from Wind, 75:012082, 2007. doi: 10.1088/1742-6596/524/1/012082.

[13] C. Bak. Research in aeroelasticity EFP-2006. Technical report, Risø-R-1611(EN), 2007.

[14] C. Bak and J. Johansen. Three-dimensional corrections of airfoil characteristics for wind turbines based on pressure distributions. In *Proceedings of the EWEC*, Athens, Greece, 2006.

[15] C. Bak, F. Zahle, R. Bitsche, T. Kim, A. Yde, L. C. Henriksen, A. Natarajan, and M. H. Hanse. Description of the DTU 10 MW reference wind turbine. Technical report, DTU Wind Energy Report-I-0092, 2013.

[16] T. K. Barlas and H. A. Madsen. Influence of actuator dynamics on the load reduction potential of wind turbines with distributed controllable rubber trailing edge flaps (CRTEF). In *Proceedings of the 22nd International Conference on Adaptive Structures and Technologies*, Corfu, Greece, 2011.

[17] T. K. Barlas and G. A. M. van Kuik. Aeroelastic modelling and comparison of advanced active flap control concepts for load reduction on the UpWind 5MW wind turbine. In *Proceedings of the EWEC*, Marseille, France, 2009.

[18] T. K. Barlas and G. A. M. van Kuik. Review of state of the art in smart rotor control research for wind turbines. *Progress in Aerospace Sciences*, 46(1):1–27, 2010. doi: 10.1016/j.paerosci.2009.08.002.

[19] T. K. Barlas, J. W. van Wingerden, A. W. Hulskamp, and G. A. M. van Kuik. Closed-loop control wind tunnel tests on an adaptive wind turbine blade for load reduction. In *Proceedings of the 46th AIAA Aerospace Sciences Meeting and Exhibition*, Reno, NV, USA, 2008. doi: 10.2514/6.2008-1318.

[20] T. K. Barlas, G. J. van der Veen, and G. A. M. van Kuik. Model predictive control for wind turbines with distributed active flaps: Incorporating inflow signals and actuator constraints. *Wind Energy*, 15(5):757–771, 2012. doi: 10.1002/we.503.

[21] T. K. Barlas, W. van Wingerden, A. W. Hulskamp, G. A. M. van Kuik, and H. E. N. Bersee. Smart dynamic rotor control using active flaps on a small-scale wind turbine: Aeroelastic modeling and comparison with wind tunnel measurements. *Wind Energy*, 16(8):1287–1301, 2013. doi: 10.1002/we.1560.

[22] M. S. Barlett. Periodogram analysis and continuous spectra. *Biometrika*, 37(1-2):1–16, 1950. doi: 10.1093/biomet/37.1-2.1.

[23] S. Basualdo. Load alleviation on wind turbine blades using variable airfoil geometry. *Wind Engineering*, 29(2):169–182, 2005.

[24] D. E. Berg, D. G. Wilson, B. R. Resor, M. F. Barone, and J. C. Berg. Active aerodynamic blade load control impacts on utility-scale wind turbines. In *Proceedings of the AWEA Windpower*, Chicago, IL, USA, 2009.

[25] D. E. Berg, J. C. Berg, D. G. Wilson, J. White, B. R. Resor, and M. A. Rumsey. Design, fabrication, assembly and initial testing of a SMART rotor. In *Proceedings of the 49th AIAA Aerospace Sciences Meeting and Exhibition*, Orlando, FL, USA, 2011. doi: 10.2514/6.2011-636.

[26] J. C. Berg, D. E. Berg, and J. White. Fabrication, integration, and initial testing of a SMART rotor. In *Proceedings of the 50th AIAA Aerospace Sciences Meeting and Exhibition*, Nashville, TN, USA, 2012. doi: 10.2514/6.2012-1291.

[27] J. C. Berg, M. F. Barone, and N. C. Yoder. SMART wind turbine rotor: Data analysis and conclusions. Technical report, SAND2014-0712, 2014.

[28] J. C. Berg, B. R. Resor, J. A. Paquette, and J. R. White. SMART wind turbine rotor: Design and field test. Technical report, SAND2014-0681, 2014.

[29] L. Bergami and M. Gaunaa. Stability investigation of an airfoil section with active flap control. *Wind Energy*, 13(2-3):151–166, 2010. doi: 10.1002/we.354.

[30] L. Bergami and M. Gaunaa. Analysis of aeroelastic loads and their contributions to fatigue damage. In *The Science of Making Torque from Wind*, Oldenburg, Germany, 2012.

[31] L. Bergami and M. Gaunaa. ATEFlap aerodynamic model, a dynamic stall model including the effects of trailing edge flap deflection. Technical report, Risø-R-1792(EN), 2012.

[32] L. Bergami and L. C. Henriksen. Cyclic control optimization for a smart rotor. In *Proceedings of the 8th PhD Seminar on Wind Energy in Europe 2012*, Zurich, Switzerland, 2012.

[33] L. Bergami and N. K. Poulsen. A smart rotor configuration with linear quadratic control of adaptive trailing edge flaps for active load alleviation. *Wind Energy*, 2014. doi: 10.1002/we.1716.

[34] L. Bergami, M. Gaunaa, and J. Heinz. Indicial lift response function: An empirical relation for finite-thickness airfoils, and effects on aeroelastic simulations. *Wind Energy*, 16(5):681–693, 2013. doi: 10.1002/we.1516.

[35] L. Bergami, V. A. Riziotis, and M. Gaunaa. Aerodynamic response of an airfoil section undergoing pitch motion and trailing edge flap deflection: A comparison of simulation methods. *Wind Energy*, 2014. doi: 10.1002/we.1759.

[36] A. P. F. Bernhard and I. Chopra. Trailing edge flap activated by a piezo-induced bending-torsion coupled beam. *Journal of the American Helicopter Society*, 44(1):3–15, 1998. doi: 10.4050/JAHS.44.3.

[37] R. L. Bielawa. *Rotary wing structural dynamics and aeroelasticity*. American Institute of Aeronautics and Astronautics, Reston, VA, USA, 2006.

[38] G. S. Bir. User's guide to MBC3 (multi-blade coordinate transformation utility for 3-bladed wind turbines). Technical report, NREL, 2008.

[39] G. S. Bir and J. M. Jonkman. Aeroelastic instabilities of large offshore and onshore wind turbines. Technical report, NREL/CP-500-41804, 2007.

[40] S. Bittanti and G. Guardabassi. Optimal periodic control and periodic systems analysis: An overview. In *Proceedings of the 25th Conference on Decision and Control*, Athens, Greece, 1986.

[41] E. A. Bossanyi. The design of closed loop controllers for wind turbines. *Wind Energy*, 3(3):149–163, 2001. doi: 10.1002/we.34.

[42] E. A. Bossanyi. Individual blade pitch control for load reduction. *Wind Energy*, 6(2): 119–128, 2003. doi: 10.1002/we.76.

[43] E. A. Bossanyi. GH bladed theory manual. Technical report, 282/BR/009, 2003.

[44] E. A. Bossanyi. Further load reductions with individual pitch control. *Wind Energy*, 8 (4):481–485, 2005. doi: 10.1002/we.166.

[45] E. A. Bossanyi, A. Kumar, and O. Hugues-Salas. Wind turbine control applications of turbine-mounted lidars. In *The Science of Making Torque from Wind*, Oldenburg, Germany, 2012.

[46] E. A. Bossanyi, B. Savini, M. Iribas, M. Hau, D. Fischer, B. Schlipf, T. van Engelen, M. Rossetti, and C. E. Carcangiu. Advanced controller research for multi-MW wind turbines in the UpWind project. *Wind Energy*, 15(1):119–145, 2012. doi: 10.1002/we.523.

[47] C. L. Bottasso, F. Campagnolo, A. Croce, and C. Tibaldi. Optimization-based study of bend-twist coupled rotor blades for passive and integrated passive/active load alleviation. *Wind Energy*, 16(8):1149–1166, 2013. doi: 10.1002/we.1543.

[48] C. L. Bottasso, A. Croce, C. E. D. Riboldi, and Y. Nam. Multi-layer control architecture for the reduction of deterministic and non-deterministic loads on wind turbines. *Renewable Energy*, 51:159–169, 2013. doi: 10.1016/j.renene.2012.08.079.

[49] C. L. Bottasso, S. Cacciola, and R. Riva. Floquet stability analysis of wind turbines using input-output models. In *Proceedings of AIAA Scitech - 32nd ASME Wind Energy Symposium*, National Harbor, MD, USA, 2014. doi: 10.2514/6.2014-0713.

[50] C. L. Bottasso, P. Pizzinelli, C. E. D. Riboldi, and L. Tasca. LiDAR-enabled model predictive control of wind turbines with real-time capabilities. *Renewable Energy*, 71: 442–452, 2014. doi: 10.1016/j.renene.2014.05.041.

[51] A. R. S. Bramwell, G. Done, and D. Balmford. *Bramwell's helicopter dynamics*. Butterworth-Heinemann, Oxford, UK, 2nd edition, 2001.

[52] N. Buckney, A. Pirrera, P. M. Weaver, and D. T. Griffith. Structural efficiency analysis of the Sandia 100m wind turbine blade. In *Proceedings of AIAA Scitech - 32nd ASME Wind Energy Symposium*, National Harbor, MD, USA, 2014. doi: 10.2514/6.2014-0360.

[53] T. Buhl, M. Gaunaa, and C. Bak. Potential load reduction using airfoils with variable trailing edge geometry. *Journal of Solar Energy Engineering*, 127(4):503–516, 2005. doi: 10.1115/1.2037094.

[54] C. S. Burrus, J. H. McClellan, A. V. Oppenheim, T. W. Parks, R. W. Schafer, and H. W. Schuessler. *Computer-based exercises for signal processing using MATLAB*. Prentice Hall, Englewood Cliffs, NJ, USA, 1994.

[55] T. Burton. *Wind energy handbook*. Wiley, Chichester, UK, 2nd edition, 2011.

[56] R. A. Calicom and W. E. Wiese. Control of time-periodic systems. *AIAA Journal of Guidance*, 7(6):671–676, 1984. doi: 10.2514/3.19911.

[57] C. W. Campbell. Monte Carlo turbulence simulation using rational approximations to von Kármán spectra. *AIAA Journal*, 24(1):62–66, 1986. doi: 10.2514/3.9223.

[58] D. Castaignet, N. K. Poulsen, T. Buhl, and J. J. Wedel-Heinen. Model predictive control of trailing edge flaps on a wind turbine blade. In *Proceedings of the American Control Conference*, pages 4398–4403, San Francisco, CA, USA, 2011.

[59] D. Castaignet, I. Couchman, N. K. Poulsen, T. Buhl, and J. J. Wedel-Heinen. Frequency-weighted model predictive control of trailing edge flaps on a wind turbine blade. *IEEE Transaction on Control Systems Technology*, 21(4), 2013. doi: 10.1109/TCST.2013.2260750.

[60] D. Castaignet, T. Barlas, T. Buhl, N. K. Poulsen, J. J. Wedel-Heinen, N. A. Olesen, C. Bak, and T Kim. Full-scale test of trailing edge flaps on a Vestas V27 wind turbine: Active load reduction and system identification. *Wind Energy*, 17(4):549–564, 2014. doi: 10.1002/we.1589.

[61] J-J. Chattot. Helicoidal vortex model for wind turbine aeroelastic simulation. *Computers and Structures*, 85(11-14):1072–1079, 2007. doi: 10.1016/j.compstruc.2006.11.013.

[62] P. K. Chaviaropoulos and M. O. L. Hansen. Investigating three-dimensional and rotational effects on wind turbine blades by means of a quasi-3D Navier-Stokes solver. *Journal of Fluids Engineering*, 122(2):330–336, 2000. doi: 10.1115/1.483261.

[63] I. Chopra and J. Sirohi. *Smart Structures Theory.* Cambridge University Press, New York, USA, 2014.

[64] R. P. Coleman. Theory of self-excited mechanical oscillations of hinged rotor blades. Technical report, NACA 1351, 1958.

[65] R. Cook. *Robust control of high altitude long endurance unmanned aerial vehicles using novel lift effectors.* PhD thesis, Imperial College London, UK, 2012.

[66] R. Cook, R. Palacios, P. J. Goulart, and I. Roberts. Robust manoeuvring and gust alleviation of very flexible aircraft using novel control. In *Proceedings of the International Forum of Aeroelasticity and Structural Dynamics*, Paris, France, 2011.

[67] R. Cook, R. Palacios, and P. J. Goulart. Robust gust alleviation and stabilization of very flexible aircraft. *AIAA Journal*, 51(2), 2013. doi: 10.2514/1.J051697.

[68] A. Cordle and J. M. Jonkman. State of the art in floating wind turbine design tools. In *Proceedings of the 21st International Offshore and Polar Engineering Conference*, Maui, HI, USA, 2011.

[69] D. A. Corson, T. Griffith, T. Ashwill, and F. Shakib. Investigating aeroelastic performance of multi-megawatt wind turbine rotors using CFD. In *Proceedings of the 53rd AIAA Structures, Structural Dynamics, and Materials Conference*, Honolulu, HI, USA, 2012. doi: 10.2514/6.2012-1827.

[70] N. Cosack. *Fatigue load monitoring with standard wind turbine signals.* PhD thesis, University of Stuttgart, Germany, 2010.

[71] F. N. Coton and T. Wang. The prediction of horizontal axis wind turbine performance in yawed flow using an unsteady prescribed wake model. *Proceedings of the Institution of Mechanical Engineers, Part A: Journal of Power and Energy*, 213(1):33–43, 1999. doi: 10.1243/0957650991537419.

[72] J. Dizy, R. Palacios, and S. T. Phino. Homogenisation of slender periodic composite structures. *International Journal of Solids and Structures*, 50(9), 2013. doi: 10.1016/j.ijsolstr.2013.01.017.

[73] S. D. Downing and D. F. Socie. Simple rainflow counting algorithms. *International Journal of Fatigue*, 4(1):31 – 40, 1982. doi: 10.1016/0142-1123(82)90018-4.

[74] D. M. Eggleston and F. S. Stoddard. *Wind turbine engineering design.* Springer, New York, USA, 1st edition, 1987.

[75] T. Ekelund. Dynamics and control of structural loads of wind turbines. In *Proceedings of the American Control Conference*, volume 3, pages 1720–1724, Philadelphia, PA, USA, 1998. doi: 10.1109/ACC.1998.707300.

[76] Enercon. http://www.enercon.de/en-en/. Accessed: 17-May-2014.

[77] M. Frederick. *Load reduction using rapidly deployed trailing-edge flaps.* PhD thesis, Imperial College London, UK, 2008.

[78] M. Frederick, E. C. Kerrigan, and J. M. R. Graham. Gust alleviation using rapidly deployed trailing-edge flaps. *Journal of Wind Engineering and Industrial Aerodynamics*, 98(12):712–723, 2010. doi: 10.1016/j.jweia.2010.06.005.

[79] G. Freebury and W. Musial. Determining equivalent damage loading for full-scale wind turbine blade fatigue tests. In *Proceedings of the 19th American Society of Mechanical Engineers Wind Energy Symposium*, Reno, NV, USA, 2000.

[80] Y. C. Fung. *An introduction to the theory of aeroelasticity.* Dover Publications, New York, USA, 1969.

[81] Gamesa. http://www.gamesacorp.com/en/. Accessed: 17-May-2014.

[82] M. Gaunaa. Unsteady 2D potential-flow forces on a thin variable geometry airfoil undergoing arbitary motion. Technical report, Risø-R-1478(EN), 2006.

[83] M. Gaunaa and P. B. Andersen. Load reduction using pressure difference on airfoil for control of trailing edge flaps. In *Proceedings of the EWEC*, Marseille, France, 2009.

[84] W. Gawronski. *Advanced structural dynamics and active control of structures.* Springer, New York, USA, 2004.

[85] GE Energy. http://www.ge-energy.com/wind. Accessed: 17-May-2014.

[86] M. Géradin and A. Cardona. *Flexible multibody dynamics: A finite element approach.* John Wiley, Chichester, England; New York, USA, 2001.

[87] M. Géradin and D. Rixen. *Mechanical vibrations: Theory and application to structural dynamics.* John Wiley, Chichester, England; New York, USA, 2nd edition, 1997.

[88] M. Geyler and P. Caselitz. Individual blade pitch control design for load reduction on large wind turbines. In *Proceedings of the EWEC*, Milan, Italy, 2007.

[89] I. P. Girsang, J. S. Dhupia, E. Muljadi, N. Singh, and L. Y. Pao. Gearbox and drivetrain models to study dynamic effects of modern wind turbines. In *Proceedings of IEEE Energy Conversion Congress and Exposition*, Denver, CO, USA, 2013.

[90] H. Glauert. *Airplane propellers. In Aerodynamic Theory. Durand, W. F. (Editor).* Dover, New York, USA, 1963.

[91] K. Glover. All optimal Hankel-norm approximations of linear multivariable systems and their l^{∞}-error bounds. *International Journal of Control*, 39(6):1115–1193, 1984. doi: 10.1080/00207178408933239.

[92] M. Goland. The flutter of a uniform cantilevered wing. *Journal of Applied Mechanics*, 12(4):A197A208, 1945.

[93] M. Green and D. J. N. Limebeer. *Linear robust control*. Prentice-Hall information and system sciences series. Prentice Hall, Englewood Cliffs, NJ, USA, 1995.

[94] D. T. Griffith. The SNL100-01 blade: Carbon design studies for the Sandia 100-meter blade. Technical report, SAND2013-1178, 2013.

[95] D. T. Griffith and T. D. Ashwill. The Sandia 100-meter all-glass baseline wind turbine blade: SNL100-00. Technical report, SAND2011-3779, 2011.

[96] D. T. Griffith, T. D. Ashwill, and B. R. Resor. Large offshore rotor development: Design and analysis of the Sandia 100-meter wind turbine blade. In *Proceedings of 53rd AIAA Structures, Structural Dynamics, and Materials Conference*, Honolulu, HI, USA, 2012. doi: 10.2514/6.2012-1499.

[97] S. Gupta and J. G. Leishman. Comparison of momentum and vortex methods for the aerodynamic analysis of wind turbines. In *Proceedings of the 43rd Aerospace Sciences Meeting and Exhibition*, Reno, NV, USA, 2005. doi: 10.2514/6.2005-594.

[98] M. H. Hansen. Aeroelastic instability problems for wind turbines. *Wind Energy*, 10(6): 551–577, 2007. doi: 10.1002/we.242.

[99] M.H. Hansen, M. Gaunaa, and H. A. Madsen. A Beddoes-Leishman type dynamic stall model in state-space and indicial formulations. Technical report, Risø-R-1354(EN), 2004.

[100] M.O.L. Hansen. *Aerodynamics of wind turbines*. Earthscan, Padstow, UK, 2nd edition, 2008.

[101] M.O.L. Hansen and H. A. Madsen. Review paper on wind turbine aerodynamics. *Journal of fluids engineering*, 133(11):114001–1–12, 2011.

[102] M.O.L. Hansen, J. N. Sørensen, S. G. Voutsinas, N. Sørensen, and H. A. Madsen. State of the art in wind turbine aerodynamics and aeroelasticity. *Progress in Aerospace Sciences*, 42(4):285–330, 2006. doi: 10.1016/j.paerosci.2006.10.002.

[103] S. Hauptmann, M. Bülk, S. Erbslöh, K. Boorsma, F. Grasso, M. Kühn, and P. W. Cheng. Impact of the lifting-line free vortex wake method on the simulated loads of multi-MW wind turbines. In *The Science of Making Torque from Wind*, Oldenburg, Germany, 2012.

[104] J. Helsen, G. Heirman, D. Vandepitte, and W. Desmet. The influence of flexibility within multibody modelling of multimegawatt wind turbine gearboxes. In *Proceedings of the International Conference on Noise and Vibration Engineering*, Leuven, Belgium, 2008.

[105] H. B. Hendriks and B. H. Bulder. Fatigue equivalent load cycle method - a general method to compare the fatigue loading of different load spectrums. Technical report, ECN-C-95-074, 1995.

[106] H. B. Hendriks and M. Zaaijer. Dutch offshore wind energy converter (DOWEC): Executive summary of the public research activities. Technical report, ECN, TU Delft, 2004.

[107] L. C. Henriksen, L. Bergami, and P.B. Andersen. A model based control methodology combining blade pitch and adaptive trailing edge flaps in a common framework. In *Proceedings of the EWEC*, Vienna, Austria, 2013.

[108] L. C. Henriksen, M. H. Hansen, and N. K. Poulsen. A simplied dynamic inflow model and its effect on the performance of free mean wind speed estimation. *Wind Energy*, 16(8):1213–1224, 2013. doi: 10.1002/we.1548.

[109] H. Hesse. *Consistent aeroelastic linearisation and reduced-order modelling in the dynamics of manoeuvring flexible aircraft.* PhD thesis, Imperial College London, UK, 2013.

[110] H. Hesse and R. Palacios. Consistent structural linearisation in flexible-body dynamics with large rigid-body motion. *Computers and Structures*, 110-111(0):1–14, 2012. doi: 10.1016/j.compstruc.2012.05.011.

[111] H. Hesse and R. Palacios. Model reduction in flexible-aircraft dynamics with large rigid-body motion. In *Proceedings of the 54th AIAA Structures, Structural Dynamics, and Materials Conference*, Boston, MA, USA, 2013. doi: 10.2514/6.2013-1895.

[112] H. Hesse and R. Palacios. Reduced-order aeroelastic models for the dynamics of maneuvering flexible aircraft. *AIAA Journal*, 52(8), 2014. doi: 10.2514/1.J052684.

[113] F. M. Hoblit. *Gust loads on aircraft: Concepts and applications.* AIAA Education Series, Washington, DC, USA, 2001. doi: 10.2514/4.861888.

[114] D. H. Hodges and G. A. Pierce. *Introduction to structural dynamics and aeroelasticity.* Cambridge aerospace series. Cambridge University Press, Cambridge, England; New York, USA, 2002.

[115] J. G. Holierhoek, J. B. de Vaal, A. H. van Zuijlen, and H. Bijl. Comparing different dynamic stall models. *Wind Energy*, 16(1):139–158, 2013. doi: 10.1002/we.548.

[116] I. Houtzager, J. W. van Wingerden, and M. Verhaegen. Wind turbine load reduction by rejecting the periodic load disturbances. *Wind Energy*, 16(2), 2013. doi: 10.1002/we.547.

[117] IEC 61400-1. Wind turbines - part 1: Design requirements. Technical report, International Electrotechnical Commission, 2006.

[118] IEC 61400-3. Wind turbines - part 3: Design requirements for offshore wind turbines. Technical report, International Electrotechnical Commission, 2009.

[119] C. S. Jakobsen, J. F. Camino, and I. F. Santos. Rotor-blade vibration control using a periodic LQR controller. In *Proceedings of the Brazilian Symposium on Intelligent Automation*, Fortaleza, Brazil, 2013.

[120] S. J. Johnson, J. P. Baker, C. P. van Dam, and D. Berg. An overview of active load control techniques for wind turbines with an emphasis on microtabs. *Wind Energy*, 13 (2-3), 2010. doi: 10.1002/we.356.

[121] B. L. Jones and E. C. Kerrigan. When is the discretization of a spatially distributed system good enough for control? *Automatica*, 46(9):1462–1468, 2010. doi: 10.1016/j.automatica.2010.06.001.

[122] B. J. Jonkman and L. Kilcher. NWTC Computer-Aided Engineering Tools (TurbSim). http://wind.nrel.gov/designcodes/preprocessors/turbsim/. Accessed 5-February-2014.

[123] B. J. Jonkman and L. Kilcher. TurbSim user's guide: Version 1.06.00. Technical report, NREL, 2012.

[124] J. M. Jonkman. Dynamics modeling and loads analysis of an offshore floating wind turbine. Technical report, NREL/TP-500-41958, 2007.

[125] J. M. Jonkman. Dynamics of offshore floating wind turbines - model development and verification. *Wind Energy*, 12:459–492, 2009. doi: 10.1002/we.347.

[126] J. M. Jonkman. Definition of the floating system for phase IV of OC3. Technical report, NREL/TP-500-47535, 2010.

[127] J. M. Jonkman and M. L. Buhl Jr. FAST user's guide. Technical report, NREL/EL-500-38230, 2005.

[128] J. M. Jonkman and W. Musial. Offshore code comparison collaboration (OC3) for IEA task 23 offshore wind technology and deployment. Technical report, NREL/TP-5000-48191, 2010.

[129] J. M. Jonkman, S. Butterfield, W. Musial, and G. Scott. Definition of a 5-MW wind turbine for offshore system development. Technical report, NREL/TP-500-38060, 2009.

[130] B. S. Kallesøe. A low-order model for analysing effects of blade fatigue load control. *Wind Energy*, 9(5):421436, 2006. doi: 10.1002/we.195.

[131] J. Katz and A. Plotkin. *Low speed aerodynamics*. Cambridge aerospace series. Cambridge University Press, Cambridge, UK; New York, USA, 2nd edition, 2001.

[132] N. D. Kelley and B. J. Jonkman. Overview of the TurbSim stochastic inflow turbulence simulator. Technical report, NREL/TP-500-41137, 2007.

[133] G. Kocer, M. Mansour, N. Chokani, R. S. Abhari, and M. Müller. Full-scale wind turbine near-wake measurements using an instrumented uninhabited aerial vehicle. *Journal of solar energy engineering*, 133(4):041011–1–8, 2011. doi: 10.1115/1.4004707.

[134] H. Küssner. Zusammenfassender Bericht über den instationären Auftried von Flügeln. *Luftfahrtforschung*, 13(12):410–424, 1935.

[135] M. A. Lackner and M. A. Rotea. Structural control of floating wind turbines. *Mechatronics*, 21:704–719, 2011. doi: 10.1016/j.mechatronics.2010.11.007.

[136] M. A. Lackner and G. A. M. van Kuik. A comparison of smart rotor control approaches using trailing edge flaps and individual pitch control. In *Proceedings of the 47th AIAA Aerospace Sciences Meeting and Exhibition*, Orlando, FL, USA, 2009. doi: 10.2514/6.2009-685.

[137] H. Lamb. *Hydrodynamics*. Cambridge University Press, Cambridge, UK; New York, USA, 6$^{\text{th}}$ edition, 1997.

[138] S. Lang and E. McKeogh. LIDAR and SODAR measurements of wind speed and direction in upland terrain for wind energy purposes. *Remote Sensing*, 3(9):1871–1901, 2011. doi: 10.3390/rs3091871.

[139] A. Lanzon and G. Papageorgiou. Distance measures for uncertain linear systems: A general theory. *Automatic Control, IEEE Trans*, 54(7):1532–1547, 2009. doi: 10.1109/TAC.2009.2022098.

[140] G. C. Larsen, H. A. Madsen, F. Bingöl, J. Mann, S. Ottm, J. N. Sørensen, V. Okulov, N. Troldborg, M. Nielsen, K. Thomsen, T. J. Larsen, and R. Mikkelsen. Dynamic wake meandering modeling. Technical report, Risø-R-1607(EN), 2007.

[141] T. J. Larsen and A. M. Hansen. How 2 HAWC2, the user's manual. Technical report, Risø-R-1597(ver. 4-3)(EN), 2012.

[142] T. J. Larsen, H.A. Madsen, and K. Thomsen. Active load reduction using individual pitch, based on local blade flow measurements. *Wind Energy*, 8(1):67–80, 2005. doi: 10.1002/we.141.

[143] A. J. Laub, M. T. Heath, C. C. Paige, and R. C. Ward. Computation of system balancing transformations and other applications of simultaneous diagonalization algorithms. *Automatic Control, IEEE Trans*, 32(2):115–122, 1987. doi: 10.1109/TAC.1987.1104549.

[144] T. Lee and I. Chopra. Design of piezostack-driven trailing-edge flap actuator for helicopter rotors. *Smart Materials and Structures*, 10(1):15–54, 2001. doi: 10.1088/0964-1726/10/1/302.

[145] J. G. Leishman. Challenges in modeling the unsteady aerodynamics of wind turbines. In *Proceedings of the 21st ASME Wind Energy Symposium*, Reno, NV, USA, 2002. doi: 10.2514/6.2002-37.

[146] J. G. Leishman. *Principles of helicopter aerodynamics*. Cambridge aerospace series. Cambridge University Press, Cambridge, UK; New York, USA, 2$^{\text{nd}}$ edition, 2006.

[147] J. G. Leishman and T. S. Beddoes. A semi-empirical model for dynamic stall. *Journal of the American Helicopter Society*, 34(3):3–17, 1989.

[148] W. E. Leithead, V. Neilson, S. Dominguez, and A. Dutka. A novel approach to structural load control using intelligent actuators. In *Proceedings of the 17th Mediterranean Conference on Control and Automation*, Makedonia Palace, Thessaloniki, Greece, 2009. doi: 10.1109/MED.2009.5164719.

[149] N. Li and M. J. Balas. Aeroelastic control of a wind turbine blade using microtabs based on UA97W300-10 airfoil. *Wind Engineering*, 37(5), 2013. doi: 10.1260/0309-524X.37.5.501.

[150] C. Lindenburg. Aeroelastic modelling of the LMH64-5 blade. Technical report, DOWEC-02-KL-083/0, 2002.

[151] D. W. Lobitz. Flutter speed predictions for MW-sized wind turbine blades. In *Proceedings of the EWEA Special Topic Conference: The Science of Making Torque from the Wind*, Delft, Netherlands, 2004.

[152] D. W. Lobitz. Parameter sensitivities affecting the flutter speed of a MW-sized blade. *Journal of Solar Energy Engineering*, 127(4):538–543, 2005. doi: 10.1115/1.2037091.

[153] D. W. Lobitz and P. S. Veers. Aeroelastic behavior of twist-coupled HAWT blades. In *Proceedings of the ASME Wind Energy Symposium held at 36th AIAA Aerospace Sciences Meeting and Exhibition*, Reno, NV, USA, 1998. doi: 10.2514/6.1998-29.

[154] D. W. Lobitz and P. S. Veers. Load mitigation with bending/twist-coupled blades on rotors using modern control strategies. *Wind Energy*, 6(2):105–117, 2003. doi: 10.1002/we.74.

[155] Q. Lu, R. Bowyer, and B. L. Jones. Analysis and design of Colemen transform-based individual pitch controllers for wind turbine load reduction. *Wind Energy*, 2014. doi: 10.1002/we.1769.

[156] J. M. Maciejowski. *Multivariable feedback design.* Addison-Wesley, Wokingham, UK, 1989.

[157] J. M. Maciejowski. *Predictive control with constraints.* Prentice Hall, Englewood Cliffs, NJ, USA, 2002.

[158] H. A. Madsen, P. B. Andersen, T. L. Andersen, C. Bak, and T. Buhl. The potentials of the controllable rubber trailing edge flap. In *Proceedings of the EWEC*, Warsaw, Poland, 2010.

[159] D. J. Malcolm and Hansen A. C. WindPACT turbine rotor design study. Technical report, NREL/SR-500-32495, 2006.

[160] J. Mann. Wind field simulation. *Probabilistic Engineering Mechanics*, 13(4), 1998. doi: 10.1016/S0266-8920(97)00036-2.

[161] J. F. Manwell, J. G. McGowan, and A. L. Rogers. *Wind energy explained: Theory, design and application*. Wiley, Chichester, UK, 2nd edition, 2009.

[162] H. Markou, P. B. Andersen, and G. C. Larsen. Potential load reductions on megawatt turbines exposed to wakes using individual-pitch wake compensator and trailing-edge flaps. *Wind Energy*, 14(7):841–857, 2011. doi: 10.1002/we.431.

[163] B. A. H. Marrant and T. van Holten. Concept study of smart rotor blades for large offshore wind turbines. In *Proceedings of OWEMES 2006*, Rome, Italy, 2006.

[164] K. W. McAlister, O. Lambert, and D. Petot. Application of the ONERA model of dynamic stall. Technical report, NASA TR 84-A-3, 1984.

[165] D. Micallef, M. Kloosterman, C. S. Ferreira, T. Sant, and G. van Bussel. Validating BEM, direct and inverse free wake models with the MEXICO experiment. In *Proceedings of the 52nd AIAA Structures, Structural Dynamics and Materials Conference*, Orlando, FL, USA, 2010. doi: 10.2514/6.2010-462.

[166] G. Moe. Linear wave theory. Technical report, IEA task 23 offshore wind technology and deployment subtask 2 Code Comparison Collaborative OC3, 2007.

[167] B. Moore. All optimal Hankel-norm approximations of linear multivariable systems and their l^∞-error bounds. *IEEE Transactions on Automatic Control*, 26(1):17–32, 1981. doi: 10.1109/TAC.1981.1102568.

[168] J. Murua. *Flexible aircraft dynamics with a geometrically-nonlinear description of the unsteady aerodynamics*. PhD thesis, Imperial College London, UK, 2012.

[169] J. Murua, R. Palacios, and J. Peiró. Camber effects in the dynamic aeroelasticity of compliant airfoils. *Journal of Fluids and Structures*, 26(4):527–543, 2010. doi: 10.1016/j.jfluidstructs.2010.01.009.

[170] J. Murua, R. Palacios, and J. M. R. Graham. Applications of the unsteady vortex-lattice method in aircraft aeroelasticity and flight dynamics. *Progress in Aerospace Sciences*, 55:46–72, 2012. doi: 10.1016/j.paerosci.2012.06.001.

[171] J. Murua, R. Palacios, and J. M. R. Graham. Assessment of wake-tail interference effects on the dynamics of flexible aircraft. *AIAA Journal*, 50(7):1575–1585, 2012. doi: 10.2514/1.J051543.

[172] W. Musial and S. Butterfield. Energy from offshore wind. Technical report, NREL/CP-500-39450, 2006.

[173] W. Musial, S. Butterfield, and A. Boone. Feasibility of floating platform systems for wind turbines. Technical report, NREL/CP-500-34874, 2004.

[174] H. Namik and K. Stol. Individual blade pitch control of floating offshore wind turbines. *Wind Energy*, 13(1):74–85, 2010. doi: 10.1002/we.332.

[175] National Renewable Energy Laboratory. http://www.NREL.gov. Accessed: 20-December-2011.

[176] B. F. Ng. Active aeroelastic design of large wind turbine blades for an increased fatigue life. Technical report, Imperial College London, 2012.

[177] B. F. Ng, R. Palacios, J. M. R. Graham, and E. C. Kerrigan. Robust control synthesis for gust load alleviation from large aeroelastic models with relaxation of spatial discretisation. In *Proceedings of the EWEC*, Copenhagen, Denmark, 2012.

[178] B. F. Ng, R. Palacios, J. M. R. Graham, and E. C. Kerrigan. Robust control synthesis for gust load alleviation from large aeroelastic models. In *Proceedings of the 8th PhD Seminar on Wind Energy in Europe*, Zurich, Switzerland, 2012.

[179] B. F. Ng, H. Hesse, R. Palacios, J. M. R. Graham, and E. C. Kerrigan. Aeroservoelastic modeling and load alleviation of very large wind turbine blades. In *AWEA Windpower*, Chicago, IL, USA, 2013.

[180] B. F. Ng, H. Hesse, R. Palacios, J. M. R. Graham, and E. C. Kerrigan. Aeroservoelastic state-space vortex lattice modeling and load alleviation of wind turbine blades. *Wind Energy*, 2014. doi: 10.1002/we.1752.

[181] B. F. Ng, R. Palacios, J. M. R. Graham, E. C. Kerrigan, and H. Hesse. Aerodynamic load control in HAWT with combined aeroelastic tailoring and trailing-edge flaps. *Wind Energy*, 2014. [Submitted].

[182] NWTC Computer-Aided Engineering Tools (FAST by Jason Jonkman, Ph.D.). http://wind.nrel.gov/designcodes/simulators/fast/. Accessed: 20-December-2011.

[183] K. Ogata. *Modern control engineering.* Prentice Hall, Upper Saddle River, NJ, USA, 4$^{\text{th}}$ edition, 2002.

[184] A. V. Oppenheim, R. W. Schafer, and J. R. Buck. *Discrete-time signal processing.* Prentice Hall, Upper Saddle River, NJ, USA, 2nd edition, 1999.

[185] S. Øye. Flex4 simulation of wind turbine dynamics. In *Proceedings of the IEA 28th Meeting of Experts on State of the Art of Aeroelastic Codes for Wind Turbine Calculations*, pages 71–76, Lyngby, Denmark, 1996.

[186] L. D. Paarmann. *Design and analysis of analog filters: A signal processing perspective.* Kluwer Academic Publishers, New York, Boston, Dordrecht, London, Moscow, 2003.

[187] R. Palacios. Structural dynamics part 2: Advanced topics and aeroelasticity. Technical report, A.430 Course notes, Imperial College London, 2010.

[188] R. Palacios and C. Cesnik. Cross-sectional analysis of non-homogeneous anisotropic active slender structures. *AIAA Journal*, 43(12):2624–2638, 2005. doi: 10.2514/1.12451.

[189] R. Palacios, J. Murua, and R. Cook. Structural and aerodynamic models in the non-linear flight dynamics of very flexible aircraft. *AIAA Journal*, 48(11):2559–2648, 2010. doi: 10.2514/1.J050513.

[190] P. Passon, M. Kühn, S. Butterfield, J. M. Jonkman, T. Camp, and T. J. Larsen. OC3 - benchmark exercise of aero-elastic offshore wind turbine codes. *Journal of Physics Conference Series: The Science of Making Torque from Wind*, 75:012071, 2007. doi: 10.1088/1742-6596/75/1/012071.

[191] C. Plumley, W. Leithead, P. Jamieson, E. Bossanyi, and J. M. R. Graham. Comparison of individual pitch and smart rotor control strategies for load reduction. *Journal of Physics Conference Series: The Science of Making Torque from Wind*, 524:012054, 2014. doi: 10.1088/1742-6596/524/1/012054.

[192] S. Putter and H. Manor. Natural frequencies of radial rotating beams. *Journal of Sound and Vibration*, 56(2):175–185, 1978. doi: 10.1016/S0022-460X(78)80013-3.

[193] J. B. Rawlings and D. Q. Mayne. *Model predictive control: Theory and design*. Nob Hill, Madison, USA, 2009.

[194] RECOFF. http://www.risoe.dk/vea/recoff/. Accessed: 11-Apr-2014.

[195] B. Resor and J. Paquette. Uncertainties in prediction of wind turbine blade flutter. In *Proceedings of the 52nd AIAA Structures, Structural Dynamics, and Materials Conference*, Denver, CO, USA, 2011. doi: 10.2514/6.2011-1947.

[196] B. Resor, J. Paquette, D. Laird, and T. Griffith. An evaluation of wind turbine blade cross section analysis techniques. In *Proceedings of the 48th AIAA Aerospace Sciences Meeting Including the New Horizons Forum and Aerospace Exposition*, Orlando, FL, USA, 2010. doi: 10.2514/6.2010-2575.

[197] B. Resor, D. Wilson, D. Berg, and J. Berg. Impact of higher fidelity models on simulation of active aerodynamic load control for fatigue damage reduction. In *Proceedings of the 48th AIAA Aerospace Sciences Meeting Including the New Horizons Forum and Aerospace Exposition*, Orlando, FL, USA, 2010. doi: 10.2514/6.2010-253.

[198] V. A. Riziotis and S.G. Voutsinas. Aero-elastic modelling of the active flap concept for load control. In *Proceedings of the EWEC*, Brussels, Belgium, 2008.

[199] B. Roget and I. Chopra. Wind-tunnel testing of rotor with individually controlled trailing-edge flaps for vibration reduction. *Journal of Aircraft*, 45(3):868–879, 2008. doi: 10.2514/1.28455.

[200] M. Sathyajith. *Wind energy: Fundamentals, resource analysis and economics*. Springer, Netherlands, 2006.

[201] D. Schlipf, D. J. Schlipf, and M. Kühn. Nonlinear model predictive control of wind turbines using lidar. *Wind Energy*, 16(7), 2013. doi: 10.1002/we.1533.

[202] A. K. Scholbrock, P. A. Fleming, L. J. Fingersh, A. D. Wright, D. Schlipf, and F. Haizman, F. Belen. Field testing LIDAR based feed-forward controls on the NREL Controls Advanced Research Turbine. In *Proceedings of the 51st AIAA Aerospace Sciences Meeting Including the New Horizons Forum and Aerospace Exposition*, Grapevine, TX, USA, 2013. doi: 10.2514/6.2013-818.

[203] K. M. Schweigler. *Aerodynamic analysis of the NREL 5-MW wind turbine using vortex panel methods.* PhD thesis, Chalmers University of Technology, Gothenburg, Sweden, 2012.

[204] T. Sebastian and M. A. Lackner. Development of a free vortex wake method code for offshore floating wind turbines. *Renewable Energy*, 46:269–275, 2012. doi: 10.1016/j.renene.2012.03.033.

[205] T. Sebastian and M. A. Lackner. Characterization of the unsteady aerodynamics of offshore floating wind turbines. *Wind Energy*, 16:339–352, 2013. doi: 10.1002/we.545.

[206] K. Selvam, S. Kanev, J. W. van Wingerden, and T. van Engelen. Feedback-feedforward individual pitch control for wind turbine load reduction. *International Journal of Robust and Non-linear Control*, 19(1):72–91, 2009. doi: 10.1002/rnc.1324.

[207] W. Z. Shen, R. Mikkelsen, J. N. Sørensen, and C. Bak. Tip loss corrections for wind turbine computations. *Wind Energy*, 8(4):457–475, 2005. doi: 10.1002/we.153.

[208] B. A. Shenoi. *Introduction to digital signal processing and filter design.* John Wiley, Hoboken, NJ, USA, 2006.

[209] Siemens. http://www.energy.siemens.com/hq/en/. Accessed: 17-May-2014.

[210] D. Simms, S. Schreck, M. Hand, and L.J. Fingersh. NREL unsteady aerodynamics experiment in the NASA-Ames wind tunnel: A comparison of predictions to measurements. Technical report, NREL/TP-500-29494, 2001.

[211] J. C. Simo and L. Vu-Quoc. On the dynamics in space of rods undergoing large motions - a geometrically exact approach. *Computer Methods in Applied Mechanics and Engineering*, 66(2):125–161, 1988. doi: 10.1016/0045-7825(88)90073-4.

[212] F. J. Simoes and J. M. R. Graham. Application of a free vortex wake model to a horizontal axis wind turbine. *Wind Engineering and Industrial Aerodynamics*, 39(1-3): 129–138, 1992. doi: 10.1016/0167-6105(92)90539-M.

[213] R. J. S. Simpson, R. Palacios, and J. Murua. Induced drag calculations in the unsteady vortex-lattice method. *AIAA Journal*, 51(7):1775–1779, 2013. doi: 10.2514/1.J052136.

[214] P. F. Skjoldan. *Aeroelastic modal dynamics of wind turbines including anisotropic effects*. PhD thesis, Technical University of Denmark, 2011.

[215] S. Skogestad and I. Postlethwaite. *Multivariable feedback control: Analysis and design*. John Wiley, Chichester, England, UK; Hoboken, NJ, USA, 2nd edition, 2005.

[216] J. Smit, L. O. Bernhammer, W. Navalkar, L. Bergami, and M. Gaunaa. Sizing and control of trailing edge flaps on a smart rotor for maximum power generation in low fatigue wind regimes. In *Proceedings of AIAA Scitech - 32nd ASME Wind Energy Symposium*, National Harbor, MD, USA, 2014. doi: 10.2514/6.2014-0874.

[217] S. W. Smith. *The scientist and engineer's guide to digital signal processing*. California Technical Publishing, San Diego, CA, USA, 1997.

[218] H. Snel. Heuristic modelling of dynamic stall characteristics. In *Proceedings of the EWEC*, pages 429–433, Dublin Castle, Ireland, 1997.

[219] H. Snel and J. G. Schepers. Engineering models for dynamic inflow phenomena. *Journal of Wind Engineering and Industrial Aerodynamics*, 39(1-3):267–281, 1992. doi: 10.1016/0167-6105(92)90552-L.

[220] H. Snel, B. Houwink, J. Bosschers, W. J. Piers, and G. J. W. van Bussel. Sectional prediction of 3-D effects for stalled flow on rotating blades and comparison with measurements. In *Proceedings of the EWEC*, Travemunde, Germany, 1993.

[221] J. N. Sørensen. *Three-level viscous-inviscid interaction technique for the prediction of separated flow past rotating wing*. PhD thesis, Technical University of Denmark - AFM-83-03, 1983.

[222] R. H. Stewart. Introduction to physical oceanography. Technical report, Department of Oceanography, Texas A & M University, 2008.

[223] K. A. Stol, M. Balas, and G. S. Bir. Floquet modal analysis of a teetered-rotor wind turbine. *Journal of Solar Energy Engineering*, 124(4):364–371, 2002. doi: 10.1115/1.1504846.

[224] K. A. Stol, W. Zhao, and A. D. Wright. Individual blade pitch control for the Controls Advanced Research Turbine (CART). *Journal of Solar Energy Engineering*, 128(4): 498–505, 2006. doi: 10.1115/1.2349542.

[225] J. G. Stuart, A. D. Wright, and C. P. Butterfield. Considerations for an integrated wind turbine controls capability at the National Wind Technology Center: An aileron control case study for power regulation and load mitigation. In *Proceedings of the AWEA Windpower*, Denver, CO, USA, 1996.

[226] J. G. Stuart, A. D. Wright, and C. P. Butterfield. Wind turbine control systems: Dynamic model development using system identification and the FAST structural dynamics code. In *Proceedings of the 35th AIAA Aerospace Sciences Meeting and Exhibit*, Reno, NV, USA, 1997. doi: 10.2514/6.1997-975.

[227] T. Theodorsen. General theory of aerodynamic instability and the mechanism of flutter. Technical report, NACA 496, 1936.

[228] Robust Control Toolbox. http://www.mathworks.co.uk/help/toolbox/robust. Accessed: 30-October-2010.

[229] N. Troldborg. *Computational study of the Risø-B1-18 airfoil equipped with actively controlled trailing edge flaps.* PhD thesis, Technical University of Denmark, 2004.

[230] UpWind. http://www.upwind.eu/. Accessed: 11-Apr-2014.

[231] U.S. Military specification. MIL-F-8785C. Technical report, 1980.

[232] C. P. van Dam, R. Chow, J. R. Zayas, and D. E. Berg. Computational investigations of small deploying tabs and flaps for aerodynamic load control. *Journal of Physics Conference Series: The Science of Making Torque from Wind*, 75:012027, 2007. doi: 10.1088/1742-6596/75/1/012027.

[233] G. J. van der Veen, J. W. van Wingerden, and M. Verhaegen. Closed-loop system identication of wind turbines in the presence of periodic effects. In *The Science of Making Torque from Wind*, Eraklion, Crete, Greece, 2010.

[234] T. G. Van Engelen and E. L. Van der Hooft. Individual pitch control inventory. Technical report, ECN-E-03-138, 2005.

[235] J. W. van Wingerden, A. W. Hulskamp, T. Barlas, B. Marrant, G. A. M. van Kuik, D. P. Molenaar, and M. Verhaegen. On the proof of concept of a 'Smart' wind turbine blade rotor blade for load alleviation. *Wind Energy*, 11:265–280, 2008. doi: 10.1002/we.264.

[236] J-W. van Wingerden, A. Hulskamp, T. Barlas, I. Houtzager, H. Bersee, G. A. M. van Kuik, and M. Verhaegen. Two-degree-of-freedom active vibration control of a prototyped 'Smart' rotor. *Control Systems Technology, IEEE Transactions*, 19(2):284–296, 2011. doi: 10.1109/TCST.2010.2051810.

[237] P. Veers. Three-dimensional wind simulation. Technical report, SAND88-0152, 1988.

[238] P. S. Veers, T. D. Ashwill, H. J. Sutherland, D. L. Laird, D. W. Lobitz, D. A. Griffin, J. F. Mandell, W. D. Musial, K. Jackson, M. Zuteck, A. Miravete, S. W. Tsai, and J. L. Richmond. Trends in the design, manufacture and evaluation of wind turbine blades. *Wind Energy*, 6(3):245259, 2003. doi: 10.1002/we.90.

[239] R. W. Vesel Jr and Jack. J. McNamara. Performance enhancement and load reduction of a 5 MW wind turbine blade. *Renewable Energy*, 66:391–401, 2014. doi: 10.1016/j.renene.2013.12.019.

[240] Vestas. http://www.vestas.com. Accessed: 17-May-2014.

[241] G. Vinnicombe. The robustness of feedback systems with bounded complexity controllers. *Automatic Control, IEEE Transactions*, 41(6):795–803, 1996. doi: 10.1109/9.506232.

[242] S. G. Voutsinas. Vortex methods in aeronautics: How to make things work. *International Journal of Computational Fluid Dynamics*, 20(1):3–18, 2006. doi: 10.1080/10618560600566059.

[243] H. Wagner. Über die Entstehung des dynamischen Auftriebes von Tragflügeln. *Zeitschrift für Angewandte Mathematik und Mechanik*, 5(1):17–35, 1925.

[244] Z. Wang, P. C. Chen, D. D. Liu, D. T. Mook, and M. J. Patil. Time domain nonlinear aeroelastic analysis for HALE wings. In *Proceedings of the 47th AIAA Structures, Structural Dynamics and Materials Conference*, Newport, Rhode Island, USA, 2006. doi: 10.2514/6.2006-1640.

[245] P. D. Welch. The use of fast Fourier transform for the estimation of power spectra: A method based on time averaging over short, modified periodograms. *IEEE Trans. Audio Electroacoustic*, AU-15(2), 1967. doi: 10.1109/TAU.1967.1161901.

[246] S. Y. Wie, S. Lee, and D. J. Lee. Potential panel and time-marching free-wake coupling analysis for helicopter rotor. *Journal of Aircraft*, 46(3), 2009. doi: 10.2514/1.40001.

[247] D. G. Wilson, D. E. Berg, D. W. Lobitz, and J. R. Zayas. Optimized active aerodynamic blade control for load alleviation on large wind turbines. In *Proceedings of the AWEA Windpower*, Houston, TX, USA, 2008.

[248] D. G. Wilson, D. E. Berg, M. F. Barone, J. C. Berg, B. R. Resor, and D. W. Lobitz. Active aerodynamics blade control design for load reduction on large wind turbines. In *Proceedings of the EWEC*, Marseille, France, 2009.

[249] D. G. Wilson, D. E. Berg, B. R. Resor, M. F. Barone, and J. C. Berg. Combined individual pitch control and active aerodynamic load controller investigation for the 5MW UpWind turbine. In *Proceedings of the AWEA Windpower*, Chicago, IL, USA, 2009.

[250] D. G. Wilson, B. R. Resor, D. E. Berg, T. K. Barlas, and G. A. M. van Kuik. Active aerodynamic blade distributed flap control design procedure for load reduction on the UpWind 5MW wind turbine. In *Proceedings of the 48th AIAA Aerospace Sciences Meeting and Exhibition*, Orlando, FL, USA, 2010. doi: 10.2514/6.2010-254.

[251] WindPACT. http://www.nrel.gov/wind/windpact.html. Accessed: 11-Apr-2014.

[252] XFOIL. http://web.mit.edu/drela/Public/web/xfoil/. Accessed: 30-April-2013.

[253] F. Zahle, C. Bak, S. Guntur, N. N. Sørensen, and N. Troldborg. Comprehensive aerodynamic analysis of a 10 MW wind turbine rotor using 3D CFD. In *Proceedings of AIAA Scitech - 32nd ASME Wind Energy Symposium*, National Harbor, MD, USA, 2014. doi: 10.2514/6.2014-0359.

[254] T. A. Zeiler. Results of Theodorsen and Garrick revisited. *Journal of Aircraft*, 37(5): 918, 2000.

[255] K. Zhou and J. C. Doyle. *Essentials of robust control*. Prentice Hall, Englewood Cliffs, NJ, USA, 1998.